High resolution X-ray spectroscopy on hydrothermal fluids

Mohammed Irar

Communauté
UNIVERSITÉ Grenoble Alpes

THÈSE

Pour obtenir le grade de

DOCTEUR DE LA COMMUNAUTE UNIVERSITE GRENOBLE ALPES

Spécialité : **PHYSIQUE DES MATERIAUX**

Arrêté ministériel : 25 mai 2016

Présentée par

Mohammed Irar

Thèse dirigée par **Jean-Louis Hazemann,** DR, CNRS, Grenoble

préparée au sein du **Laboratoire de l'institut Néel, CNRS,**
dans **l'École Doctorale de Physique**

Spectroscopie X haute résolution appliquée à l'étude des fluides hydrothermaux

High resolution X-ray spectroscopy applied to the study of hydrothermal fluids

Thèse soutenue publiquement le **22 Septembre 2017** ,
devant le jury composé de :

Mr. Laurent TRUCHE
Professeur à l'Université UGA, Grenoble, Président.
Mr. Rodolphe VUILLEUMIER
Professeur à l'Université ENS UPMC, Paris, Rapporteur.
Mr. Manuel MUNOZ
Professeur à l'Université Montpellier, Montpellier, Rapporteur.
Mme Marie-Christine BOIRON
Chargée de Recherche CNRS, G2R, Nancy, Examinateur.
Mme Elena BAZARKINA
Chargée de Recherche, IGEM, Moscow, Examinateur.
Mr. Jean-Louis HAZEMANN
Directeur de Recherche , CNRS, Institut Néel, Grenoble, Directeur de thèse.

Dedication

I dedicate my dissertation work to my family and many friends. A special feeling of gratitude to my late father, To my mother which the words can never express the deepest gratitude I have for her, she has been there for me my whole life and I love you so much for it. I mostly admire and love you for the person YOU are. To my brothers and sisters for their moral and psychological support in my life and espcially the days of my studies.

I also dedicate this work with a special feeling to my wife, a hidden energy and massive reality of my love, whose words of encouragement and push for tenacity ring in my ears daily. I still remember her words, which were shocked me, that she Keen on a bright future together and forever more than me. Surely, let me say that you are a great real wife and you wroth all of my soul.

I also dedicate this dissertation to my many friends who have supported me throughout the process. I will always appreciate all they have done, especially FAME and FAME-UHD beamlines team for their kindness, enthusiasm and dynamism during our collaboration, despite a fruitless result. Especially, my supervisor Dr. Jean-Louis Hazemann for his help and support at all levels, scientific and social lifes, I will never forget his keenness and stand up with me step by step, you worth all my greetings and appreciations. By judje my experience, work and disscussion with you, I can say seriously without hesistate a moment that you are a "GREAT MAN".

I dedicate this work and give special thanks to my best friend Prof. Ahmad BSIESY, Dr. Messaoud HARFOUCHE, my own doctor Dr. Suleiman DAHSHAN and Dr. Saleh AMRO for their kindfull help at all levels in France.

Finally, For those people are living in Genoble and working at UGA, CEA, ESRF and Néel Institute, I dedicate this work and seriously appreciate their efforts of a stand up with me.

Declaration

I certify that the work in this thesis entitled " High resolution X-Ray spectroscopy on hydrothermal fluids" has not previously been submitted for a degreen or has been submitted as a part of requirement for a degree to any other university or institute other than Grenoble Alpes University (UGA) or Néel Institute. I also certify that the thesis is an original piece of research and myself have written it. Any help and asistance that i have recieved in my research work and the preparation of the thesis itself have been appropriately acknowledged.

Materials of work and experiments have been carried out at European Synchrotron Radiation Facility (ESRF) / FAME beamline, and Néel Institute for preparation the materials and samples needed.

In addition, I certify that all information sources and literatures used are indicated in the thesis.

The work was done under the supervision of Dr. Jean-Louis HAZEMANN, Néel institute, Grenoble, France.

Mohammed M. A. IRAR

Acknowledgements

Many persons helped and supported me during my education in France and the three years of this PhD thesis at CNRS and ESRF at Grenoble.

Many thanks to Campus France for a financial support in the whole of my period study, as well as, my gratitude to French consulate at Jerusalem for their help and respects.

The first person I want to thank is of course my Ph.D. supervisor Dr. Jean-Louis HAZEMANN. He was a real ‘doctor father’ to me. I really appreciated you support through these three years and the many hours you dedicated to teach me how to manage things in my scientific life, to help me conduct the experiments at the synchrotron and especially to try to teach me, via countless corrections, how to communicate my results to the scientific community. I also liked your honesty, as I always found important to hear things, them being good or bad.

Many, many thanks for my colleagues Elena BAZARKINA, Olivier PROUX and Denis TESTEMALE for their help and discussion daily of the synchrotron and gave useful directions, comments or corrections during the data analyses and the writing of the thesis manuscript.

I will never to thank my colleagues Antonio Aguilar-Tapia for linguistic and scientific corrections for my thesis, and Olivier Proux for my help in EXAFS work and modifications.

In addition I also have to thanks all my colleagues from FAME beamline group for sharing tips in the lab or in the office, Isabelle Kieffer, William Del Net, Eric Lahera, Isabelle Llorens, Mauro Rovezzi, Antonio Aguilar-Tapia. Also, I would like to present many thanks to all the friends with whom I enjoined lunchs, dinners, coffee break, and amazing workshops sessions from CRG's group at ESRF and CNRS. Also I have to acknowledge all the people that made the life in the Institute so nice: Yves Joly and Michel Pirocchi.

Finally I want to thank my mother, my wife, and my family for all the support and the encouragements for always pushing me forward.

Abstract (English)

Knowledge about the properties of hydrothermal fluids, *i.e.* aqueous solutions at high temperature (T) and high pressure (P), are essential in the fields of earth sciences, prebiotic chemistry, nuclear industry and environmental sciences. Near the critical point (Pc, Tc) and under the pseudocritic conditions (*i.e.* at the critical density at T-P above Tc-Pc), the fluid properties change radically. These changes take place at different scales: the macroscopic scale (density and compressibility changes), the mesoscopic scale (agglomeration process between different clusters) and finally, the molecular scale (local organization of atoms and molecules, for example hydrogen bonds).

This study focuses on the solvation effects in different electrolytes as a function of temperature, pressure and concentration. The experimental study was carried out by X-ray absorption measurements, the technique suitable for probing both fluid density evolution and local atomic environment around the solutes. This study was carried out on pure water and salt solutions at different pressures (up to ~ 1.3Pc) and temperatures (up to ~ 2Tc), to pass from the liquid to the supercritical domain. A high pressure-high temperature, cell was used permitting to completely decouple the effects of pressure and temperature.

We have obtained experimental proofs about the displacement of the critical point and the isochore and their dependence on the salt concentration in the case of NaCl (0.3, 0.5 and 1.0 moles NaCl per kilogram of water). We have also observed a density anomaly in the supercritical region (SC) and the appearance of liquid-vapor phase separation for some aqueous solutions. The relative density increase in the critical zone is more pronounced for Cs>Rb>K>Na>Li for bromides and chlorides. The structural change in this region was followed by high-resolution XANES spectroscopy at the K-threshold of bromine for various alkali bromide. The interpretation of the XANES spectra clearly indicates drastic changes in the fluid structure related to this anomaly, which can be interpreted by the appearance of ionic pairs.

These new observations are related to water structure and solvation properties evaluation and consequently with hydrogen bonding changes under high T-P.

Keywords : X-Ray Absorption Spectroscopy, XANES, EXAFS, Ion-pairing, FDMNES, Density fluctuation, Supercritical fluids.

Abstract (French)

Les connaissances des propriétés des fluides hydrothermaux, c'est-à-dire des solutions aqueuses à haute température (T) et haute pression (P), sont essentielles dans les domaines des sciences de la terre, de la chimie prébiotique, de l'industrie nucléaire ou encore des sciences environnementales. Près du point critique (P_c, T_c) et dans les conditions pseudocritiques (*i.e.* pour des densités au dessus de T_c-P_c), les propriétés des fluides changent de manière radicale. Ces modifications ont lieu à différentes échelles: à l'échelle macroscopique (changements de densité et de compressibilité), à l'échelle mésoscopique (processus d'agglomération entre les différentes clusters) et enfin à l'échelle moléculaire (organisation local entre les atomes et les molécules, par exemple les liaisons hydrogène, H).

Cette étude est centrée sur les effets de la solvatation aqueuse de différents électrolytes en fonction de la température, pression et concentration. L'étude expérimentale a été conduite par les mesures d'Absorption X, technique de choix pour mesurer d'une part l'évolution de la densité du fluide et d'autre part sonder l'environnement atomique local autour des solutés. Cette étude a été faite sur l'eau pure et sur différentes solutions salines à différentes pressions (jusqu'à ~1.3P_c) et à température variable (jusqu'à ~2T_c), pour passer du domaine liquide au domaine supercritique, dans une cellule permettant de découpler totalement l'effet de la pression et de la température.

Nous avons obtenu des preuves expérimentales du déplacement du point critique et de l'isochore et de leur dépendance en fonction de la concentration en sel pour NaCl (0,3, 0,5 et 1,0 moles NaCl par kilogramme d'eau). Nous avons également observé une anomalie de densité dans la région supercritique (SC) et l'apparition d'une séparation des phases liquide-vapeur pour certaines solutions aqueuses. L'augmentation de la densité relative dans cette zone critique est plus prononcée pour Cs>Rb>K>Na>Li pour les bromures et les chlorures. Le changement structural dans cette région a été suivi par spectroscopie XANES haute résolution au seuil K du brome pour différents bromures d'alcalin. L'interprétation des spectres XANES indiquent clairement un changement drastique dans la structure locale du fluide au moment de l'apparition de cette anomalie pouvant être interprétée par l'apparition des paires ioniques.

Ces nouvelles observations sont a relier au changement structurale du solvant et principalement à l'évolution de son pouvoir de solvatation lié à l'évolution des liaisons hydrogène à hautes T-P.

Mots clés : Spectroscopie d'absorption des rayons X , XANES, EXAFS, paire d'ions, FDMNES, Fluctuation de densité, Les fluides supercritiques.

List of contents

List of Figures

2.9 - Picture showing the 0.8 mm Be window, Which install 3 of them in the area 4 in FIG. 2.8.

2.10 - Photograph of an oven (left) and a thermocouple (right) used in our experiments.

2.11 - Photograph of a vitreous carbon cell used for absorption measurements X (absorption and fluorescence). The pistons are shown with length 38 mm and 28 mm.

2.12 - Sketch of the two internal set-up. I_0, I_1, and I_2 correspond to the incident, transmitted, and fluorescence (or scattered) beams for aqueous samples. (1) Cylindrical internal cell with two inner tubes (in gray) above and below the sample. (2) Canal for the expanding sample. (3) Liquid metal sample. (4) Furnace.

3.1 - Setup of classical XAS measurements in the experimental hutch of FAME beamline "BM30b" at ESRF synchrotron.

3.2 - Liquid gas coexistence curve and critical isochore for pure water, calculated according to Ref.[1] (left). The solid lines mark the boundaries of the supercritical domain, the horizontal dashed lines the experimental isobars and the vertical ones the corresponding values of the temperature. Experimental absorption and density for pure water as a function of temperature " T without gradient temperature for isobaric process (right). Solid colour points are experimental T-P values at ρc extracted from absorption at given energy 13.7 KeV.

3.3 - The fit of real and experimental temperature in pure water at different pressures (280, 300, 345, 400 bars) . Temperature different between cell (T_{cell}) and real (T_{real}) values as a function of experimental density. Measurements are offset for clarity.

3.4 - Temperature difference between T_{cell} and T_{real} values measured in pure water (up) in comparison with it's specific heat capacity (down) in isobaric conditions as a function of density. Straight line corresponds to critical density.

3.5 - A) Theoretical density has taken from NIST[1] and B) Calculated density of pure water as a function of temperature extracted from X-ray absorption experiments at (280, 300 and 400 bar) done at 15 KeV.

3.6 - Experimental and theoretical fit comparison X-ray absorption of water at 280 bras, 300 bars and 400 bars at 15 KeV. The best base line (A) expected is 0.2563 of 280 bars, 0.2666 of 300 bars, and 0.27127 of 400 bars. The best sample thickness is 0.398 mm for all pressures used. (Theoretical extracted values from NIST database [1]).

3.7 - T–ρ diagram for H_2O. The solid curves represent an experimental and theoretical p–ρ isotherms at selected temperatures. The dashed curve represents the coexistence curve bounding the region of vapor–liquid equilibrium. The critical point is located at the top of the coexistence curve.

3.8 - Experimental X-ray absorption measurements in transmission mode for NaCl aqueous solutions at 13.7KeV as a function of temperature in comparison with pure water and theoretical prediction. The expected base line is - 0.9262 and sample thickness 0.398

cm, theoretical fit values of NaCl have been obtained from Thomas Driesner software "sawatflinc_ptx, version 0.2".[3,4]

3.9 - Compilation of theoretical data for vapor-liquid isotherms of NaCl-H_2O from 399°C to 451°C have been extracted from Thomas Driesner program "sawatflinc_ptx, version 0.2"[3,4].

3.10 - Liquid gas coexistence curve and critical isochore for pure water, calculated according to Ref.[1], and critical points of NaCl aqueous solutions (0.3 mol/kg, 0.5 mol/kg and 1.0 mol/kg). The solid lines mark the boundaries of the supercritical domain, the horizontal dashed lines the experimental isobars and the vertical ones the corresponding values of the temperature.

3.11- Different density of experimental and theoretical absorption in transmission mode measured in NaCl aqueous solutions at 13.7KeV as a function of temperature in comparison with pure water and theoretical prediction at 400 bars (left). Experimental X-ray absorption in transmission mode measured in NaCl aqueous solutions at 13.7KeV as a function of temperature in comparison with pure water and theoretical prediction at 400 bars (right). The expected base line is - 0.9301 and sample thickness 0.398 cm, theoretical fit values of NaCl were obtained from Thomas Driesner software "sawatflinc_ptx, version 0.2".[3,4]

3.12- Vapor-liquid critical locus of sodium chloride aqueous solution. given at certain concentration showing the parameters used in the equations.[5]

3.13- Experimental X-ray absorption measured in transmission mode of NaCl aqueous solutions 1.0 mol/kg at 13.7 KeV as a function of temperature under isobaric conditions at 345 bars in comparison with pure water and the theoretical prediction. The expected base line is - 0.9301 and sample thickness 0.398 cm. LF: Lower Fixed and UF: Upper Fixed.

3.14 - Experimental X-ray absorption in transmission mode measured in NaCl_1.0M aqueous solutions at 13.7KeV as a function of temperature in comparison with pure water and theoretical prediction. A) A carbon cell adapting for HPHT, B) scan of the carbon cell in vertical axis, C) classical XAS measurement. The expected base line is - 0.9301 and sample thickness 0.398 cm, theoretical fit values of NaCl have been extracted by Thomas Driesner program "sawatflinc_ptx, version 0.2"[3,4]. The beam path at the center of cell.

3.15- Experimental X-ray absorption in transmission mode measured in LiCl aqueous solutions at 15 KeV as a function of temperature in comparison with pure water and theoretical prediction. The expected base line is 0.27127 and sample thickness 0.398 cm.

3.16 - Experimental X-ray absorption measured in transmission mode for bromide, chloride, sulfate, and nitrate aqueous solutions (0.3 mol/kg) at 15KeV as a function of temperature in comparison with pure water at 300 bar. Sample thickness is 0.398 cm, without base line.

3.17- Experimental X-ray absorption measured in transmission mode for sulfate aqueous solutions 1.0 mol/kg at 12.5 KeV as a function of temperature in comparison with pure water. Sample thickness is 0.398 cm, and base line is 0.482.

3.18- Experimental X-ray absorption measured in transmission mode nitrate aqueous solutions at 12.5 KeV for 1.0 mol/kg as a function of temperature in comparison with pure water. Sample thickness is 0.398 cm, and base line is 0.482.

3.19 - Experimental X-ray absorption measured in transmission mode for LiBr aqueous solutions (1.0 mol/kg) at 13.7KeV as a function of temperature under isobaric conditions of 345 bars in comparison with pure water and theoretical prediction. The expected base line is - 0.9301 and sample thickness 0.398 cm. LF: Lower Fixed and UF: Upper Fixed.

3.20 - The set-up of experiments in the experimental hutch located on BM30b /CRG FAME beamline at ESRF, Grenoble - France.

3.21 - Scan of the carbon cell in vertical position of an experimental X-ray absorption in transmission mode measured in NaBr_1.0M aqueous solutions at 13 KeV (A) and 13.5 KeV (B) as a function of temperature at 400 bars. The expected base line is 0.482 and sample thickness 0.398 cm, The beam path fixed at lower part of cell.

3.22 - Set-up in the experimental hutch located in BM30B /CRG FAME beamline at ESRF, Grenoble - France.

3.23 - Experimental X-ray absorption measured in transmission mode for milli-Q water at isobaric condition (280 bars) as a function of temperature.

3.24 - Normalized XANES spectra at Br-K edge of 5 wt% alkaline Bromide salts at ambient conditions in transmission mode and HERFD-XAS collected from. Spectra are offset for clarity. The black arrow shows the pre-edge and peak features of high resolution of crystal analyzer spectrometer (CAS).

3.25 - Crystal tests of different energy ranges with two kind of crystal reflections Si and Ge. Analyzer energy, analyzer angle (α), bragg angle and elements positions are shown. The theoretical resolution (ΔE) of Br $K\beta_{1,3}$ is 0.89 eV whereas, experimentally is 1.4 eV.

3.26 - Normalized Br-K edge XANES spectra collected in transmission mode on alkaline bromide aqueous solutions (0.3 mol/kg) at 280 bars from ambient to supercritical conditions.

3.27 - Normalized Br-K edge XANES spectra collected in HERFD-XAS for alkaline bromide aqueous solutions (0.3 mol/kg) at 280 bar from ambient to supercritical conditions.

3.28 - Normalized Br-K edge XANES spectra collected in transmission detection mode of cesium bromide aqueous solutions (0.3 mol/kg) at 300 and 600 bar from ambient to supercritical conditions.

3.29 - Normalized Br-K edge XANES spectra collected in HERFD-XAS of cesium bromide aqueous solutions (0.3 mol/kg and 1.0 mol/kg) at 300 and 600 bar from ambient to supercritical conditions.

3.30 - Normalized Br-K edge and Rb-K edge XANES spectra collected in HERFD-XAS on cesium and rubidium bromide aqueous solutions (0.3 mol/kg) at 300 bar at supercritical region. Black spectrum in left figure is 5 wt% CsBr and black spectrum in right figure is saturated RbBr 6.0 mol/kg.

3.31 - Normalized Br-K edge and Rb-K edge XANES spectra collected in HERFD-XAS (0.3 mol/kg) at 300 bar and of Hydrogen bromide and Rubidium hydroxide aqueous solutions from ambient to supercritical conditions. Black spectra are saturated RbBr 6.0 mol/kg.

3.32 - Br K-edge XANES white lines collected in HERFD-XAS of alkaline bromide aqueous solutions (0.3 mol/k and 1.0 mol/kg) at 280, 300, and 600 bar as a function of temperature. The black arrow shows the dehydration process before increase the white lines. The vertical dashed line is guide the temperature value by increase the white line in anomalous effect.

3.33 - Br k-edge k^2-weighted EXAFS oscillation of alkaline aqueous solutions at 300 bar as a function of temperature. Spectra are corrected from the MEE effects.

3.34 - Br k-edge k^2-weighted DiffEXAFS oscillation of alkaline aqueous solutions at 300 bar as a function of temperature. Spectra are corrected from the MEE effects. Br-O and Br-alkaline backscattering amplitude functions were superimposed to determine visually if ion pairing occurs.

List of Tables

List of Abbreviations

FT	Fourier Transform
m	Molality units (number of moles of component per kg of water)
M	Molarity units (number of moles of components per liter of solvent)
ppm, ppb, ppt	Weight units: Part-Per-Million, Part-Per-Billion, Part-Per-Trillion
XAS	X-ray Absorption Spectroscopy
XAFS	X-ray Absorption Fine Structure
EXAFS	Extended X-ray Absorption Fine Structure
XANES	X-ray Absorption Near Edge Structure
wt%	Weight percents units: part-per-hundred
ESRF	European Synchrotron Radiation Facility
CNRS	Centre National de la Recherche Scientifique
FAME	French Absorption spectroscopy beamline in Material and Environmental sciences
XRS	X-ray Raman Scattering
FDMNES	Finite Difference Method Near Edge Structure
SCW	Supercritical Water
SCR	Supercritical Region
HERFD	High Energy resolution Fluorescence Detection
FWHM	Full width at half-maximum, Å
DCM	Double-crystal monochromator
ħ	Planck's constant, $\hbar = h/2\pi = 6.582 \times 10^{-16}$ eV.s
I	Transmitted X-ray photon intensity
$\mathbf{I_0}$	Incident X-ray photon intensity
$\mathbf{I_f}$	Intensity of fluorescence radiation
μ(E)	Experimental X-ray absorption coefficient, cm^2/g
RDF	Partial radial distribution function

Chapter 1: *Supercritical aqueous solutions*

1. Supercritical aqueous solutions

At a temperature and pressure above the critical point, a new domain is define in the phase diagram. This domain called "supercritical region" presents special properties. Supercritical water (SCW) is unique in that it exhibits both gas-like and liquid-like properties.[11] There are two important differences between liquid water at room temperature and water in the critical region. Firstly, the dielectric constant ε of water in the critical region is much lower than that of liquid water (Є = 78 at 27 C° and 5.3 at Tc),[11] as always happens at high temperatures and low densities. Secondly, liquid water is almost incompressible, but near to the critical point, water is a highly compressible fluid, which implies a large thermal-expansion coefficient and a large isobaric heat capacity. So for these reasons, water at critical region is very different than liquid water at room temperature. However, there are still some features, which remain unclear both for supercritical water and aqueous solutions. Specifically, the large decrease of the water dielectric constant ε decreasing the density is an indication of changes in the hydrogen bond network and which may, as well, affect the ion solvation.[12]

1.1 Introduction

Supercritical fluids are currently the subject of an increasing interest in both fundamental and applied research. Among supercritical fluids, water and aqueous solutions play a crucial role in many biochemical and geological processes.

Supercritical fluids are suitable as a substitute for organic solvents in a range of industrial and laboratory processes. Carbon dioxide and water are the most commonly used supercritical fluids, for decaffeination and power generation, respectively. CO_2 is the kind of extraction solvents for botanicals, it extraction process creates phase changes in carbon dioxide utilizing temperature and pressure. It leaves no toxic residue behind. Its extraction properties can be widely and precisely manipulated with subtle changes in pressure and temperature.[13–15]

Water is probably the most familiar chemical compound in the human experience, and also the most necessary. Water has a density ρ of about 1000 $Kg.m^{-3}$ at room temperature. All known life depends on the biochemistry that takes place in aqueous solution. Diverse disciplines in science as biochemistry, meteorology, and geology require the knowledge of properties of water and aqueous solutions. In the high-temperature aqueous physical chemistry of interest in my study, water is always present in the background as a medium, and sometimes takes a more active role. In 1913, Lawrence Henderson was recognized in his book "The Fitness of the Environment: An Inquiry into the Biological Significance of the Properties of Matter " which still very readable, since then more has been learned about the structure and properties of water at the molecular level, much of it through spectroscopic and thermodynamic experiments.[16]

The aim of my study is to obtain a qualitative or quantitative understanding of the thermophysical properties of water, particularly on how those properties behave at high temperatures and high pressures, and obtaining the most accurate values for the properties of pure water and aqueous solutions *i.e.* density, dielectric constant, etc. Therefore it is fundamental to understand and describe the intra- and intermolecular interactions involving the H_2O molecule, and in particular the role of hydrogen bonding, which is responsible for a large number of water features.

Water is a liquid at the temperatures and pressures that are most adequate for life. Specifically, water is a liquid in the range of 273.15 K (0 °C) and 373.15 K (100 °C) at 1 bar of pressure. In thermodynamics the triple point is defined by the temperature and the pressure at three phases (solid, liquid and gas) of that substance coexist in thermodynamic equilibrium, the single combination of pressure and temperature can coexist in a stable equilibrium the three phases of water at exactly 273.16 K (0.01 °C).[17–19]

The solubility of water as a solvent is very important for different compounds. Water is a polar solvent, so it is a good solvent for polar substances. In the other hand, nonpolar compounds are not easily incorporated into water molecules and the system become inhomogeneous. The increase of solubility of water as an effect of temperature is not easy to simplify. The dielectric constant and the degree of hydrogen bonding decrease at high temperatures therefore water behaves more like a nonpolar solvent (more able to dissolve nonpolar substances, less able to dissolve electrolytes) at those conditions.[12]

Supercritical fluids have properties between those of a gas and a liquid. In Table 1, the critical properties are shown for some components, which are commonly used as supercritical fluids.

In general, supercritical fluids have properties between those of a gas and a liquid and they can be summarized as:

(i) Supercritical fluids have highly compressed gases, which combine properties of gases and liquids in an intriguing manner.

(ii) Supercritical fluids can lead to reactions, which are difficult or even impossible to achieve in conventional solvents.

(iii) Solubility increases at increasing density (*i.e.* increasing pressure). Rapid expansion of supercritical solutions leads to precipitation of a finely divided solid.

(iv) The fluids are commonly miscible with permanent gases (*e.g.* N_2 or H_2) and it leads to much higher concentrations of dissolved gases than can be achieved in conventional solvents.[6,7,20]

Table 1: Critical properties for some components commonly used as supercritical fluids[6,7]

Solvent	Molecular weight (g/mol)	Critical Temperature (°C)	Critical Pressure (Bar)	Critical Density (g/cm^3)
Water-H_2O	18.015	373.95	220.64	0.322
Carbon dioxide (CO_2)	44.01	30.95	73.8	0.469
Methane (CH_4)	16.04	- 82.75	46	0.162
Ethane (C_2H_6)	30.07	32.15	48.7	0.203
Ethylene (C_2H_4)	28.05	9.5	50.4	0.215

1.2 Properties of pure water:

Water is an universal solvent in our planet and plays an important role in inorganic chemistry, it is important for life and humanity, one of the things that makes our planet special. The study of water properties is completely different than those at supercritical conditions. At this conditions a new phase of water make us curious to going deeply discovering its structure and features. Certainly, understanding of water behavior will lead us to understand the behavior of a solution when adding ions (salts) and about its physicochemical properties (density, viscosity, molecular shape, solubility, etc).

1.2.1 Properties and structure of the water

The water molecule is composed of one oxygen and two hydrogen atoms at normal conditions. The bonding angle of the two hydrogens is approximately 104.45°, and the distance from the center of the oxygen atom to the center of each hydrogen atom is approximately 0.096 nm as show in FIG 1.1. This geometry varies slightly, depending on the rotation and vibration state of the molecule and on its surroundings. The structure also will change if the surrounding conditions change, and also its physical and chemical characteristics.

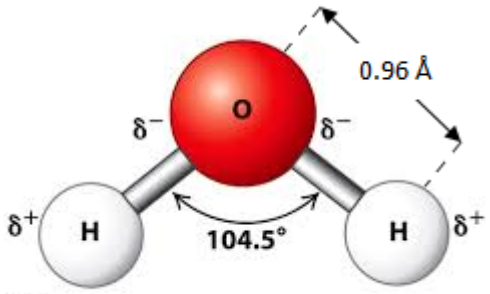

FIG. 1.1 - Structure of water molecule.[12]

Beyond the critical point (> 220.064 bar, > 373.95 °C, 0.322 g/cm3), the interest studies of the structure and dynamics of water at high temperature and pressure has been increasing and in particular, at supercritical conditions, the thermochemical properties of sub and supercritical water are remarkable different from those of ambient water. At supercritical conditions, water characterized at the microscopic scale by density fluctuations: areas with gaslike density coexist with area with liquid-like density. SCW existing as small but liquid-like hydrogen-bonded clusters dispersed within a gas-like phase, where physical properties, such as gas-like or liquid-like behavior, vary in response to changing temperature, pressure and density and the normal distinction between gas and liquid has disappeared. The most important aspect of the phase diagram for most purposes is the coexistence between vapor and liquid. The vapor pressure increases with temperature up to reaching a point where the liquid (expanded with increasing temperature) and the vapor (compressed by the higher pressure) become identical.[21,22]

The properties of supercritical water are different from ambient liquid water. For example, supercritical water is a poor solvent for electrolytes, which tend to form ion pairs. However, it is such an excellent solvent for non-polar molecules, due to its low relative permittivity (dielectric constant) and poor hydrogen bonding, that many are completely miscible when increase the tempeature at SC region. Viscosity and dielectric constant both decrease substantially whereas self-dissociation increases substantially. The physical properties of water close to the critical point (near-critical) are particularly strongly affected by density and has high compressibility.[13,22,23]

The decrease of the dielectric constant of SCW allows non polar substances to be dissolved. The solubility of ionic and polar substances decrease at this conditions; moreover, the molecular mobility is enhanced in SCW conditions due to the decrease in viscosity. Therefore, chemical reactions kinetics can be monitored by changing the density which can be tuned from gas-like to liquid-like densities. The behavior of SCW is thought to be related to the change of the hydrogen bond network. The experimental investigations of the intermolecular structure will provide an idea for understanding the properties of SCW. The structure of SCW has been investigated using X-ray and neutron experiments in various techniques. It has been found that the tetrahedral arrangement of water molecule observed in liquid water vanishes in supercritical state. Thus the number of hydrogen bonds per water molecule, which is about 3.5 in the liquid state, decreases to about 1.8 in dense SCW. Simulations softwares as Molecular Dynamics and Mote Carlo have been widely used to provide some insights in the underlying structure of SCW. Spectroscopic studies have been reported because the experimental challenge of high temperature and pressures. The temperature for the total breakdown of hydrogen bonding has been debated for many years, with most experimental studies, including Raman spectroscopy, X-ray scattering, and infrared spectroscopy, suggesting that tetrahedral bonding persists to at least 650 K and possibly up to 770 K at 100 MPa.[13,15,24,25]

1.2.2 Phase diagram of water

A phase diagram is a graphical representation of the properties of any substance and the points at which it changes phase. It is used in thermodynamics to denote the necessary conditions for a transition of a substance between its three states: solid, liquid, and gas. The triple point is a unique condition where the three phases coexist at the same point. The triple point of water is reached at 273.16 K and 611.657 ± 0.01 Pa. FIG. 1.2 shows a typical pressure-temperature phase diagram [12,26,27]. The phase diagram of water is complex, having a number of triple points and critical points. Many of the crystalline forms may remain metastable in much of the low-temperature phase space at lower pressures. Thermodynamic functions of the phase transitions have been described. The region we are interested to study is SC region, it begins from the critical point when increase the temperature and pressure.

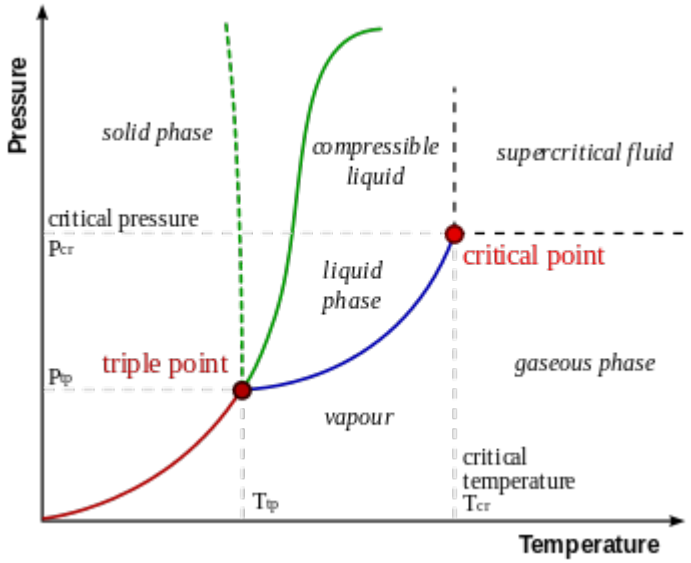

FIG. 1.2 - The liquid-vapor critical point in a pressure–temperature phase diagram is at the high-temperature extreme of the liquid–gas phase boundary. The dotted green line shows the anomalous behavior of water.[27,28]

A phase diagram typically shows temperature along the x-axis, and pressure along the y-axis. Liquids occupy the area of the phase diagram corresponding to relatively high temperatures and high pressures. Gases or vapors, on the other hand, can exist at very low temperatures, but only if the pressure is also low. Above the melting point of water, gases exist at higher pressures and higher temperatures. For simple substances, such as water, the solid form of the substance appears at a relatively low temperature and at pressures anywhere from zero upward. The single combination of pressure and temperature at which liquid water, solid ice, and water vapor can coexist in a stable equilibrium occurs at exactly 273.16 K. The equation given by Wagner describe the water with temperature below an equilibrim point. In thermodynamics, there is a representation from 190 to 273.16 K by a equation (1) given by Wagner in 1994:[12,29]

$$\ln\left(\frac{P_{sub1}}{P_t}\right) = a_1\left(1-\theta_t^{-1.5}\right) + a_2\left(1-\theta_t^{-1.25}\right), \qquad (1)$$

where $\theta_t = T/T_t$, $T_t = 273.16$ K, $P_t = 611.657$ Pa, $a_1 = -13.92817$, and $a_2 = 34.70782$.

The most important aspect of the phase diagram for most purposes is the coexistence between vapor and liquid (vapor-pressure curve). The vapor pressure increases with temperature, up to reaching a point where the liquid and the vapor become identical.[12,16,22] The vapor pressure of water at a given temperature is lower than that of other substances (such as H2S and NH3). The interactions between water molecules increase the thermal energy required to remove molecules from the liquid to the vapor and appearance strong hydrogen bonding in liquid water. FIG. 1.3 shows the phase diagram with a constant of density at different T-P.

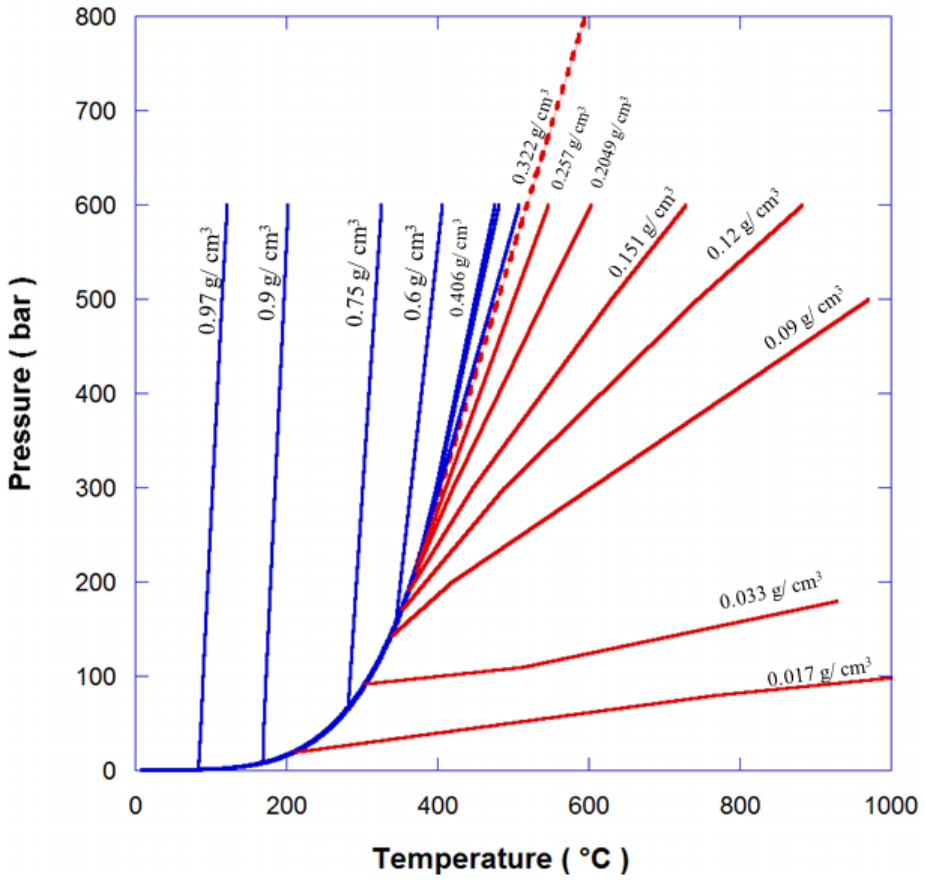

FIG. 1.3 - Liquid gas coexistence curve and critical isochore for pure water, showing the isolette at different densities.[1]

1.2.3 Critical point and Supercritical region

The critical point is the end point of a phase equilibrium curve this end point of the pressure-temperature curve that indicates the conditions at which a liquid and its vapor can coexist. The values of critical point for water other solutions have been shown in the Table 1. Above the critical point the substance exists a state of matter that is continuously connected with both the liquid and the gaseous state. It is called supercritical fluid, whereas this region locate at a temperature and pressure above its critical point. Carbon dioxide and water are the most commonly used supercritical fluids.

At critical point, the isothermal compressibility $K_T = -1/V(\partial V/\partial p)_T$ from the diverging fluid, also the isobaric compressibility $K_p = 1/V(\partial V/\partial T)_P$, $(\partial p/\partial V)_T = 0$ and $(\partial p^2/\partial V^2)_T = 0$. Which corresponds to infinitely fast local fluctuations of the density during an isothermal variation of the pressure.[30] Moreover, these fluctuations in density give the supercritical fluids properties both of the gas type and of the liquid type. Thus, these fluids are known to have exceptional transport capacities and speeds, amplified by a low gas-like viscosity. More precisely, the dynamic viscosity of the supercritical fluids is of the order of 10^{-5} to 10^{-4} Pa.s, while that of the gases is of the order of 10^{-5} Pa.s and that of the liquids of 10^{-3} Pa.s. Moreover, the transport speed is given by the diffusion coefficient, for example for small molecules, which is of the order of 10^{-8} $m^2.s^{-1}$ (in the case of supercritical fluids), 10^{-9} $m^2.s^{-1}$ (liquids) and 10^{-5} $m^2.s^{-1}$ (gases).[12,30,31]

Regarding the divergence of the isothermal compressibility of the supercritical fluids, it is possible to control very precisely the density of the medium by finaly varying the temperature and the pressure and therefore its transport properties. This capacity that is used in many industrial processes ranging from extraction (coffee, essential oils ...) to oxidation and synthesis mechanisms.

At the critical point there is about 30% free monomeric H_2O molecules and only about 17% hydrogen bonding; but this is far greater than in the gas phase. It is heterogeneous, and instantaneous properties vary over a wide range between the different structural forms, giving 'average' properties that are, perhaps, not representative. Supercritical water, as with other supercritical fluids, has no surface tension with its gas or liquid phase or any other supercritical phase because such interfaces does not exist. Above 647.096 K, water vapor cannot be liquefied by increasing pressure.[32–35]

In case of properties at critical point, phase boundaries of liquid water and vapor disappear. In water, the critical point occurs at around 647 K (374 °C; 705 °F) and 22.064 MPa (3200 PSIA or 218 atm). At the critical point there is no change of state when pressure or temperature are increased. Thus, the water and steam can not be distinguished. To understand what happens at the critical point, consider the effects of temperature and pressure on the densities of liquids and gases, respectively. As the temperature or pressure of a liquid increases, its density decreases. At the critical point, the liquid and gas phases have exactly the same density, and only a single phase exists. This single phase is called ' supercritical fluid' and exhibits many of the properties of a gas but has a more typical density of a liquid. For example, the density of water at its critical point (T = 374°C, P = 22.064 MPa) is 0.32

g/ml, about one-third than liquid water at room temperature but much greater than that of water vapor under most conditions.

Briefly, we can say that the properties of supercritical water are very different from liquid ambiet water. For example, supercritical water is a poor solvent for electrolytes and tends to form ion pairs. However, it is such an excellent solvent for non-polar molecules, due to its low relative permittivity (dielectric constant) and poor hydrogen bonding, that many are completely miscible. Viscosity and dielectric constant both decrease substantially whereas auto-dissociation increases substantially. The physical properties of water close to the critical point (near-critical) are particularly strongly affected by density. Extreme density fluctuations around the critical point causes opalescent turbidity. Neutron diffraction has shown that tetrahedral liquid-like states are observed in supercritical water at above a threshold density, while below this threshold density gas-like water forms small, trigonal, sheet-like configurations.[12,36]

1.2.4 Hydrogen bonds

Molecule water in liquid phase

Attractive forces, essentially of electrostatic origin, are present in the liquid water, leading to the formation of bonds, between the electronegative atoms of oxygen and the hydrogen atoms. The hydrogen of a molecule remains bouned covalently to the oxygen atom, but is attracted by the oxygen of a neighboring water molecule. The energy of this type of bond is about 19 $kJ \bullet mol^{-1}$, which is higher than the Van-Der Waals interactions (between 1 and 4 $kJ \bullet mol^{-1}$), but much lower than the binding energies of covalence (between 200 and 800 $kJ \bullet mol^{-1}$, 492 $kJ \bullet mol^{-1}$ for the intramolecular O-H bond).[31,37–39]

These bonds are very special in nature, because they involve only hydrogen atoms, which very small size and tendency to positively polarize allow a fairly intense interaction with the neighboring electronegative atoms. The structure of liquid water is thus given by the existence of the bond hydrogen.[40] Thus, a short-range order corresponds to the formation of aggregates of water molecules with a tetrahedral structure close to that of ice *I* (The ice-like solid phase *I* has a hexagonal structure, where the typical hydrogen bond distance is around 1.8 Å).[37] The structure is shown in FIG. 1.4, each water molecule can theoretically form four hydrogen bonds.

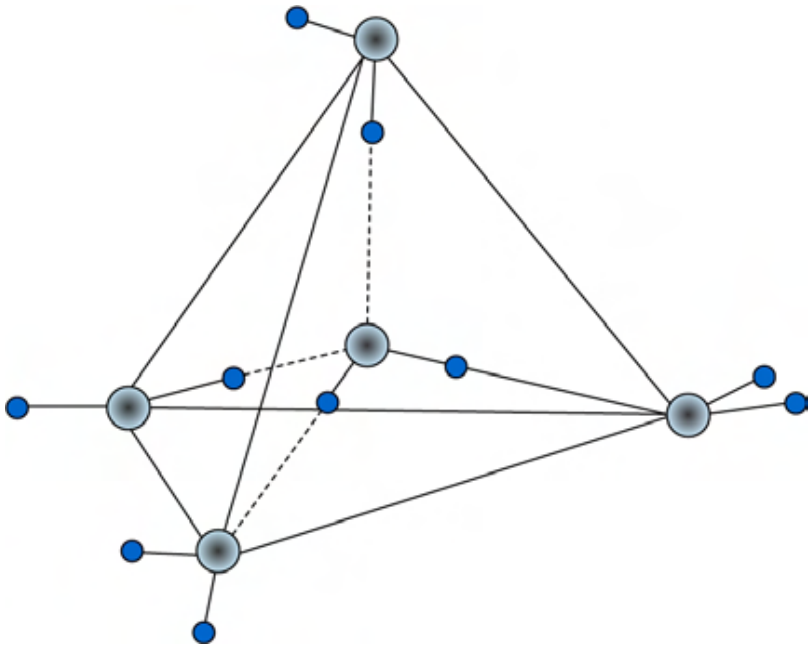

FIG. 1.4 - Schematic of tetrahedral coordination of water molecules by hydrogen bonds.[37]

Definition of hydrogen bonding

Two criteria are possible and important in hydrogen bonds, the geometry and energy. The first describes the distances and the angles corresponding to the considered connections. The energy definition consists in choosing a threshold value for the interaction energy of a ionic pair: below the threshold, there is no hydrogen bonding, while above, the energy corresponds to two linked molecules. On the other hand, the average number of hydrogen bonds per water molecule can be written by nH, and in ambient conditions of temperature and pressure, the definition is precisely bound of hydrogen bonds[22]. The average number of hydrogen bonds nH depends on the critera, the influence of the simulations is between 3.5 and 3.73, which means that between 77% and 81% of the water molecules have structures with 3 or 4 hydrogen bonds per molecule.[31,41]

At ambient condition, the life time for hydrogen bond is 10^{-13} to 10^{-12} seconds for water at 80 °C and the super cooled water at -20 °C.[37] The presence of these hydrogen bonds influences the dipole moment, If we no longer consider the isolated molecule but immersed in its aqueous environment, the dipole moments of each molecule are influence by those of the neighboring molecules. This interaction corresponds to the Van der Waals interaction between the dipoles, thus, the dipole moment in the gaseous phase is equal to 1.85 Debye for an isolated molecule, and approximately 2.8 Debye in liquid water.[42]

Covalence of hydrogen bonding

The chemical bonds that occur between atoms and molecules are very important type of bonds, they are hydrogen bonds and covalent bonds. A bond between two non-metals is usually covalent whereas a bond between a metal and a non-metal is ionic. By definition, a covalent bond is a form of a chemical bond that occurs due to the sharing of electron pairs

between the same or distinct atoms.[42–45] Covalent bond, in turn, refers to the stable balance of force (both attractive and repulsive) between atoms when they share electrons.[46] The sharing allows each atom involved to attain an outer shell that is equivalent to a full valence shell or outer shell. This accounts for a stable configuration of electrons. In contrast, a hydrogen bond is an electrostatic attraction between special types of molecules, known as polar molecules. The bond only occurs when a hydrogen atom already bonded to a highly electronegative atom (oxygen, nitrogen or fluorine) experiences another force of attraction from a nearby atom that is also highly electronegative.[38,39,47,48]

This implies that the two atoms do not need be from the same element but they should have a comparable electronegativity allow stronger bonds. However, hydrogen bonds are intermolecular, *i.e.* occur between molecules or between different parts of one molecule. The hydrogen bonds are pretty strong; stronger than van der Waals forces but are weaker than covalent and ionic bonds. B. Guillot had worked on subjects of interest allowing to improve the different simulations about the liquid water, or supercritical. The covalent nature of the hydrogen bond can be effect on a partial localization of the electrons. Thus, the charge transfer effect will have consequences on the description of the hydrogen bond.[38,39,43–46,49]

The evolution of hydrogen bonds

The existence of the hydrogen bond in the supercritical domain is a fundamental question in supercritical water, the number of hydrogen bonds persist at this conditions. Despite the disappearance of the tetrahedral structure, the hydrogen bonds lead to the formation of water molecules, which can be explained a density even in relatively strong.[50]

Structural studies of liquid water have been recently extended to the supercritical state, *i.e.* above the critical point of water (H_2O and D_2O: T_c ~ 371 °C, P_c ~ 217 bar, ρ_c ~ 0.36 g.cm^{-3}). The peculiar behaviour of supercritical water is thought to be related to the change of the intermolecular structure at elevated temperatures, especially to the change in the hydrogen bond network.[25,40,51]

There are some reports using X-ray and neutron scattering to characterize the water. Structural studies indicate that when water is placed under high pressure, the number of hydrogen bonds per water molecule do not change by any appreciable amount relative to the ambient state. The effect of pressure is particularly noticeable in the $g_{OO}(r)$, where the second peak is a signature of local tetrahedral structure diminishes as pressure is increased. The liquid structure at high pressure is nearly independent of temperature variation.[22,23]

Using the neutron scattering method of isotopic substitution, Postorino *et al.*[50] reported partial correlation functions at one supercritical state point of T = 673 K and ρ = 0.66 g/mL. They showed the disappearance of the hydrogen-bonding peak in $g_{OH}(r)$. This was in contrast to partial correlation functions derived from simulation using popular two body and polarizable water force fields, which exhibit a persistence of hydrogen bonding higher temperatures.[52,53]

At ambient conditions, differences in the height and sharpness are more clearly than supercritical conditions of the first peak of gOO(r) result in changes in the coordination number which can be shows in the equation (2) bellow, N_c:[22]

$$N_c = 4\pi\rho\int_0^{r_{\min}} r^2 dr g_{OO}(r), \qquad (2)$$

Where ρ is the density of water and r_{min} is the location of the first minimum in $g_{OO}(r)$. We found values of N_c of 5.1, 5.2, and 4.7, for Narten and Levy[54], Soper, Bruni, and Ricci,[55,56] and the Hura *et al.*[57] work, respectively.

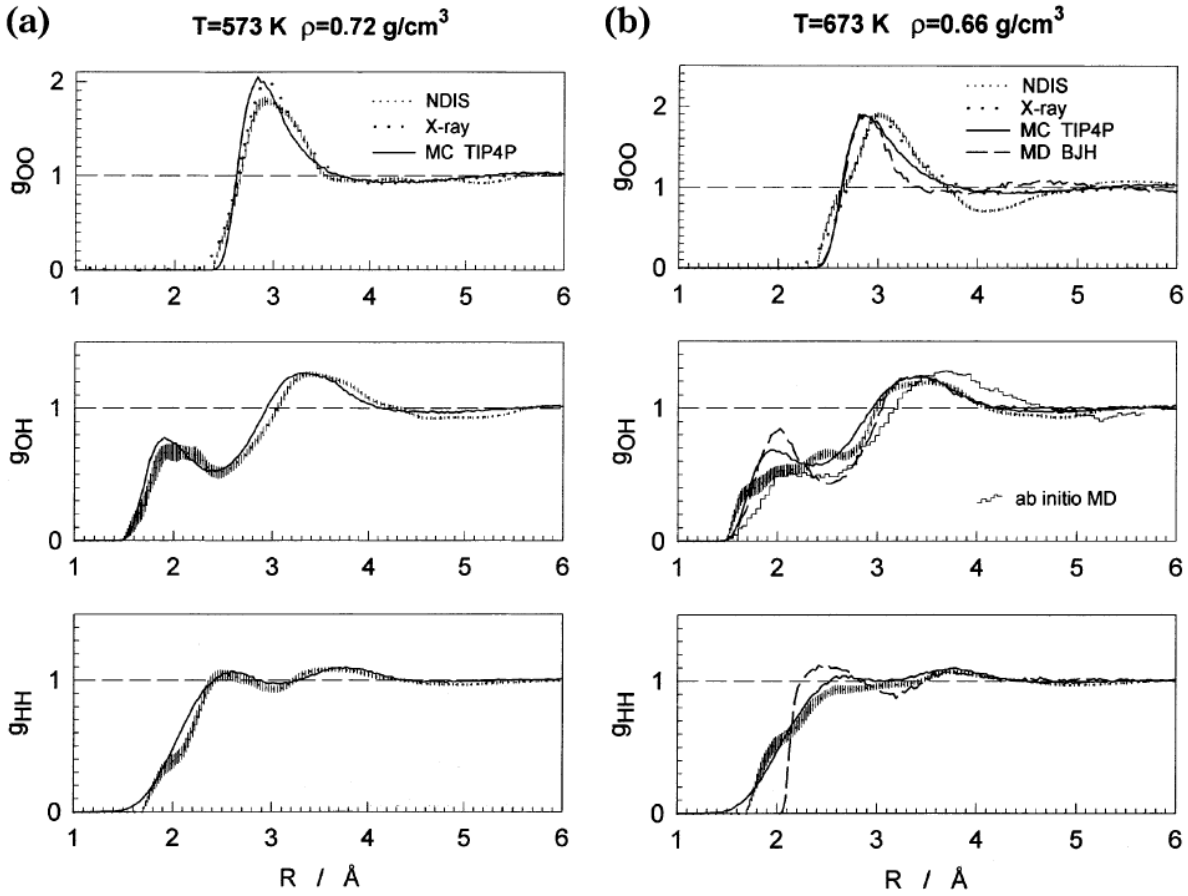

FIG. 1.5 - Experimental scattering data and simulations for supercritical water at (a) T = 573 K and ρ = 0.72 g/mL for $g_{OO}(r)$ (top), $g_{OH}(r)$ (middle), and $g_{HH}(r)$ (bottom); (b) T = 673 K and ρ = 0.66 g/mL for $g_{OO}(r)$ (top), $g_{OH}(r)$ (middle), and $g_{HH}(r)$ (bottom).[22]

FIG. 1.5 shows a comparison of the partial radial distribution functions from X-ray scattering, neutron scattering, and simulations using the TIP4P water model at the subcritical state T = 573 K and ρ = 0.72 g/mL and supercritical state of T = 673 K and ρ = 0.66 g/mL. The number of hydrogen bonds is estimated by integration under the first peak of $g_{OH}(r)$, similar to that used in eq 2 for the water coordination number. At ambient conditions n_{HB} =

3.3, while at T = 573 K and ρ = 0.72 g/mL it is now n_{HB} = 2.4. The agreement between simulation and experiment is very good for the subcritical thermodynamic point.

Neutron diffraction by isotopic substitution applied to water makes it possible to determine the three correlation functions of partial pairs g_{OO}, g_{OD} and g_{DD}. Compared to the pair correlation function, g(r), these functions distinguish between the different atoms and are obtained by Fourier integration of the corresponding partial or total experimental structural factors, S(q), S_{OO}, S_{OH} and finally S_{HH}. The Fourier integration procedure and the truncation effects of the domain in q, which should theoretically be infinite, can lead to calculation errors.[22,50]

In a simplified way, the disappearance of the tetrahedral structure is evidenced by the disappearance of the second peak in the gOO (r) pair correlation function while the decrease in the number of hydrogen bonds is distinguished by the reduction in the amplitude of the second peak of g_{OD} (r), even if the latter assertion is always contentious. The same conclusions apply to X-ray diffraction by considering the total pairs correlation function.

Yu. E. Gorbaty and A. G. Kalinichev, they have observed the hydrogen bonding in supercritical water. The upper maximum temperature for the existence of hydrogen bonding in supercritical water is discussed with respect to the recent statement by Postorino *et al*.[50] at 673 K. They demonstrate that hydrogen bonds in supercritical water can be observed experimentally at least up to 800 K using both spectroscopic and diffraction techniques, it may be predicted that hydrogen bonding persists even at higher temperatures. An attempt to estimate quantitatively the temperature dependence of the degree of hydrogen bonding[47] has been made.

The lower hydrogen bonding the lower dielectric constant of water. In a neutron diffraction study of water at 400 °C[50,58], Postorino *et al*. observed complete disappearance of a peak located at ~1.9 Å, which is a direct evidence of hydrogen bonding, in the oxygen–hydrogen pair radial distribution function $g_{OH}(r)$[47,59]. Yutaka Ikushima *et al*. have been working on Raman spectroscopy study of subcritical and supercritical water. The peculiarity of hydrogen bonding near the critical point. The Raman spectra of water are measured up to 510 °C and up to 40 MPa. The peak frequency increases with temperature, indicating the break of hydrogen bonding, and it changes only slightly at higher temperatures above the critical point. The peak frequency has a maximum near the critical pressure, and the extent of hydrogen bonding significantly changes with pressure in this near-critical region.[60–62]

1.2.5 Fluids density fluctuations appearance

X-ray and neutron diffraction methods allowed us to reveal the structures of hydrogen bonded liquids like water and electrolyte solutions under subcritical and supercritical conditions, the density of the supercritical fluids varies rapidly in a small range of temperature and pressure, which makes possible to vary their macroscopic properties. Thus, It is possible to distinguish supercritical water of high and low density. The critical isochore can be defined as the analytic continuation of the liquid-gas coexistence curve on which the density of the

fluid is equal to the critical density. The FIG. 1.6 illustrate the transition between these two regions became faster approaching the critical point CP.

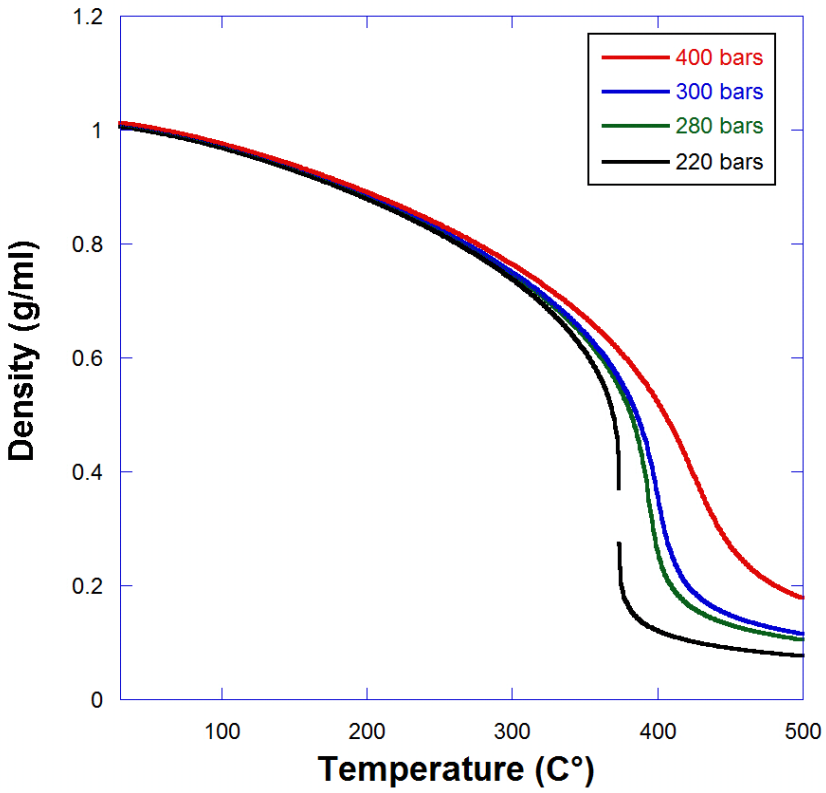

FIG. 1.6 - Theoretical density has taken from NIST[1] of the pure water as a function of temperature for the pressures (220, 280, 300 and 400) bar.

The distribution of the local density of water molecules (mesoscopic scale) seems to be inhomogeneous in time and space. Then we can define the concept of Local Density Inhomogeneities, which corresponds to the existence of zones whose density is greater than the global density of the medium.

From a microscopic perspective, many of the unique features of SCW are due, in large part, to the changes that take place in the intermolecular structure and hydrogen bonding of water at elevated temperatures. In fact, a wide variety of experimental investigations as well as molecular-based computer simulations in the past decade have shown that at supercritical conditions, the infinite H-bond network of the molecules present in ambient water crosses a percolation transition, *i.e.* breaks down to form small clusters of bonded water molecules in various tetrahedral configurations surrounded by non bonded gas-phase-like molecules. SCW can be regarded that of an inhomogeneous medium with coexisting high and low-density regions. In this dynamic equilibrium ensemble, the hydrogen bonded molecular clusters present on it are continuously broken and reformed, allowing large local density or

configurational fluctuations[35,63–65]. However, molecular dynamics simulations have shown that even at gaslike densities (< 0.2 g/cm^3), SCW still retains some non-negligible “liquid waterlike” structure on a microscopic level.[48,66]

In the pioneering work performed by C. A. Eckert *et al*.[67] the term "cluster" is used, denoting aggregates of water molecules, the density of which is locally of the same order of magnitude as the liquid, surrounded by zones whose density corresponds approximately to that of the gases. In the theory of liquids and critical phenomena[68], the divergence in the size of clusters of water molecules are related to the divergence of isothermal compressibility K_T. Hence, the closer you get to the critical point, more K_T and the size of ξ have local inhomogeneities of density increase. ξ means the correlation length of density fluctuations. Thus, in the compressible regime, that's say for the area of the phase diagram, whereas $T > T_C$, and the value of compressibility is high[69]. These sizes have a mesoscopic scale, whereas they tend towards macroscopic dimensions locally around the critical point, which corresponds to a mathematical divergence of K_T. Since these dynamic inhomogeneities imply the existence, on average, of zones of density of liquid type and of other type of gas.[67,69–74]

Therefore it appears a contrast of electronic and atomic density between these regions of the fluid. Small-angle scattering of X-rays and neutrons SAXS and SANS (Small Angle X-ray/Neutron Scattering) are particularly sensitive tecniques to detect this contrast[68]. Experimentally, small angles X-ray scattering under supercritical conditions is becoming increasingly numerous at supercritical region on carbon dioxide (CO_2) and trifluoromethane (CF_3H),[75–79] as well on supercritical water H_2O,[80] Similarly, SANS measurements on supercritical D_2O heavy water have recently been done.[81,82]

The aim of all this work consists in the experimental determination of the mean size ξ and of the amplitude of the density fluctuations of the molecules of the solvent. In the case of water, D.M. Sullivan *et al*.[81] performed small angle neutron scattering experiments on D_2O on the critical isochore. The corrected scattering data were used to extract values for the correlation length of the critical density fluctuations, ξ , and the thermodynamic limit of the structure factor, S(0). Results confirm that D_2O belongs to the three-dimensional Ising universality class. This will give me a vision and potential to study the density fluctuations for a supercritical fluids using XAS in both mode " absorption and fluorescence "and the ion-pairing near critical points of solutions.

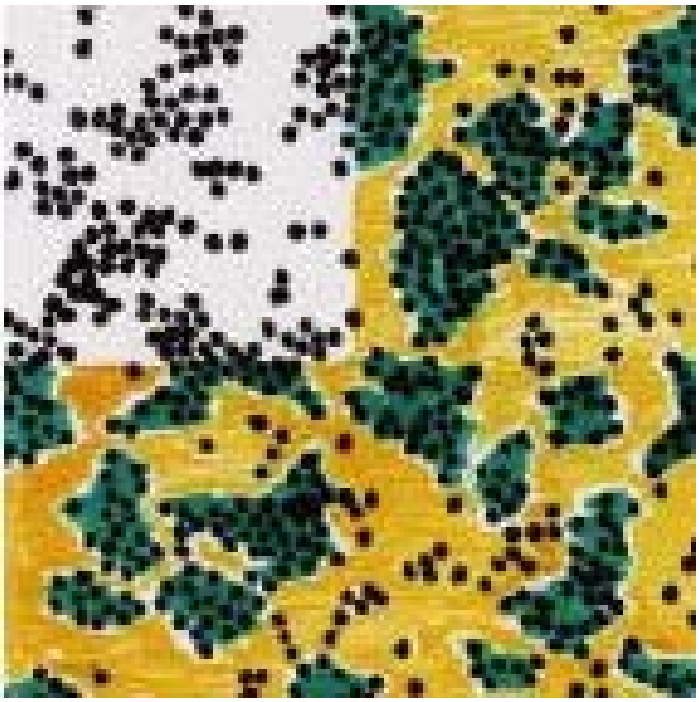

FIG. 1.7 - Instant configuration of two-dimensional Lennard Jones fluid molecules (T_r = T/T_C = 1.17 and $\rho_r = \rho/\rho_C$ = 0.86, respectively relative temperature and relative density to the values of the critical point of the fluid).[83]

The dominant effect at this mesoscopic scale corresponds to the inhomogeneous and dynamic distribution of the local density of the water molecules (Local Density Inhomogeneities).[64,71,72,84–87] It corresponds to the existence of zones whose density is greater than the overall density of the liquid. Therefore, these areas coexist with others whose density is less than the overall density. In the pioneering work of Eckert *et al*.[67] The term "cluster" is used. The term LDI only relates to the density of the water molecules.

FIG. 1.7 represents an instantaneous configuration, derived from molecular dynamics (DM) calculations, for molecules of a simple liquid in supercritical conditions. Even if the water, strongly associated by H bonds, ca not be correctly described by a Lennard-Jones type interaction because the H bonds are not taken into account, this image clearly represents the phenomena of fluctuations involved. Petsche and Debenedetti highlight the universal character of critical phenomena of divergence in the size of clusters, irrespective of the type of interaction between molecules (Lennard-Jones).[74] In the theory of liquids and critical phenomena,[68,88] these phenomena of divergence in the size of water molecules clusters are related to the divergence of the isothermal compressibility (χ_T). Thus, the closer you get to the critical point, More χ_T and the size of ξ are increase in LDI. Whereas ξ is the correlation length of density fluctuations.

1.3 Electrolytes solutions

An electrolyte solution is a solution that generally contains ions, atoms or molecules that have lost or gained electrons, and is electrically conductive. For this reason they are often called ionic solutions. However there are some cases where the electrolytes are not ions. A basic principle of electrostatics is that opposite charges attract and like charges repel. It also requiresa great deal of force to overcome this electrostatic attraction. A common example of an electrolyte is ordinary salt, sodium chloride. Solid NaCl and pure water are both non-conductive, but a solution of salt in water is readily conductive.[89,90]

Water is an ideal electrolyte solvent (as discussed in section 1.2). It is important to understand that electrolytic solutions would not exist without the active involvement of the solvent reducing the strong attractive forces that hold solid salts and molecules such as HCl together. Water is not the only liquid capable of forming electrolytic solutions, but it is by far the most important. It is therefore essential to understand those properties of water that influence the stability of ions in aqueous solution.

1.3.1 The effect of salt on Hydrogen bonds of water

Mixing salt with water results in the salt dissolving in the water to produce a saline solution. The salt splits up into positively and negatively charged ions that exist independently in the solution. Sodium chloride is an ionic solid made of positively charged sodium ions and negatively charged chloride ions, which form a strong crystalline structure due to the electrical charges between them. When salt is mixed with water, the charged ions instead form weak hydrogen bonds with water molecules. Adding salt to water leads to an attraction between water molecules and either the sodium or chlorine ions, depending on the particular molecule, and this attraction is stronger than the bond between sodium and chlorine. As a result, the water pulls the lattice apart dissolving the salt.

In my case of study, the influence on H-bonding of water (H_2O) coming by adding salts and increasing of a temperature and pressure. Adding salts increase the ions to the water, numerous experimental and theoretical studies have been carried out diluting supercritical solutions, where the solute differs significantly from the solvent in its size and interaction strength. The results of these studies indicate that the local environment around such solute can differ dramatically from the bulk, both in terms of its density and its composition[64,91]. In this case, we can specify the solute-solvent and solvent-solvent model potentials. We assume that the solvent particles interact with each other via the familiar LJ potential:[71]

$$\phi_s(r) = 4\varepsilon_s\left[\left(\frac{\sigma_s}{r}\right)^{12} - \left(\frac{\sigma_s}{r}\right)^{6}\right], \qquad (3)$$

Where ε_s is the potential well depth and σ_s is the effective diameter of the solvent particle. The solute-solvent pair potential is taken to be of the Yukawa form

$$\phi(r) = \begin{cases} \infty, r < \sigma \\ -\alpha\sigma\varepsilon_s \exp\left[-K(r-\sigma)/\sigma_s\right]/r, r \geq \sigma. \end{cases} \quad (4)$$

Where σ is the solute–solvent size parameter, while α and K are two-dimensionless parameters, which control the strength and the range of the solute–solvent interaction, respectively.

There is extensive data supporting the idea that ions have significant impact on local water hydrogen bonding behavior[92]. In fact, one theoretical model, developed by Marcus,[93,94] has been able to account fairly well for several thermodynamic parameters for a variety of ions in solution purely through modeling ion effects on the first hydration layer[93]. Salt effects on water have been most commonly described in terms of the chaotropicity or kosmotropicity of the solutes. Perhaps the best description of the chaotrope/kosmotrope designation is that offered by Collins:[95] binding of chaotropes to water molecules is weaker than binding of water molecules to each other; binding of kosmotropes to water is stronger than binding of water molecules to each other.[91,96,97] Chaotropicity seems to correlate with a low charge density, thus large singly-charged ions tend to be chaotropic. Their low charge density means that they have smaller effects on the local hydrogen bonding. Kosmotropicity correlates with a high charge density, thus small or multiply-charged ions tend to be kosmotropic. Their high charge density means that they interfere strongly with local water hydrogen bonding.

Adding a solute to the water leads multiple effects on the solvent and on some of the properties *i.e.* density, viscosity, dielectric constant, etc. Studies on how water interacts with dissolved solutes are essential to understand the physical, chemical and biological changes that exist in solution, as pointed out by Soper and Rossky.[98] In General, supercritical fluids applicable to water, Debenedetti *et al*.[99,100] classified solutes into three categories: repellent, weak attractant and attractive solutes. These categories correspond respectively to the following three cases: The interaction between the solute and the water molecules is repulsive, the interaction between the solute and the water molecules is attractive but weaker than that between two molecules of water, and the interaction between the solute and the water molecules is attractive but more than those between two water molecules. Then, the interaction between the solute and the water molecules is divided into two contributions,[101] The first corresponds to the **direct** interaction between a molecule (or an atom) of the solute and a molecule of water. Its spatial extension is on the order of the range of attractive (or repulsive) potential between the two elements. The second is an **indirect** interaction between the solute and other water molecules, outside the first hydration layer and the scope of direct interaction potential. This interaction originates the phenomena of correlation (*i.e.* density fluctuations) existing between molecules of a compressible fluid.

The effects on the structure of the solvent are different for the three types of solute. In the case of a repulsive solute, a depletion effect of the neighboring water molecules is locally observed. Their density around the solute is locally lower than the overall mean value of the water density. Conversely, in the case of an attractive solute (weakly or not), the density of water molecules is locally higher than the overall mean density. It is sometimes called electrostriction when the interactions involved are electrostatic (the solute is an ion). The

distinction between the two cases of attractive solute is finer. A simplified view is to say that for a system where the number of molecules of solvent and solute is constant, the addition of a molecule of solute causes the expansion of the volume in the case of a weakly attractive solute and its decrease in the case of an attractive solute.

The quantities in relation to the effects of charge in the aqueous medium. There is a conductivity σ ($S.cm^{-1}$) and the permittivity ε (static component of the dielectric constant, arbitrary units), σ describes the ability of the medium to move a charge. It depends strongly on the quantity of charged species present and their mobility, as a function of T and P. ε represents the reactivity of the medium to the application of an electric field. It is directly related to the polarizability of the medium and the value of the dipole moment of the water molecule (in debye D). The high value of this magnitude at ambient temperature (a value of ε around 80 is commonly accepted, experimentally and theoretically)[11] makes this particular solvent and reflects its character of hydrogen-bonded liquid.

When the solution is brought to supercritical subject conditions, the solvent-specific density fluctuations increase, and particularly the correlations between the water molecules of hydration spheres of the solute and those free of solute zones. Note that the divergence of the correlation length of the IGs containing one (or more) solute atom is only due to the divergence of the correlation length ξ of the water density fluctuations. Indeed, the range of direct interaction between solute and water molecules is always finite, even very close to the critical point.[52]

In the specific case of ions in solution, the solute is attractive. we observe a local increase in the density of water molecules around the ions. However, and as we illustrated in these same ions interact with each other by Colombian interaction (discussed later on section 1.3.3) between charged species, and the attractive forces are inversely proportional to the permittivity ε of the medium. In the case of sub- and supercritical aqueous solutions, the fall of the ε value with temperature (section 1.2) increases these interactions between ions. Under these conditions of temperature and pressure, a competition between the effects of ions by Coulomb interaction, and the local increase in the density of H_2O molecules around these ions by direct and indirect interaction, which tends to screen them (Coulomb force between them reduce).

There are several methods and experiments performed at this conditions, the neutron scattering NDIS, to determine the size and density of LDI around a solute. All these spectrosopic methods are used to measure the solute as a target. They consist in measuring the displacement of an absorption line specific to this target (often of vibrational origin), under the effect of the modification of the local structure of the hydration layers.

1.3.2 Critical properties

Water is a good solvent for electrolytes around room temperature as well as for many inorganic and organic substances with molecules containing polar functional groups, and a poor solvent for nonpolar substances like hydrocarbons. Near the critical point, water is a low-dielectric fluid and thus a poor solvent for electrolytes.[12,59]

In this supercritical domain, fluids are characterized at the microscopic scale by density fluctuations: areas with gaslike density coexist with liquid-like density.[64] In this region, the solvent criticaly makes the solution thermodynamics peculiar. Traditional approaches developed for water below its boiling point experience great difficulty describing anomalous properties of dilute solutions near the critical point of the solvent. We shall argue that the properties of both nonelectrolyte and electrolyte aqueous solutions in a large range around the water critical point can be most easily grasped in analogy with those of other compressible fluid mixtures.[12,102]

At near and supercritical temperatures, aqueous electrolyte solutions pose three kinds of problems: (1) incorporating the effects of phase separation, mixture criticality, and proximity of the solids in the thermodynamic characterization; (2) adapting the customary formulation of charge effects in liquid water to a medium that is compressible, has a low dielectric constant, and in which ions associate; and (3) generalizing the scaling laws for fluid mixtures in order to incorporate the charges.[12]

The phase behavior and critical lines, when temperature is raised, water expands and becomes more compressible. The dielectric constant falls, and the ions will tend to associate. At the critical point of the solution, the vapor and liquid phases become identical, and the ions dissolve equally (but poorly) in both phases. Thus, ions will start to dissolve in the vapor phase as water is heated to near its critical temperature. In supercritical water conditions, the solubility of ions will be poor at low densities, but increase strongly as the pressure increasesand the density exceeds the critical density.[89,90,103,104]

1.3.3 Ion-Pairing

Ion pairing describes the (partial) association of opposite charged ions in electrolyte solutions to form distinct chemical species called ion pairs. Ion pair formation is invoked as the most plausible explanation either of certain types of direct experimental evidence (the appearance of a new band in the vibrational spectrum *i.e.* the common forms of spectroscopy electronic (UV), vibrational (IR and Raman), and nuclear magnetic resonance (NMR) or of deviations observed at moderate concentrations from predictions of electrolyte theories that accurately describe the properties of very dilute electrolyte solutions. Various theories have been proposed for choosing the value of R " specified cutoff distance" and for describing the properties of the ion pairs and free ions that together produce the observed behavior of electrolyte solutions[89,90,94,105]. For ion pairs to be treated as distinct entities (chemical species) in electrolyte solutions, valid evidence for them must exist. For example, in different situations: “An ion pair must be long-lived enough to be a recognizable kinetic entity in the solution.[89]

There is no a valid range of lifetimes of ion pairs, but rate constants for their dissociation approaching 10^9 s^{-1}, corresponding to a lifetime of ~ 1 ns, Regardless of their lifetimes, ion pairs can be considered to be at the chemical equilibrium with the free ions, with the extent of formation quantified by the fraction α of the total number of ions remaining free and (1-α) as the fraction associated, with an association constant K_A. Consider the ion-pairing equilibrium in an electrolyte solution of concentration c (usually as molarity, M):

$$C^{c+} + A^{\alpha-} \leftrightarrow CA^{(c-\alpha)+} \quad (5)$$

Where C^{c+} is the cation, $A^{\alpha-,}$ is the anion, and $CA^{(c-\alpha)+}$ is the ion pair, with all species being solvated to an extent determined by the interaction of each species with the surrounding solvent. The net charge of the ion pair (c - α) may be zero (for a symmetrical electrolyte) but need not be so. The fraction α and (1 - α) is obtained experimentally by various methods. Using the usual relationship between activities and concentrations on the molarity concentration scale ($a_i = c_i y_i$), the formation of the ion pair can be quantified in terms of the equilibrium concentration quotient, K_A, or in terms of the standard (infinite dilution) association constant $K_A°$ and a ratio of activity coefficients:

$$K_A = (1-\alpha)c/(\alpha c)^2 = (1 - \alpha)/\alpha^2 c = K_A°(y_{\pm}'^2/y_{IP}) \quad (6)$$

Where $y_{\pm}'$ is the mean ionic activity coefficient of the free ions and y_{IP} is the activity coefficient of the ion pair.[89,90,94]

The general form of Coulomb's law describes the force of attraction between charges, the force between two charged particles is directly proportional to the product of the two charges, and inversely proportional to the square of the distance between them:

$$f \propto \frac{q_1 q_2}{D r^2} \quad (7)$$

Where f is the force (N), q_1q_2, are the charges in coulombs, D, is the dielectric constant of medium, and r, is the distance between point charges (m). The proportionality constant D is the dimensionless dielectric constant.[89,90] Its value in empty space is unity, but in other media it will be larger. When an ion is introduced into a solvent, the attractive interactions between the solvent molecules must be disrupted to create space for the ion. This reqiures energy and would tend to inhibit dissolution by itself. However, if the solvent has a high permanent dipole moment, the energy cost is more than recouped by the ion-dipole attractions between the ion and the surrounding solvent molecules.[106]

Ion-pairing studies have been performed mostly on single electrolytes in dilute solutions, although more concentrated solutions (where higher aggregates may occur) have also received attention. Polyelectrolytes are a special case of ion pair aggregates and they are briefly reviewed here, because their behavior merits a comprehensive separate review. The formation of ion pairs is strongly influenced by the solvation of the ions. Ion pairing has been the subject of chapters in the classic treatises on electrolyte solutions: The Physical Chemistry of Electrolytic Solutions by Harned and Owen[90], and Electrolyte Solutions by Robinson and Stokes.[89] The monographs Electrolytic Dissociation by Monk[103], and Ion Association by Davies,[104] described the “state of the art”, at that time (early 1960s) including the methods used and the results obtained, along with their interpretation and consequences.

A previous study about the formation of ion pairing by XAS measurments is described by Ferlat et al.[107] It based on the assumptions that the anion-oxygen and anion-cation PRDFs are independent of each other. A quantitative evaluation of the degree of association can be obtained by coupling EXAFS and Molecular Dynamic simulation. They have been derived the ion-pairs for 0.2 mola KBr, RbBr and CsBr aqueous electrolytes at P = 450 bar and T = 450°C. Some defect of ion-ion contributions obtained in the simulations were observed, although further measurements would be necessary to correct the potential parameters. The phase contrast method based on a substitution of the ion which acts as an X-ray scatter in the ion absorber environment, offers new opportunities for the exploration of the ion-pairing n the other systems or thermodynamic conditions.

The measurements performed by Cécile Da Silva et al.,[108] concerne also the influence of monovalent ions on density fluctuations in hydrothermal aqueous solutions by small angle X-ray scattering. The correlation length and the structure factor were extracted from the data following the Ornstein-Zernike formalism. They obtained experimental evidence of the shift of the critical point and isochore and their dependence on the ions concentration (0.33 mol/kg and 1.0 mol/kg). They also observed that the size of the density fluctuations and the structure factor increase with the presence of the ions and that this effect is positively correlated with the atomic number of the cation.

1.4 Summary (English)

In this chapter, I have described the physical and chemical properties of water and aqueous solutions at supercritical region and in particular the evolution of the hydrogen bonds, a phase diagram with its critical point have been illustrated. The effect of salts on hydrogen bonds of water and critical properties have been shown, as well as, the ion-pairing of electrolytes solutions characteristics based on previous studies.

Pure water and electrolytes solutions have been measured by several techniques from ambient to supercritical conditions *i.e.* X-ray absorption spectroscopy (XAS), X-ray scattering, Neutron scattering, Raman spectroscopy. In this supercritical domain, fluids are characterized at the microscopic scale by density fluctuations: areas with gas-like density coexist with area with liquid-like density.

1.5 Summary (French)

Dans ce chapitre, je décris les propriétés physiques et chimiques de l'eau et des solutions aqueuses dans la région supercritique, avec un point particulier sur l'évolution de la liaison hydrogène dans ce domaine. Un diagramme de phase général de l'eau incluant son point critique est présenté. L'effet des sels sur les liaisons hydrogène de l'eau, la formation des paires d'ions et l'évolution de ses propriétés critiques sont illustrées à l'aide de travaux antérieurs.

Des solutions d'eau pure et d'électrolytes en conditions sub et supecritiques ont été mesurés par différentes techniques notamment par spectroscopie d'absorption des rayons X (XAS), par diffusion des rayons X, par diffusion de neutrons et par spectroscopie Raman. Dans ce domaine supercritique, les fluides sont caractérisés à l'échelle microscopique par des fluctuations de densité: des zones à densité gazeuse coexistent avec une zone à densité liquide.

Chapter 2: *Methods*

2. Methods

In this chapter, a description of the different experimental methods and their particularity for the study of hydrohermal solutions are presented. The first method is the X ray abosrption spectrocopy and in particular the used of the High resolution spectroscopy. The X-ray Absorption Spectroscopy (XAS) technique is another powerful spectroscopic method. The energy excitations correspond to an electronic transition to the unoccupied states (of the solute atom) whose geometric and electronic structure is highly dependent on the local environment. The sensitivity of the XAS is a few angstroms. It is therefore a technique of choice in the case of aqueous solutions to describe precisely (geometrically and electronically) the first layers of neighbors of the solute. A particular advantage of this technique, apart from its very local sensitivity, is its chemical selectivity: in the case of the presence of several elements in solution, only one of these elements is chosen by working in an energy range corresponding to the threshold of this atom. In our case, we did XAS experiments for fluids density measurements, as well experiments using CAS, both experiments give consistent results and tend us that at specific temperatures, the structure and bonds reformation and distribution in a heterogeneous system.

2.1 X-ray Absorption spectroscopy (XAS)

2.1.1 Theory

X-ray absorption spectroscopy (XAS) is an element specific spectroscopy sensitive to the local chemical and structural order of the absorber element. XAS is nowadays increasingly used for the speciation analysis of chemical elements owing to the development of new synchrotron radiation facilities worldwide. XAS can be divided into X-ray absorption near edge structure (XANES), which provides information primarily about the geometry and oxidation state, and extended X-ray absorption fine structure (EXAFS), which provides information about metal site ligation.

X-ray absorption spectroscopy (XAS) were often used in the literature to study supercritical fluids, such as supercritical water and solution when adding ions to water "aqueous solutions". supercritical water and aqueous solutions (a mixture of water) studied by XAS. The measurements and evolution of density can be correlated to the water behavior with pressure and temperature and so linked to its local structure in particular hydrogen bonds evolution with temperature.[12]

XAS has grown with the achievement of synchrotron radiation facilities which enabled to provide intense X-ray sources; reaching the appropriate energy to probe inner shell electronic structures of the elements, and with appropriate intensity to allow the detection of the photo-electron interactions. When the X-rays hit a sample, the oscillating electric field of

the electromagnetic radiation interacts with the electrons bound in an atom. Either the radiation will be scattered by these electrons, or absorbed and excite the electrons.[109,110]

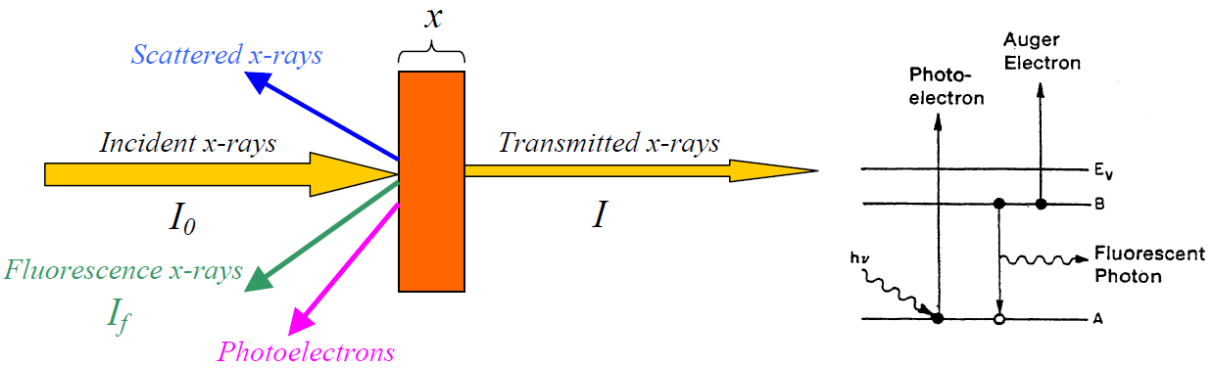

FIG. 2.1 - Schematic illustration of an experimental design for XAFS experiments for various techniques (left) and photoelectric absorption process from a 1s core electron (right).

A narrow parallel monochromatic X-ray beam of intensity $\mathbf{I_0}$ passing through a sample of thickness x will get a reduced intensity **I** according to the expression:

$$\ln (I/I_0) = \mu/\rho \,.\, \rho \,.\, x \qquad (8)$$

where μ is the linear absorption coefficient, which depends on the types of atoms and the density ρ of the material. At certain energies the absorption increases drastically, and gives rise to an absorption edge. The edge occurs when the energy of the incident photons is just sufficient to cause excitation of a core electron of the absorbing atom to a continuum state, *i.e.* to produce a photoelectron.[110–112] Thus, the energies of the absorbed radiation at these edges correspond to the binding energies of electrons in the K, L, M, etc, shells of the absorbing elements. In our experiment, this classical absorption measurement permits us to calculate precisely the evolution of the fluid density and/or the varation of the concentration of salt in the solution.

What is XAFS?

X-ray **A**bsorption **F**ine **S**tructure is the oscillatory variation of the X-ray absorption as a function of photon energy beyond an absorption edge.

EXAFS and XANES

XAFS is also referred to as X-ray Absorption Spectroscopy (XAS) and is devided into 2 regions (FIG. 2.2):

XANES : **X**-ray **A**bsorption **N**ear-**E**dge **S**pectroscopy
EXAFS : **E**xtended **X**-ray **A**bsorption **F**ine-**S**tructure

The different energy range between XANES and EXAFS can be also explained in a simple manner by the comparison between the photoelectron wavelength λ and the inter

atomic distance of the photo absorber-back-scatterer pair. The photoelectron kinetic energy is connected with the wavelength λ by the following relation:

$$E_{kinetic} = h\nu - E_{binding} = \hbar^2 k^2 /(2m) = (2\pi)^2 \hbar^2/(2m\lambda^2) \quad (9)$$

Equation (9) contains related but slightly different information about an element local coordination and chemical state. The XANES extends up to a few 10s of eVs above the edge (FIG. 2.2 blue area). The EXAFS may extend up to 1000eV or more above the edge (FIG. 2.2 pink area).[109,110]

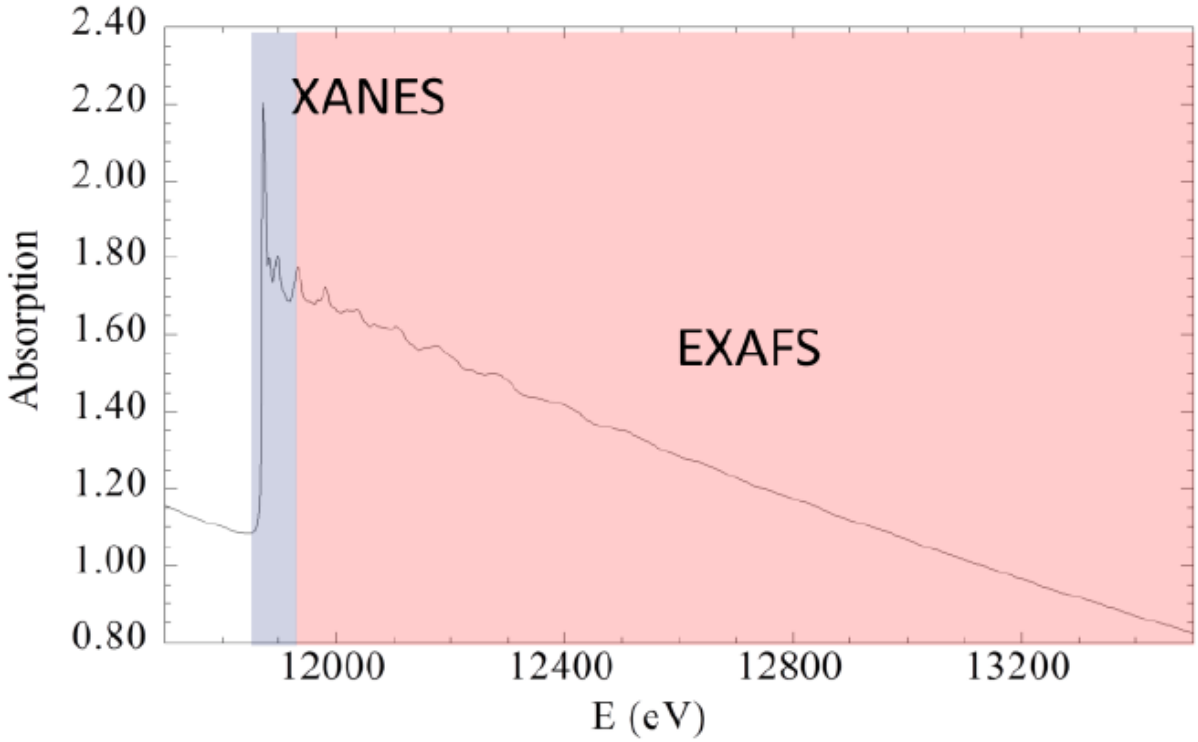

FIG. 2.2 - The K-shell absorption edge of Arsenic. The fundamental phenomenon underlying EXAFS is the absorption of an x-ray photon by a core level of an atom in a solid and the consequent emission of a photoelectron.

These oscillations appear because the proximity of neighboring atoms strongly modulates the absorption coefficient. The As K-edge absorption spectrum of a pseudo-binary semiconductor $lnAs_x P_{1-x}$ is plotted in FIG. 2.2.

In the XANES region, transitions are to unfilled bound states, nearly bound states, or to the continuum, where the photoelectron has a low kinetic energy (E_{kin} ~ few eVs).

In the EXAFS region, the photoelectron is always excited to the continuum, and has a larger kinetic energy (E_{kin} ~ 50-1000 eV). High energy electrons do not travel much in matter, *i.e.* their mean free path is limited to a few Å, as shown in the plot below. The difference between the kinetic energy of the photoelectron essentially differentiates these two regimes. Thanks to the very low mean free path of the photoelectron, approximations can be used to

interpret EXAFS, that are not valid for XANES. For this reason, the fine structure that appears in the XANES and EXAFS region cannot be analized in the same way[113,114].

The features in the pre-edge region are usually due to the electron transitions from the core level to higher unfilled or half-filled orbitals (*e.g*, s→ p, or p → d). In the XANES region, transitions of core electrons to non-bound levels with close energy occur. Because of the high probability of such transition, a sudden raise of absorption is observed. In NEXAFS, the ejected photoelectrons have low kinetic energy ($E-E_0$ is small) and experience strong multiple scattering by the first and even higher coordinating shells. In the EXAFS region, the photoelectrons have high kinetic energy ($E-E_0$ is large), and single scattering by the nearest neighbouring atoms normally dominates.[113–115]

The EXAFS Equation

The absorption process X involves the emission of a core electron from the atom, called a photoelectron. When the energy hν of the incident photon is higher than the binding energy E_0 of an electron of the core, the latter is excited towards an empty state of the pseudocontinuum and becomes a photoelectron. Its kinetic energy is then a function of the energy of the incident photon : $Ec = h\nu - E_0$. As the excited atom has an electron gap on one of its layers, the relaxation takes the form of an emission of either an Auger electron or a fluorescence photon.

A spherical wave wave vector k may be associated with the mass photoelectron emitted by the absorber atom. This wave describes the excited final state of the atom. K can be expressed using me and the kinetic energy of the Ec photoelectron as: $k = \sqrt{\frac{2m_e E_c}{\hbar}}$

The normalized EXAFS oscillations are represented by the factor χ(k) which is expressed using the absorption coefficients μ (k) and μ_0 (k) (for an isolated atom):

$$\chi(k) = \frac{\mu(k) - \mu_0(k)}{\mu_0(k)} \tag{10}$$

The relation $k = \sqrt{2m_e E_c / \hbar}$ makes it possible to express k as a function of its kinetic energy Ec, Which can itself be written as a function of the incident energy of the photon hν and binding energy of the core electron E_0: $E_c = h\nu - E_0$

The absorption coefficient is described by Fermi's golden rule:

$$\mu \propto \sum \left| \langle f | H | i \rangle \right|^2 \delta(E_i - E_f + h\nu) \tag{11}$$

| i > and f > are the wave functions describing the atom in its initial and final state, respectively. H is the Hamiltonian of radiation-matter interaction. The summation must be

carried out on all the final states which retain the total energy of the system. Different approximations allow to develop the EXAFS oscillations denoted χ.

First, we place ourselves in the electric dipole approximation:
The Hamiltonian of interaction is then equal to $\vec{r}.\vec{\varepsilon}$, where $\vec{r}$ is the coordinate of the photoelectron and $\vec{\varepsilon}$ the polarization vector of the electric field related to the wave of the incident photon. This approximation is valid because the wavelength of the radiation is greater than the spatial extension of the interaction region. Moreover, the angular dependence will not be taken into account in this study, and the expressions proposed will be valid only in the case of non-oriented samples, of the powder, liquid or polycrystalline type. In the first step, this formalism is developed in the case of simple backscattering. All the paths considered are back and forth between the absorber atom and a neighboring atom, that is to say a diffusion with an angle π.

Finally, we assume that the incident wave is plane in the vicinity of the backscattering (and not spherical) atoms, which will affect the writing of the backscattering function f (k, p). The oscillations are then expressed in the form:

$$\chi(k) \propto \frac{|f(k,\pi)|}{kr^2}\sin(2kr + \psi(k)) \tag{12}$$

The term (2kr + Ψ (k)) corresponds to the total phase shift between the waves representing the ejected photoelectron and the photoelectron after backscattering. Corrective terms must then be added in order to take into account different phenomena:

- The elastic scattering of the photoelectron can only take place on a short distance corresponding to the free electronic path λ, which is a function of the kinetic energy and therefore of the wave vector k. A damping term of phenomenological origin is then added, exp (-2r/λ(k)). This mean free path takes into account the effects of inelastic diffusion undergone by the photoelectron around the absorber atom.

- Thermal agitation and structural disorder subject the interatomic distances r to fluctuations. The factor σ called "Debye-Waller" is therefore introduced, and will have an influence on the oscillations through a Gaussian of width σ, that is a corrective term equal to exp ($-2k^2\sigma^2$). This last hypothesis is referred in the literature as the harmonic approximation, and can be used only in the case of a limited disorder. If the disorder is more important, corrective terms must be used.

Finally, the EXAFS oscillations are described as:

$$\chi(k) \approx S^2 \sum_j N_j \frac{f_j(k)}{kR_j^2} e^{-2R/\lambda(k)} e^{-2k^2\sigma_j^2} \sin[2kR_j + \delta_j(k)] \tag{13}$$

where N_j is the number of equivalent backscattering atoms j at a distance R_j from the absorbing atom, $f(k)$ and $\delta(k)$ are photoelectron scattering properties of the neighboring atom. This factor can be set on fitting, on the basis of fits to model compounds. Thus, the EXAFS contribution from each backscattering atom j is a damped sine wave in k-space, with an amplitude, and a phase, both dependent on k. Additionally, S^2 is introduced as an amplitude reduction factor due to shake-up/shake-off processes at the central atom(s). The sum is over "shells" of similar neighboring atoms. If we know $f(k)$ and $\delta(k)$ we can determine:

R distance of neighboring atom.

N coordination number of neighboring atom.

σ^2 mean-square disorder of neighbor distance

As mentioned, the scattering amplitude $f(k)$ and the phase-shift $\delta(k)$ depend on atomic number Z of the scattering atom, so the species of the neighboring atom can be also determined.[113,114]

In the context of supercritical solutions, XAS as a local probe is very well adapted. But as demonstrated by ferlat et al, due to the high level of disorder in supercritical region, we have developped an experimental setup dedicated to increase the resolution of the XANES using HERFD-XAS.

2.1.2 Experimental setup

The measurements have been carried out on FAME beamline are in transmission and fluorescence (HERFD-XAS) detecion modes. Fluorescence detection is classically achieved with a solid state detector (SSD) on X-ray absorption spectroscopy (XAS) beamlines. This kind of detection however presents some limitations related to the limited energy resolution and saturation. Crystal analyzer spectrometers (CAS) based on a Johann_type geometry have been developed to overcome these limitations. The CAS allows to collect X-ray photons from a large solid angle with five spherically bent crystals. It will cover a large energy range allowing to probe fluorescence lines characteristic of all the elements from Ca (Z = 20) to U (Z = 92). High-energy resolution fluorescence detected XANES and EXAFS have a better spectral resolution than conventional XANES and EXAFS. The performances of the CAS are illustrated by two experiments that are difficult or impossible to perform with SSD and the complementarity of the CAS vs SSD detectors is discussed.[116]

2.1.3 Crystal Analyzer Spectrometer (CAS)

The BM30B/CRG-FAME beamline at the European Synchrotron Radiation Facility (ESRF, Grenoble, France) is dedicated to X-ray absorption spectroscopy (XAS) applied to a wide variety of research fields: condensed matter physics, materials science, biophysics,

chemistry, and mainly geochemical topics, with special emphasis on highly diluted samples. The final assembly has different characteristics that will be detailed: The geometry of the experiment, the final configuration, which is intended to be able to comprise several crystals, the nature of the crystal, and finally the energy resolution of this system.

2.1.3.1 Experimental Description

Johann geometry. Different geometries can be envisaged: for example the so-called geometry of "Johansson", a curved crystal with curved refractive planes of a double radius, allows a detection well resolved in energy. Indeed, this geometry does not impose any degradation of the resolution. Unfortunately, its elevated cost and the difficulty on making the crystals used made us prefer the so-called geometry of (Johann).

In the Johann configuration as shown in FIG. 2.3, the crystal is tangent at its center (C) to a fictitious circle, called (Rowland circle), radius r twice less than the radius of curvature R of the crystal,[117] the source of the radiation, *i.e*. the sample, and the detector is located on the Rowland circle and determine the angle α of incidence selected ($\alpha = \pi/2 - \theta$, with Bragg angle θ). The detector is located on the focal point, opposite the source with respect to the reflection axis of the crystal.

The incidence angle is exact only at the center of the crystal. On the remaining surface the angular error ($\alpha - \acute{\alpha}$) is a function of the distance h and creates a slight geometric defect in the resolution of the detector. The angle ά characterizes the angular acceptance of the crystal, and depends mainly on the height h. The differentiation of the Bragg law makes it possible to calculate the geometric error as a function of h.

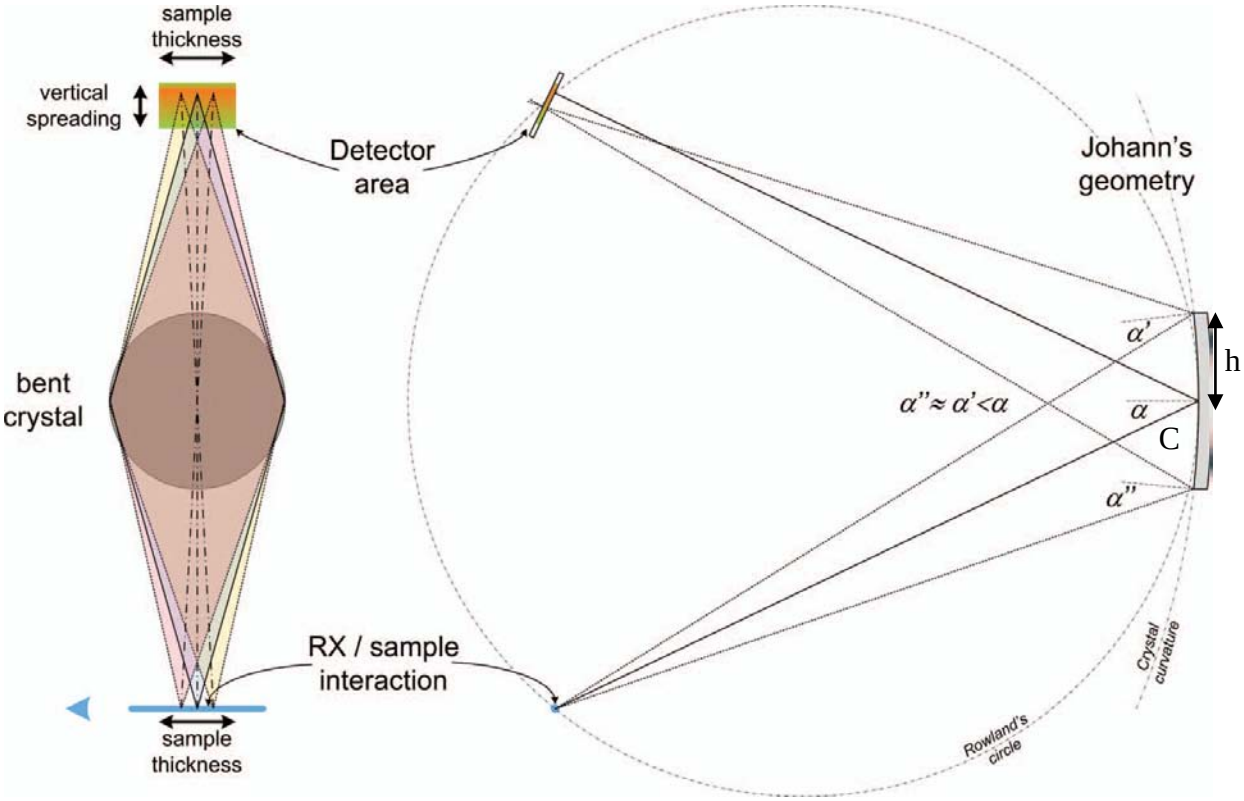

FIG. 2.3 - Visualisation of the intersection between the incident beam and the detection cone and resolution effect – vertical spreading of the focal spot on the detector: The "source" (*i.e.* the sample), the crystal, tangent to the Rowland circle at point C, and the detector, placed vertically on the sample. the angles, α and ά correspond to two different optical paths, and they are used when calculating the energy resolution due to the geometric error.[116]

The values of α when increase, is important because that's means more selected energy, as well, more the energy resolution is degraded. My study was carried out using crystal reflection 880, distance d_{hkl} is 5.4307 Å, the incident energy chosen corresponds to $K\alpha_1$ of the bromide is 13 491.4 eV, the angle of α is 13.673°, and the theoretical resolution of the crystal is 0.89 eV, and from our experiments, the experimental resolution is 1.4 eV was measured, This total resolution gives account of several parameters which we will detail in the next paragraphs.

Choice of the crystal. Different monocrystalline materials can be envisaged for this type of set-up, mainly germanium or silicon. The Germanium has a larger atomic number, *i.e.* a bigger structural factor. However, the technology associated with this material is less developed than that of silicon, so the manufacture of a crystal in Germanium is diffecult, expensive, and its crystallinity will be less good (*i.e.* more defects may be present), this material has therefore been eliminated in favor of silicon.[117]

Since the inelastic scattering section is relatively small, the curved analyzer used increases the solid detection angle in Johann's geometry. A similar method consists using an analyzer made of a multitude of small crystals glued on a curved support (their number can

thus vary between 10^4 and 10^{12}, the interest is to use only perfect crystals (in our case, the crystal is curved in an artificial way, which does not induces defects in its structure), and thus improves the diffracting power.[118] The chosen crystal is circular, with a radius ρ of 50 mm, for a thickness of 500 μm, curved spherically (with a radius of curvature R of 500 mm). The choice of the radius of curvature results from a compromise between the size of the system and the efficiency of the crystal. Indeed, if a larger a radius of curvature crystal is selected, the angular errors will be finer. However, a solid angle constant is prefered (to have the same counting rate), it will be necessary to have a larger diffractive surface, so the same angular errors as before will be find. Moreover, the distance to be traveled for the photons will be large, which implies, a certain amount of space and, a path in the air (or helium) that is too long, which further reduces the Counting. Thus, a relatively small radius of curvature has been chosen.

Moreover, the choice of the size of the crystal (the radius ρ) has an influence on the resolution: over this size, the most important number of photons collected is unfortunately in spite of the resolution deteriorates when the distance from the center of the crystal.

The 5 crystal analyser spectrometer was installed in the experimental hutch on the BM30B/CRG-FAME XAS beamline at the ESRF, This set-up however presents some limitations related to the limited energy resolution and saturation. Crystal analyzer spectrometers (CAS) based on a Johann_type geometry have been developed to overcome these limitations. I had tested this system dedicated to the structural investigation of high dilute systems in environmental, material and biological sciences. The spectrometer has been designed to be a mobile device for easy integration in multi-purpose hard x-ray synchrotron beamlines or even with a laboratory x-ray source. The CAS allows to collect X-ray photons from a large solid angle with five spherically bent crystals. It will cover a large energy range allowing to probe fluorescence lines characteristic of all the elements from Ca (Z = 20) to U (Z = 92). It provides an energy resolution of 1–2 eV.[116] XAS spectroscopy is the main application of this device even if other spectroscopic techniques (RIXS, XES, XRS, etc.) can be also achieved with it.

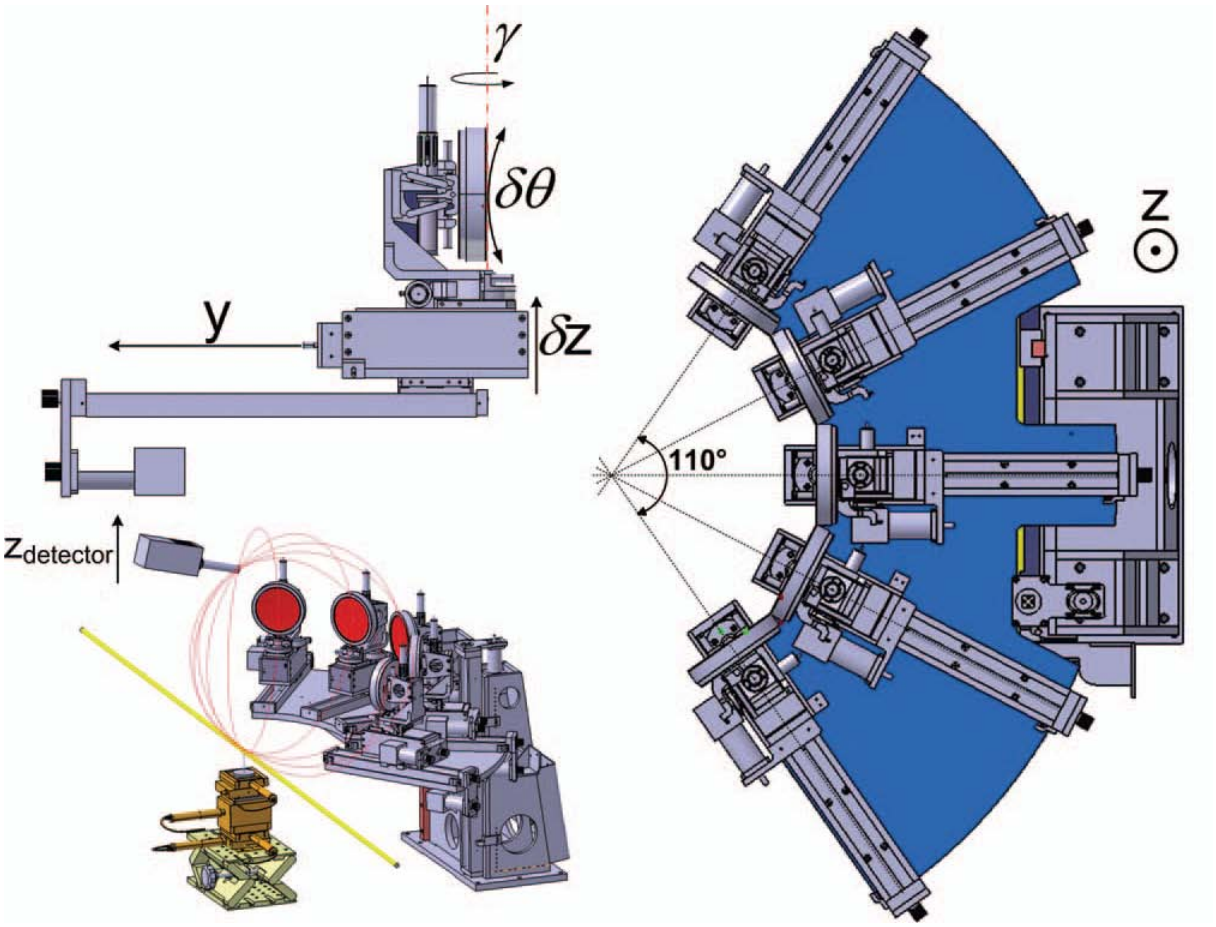

FIG. 2.4 - View of the spectrometer: detail of crystal assemblage (left—top position), view of the spectrometer on the beamline with the Vortex EX-90 as detector (left—down position), and top-view of a spectrometer drawing (right).[116]

The three main elements, (the sample or source, the center of the crystal and the detector) must be part of the Rowland circle. In a multi-crystal system, the source and detector must occupy the intersection points of the different Rowland circles of each crystal. We chose to place the detector above the source, the crystals will be positioned around the source all at the same height (FIG. 2.4). The Bragg angle is adjusted directly by the position of the crystal, which will be motorized along the vertical and horizontal axis. These two main movements of translation will be complemented by two finer angular movements. Moreover such a detector can be used to isolate the appropriate signal induced by the x-ray beam sample interaction, so as to discriminate the signals from the sample and from its container. Finally it also allows to focus the diffracted photons on different areas on this detector, to monitor each crystal separately[116,119,120].

Energy resolution. The energy resolution of the detection system using an analyzer crystal is first of all related to the geometrical configuration, in our case the Johann configuration. Other parameters must be taken into account[117]. Thus, a perfect crystal contributes intrinsically to the energy resolution by its Darwin factor:

$$\Delta E_{Darwin} = \frac{2hc\cos(\theta_B)\lambda_e |F_{hkl}| \exp(-M)}{\pi V_0 \sin(2\theta_B)} \quad (14)$$

Where h is Planck's constant, c the speed of light, θ_B the selected Bragg angle, λ the wavelength of the incident beam, r_e the electron beam, F_{hkl} the structural factor, exp(-M) the Debye-Waller factor, and V_0 the volume of the unit cell of the crystal.

It is necessary to take into account the finite size of the source, which corresponds to the width of the sample illuminated by the beam also having a finite size. As a vertical configuration has been chosen, only the vertical width of the beam, so the source Is taken into account. This width, related to the differentiation of Bragg's law, can be written by:

$$\Delta E_v = E\cot(\theta_B)\Delta\theta \quad with \quad \Delta\theta \approx \frac{\Delta h}{L} \quad (15)$$

Where E is the energy of the incident beam, Δθ describes the angular width of the source viewed from a point of the crystal, The vertical width of the beam is described by the parameter Δh, and L is the distance between the source and the point of the crystal considered.

It is necessary to take into account the energy resolution provided by the optics of the line of light, In particular the role of the monochromator. In the CRG-FAME-BM30B, the total resolution of the beam is in the order of the intrinsic resolution of the crystals of the monochromator, $\Delta E/E = 5.6*10^{-6}$ for diffractive silicon crystals[121].

Solid state detectors do not have any spatial detection resolution. Thus, any fluorescence, elastic, and inelastic scattering signal from a sample holder, or more generally from the experimental setup, cannot be filtered. One solution is to install fluorescence soller slits between the sample and the detector but this does not give significant improvement[122].

The work performed by Llorens *et al.*[116] High energy resolution five-crystal spectrometer for high quality fluorescence and absorption measurements on a X-ray absorption spectroscopy beamline. Fluorescence detection is classically achieved with a solid state detector (SSD) on X-ray absorption spectroscopy (XAS) beamlines. This kind of detection however presents some limitations related to the limited energy resolution and saturation. Crystal analyzer spectrometers (CAS) based on a Johann_type geometry have been developed to overcome these limitations. They have tested and installed such a system on the BM30B/CRG-FAME XAS beamline at the ESRF. For more details about saturation, optics, detection, etc.[116]

In the following sections 2.1.3.2 and 2.1.3.3, we present the gain of the HERFD-XAS in the XAS analysis under an article showing the the difference of both measurements by classical and HERFD-XAS. Describing the method of Crystal Analyzer Spectrometer (CAS) in details by the giving an energy resolution at each threshold used and type of crystal refelcetion. CAS helps to overcome the restrictions coming from the optical componenets on sample concentrations. CAS based on a Johann_type geometry have been developed to overcome these limitations, it covers a large energy range allowing to probe fluorescence

lines characteristic of all the elements. In this case, it is interesting to compare total fluorescence and HERFD-XAS, and thus quantify in which case using a CAS is more appropriate than a SSD. The interest of using the CAS is shown in FIG. 3 of Sec. 2.1.3.2 which represents typical emission fluorescence spectra collected with the CAS and the SSD.

2.1.3.2 Interest of High-Energy Resolution Fluorescence Detected X-Ray Absorption Spectroscopy

Olivier Proux, Eric Lahera, William Del Net, Isabelle Kieffer, Mauro Rovezzi, Denis Testemale, Mohammed Irar, Sara Thomas, Antonio Aguilar-Tapia, Elena F. Bazarkina, Alain Prat, Marie Tella, Mélanie Auffan, Jérôme Rose, and Jean-Louis Hazemann*

Supplemental material is available online for this article. O. Proux, E. Lahera, W. Del Net, I. Kieffer, and M. Rovezzi, Observatoire des Sciences de l'Univers de Grenoble (OSUG), UMS 832 CNRS, Univ. Grenoble Alpes, F-38041 Grenoble, France; D. Testemale, M. Irar, S. Thomas, A. Aguilar-Tapia, E.F. Bazarkina, A. Prat, and J.-L. Hazemann, Inst. Néel, UPR 2940 CNRS, Univ. Grenoble Alpes, F-38000 Grenoble, France; S. Thomas, Dep. of Civil and Environmental Engineering, Northwestern Univ., Evanston, IL 60208; S. Thomas, Laboratoire de Chimie et Biologie des Métaux (LCBM) UMR 5249 CNRS, CEA, Univ. Grenoble Alpes, F-38054 Grenoble, France; E.F. Bazarkina, Institute of Geology of Ore Deposits, Mineralogy, Petrography and Geochemistry, Russian Academy of Sciences, IGEM RAS, 119017 Moscow, Russia; M. Tella, Centre de Coopération Internationale en Recherche Agronomique pour le Développement (CIRAD), US 49 Analyze, TA B-49/01, F-34398 Montpellier Cedex 5, France; M. Auffan and J. Rose, Centre de Recherche et d'Enseignement de Géosciences de l'Environnement (CEREGE) UM34, UMR 7330, CNRS, Aix-Marseille Univ., IRD, Collège de France F-13545 Aix en Provence, France. Received 13 Jan. 2017. Accepted 3 Apr. 2017. *Corresponding authors (jean-louis.hazemann@neel.cnrs.fr). Assigned to Associate Editor Peter Kopittke.

Abbreviations: CAS, crystal analyzer spectrometer; ESRF, European Synchrotron Radiation Facility; EXAFS, extended X-ray absorption fine structure; HERFD, high-energy resolution fluorescence detected; LCF, linear combination fitting; PCA, principal component analysis; SDD, silicon-drift detector; SSD, solid-state detector; XANES, X-ray absorption near-edge structure; XAS, X-ray absorption spectroscopy; XES, X-ray emission spectroscopy.

Core Ideas
Study shows high-resolution spectroscopic data for an improved speciation determination.
Speciation of trace elements down and below the $\mu g.g^{-1}$ level is shown.
Measurements are made in vivo or at natural concentration.

Abstract

The study of the speciation of highly diluted elements by X-ray absorption spectroscopy (XAS) is extremely challenging, especially in environmental biogeochemistry sciences. Here we present an innovative synchrotron spectroscopy technique: high-energy resolution fluorescence detected XAS (HERFD-XAS). With this approach, measurement of the XAS signal in fluorescence mode using a crystal analyzer spectrometer with a ~1-eV energy resolution helps to overcome restrictions on sample concentrations that can be typically measured with a solid-state detector. We briefly describe the method, from both an instrumental and spectroscopic point of view, and emphasize the effects of energy resolution on the XAS measurements. We then illustrate the positive impact of this technique in terms of detection limit with two examples dealing with Ce in ecologically relevant organisms and with Hg species in natural environments. The sharp and well-marked features of the HERFD–X-ray absorption near-edge structure spectra obtained enable us to determine unambiguously

and with greater precision the speciation of the probed elements. This is a major technological advance, with strong benefits for the study of highly diluted elements using XAS. It also opens new possibilities to explore the speciation of a target chemical element at natural concentration levels, which is critical in the fields of environmental and biogeochemistry sciences.

Environmental biogeochemistry is a very large and diverse area of research that includes the works of biologists, toxicologists, geochemists, chemists, physicists, and others who aim to understand the interaction between a pollutant and a biotope. Such studies can be performed at different scales, from the macroscopic, microscopic, or nanoscopic (imaging techniques applied to the whole organism, organ, plant, etc.) levels to the atomic level. In this context, synchrotron radiation techniques are very powerful, particularly to study the distribution (micro X-ray fluorescence imaging) and the chemical speciation (X-ray absorption spectroscopy, XAS) of trace metals or metalloids (Sarret et al., 2013; Kopittke et al., 2017). X-ray absorption spectroscopy probes the speciation of a target chemical element (*i.e.* its valence, composition, and structure of the coordination shells) and is widely used for this aim (Lombi et al., 2011).

One characteristic of XAS measurements in the field of environmental and biogeochemical sciences is that the probed element (e.g., pollutant or metal of the metalloprotein) is often diluted in the medium, even in synthetic samples, to be representative of realistic concentrations. In studies of nanoparticles, XAS signals contain both bulk and surface contributions, the latter being much smaller than the former, even for very small particles. Due to the fact that interactions between the nano-object and its environment occur mainly at its surface, the surface signal is usually the most meaningful (e.g., for toxicology studies). Thus, XAS spectra should be of very good quality from both a statistical and spectroscopic point of view to detect weak surface changes coming from a small fraction of the sample.

The acquisition of high quality XAS spectra requires an optimized and stabilized photon flux on the sample combined with an efficient and highly sensitive detection system. Such detection has been performed in fluorescence mode for ~40 yr (Jaklevic et al., 1977). Fluorescence detection needs to be performed using an energy-resolved detector to minimize the contribution of the undesired photons, mainly elastic and inelastic scattering photons and photons produced by fluorescence of other chemical elements. On most of XAS beamlines, such detection is performed using a solid-state detector (SSD) or silicon-drift detector (SDD), with a typical energy resolution ~150 to 300 eV. Such detectors are very useful and efficient for three main reasons. First, the energy of the fluorescence photons of interest can be changed quickly and easily. Second, the energy resolution is often low enough to sort the different types of photons cited above. Third, the counting rate can be extended to ~10^6 counts s^{-1}, with the appropriate electronic and synchrotron photon bunch frequency. However, with such detectors, the intrinsic detection limit comes mainly from the overlap of elastic and inelastic scattering events with the measured signal (Hazemann et al., 2009; Heald, 2015). The state-of-the-art detection limit with an SSD is ~10 to 100 $\mu g.g^{-1}$ in weight or <1 mmol L^{-1}. As an illustration, a compilation of concentration limits for XAS measurements in bioenvironmental science fields, as reported in the literature and performed on the BM30b

beamline at the European Synchrotron Radiation Facility (ESRF, Grenoble, France), is indicated in Supplemental Fig. S1.

One way to overcome these limitations is to use a detection system with a better energy resolution, such as a crystal analyzer spectrometer (CAS). We will detail in this paper why and how XAS studies of diluted elements or nanoparticles can be particularly improved using such an efficient detector.

Materials and Methods

Solid-State Detector vs. Crystal Analyzer Spectrometer

The schematic process of the fluorescence measurements by both systems is described in Fig. 1. With SSD (or SDD) technology, the photons are collected and later electronically separated by energy (e.g., Fig. 1d). Technically, the energy resolution is limited by (i) the Fano factor (the energy loss by the photons to create an electron-hole pair is not purely statistical), (ii) the incomplete collection of the charge produced in the depletion zone, and (iii) electronic considerations such as the parasitic noise and capacitance at the input of the charge-sensitive preamplifier, and the speed of the processing electronics (e.g., the shaping time).

The typical energy bandwidth thus ranges between ΔE = 120 and 300 eV, depending on detector quality and shaping time (the faster the time, the higher the counting rate but the lower the resolution). The fluorescence photons of interest (highlighted in red in Fig. 1d) on the x-ray fluorescence spectrum are then integrated within an energy region of interest. The variation of this integrated intensity with the incident energy gives rise to the total fluorescence yield XAS spectrum (red curve in Fig. 1a).

With a CAS, the photons are first optically selected in energy (Bragg scattering) and later collected by a detector that does not necessarily need to be energy resolved. Compare with SSD, the optical adjustment of CAS is generally more time consuming, and the measurements of XAS spectra takes more time. The energy resolution of a Johann's type CAS (Supplemental Fig. S2) is limited by (Collart et al., 2005; Hazemann et al., 2009):

1. The Johann's geometry aberration. Indeed, only the center of the crystal is on the Rowland's circle, leading to an angular dispersion in the vertical plane and, consequently, an energy dispersion (Supplemental Fig. S3). This aberration is all the more limited when the Bragg angle is close to 90° and/or the radius of curvature is large. In most cases, this is the true limiting factor for the total energy resolution. Consequently, the choice of crystals used for the analysis of a given fluorescence peak must take into account this characteristic (optimized choice of crystal analyzers corresponding to a large number of elements and their associated emission line are given on Supplemental Tables S2 and S3). The emission energy range that can be covered by one crystal is consequently rather limited;

2. The intrinsic properties of the crystal reflection, the so-called Darwin width (G. W. Brindley,1933);

3. The imperfections of the bent crystal due to the bending process (Rovezzi et al., 2017).

Thus, for a CAS equipped with spherically bent crystal analyzers with a radius of curvature of 1-m range, the energy bandwidth typically ranges from 0.2 to 2 eV. This value is then smaller than the core-hole lifetime of the measured fluorescence line (Supplemental Tables S2 and S3): X-ray emission spectroscopy (XES) measurements can be achieved. Moreover, by integrating only a narrow region of the fluorescence line of interest (as shown in Fig. 1f for a fraction of the $K\beta_{1,3}$ line), the high-energy resolution fluorescence detected XAS (HERFD-XAS) can be measured (blue curve in Fig. 1a).

The main advantages of measuring fluorescence-XAS with CAS instead of SSD (or SDD) are:

1. XAS (including extended x-ray absorption fine structure [EXAFS] and X-ray absorption near edge structure [XANES]) measurements can be achieved on complex and/or diluted systems where the detection limit is determined by the fluorescence of the main constituents of the matrix and/or the scattering signals;

2. Energy resolution of HERFD XANES spectra can be sharper than what could be achieved conventionally (Hämäläinen et al., 1991; de Groot et al., 2002; Bauer, 2014), which improves the accuracy of XANES quantitative analyses;

3. Energy position of the fluorescence lines (and especially the Kβ ones for the K-edges) is sensitive to the spin state ($K\beta_{1,3}$) and to the ligands ($K\beta_{2,5}$ and its satellite lines) of the probed element. The XAS spectra obtained by measuring these lines are then spin or ligand sensitive (Bergmann et al., 1999; Rovezzi and Glatzel, 2014),

4. Other spectroscopic techniques such as XES can be performed. For example, valence-to-core XES allows discrimination between the different ligands in the first coordination sphere of the probed element (Safonov et al., 2006; Bauer, 2014; Gallo and Glatzel, 2014).

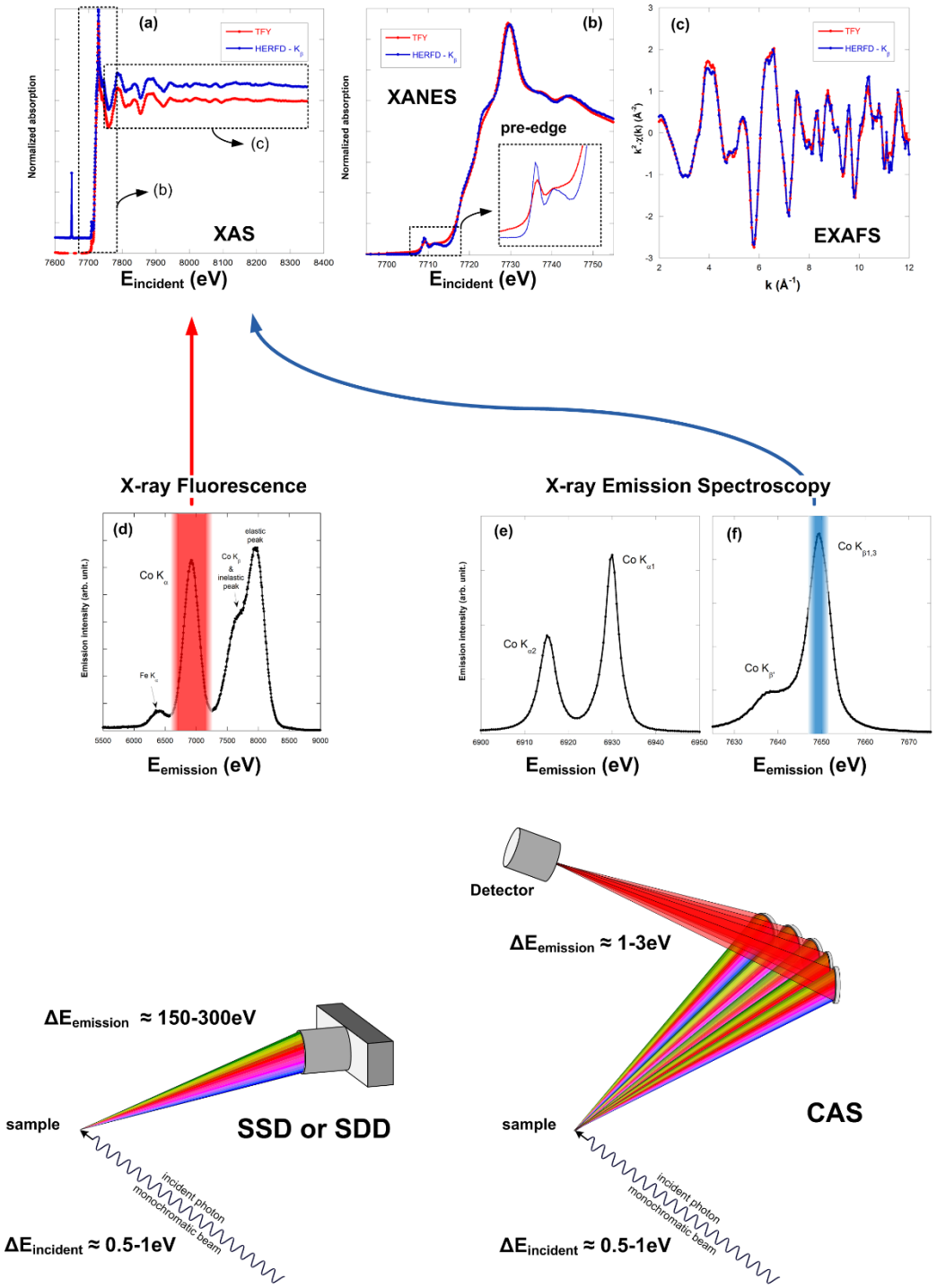

Fig. 1. Principle of X-ray absorption spectroscopy (XAS)-fluorescence measurement using solid-state detector (SSD) and crystal analyzer spectrometer (CAS). Spectra correspond to the analysis of a Co_3O_4 sample with a 30-element Ge SSD (total fluorescence yield, red spectra) and a CAS using five Ge(444) crystals optimized around the Co $K_{\beta 1,3}$ fluorescence line (high-energy resolution fluorescence detected [HERFD], blue spectra; Bordage et al., 2015). (a) XAS spectra. (b) X-ray absorption near-edge structure (XANES) spectra; insert corresponds to a zoom on the pre-edge region. (c) extended X-ray absorption fine structure (EXAFS) spectra $k^2\chi(k)$. (d) Fluorescence spectra measured with the SSD and CAS. (e) $K_{\alpha 1}$ and $K_{\alpha 2}$ X-ray emission spectroscopy (XES) spectra measured with the CAS using five

Si(440) crystals. (f) $K_{\beta 1,3}$ fluorescence line and its $K_{\beta'}$ satellite measured with the CAS using five Ge(444) crystals.

X-ray Spectroscopic Techniques

Detailed explanations of the XAS and XES theories fall outside the scope of this paper and can be found in numerous recent reviews, on core-level spectroscopy generality (de Groot and Kotani, 2008), XANES (Henderson et al., 2014; Joly and Grenier, 2016), EXAFS (Newville, 2014), XAS (Rehr and Albers, 2000; Ortega et al., 2012; Milne et al., 2014), XES (DeBeer and Bergmann, 2016), and HERFD (Bauer, 2014; Kowalska et al., 2016) applied to bioionorganic chemistry, and applications in environmental sciences (Gräfe et al., 2014). We will briefly recall the main principles of the core-level spectroscopy techniques with special attention to effects that can be better analyzed with CAS.

An X-ray interacts with the core electrons of atoms and, depending on its energy, can be absorbed by them through the photo-electric effect. The electrons can be excited to an upper empty electronic level or, if the X-ray energy is higher than the binding energy of the considered electron, to a free state as a photo-electron. The direct consequence of this excitation process is the creation of a core hole on the electron's initial level and a jump of the X-ray absorption when increasing the incident X-ray energy around the binding energy of an electron, the so-called absorption edge.

The probability of this event is the absorption cross-section, which depends on the energy of the incident X-ray photon, the considered element, and the electronic level: $\mu_{element,\ edge}(E)$. The subsequent relaxation process gives rise to the emission of either fluorescence photons or Auger electrons. When the probed element is diluted in its matrix, the total fluorescence yield is considered to be proportional to $\mu_{element,\ edge}(E)$ (Jaklevic et al., 1977).

The absorption cross-section presents a jump around the binding energy (Fig. 1a). The energy position of this absorption edge is characteristic of a given element and the considered electronic level. The probed element can then be precisely targeted. The absorption cross-section evolution versus energy can be divided in two areas. The XANES area is defined around the edge (Fig. 1b); the EXAFS area is defined beyond the edge (Fig. 1c).

The photo-electron emitted by the absorbing atom can be scattered by the electronic potentials of the neighboring atoms. The interference between the incident wave (linked to the outgoing photo-electron) and the scattered one induces modulations and oscillations of the absorption cross-section. The EXAFS signal is the oscillating part of the absorption signal above the edge, dominated by the single scattering events. It gives information on the local atomic order around the probed absorbing element (number, distance, and nature of the neighbors). The mean free path of the photo-electron being limited to few Å (roughly up to 10 Å in the considered energy area), the EXAFS information will be limited to the local order around the central atom.

In the XANES energy range, when the incident photon energy is slightly higher than the binding energy of the core level, modulation of the absorption cross-section will occur, as in

the EXAFS region, but the multiple scattering events will contribute strongly to the spectrum. X-ray absorption near-edge structure can then provide information on the site geometry of the probed element. In addition, the spectrum can present well-marked peaks characteristic of electronic transitions from the core hole excited state to empty states. X-ray absorption near-edge structure can then also provide information on the electronic structure of the probed element. The intrinsic spectroscopic limitation of this technique comes from the core hole, which can have a large lifetime and can thus induce a broadening of the peak. A way to overcome this broadening is to perform the XANES measurement in the fluorescence mode and to measure the fluorescence line intensity with an energy resolution below the core-hole lifetime broadening of the absorption edge. This is typically the case when using a CAS, and the measurement is then called HERFD XANES (Hämäläinen et al., 1991).

Another interesting energy region is the lower side of the XANES, the so-called pre-edge region (inset of Fig. 1c). Resonant structures (pre-edge peaks) may appear in this region, which are strongly sensitive to the electronic structure of the absorbing site. The analysis of such features permits the extraction of information on the spin or oxidation state, geometry, and type of ligand. The pre-edge features for K-edge XANES of 3d transition metals have been studied in detail (Westre et al., 1997; Yamamoto, 2008; de Groot et al., 2009; Cabaret et al., 2010).

In addition to HERFD-XAS, the use of a CAS permits performing XES measurements. Non resonant XES consists of scanning the emitted fluorescence with a CAS at a fixed incoming X-ray energy, above an absorption edge. X-ray emission spectroscopy also permits probing the local electronic structure of the absorbing element and has been used extensively (Bergmann and Glatzel, 2009; Glatzel and Juhin, 2013). With respect to XANES, XES probes occupied valence electrons (directly or indirectly) and are more sensitive to the local charge density. Depending on the selected transitions, XES is divided into two main regions: core-to-core (e.g., $K_{\alpha 1,2}$ or $K_{\beta 1,3}$) and valence-to-core (e.g., $K_{\beta 2,5}$). In the example of K emission lines of 3d transition metals, core-to-core XES permits the evolution of the local spin or oxidation state to be followed and may be used in turn to collect oxidation state-selective EXAFS (Glatzel et al., 2002) or XANES (Bordage et al., 2015). In addition, valence-to-core XES is more sensitive to metal-ligand mixed valence states and has been employed in chemistry to distinguish between ligands of light elements (Eeckhout et al., 2009). Such sensitivity permits in turn to collect valence-selective XAS (Hall et al., 2014).

High-Energy Resolution Fluorescence Detected XAS

We previously mentioned that measuring the fluorescence line intensity with an energy resolution around the core-hole linewidths, that is 1 to 5 eV, allows HERFD-XANES to be obtained (*i.e*. spectra showing sharper features than conventional ones; Hämäläinen et al., 1991).

This sharpening effect has been demonstrated by de Groot et al. (2002) by analyzing the resonant X-ray emission spectrum of Pt-$L_{\alpha 1}$ ($2p_{3/2}$–$3d_{5/2}$) and applied (e.g., by Swarbrick et al., 2009, for analysis at the Pb L_{III}–edge). Below are individual comparisons of the different

widths of the energy levels involved in the absorption process, detailed here for the L_{III}–edge (with the $L\alpha_1$ emission line).

In conventional XAS, for a L_{III} absorption edge, the final state has a $2p_{3/2}$ core hole with a Γ_{conv} core-hole lifetime.

In HERFD-XAS, the $L_{\alpha 1}$ fluorescence line corresponds to 3d (the final state) to $2p_{3/2}$ transition (the intermediate state). The apparent core-hole lifetime broadening of the HERFD measurement, Γ_{app}, is then given by:

$$\Gamma_{app.} = \frac{1}{\sqrt{\frac{1}{\Gamma_{int.}^2} + \frac{1}{\Gamma_{fin.}^2}}}$$

where Γ_{int} and Γ_{fin} are the intermediate ($2p_{3/2}$ for $L_{\alpha 1}$) and final state (3d for $L_{\alpha 1}$) core-hole lifetime broadening. Γ_{app} was calculated on Supplemental Table S2 (resp. Supplemental Table S3) for several elements at their K-edge (resp. L_{III}). The improvement of the HERFD-XANES spectral resolution compared with conventional spectra is a direct consequence of the difference between these final-state widths. The two examples presented below will deal with Ce and Hg L_{III}–edge analysis. Γ_{app} are calculated to 0.72 and 2.28 eV, respectively, with core-hole lifetime sof the probed level $\Gamma_{2p3/2}$ equal to 3.19 and 5.71 eV. All the features characteristics of electronic transitions (pre-edge, edge, or after-edge peaks) measured in the XANES are directly affected by the core-hole lifetime broadening. In HERFD-XANES, such features are then detected with a better energy resolution: a two- to fourfold improvement can be reached experimentally.

In the EXAFS region, the core-hole lifetime broadening also affects the amplitude of the oscillations through the mean free path (or lifetime) of the photo-electron, which includes both inelastic scattering of this electron and the lifetime of the core hole (Rehr and Albers, 2000). This effect is especially important for high *Z* elements studied at their K-edge and can be corrected using spectral deconvolution (Fister et al., 2007). For the elements that can be probed with a CAS, the effects is very limited, even indistinguishable (Fig. 1c). A comparison of XAS measurements on Cu and Pd foils performed with monochromators with different energy resolution showed that the EXAFS amplitudes, as described by the amplitude reduction factor S_0^2, are comparable (Kelly et al., 2009). In a first approximation, the EXAFS measurements with CAS do not significantly change the signal compared with the conventional measurement.

Instrumentation

Among the different possible geometries, the most frequently encountered on synchrotron beamlines are the Johann (1931), Johansson (1933), and von Hámos (1932). The technical requirements to perform a high-energy resolution fluorescence measurement are the following: (i) at least one crystal analyzer in Bragg condition with respect to the energy of the

photons of interest and (ii) a detector that collects the diffracted photons. Both geometries are in reflection mode (Bragg type; *i.e*. suitable for low-energy X-ray studies).

In the first case, the sample, the crystal, and the detector are positioned on a circle (the Rowland circle). The crystal is spherically bent, with its radius of curvature equal to the diameter of the Rowland circle. When the crystal is close to backscattering, the geometric errors are very small; the whole crystal surface meets Bragg diffraction conditions for a given energy and the diffracted photons are focused on the detector. The crystal can be considered as a monochromator. During an XES spectrum acquisition, the crystal and the detector need to be moved simultaneously, accordingly to the Rowland circle conditions.

In the second case, the shape of the crystal is no longer spherical but flat, and the Bragg angle changes depending on the position of the considered X-ray on the crystal surface. The crystal can be considered then as a polychromator. The diffracted photons are no longer focused on a single point but dispersed on a surface. The use of a two-dimensional detector enables the whole energy spectrum of the emitted photons to be obtained (*i.e*. a XES spectrum in "one shot").

The HERFD measurements can also be achieved using transmission-type (Laue-type) curved crystal spectrometers linked to a large-area detector. This geometry is suitable for high-energy photons, above ~20 keV. Recently, using a Laue-type DuMond spectrometer (Szlachetko et al., 2013), energy resolutions of 2.8 eV for the Mo Kα1 X-ray line (17.479 keV) and 17.1 eV for the Gd Kα1 X-ray line (42.996 keV) have been obtained. These values are smaller than the core-hole lifetime of the corresponding measured absorption edge (4.52 eV for Mo, 22.3 eV for Gd).

On the BM30b beamline (ESRF), we developed a CAS in the Johann geometry (Hazemann et al., 2009; Llorens et al., 2012), this geometry being more adapted to an XAS beamline than the von Hámos one (technical details on this CAS can be found in the Supplemental Material). Such a geometry is now often used on several synchrotron beamlines (Supplemental Table S1) from the pioneering spectrometers developed 20 yr ago (Stojanoff et al., 1992; Bergmann and Cramer, 1998). The growing number of papers in bioenvironmental and geochemistry sciences containing HERFD-XAS results follows this rise. A nonexhaustive review of references in bioenvironment and geochemistry sciences using XAS-CAS clearly exhibits a significant increase (Table 1): only five publications were found between 2002 and 2009, but the number rose to 13 between 2012 and 2016, illustrating the interest in the method and its performance.

Sample Preparation and Environment for Bioenvironment Studies using CAS

X-ray absorption spectroscopy (conventional or HERFD) and XES techniques are sensitive to element speciation. Two obvious points need then to be addressed when preparing these kinds of measurements.

First, the samples must be prepared without modifying the speciation of the target element. One of the most efficient ways to achieve this is to analyze the sample in its hydrated state. This preserves the chemical speciation of the probed element by keeping the water molecules inside the studied structure. Great care must be taken between the sampling and the

analysis. The sample can then be kept in a hydrated frozen state (Sarret et al., 2013). To prevent damaging the sample (especially for biological components), the cooling process can be done using isopentane cooled down by liquid nitrogen (Luster and Finlay, 2006). Furthermore, the homogeneity of the sample, with respect to beam size, is key to good-quality measurement, whatever the XAS acquisition mode. Nonhomogeneous samples will give noisier spectra than homogeneous ones.

Second, the sample has to be preserved as much as possible from radiation damage during measurements. The effects of radiation damages of samples is the same for any XANES measurement mode (conventional or HERFD), but as the characteristic features of the XANES can be more marked in the HERFD mode, the consequences of radiation damages on the XANES shape may appear enhanced. As an example, we present on Supplemental Fig. S5 HERFD and conventional XANES spectra acquired simultaneously on the same sample position, a Pt/Al_2O_3 catalyst powder (Gorczyca et al., 2014). The increase of the intense peak after the edge (the so-called white line) seems characteristic of the oxidation of the Pt with the beam. The relative evolution of the white-line height is more marked for HERFD XANES than for the conventional XANES.

Acquiring the data at low temperature strongly reduces the spurious effects induced by the X-ray beam. Furthermore, reducing the thermal motion improves the EXAFS data quality. A way to fulfill these conditions is to perform the acquisition on frozen samples placed in an appropriate cryostat (liquid nitrogen or, even better, liquid helium temperature). Another way to avoid radiation damage is to quantify the time necessary to observe a difference between spectra by doing short-time spectra centered on the edge-energy area (Sarret et al., 2013). This time is then the time limit before observing the effects of radiation damage. It is a function of the temperature, the photons' brightness on the sample, and the nature of the sample. The spectrum's duration should then be shorter than the time limit. If several acquisitions are necessary (e.g., to improve the data quality), the position of the beam on the sample will be moved between each scan to probe an untouched area of the sample.

Results

HERFD and Bioenvironment: A Tool to Study Diluted Elements

The main parameter that limits the ability to perform XAS experiments on diluted elements in optimal conditions may arise from the matrix or the bearing phase. When the probed element is diluted in a soil (which can contain clays, silicates, and iron or manganese oxides), fluorescence signals delivered by the main constituents of this matrix can saturate a SSD, even with the use of appropriate filters. Moreover, in some cases, the fluorescence peaks of some matrix constituents can be too close in energy to the fluorescence peak of the targeted element to be discriminated by the SSD. When the probed element is diluted in a liquid, a plant, or more generally light matter, the limitation comes from the scattered beams. Llorens et al. (2012) studied bromide aqueous solutions at different concentrations to have an idea of the intrinsic XAS concentration limit of the SSD. Here, the limitation is given by a partial overlap of the measured signal (Br K_α fluorescence) with the low-energy tail of scattered

beams (elastic or inelastic scattering). Using the rule that the signal of interest should be three times the unwanted signal, an intrinsic limit of XAS measurement using SSD can been estimated to 23 $\mu g.g^{-1}$ for Br in solution.

With the emergence of CAS on XAS beamlines, a set of recent publications demonstrates the advantages of this new technique. The corresponding concentrations of the elements investigated are given in Table 1. In the field of biogeochemistry, Bissardon (2016) studied the contribution of selenium in cartilage at in vivo concentrations, which are below $\mu g.g^{-1}$ or even a few hundreds of $ng.g^{-1}$. Similarly, Manceau et al. (2016) analyzed the chemical form of Hg in human hair down to 0.5 $\mu g.g^{-1}$, and Vogel et al. (2016) explored the chemical form of both Se and Hg in sewage sludge down to 0.6 and 0.8 $\mu g.g^{-1}$, respectively. These studies would not have been possible with a conventional XAS measurement.

HERFD and EXAFS Analysis

In most cases (and in all literature found on the subject in bioenvironmental studies), the interest of CAS is focused on XANES studies and not on EXAFS. However, EXAFS analysis can also benefit from high-energy resolution fluorescence measurement.

When the characteristic emission line of the probed element is very close to those of other elements located in the sample, it is difficult to perform EXAFS analysis with good measurement statistics using a SSD. In this case, the background of the EXAFS spectrum (due to the other elements) is very high compared with the edge jump, especially when the element of interest is diluted. Using a CAS, the different emission lines can be precisely separated, and the EXAFS measurement is possible with a background close to 0. This method was used by Sheng et al. (2014) to define the Eu interaction with β-MnO_2.

The problem is similar when the element of interest is diluted in a light matrix (water, biological matrix, etc.). The background signal when measuring the spectrum by an SSD is not dominated by any fluorescence but by the low-energy tail of the Compton peak (Llorens et al., 2012). Like the previous point, the use of a CAS provides a very low background for the EXAFS measurement on diluted or ultra-diluted elements.

Energy position of emission lines can change for a given element, depending on its valence state. Measurement with EXAFS (as well as XANES) can exploit this change to obtain valence-sensitive spectra, which is useful in the case of mixed-valence compounds. Grush et al. (1995) demonstrated the interest of this selectivity for EXAFS measurements on Mn compounds (mixed Mn^{2+} and Mn^{3+} compounds). Fe^{2+} and Fe^{3+} species were probed in Prussian Blue (Glatzel et al., 2002). Lambertz et al. (2014) probed the two Fe sites in an Fe-rich hydrogenase enzyme. Kühn et al. (2014) studied Co nanoparticles where the Co^0 core is protected by a Co-based shell.

Table 1. Example of high-energy resolution fluorescence detected (HERFD)-X-ray absorption spectroscopy (XAS) publications in the field of environmental biogeochemistry sciences. The elemental concentrations are given in μg g^{-1} or mol; both the temperature (*T*) and beam size on the sample are indicated as well.

Element	Field	Interest†	Concentration	*T*/beam size	Reference
Mn	Biomineralization	LS	0.01g L^{-1} δMnO_2 + 100 μM $MnCl_2$	<70 K/0.3 × 1 mm^2	Bargar et al. (2005)
Mn	Biomineralization	HR	<10 μg g^{-1}		Soldati et al. (2016)
Fe	Biochemistry	HR		RT/200 × 100 μm^2	Mijovilovich et al. (2012)
Fe	Biomineralization	HR	<0.1 mol L^{-1}	20 K/200 × 400 μm^2	Baumgartner et al. (2013)
Fe	Biomineralization	HR		10 K/200 × 400 μm^2	Lohße et al. (2014)
Fe	Bioenergy	HR			Casals et al. (2014)
Fe	Biogeochemical	LS			Blazevic et al. (2016)
As	Bioremediation	HD	1300–4800 μg g^{-1}	290 K	Masih et al. (2007)
Se	Biogeochemical	HD	0.4–3.0 μg g^{-1}	10 K/300 × 100 μm^2	Bissardon (2016)
Se	Bioenvironmental	HR and HD	0.8–9.2 μg g^{-1}	40 K	Vogel et al. (2016)
Ce	Bioenvironmental	HR	60 and 85 μg g^{-1}	10 K	Tella et al. (2015)
Eu	Chemical environment condition.	Matrix fluorescence		RT	Sheng et al. (2014)
Os	Geochemistry	Matrix fluorescence	58.3 and 65.7 μg g^{-1}	RT/200 × 800 μm^2	Takahashi et al. (2006)
Pt	Medical	HR		RT/100 × 100 μm^2	Sá et al. (2016)
Hg	Bioenvironmental	HR and HD	48, 81, and 191 μg g^{-1}	10 K/500 × 80 μm^2	Manceau et al. (2015)
Hg	Bioenvironmental	HR and HD	0.74–30.2 μg g^{-1}	10 K/700 × 80 μm^2	Manceau et al. (2016)
Hg	Bioenvironmental	HR and HD	0.6–4.4 μg g^{-1}	40 K	Vogel et al. (2016)
Hg	Biogeochemical	HR		10 K	Poulin et al. (2016)
Pb	Chemical environment condition.	HD	1200–3000 μg g^{-1}	RT/1 × 1 mm^2	Izumi et al. (2002)
Pb	Chemical environment condition.	HR	40 mM Pb	RT/0.3 × 1 mm^2	Swarbrick et al. (2009)

† LS, ligands sensitivity; HD, high dilution; HR, high resolution (HERFD).

HERFD and Bioenvironment: High-Resolution XANES Studies

The use of CAS enables the obtainment of a HERFD-XANES signal with a spectral resolution much sharper than what could be conventionally achieved. This possibility is of great interest in environmental biogeochemistry because (i) the differences between spectra are often subtle and (ii) the improved resolution gives a more precise discrimination of the local structure around the absorbing atom. This possibility was, for example, fully exploited at the Fe K-edge probing the Fe $K_{\beta 1,3}$ fluorescence line to study biomineralization processes (Baumgartner et al., 2013), to study magnetite nanoparticle evolution during conversion of biomass (Casals et al., 2014), at the Ce L_{III} edge to characterize the behavior of cerium oxide nanoparticles in aquatic mesocosms (see below; Tella et al., 2015), or at the Hg L_{III} edge to determine which chemical forms of Hg are present in human hair (Manceau et al., 2016). To highlight in more detail this real step forward, XANES measurements in conventional

methods (transmission or total fluorescence yield measurement) and in HERFD are presented below to ascertain the valence state of Ce, in the case of biotransformation of CeO_2 nanoparticles, and the speciation of Hg bound to sulfur. The consequence of this improved energy resolution are also of great importance when the experimental spectra are compared with calculated ones (Swarbrick et al., 2009; Mijovilovich et al., 2012). We will quantify here the improvement in the speciation determination when analyzing the XANES spectra by principal component analysis (PCA) and linear combination fitting (LCF), as used, for example, to study Fe biomineralization (Baumgartner et al., 2013) or Hg speciation in sewage sludge (Vogel et al., 2016).

Cerium Valence Determination

In many studies, the determination of oxidation state between Ce^{IV}/Ce^{III} or the ratio is of crucial importance in particular for its bioavailability and its toxicity. Indeed CeO_2 is a strong oxidant due to a high Ce^{IV} to Ce^{III} redox potential. Such high oxidation power directly or indirectly can create oxidative stress for living organisms and cells. Cerium oxide nanoparticles' interactions with organisms and biological media have been particularly investigated, such as with human cells (Auffan et al., 2009), biomolecules (Rollin-Genetet et al., 2015), microorganisms (Zeyons et al., 2009; Ma et al., 2013; Collin et al., 2014), plants (López-Moreno et al., 2010; Zhang et al., 2012; Hong et al., 2014), mollusks (Tella et al., 2014), and mussels (Garaud et al., 2016). In these studies, the reduction of Ce^{4+} to Ce^{3+} in CeO_2 nanoparticles was probed by conventional XANES spectroscopy. Speciation quantification was in most cases based on linear combination of CeO_2 and Ce^{3+} reference spectra (Fig. 2a). For example, for the study of CeO_2 nanoparticles interacting with human dermal fibroblasts (Auffan et al., 2009), the shoulder which appears on the XANES spectra at 5724 eV, was attributed to Ce^{3+}, and the quantification led to a Ce^{3+} contribution of 8 ± 2%. However, with conventional XANES, the shoulder at 5724 eV can be attributed either to Ce^{3+} single absorption jump, corresponding to the $2p_{3/2} \rightarrow (4f_1)$ 5d electronic transition, or crystal field splitting into e_g and t_{2g} for $Ce^{4+}O_2$ particles.

High-energy resolution fluorescence detected XANES was used in a recent study (Tella et al., 2015) addressing the environmental impact, (bio)distribution, and (bio)transformation of nano-CeO_2 in realistic exposure conditions. This required the development of an adapted experimental strategy based on indoor aquatic mesocosms that virtually mimic aquatic ecosystems (Auffan et al., 2014; Tella et al., 2014). Over 4 wk, the transfer, redox transformation, and impacts of 1-mg L^{-1} CeO_2 nanoparticles were determined respecting an ecologically relevant mollusc (*Planorbarius corneus*) living in a pond environment. Over time, CeO_2 nanoparticles tend to homo- and heteroaggregate and to accumulate on surficial sediments, where they are available to interact with benthic grazers as *P. corneus*. A transitory oxidative stress was observed in *P. corneus* after 2 wk of exposure (lipid peroxidation and increase in the antioxidant defense capacity). By combining X-ray tomography and laser ablation inductively coupled plasma mass spectrometry (ICP-MS), Ce was localized in the digestive gland of benthic organisms, where a strong biotransformation of the CeO_2 nanoparticles occurred. Using LCF of the pre-edge area of the HERFD-XANES spectra, the authors quantified that 81 ± 8% of Ce^{IV} was reduced into Ce^{III} in the digestive gland (and 22 ± 2% remained Ce^{IV})**. However, in the surficial sediment, no contribution of Ce^{III} improved**

the LCF residue. This led to the conclusion that the changes in the HERDF spectra observed were not associated with the reduction of Ce^{IV} but with changes in the crystallite size of CeO_2. These samples were also analyzed by conventional XAS. Linear combination fitting analysis of the surficial sediments and the digestive gland was found to overestimate by 20 to 30% the reduction into Ce^{III}. Consequently, without HERFD-XAS, it would have been impossible to unambiguously attribute the Ce^{III} reduction to the digestive activity of the molluscs, and not to an interaction with the biofilm present on the surficial sediments.

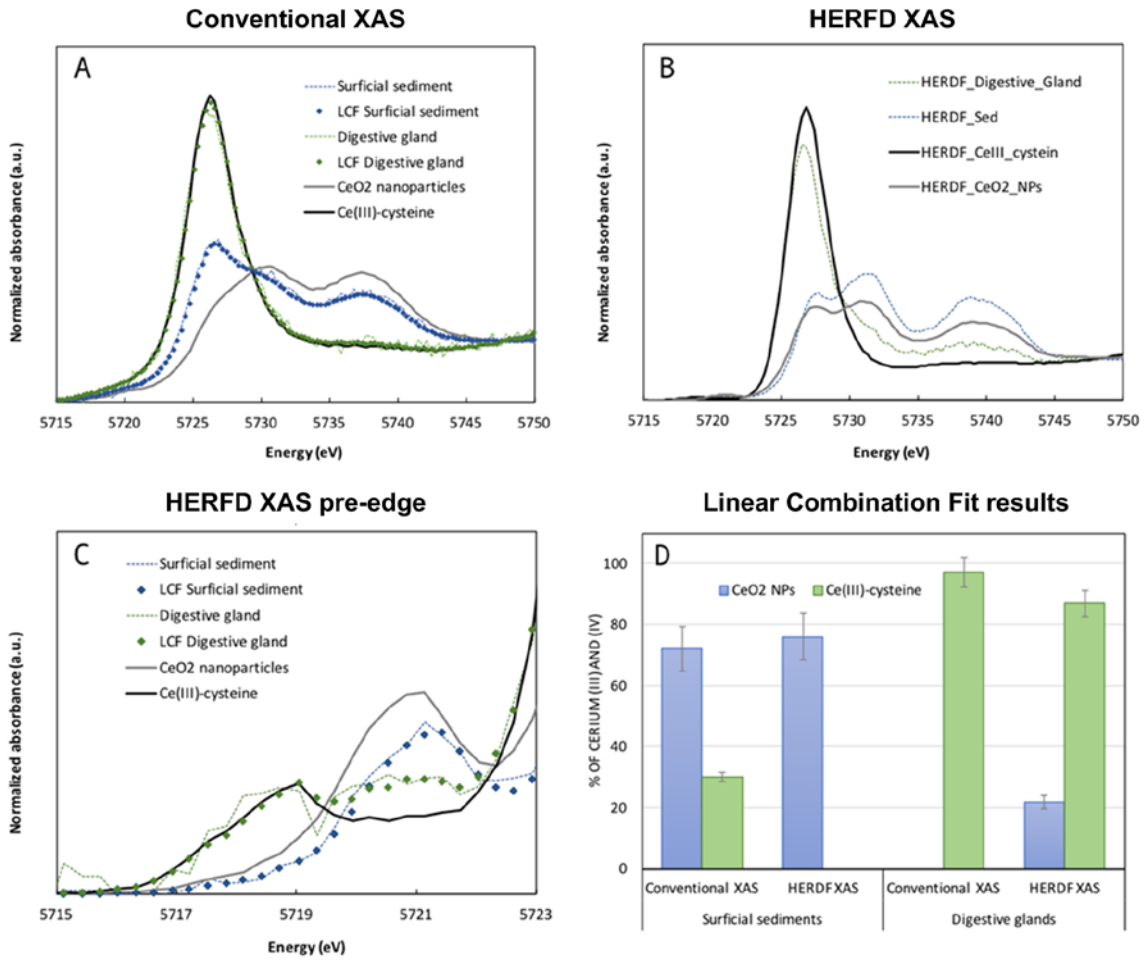

Fig. 2. (A) Conventional X-ray absorption spectroscopy (XAS) and (B) high-energy resolution fluorescence detected (HERFD) XAS analysis of the surficial sediments and the digestive gland of *P. corneus* exposed for 4 wk to CeO2 nanoparticles in aquatic mesocosms mimicking a pond ecosystem. (C) Zoom in on the pre-edge area of the HERFD XAS spectra. (D) Results of the linear combination fits performed on the conventional XAS (range 20 to 30 eV) and HERFD XAS (range −8 to −1 eV) spectra using two reference compounds, the initial CeO_2 nanoparticles and the Ce^{III}–cysteine.

Mercury Speciation

Anaerobic microorganisms are responsible for producing the neurotoxin methylmercury (MeHg) in the environment, requiring inorganic Hg^{II} as a substrate (Parks et al., 2013). Many studies have employed XAS to study Hg^{II} speciation in environmental and biological samples to better understand which Hg^{II} species are bioavailable for MeHg production (Andrews, 2006; Skyllberg et al., 2006; Nagy et al., 2011; Dunham-Cheatham et al., 2014, 2015; Thomas et al., 2014; Manceau et al., 2015). In the anoxic environments where MeHg is produced, Hg^{II} is primarily bound to thiol functional groups in organic matter or sulfide due to its high affinity for reduced sulfur. Additionally, environmental Hg^{II} concentrations are intrinsically low (<1 $\mu g.g^{-1}$). Analyses of diluted samples benefit from solely scanning the XANES region to avoid the longer scan time required for the EXAFS. However, conventional Hg L_{III} edge XANES of Hg coordinated to sulfur atoms contain few distinguishing features (Fig. 3), making it difficult to correctly identify relevant Hg^{II} species in natural environments. In contrast, the increased spectral resolution of Hg L_{III} edge HERFD-XANES provides distinct spectral signatures for different forms of Hg^{II} bound to reduced sulfur. Both the conventional and HERFD-XANES spectra of α-HgS and β-HgS were measured at room temperature (Fig. 3); thus, the observed increase in resolution is not a temperature effect. High-energy resolution fluorescence detected XANES will be an asset to future studies of Hg^{II} speciation, lowering the detection limit for Hg^{II} in natural samples.

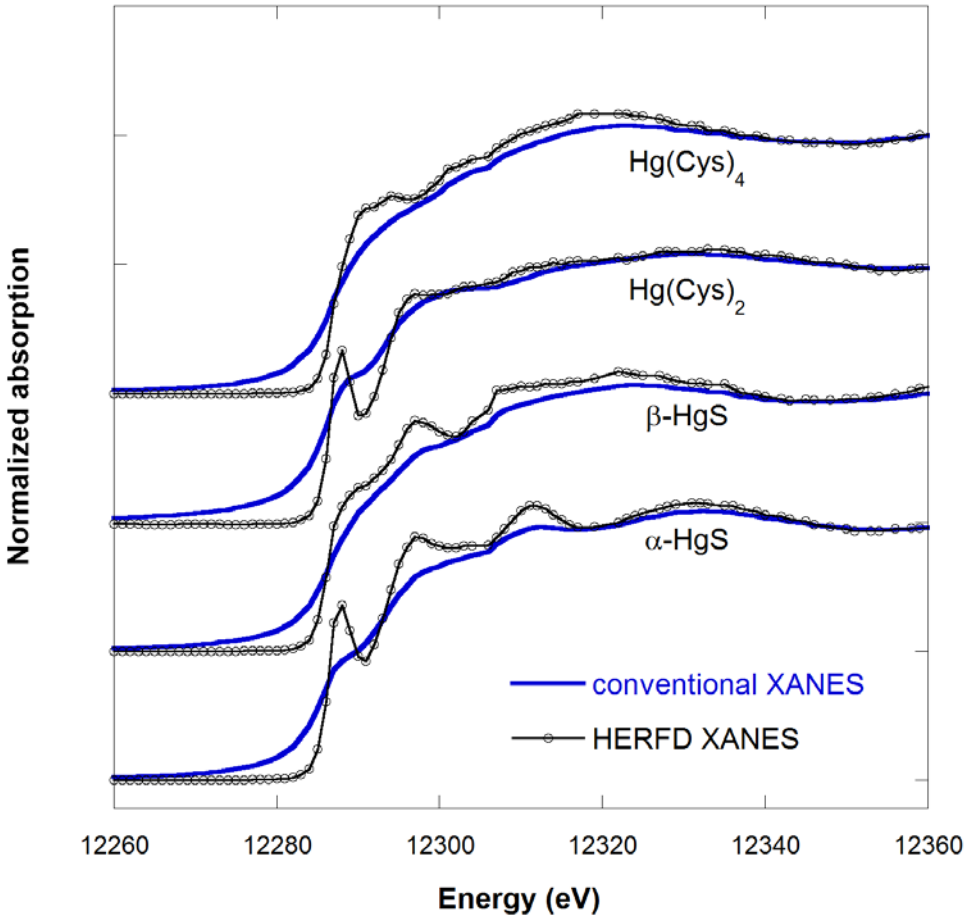

Fig. 3. Mercury L_{III} edge conventional and high-resolution X-ray absorption near-edge structure (XANES) of species of Hg^{II} with reduced sulfur coordination. The Hg^{II} in α-HgS (cinnabar) and $Hg(Cysteine)_2$ is linearly coordinated to two sulfur atoms, whereas the Hg^{II} in β-HgS (metacinnabar) and $Hg(Cysteine)_4$ is tetrahedrally coordinated to four sulfur atoms. Preparation and X-ray absorption spectroscopy (XAS) measurement details are given in the Supplemental Material and described more extensively in Thomas & Gaillard (2017). The Hg L_{III}–edge high-resolution XANES spectra were measured on BM30B and BM16, and the conventional XANES spectra were measured on the DuPont–Northwestern–Dow Collaborative Access Team (DND-CAT) beamline at the Advanced Photon Source.

Consequence on Principal Component Analysis and Linear Combination Fitting

Speciation determination of metals (or metalloids, halogens, etc.) in environmental and biogeochemical samples can be challenging when the probed element is present in several forms. An often-used way to overcome this complexity is to reconstruct the spectrum obtained for the sample with a LCF of model compound spectra (Gräfe et al., 2014). The accuracy of this reconstruction depends on several parameters, among them (i) the quality of the spectra (both of the samples and the model compounds), (ii) the relevance of the model compound spectral database (Are all the possible configurations present? Is the local order of the probed element in a well-crystallized phase comparable with the one in an ill-ordered identical phase encountered in the sample? How many independent pure model compounds spectra are needed?), and (iii) the spectral differences between the model compounds spectra.

The number of pure model compounds needed to reconstruct a dataset of spectra can be determined using a PCA statistical approach (Manceau et al., 2014). The number of eigenvalues needed to reconstruct the entire dataset is the most common indicator used to determine this number, although the results can be ambiguous and overestimation may bring better results (Manceau et al., 2014).

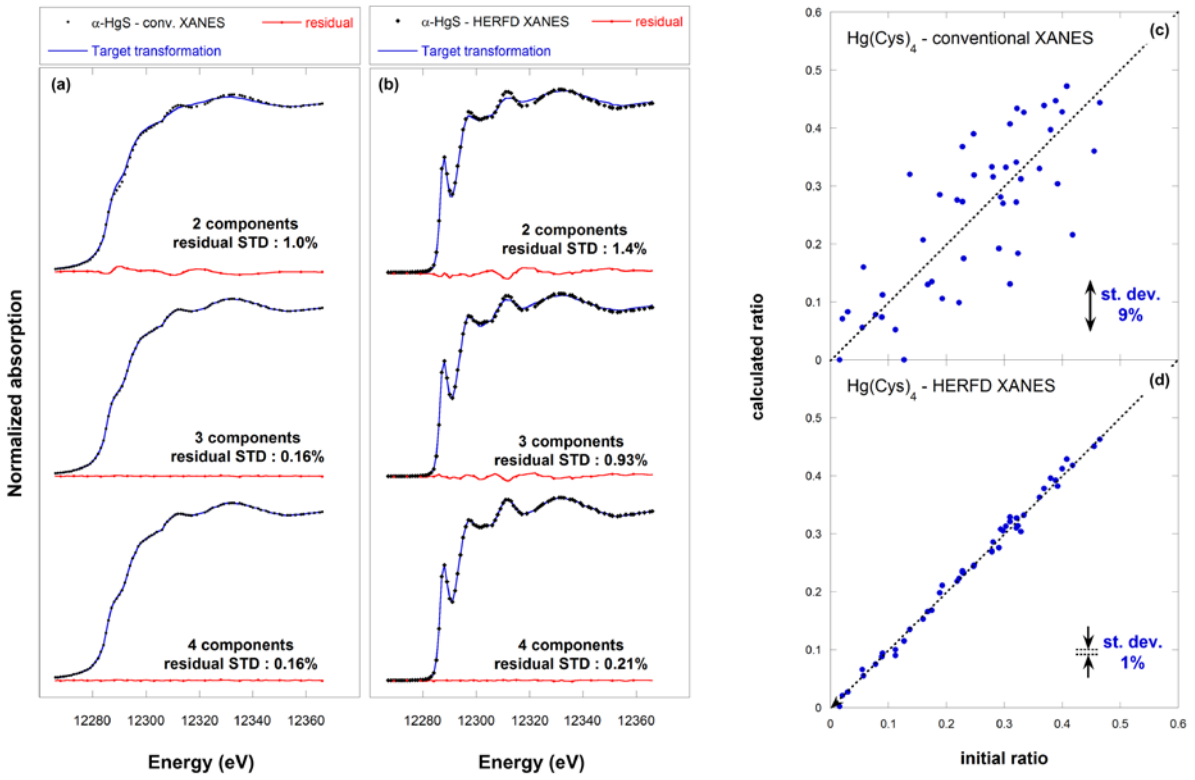

Fig. 4. Principal component analysis of a synthetic multicomponent set of 50 X-ray absorption near-edge structure (XANES) spectra obtained in conventional and high-energy resolution fluorescence detected (HERFD) mode of detection. Target transformations of the α-HgS reference spectra used to calculate the multicomponent spectra, in (a) conventional mode or (b) HERFD. Results of the least square fitting analysis of the $Hg(Cys)_4$ ratio in the random synthetic multicomponent set of XANES, obtained in (c) conventional and (d) HERFD mode: comparison between the ratio obtained from the adjustment and from the spectrum calculation.

High-energy resolution fluorescence detected XANES has a better spectral resolution than conventional XANES. This improvement can be useful for PCA and LCF approaches. We chose to illustrate this quantitatively. We created two datasets of 50 artificial Hg multicomponent spectra based on random linear combinations of the conventional or HERFD spectra of the four Hg model compounds described above. For each dataset, noise was added to each linear combination spectra, corresponding to 0.25% of the edge step. Details of the analysis are given in the Supplemental Material. Different steps of the PCA analysis are shown (Supplemental Fig. S6), as well as spectra used for the analysis (example of multicomponent spectrum, Supplemental Fig. S6a), the scree plot (number of eigenvalues, Supplemental Fig. S6b), and the target transformation of each set for conventional mode (Fig. 4a) or HERFD (Fig. 4b).

The main observation given by the scree plot (Supplemental Fig. S6b) is that the number of components needed to perform the LCF analysis is quite difficult to estimate for the conventional spectra (three or four are possible candidates), whereas the correct number of four components is more easily deduced for the HERFD spectra. This might come from the

fact that the shape of the pure component spectra is quite similar in conventional measurements. This is corroborated by the target transformation performed for each set of spectra. In conventional mode (Fig. 4a), only three components seem to be necessary to reproduce the α-HgS spectrum; a fourth component does not improve the residual of the target transformation. In HERFD mode (Fig. 4b), the α-HgS spectrum needs four components to be reproduced satisfactorily. The well-marked features obtained in HERFD mode, very different in shape and position from one reference spectrum to the other, allow clear differentiation of the components.

We performed a LCF analysis of both set of spectra using the four components, determined a ratio of each component, and compared the "LCF ratio" to the "real ratio." The results are given in Fig. 4c and 4d for the $Hg(Cys)_4$ ratio (and in Supplemental Fig. S7 for the other compounds), and the standard deviations between the "LCF ratio" and "real ratio" for each compounds measured with both modes of detection are presented in Table 2. It is no surprise to see that the determined ratio is more precise with the HERFD XANES than with the conventional ones. The precision in the determined ratio is around 10% for the conventional mode and around 2% for HERFD. These results are only given as an illustration of the improvement brought by the HERFD measurements, in this particular case, and the absolute values of determined ratio cannot be directly used for all absorption edges, all elements, and all compounds. Nevertheless, the improvement is clear.

Table 2. Determination of the ratio of Hg components in synthetic mixtures from conventional and high-energy resolution fluorescence detected (HERFD) measurements: standard deviation between the linear combination fitting result and the initial ratio for the four compounds used for the study.

Measurement	α-HgS	β-HgS	$Hg(CYS)_2$	$Hg(CYS)_4$
		%		
Conventional XANES†	14	11	7	9
HERFD XANES	3	2	3	1

† XANES, X-ray absorption near-edge structure.

Conclusions

With the development of CAS on XAS beamlines worldwide, HERFD-XAS is becoming one of the most suitable techniques for speciation analysis of metals and metalloids in environmental biogeochemistry. The new opportunities brought by this high-resolution spectroscopy are (i) the possibility to study ultra-diluted elements by filtering with great efficiency the background photons and (ii) to improve the sensitivity of the measurement with the acquisition of better-resolved XANES spectra. It is now possible to probe elements such as Se at natural levels and pollutants such as Hg or Ce at realistic concentrations ($\mu g.g^{-1}$ or below).

These measurements are already possible. In the near future, with the development or upgrade of the synchrotron sources, as well as the development of the crystal analyzer spectrometers (improved geometry, more crystals, better bent crystals, etc.), one can reasonably think of reducing the detection limits even more.

Acknowledgments

Construction of the spectrometer prototype on BM30B/FAME beamline at the ESRF, actually used on BM16/FAME-UHD, was financially supported by the French National Institute for Earth Science and Astronomy of the CNRS (INSU CNRS), ANR NANOSURF (coordinator: C. Chaneac, LCMCP), ANR MESONNET (coordinator: J.Y. Bottero, CEREGE), CEREGE laboratory (Aix en Provence, France), and Labex OSUG@2020 (ANR-10-LABX-0056). The FAME-UHD project is financially supported by the French "invest for the future" EquipEx (EcoX, ANR-10-EQPX-27-01), the CEA-CNRS CRG consortium, and the French National Institute for Earth Science and Astronomy of the CNRS (INSU CNRS). We thank A. Gorczyca and V. Moizan for their help during the work on the Pt/Al_2O_3 sample and its synthesis and preparation for the experiment, as well as IFP Énergies nouvelles (IFPEN) for the funding of the used Ge(110) crystals. A portion of this work (S.Thomas's work on Hg) is supported by the Chateaubriand Fellowship of the Office for Science & Technology of the Embassy of France in the United States. M. Irar's Ph.D. fellowship is supported by CAMPUS FRANCE.

References

Andrews, J.C. 2006. Mercury speciation in the environment using X-ray absorption spectroscopy. Struct. Bonding 120:1–35. doi:10.1007/430_011

Auffan, M., J. Rose, T. Orsiere, M. De Meo, A. Thill, O. Zeyons et al. 2009. CeO_2 nanoparticles induce DNA damage towards human dermal fibroblasts in vitro. Nanotoxicology 3:161–171. doi:10.1080/17435390902788086

Auffan, M., M. Tella, C. Santaella, L. Brousset, C. Paillès, M. Barakat et al. 2014. An adaptable mesocosm platform for performing integrated assessments of nanomaterial risk in complex environmental systems. Sci. Rep. 3:5608.

Bargar, J.R., B.M. Tebo, U. Bergmann, S.M. Webb, P. Glatzel, V.Q. Chiu, and M. Villalobos. 2005. Biotic and abiotic products of Mn(II) oxidation by spores of the marine *Bacillus* sp. strain SG-1. Am. Mineral. 90:143–154. doi:10.2138/am.2005.1557

Bauer, M. 2014. HERFD-XAS and valence-to-core-XES: New tools to push the limits in research with hard X-rays? Phys. Chem. Chem. Phys. 16:13827–13837. doi:10.1039/C4CP00904E

Baumgartner, J., G. Morin, N. Menguy, T. Perez Gonzalez, M. Widdrat, J. Cosmidis, and D. Faivre. 2013. Magnetotactic bacteria form magnetite from a phosphate-rich ferric

hydroxide via nanometric ferric (oxyhydr)oxide intermediates. Proc. Natl. Acad. Sci. USA 110:14883–14888. doi:10.1073/pnas.1307119110

Bergmann, U., and S.P. Cramer. 1998. A high-resolution large-acceptance analyzer for X-ray fluorescence and Raman spectroscopy. Proc. SPIE 3448:198–209. doi:10.1117/12.332507

Bergmann, U., and P. Glatzel. 2009. X-ray emission spectroscopy. Photosynth. Res. 102:255–266. doi:10.1007/s11120-009-9483-6

Bergmann, U., P. Glatzel, F. deGroot, and S.P. Cramer. 1999. High resolution K capture X-ray fluorescence spectroscopy: A new tool for chemical characterization. J. Am. Chem. Soc. 121:4926–4927. doi:10.1021/ja984454w

Bissardon, C. 2016. Le rôle du sélénium dans le métabolisme, la croissance et la maturation du cartilage articulaire. Ph.D. diss., Grenoble-Alpes Univ., Grenoble, France.

Blazevic, A., E. Orlowska, W. Kandioller, F. Jirsa, B.K. Keppler, M. Tafili-Kryeziu et al. 2016. Photoreduction of terrigenous Fe-humic substances leads to bioavailable iron in oceans. Angew. Chem. Int. Ed. 55:6417–6422. doi:10.1002/anie.201600852

Bordage, A., V. Trannoy, O. Proux, H. Vitoux, R. Moulin, and A. Bleuzen. 2015. In situ site-selective K-edge XAS: A powerful probe of the transformation of mixed-valence compounds. Phys. Chem. Chem. Phys. 17:17260–17265. doi:10.1039/C5CP02591E

Brindley, G.W. 1933. On the reflection and refraction of X-rays by perfect crystals. Proc. R. Soc. Lond., A Contain. Pap. Math. Phys. Character 140:301–313. doi:10.1098/rspa.1933.0070

Cabaret, D., A. Bordage, A. Juhin, M. Arfaoui, and E. Gaudry. 2010. First-principles calculations of X-ray absorption spectra at the K-edge of 3d transition metals: An electronic structure analysis of the pre-edge. Phys. Chem. Chem. Phys. 12:5619–5633. doi:10.1039/b926499j

Casals, E., R. Barrena, A. García, E. González, L. Delgado, M. Busquets-Fité et al. 2014. Programmed iron oxide nanoparticles disintegration in anaerobic digesters boosts biogas production. Small 10:2801–2808. doi:10.1002/smll.201303703

Collart, E., A. Shukla, F. Gélébart, M. Morand, C. Malgrange, N. Bardou et al. 2005. Spherically bent analyzers for resonant inelastic X-ray scattering with intrinsic resolution below 200 meV. J. Synchrotron Radiat. 12:473–478. doi:10.1107/S090904950501472X

Collin, B., E. Oostveen, O.V. Tsyusko, and J.M. Unrine. 2014. Influence of natural organic matter and surface charge on the toxicity and bioaccumulation of functionalized ceria nanoparticles in *Caenorhabditis elegans*. Environ. Sci. Technol. 48:1280–1289. doi:10.1021/es404503c

DeBeer, S., and U. Bergmann. 2016. X-ray emission spectroscopy techniques in bioinorganic applications. Encycl. Inorg. Bioinorg. Chem. doi:10.1002/9781119951438.eibc2158

de Groot, F., and A. Kotani. 2008. Core level spectroscopy of solids. Advances in condensed matter science. Vol. 6. CRC Press, Boca Raton, FL. doi:10.1201/9781420008425

de Groot, F., M.H. Krisch, and J. Vogel. 2002. Spectral sharpening of the Pt L edges by high-resolution x-ray emission. Phys. Rev. B 66:195112. doi:10.1103/PhysRevB.66.195112

de Groot, F., G. Vankó, and P. Glatzel. 2009. The 1s x-ray absorption pre-edge structures in transition metal oxides. J. Phys. Condens. Matter 21:104207. doi:10.1088/0953-8984/21/10/104207

Dunham-Cheatham, S., B. Farrell, B. Mishra, S. Myneni, and J.B. Fein. 2014. The effect of chloride on the adsorption of Hg onto three bacterial species. Chem. Geol. 373:106–114. doi:10.1016/j.chemgeo.2014.02.030

Dunham-Cheatham, S., B. Mishra, S. Myneni, and J.B. Fein. 2015. The effect of natural organic matter on the adsorption of mercury to bacterial cells. Geochim. Cosmochim. Acta 150:1–10. doi:10.1016/j.gca.2014.11.018

Eeckhout, S.G., O.V. Safonova, G. Smolentsev, M. Biasioli, V.A. Safonov, L.N. Vykhodtseva et al. 2009. Cr local environment by valence-to-core X-ray emission spectroscopy. J. Anal. At. Spectrom. 24:215–223. doi:10.1039/B808345M

Fister, T.T., G.T. Seidler, J.J. Rehr, J.J. Kas, W.T. Elam, J.O. Cross, and K.P. Nagle. 2007. Deconvolving instrumental and intrinsic broadening in core-shell x-ray spectroscopies. Phys. Rev. B 75:174106. doi:10.1103/PhysRevB.75.174106

Gallo, E., and P. Glatzel. 2014. Valence to core X-ray emission spectroscopy. Adv. Mater. 26:7730–7746. doi:10.1002/adma.201304994

Garaud, M., M. Auffan, S. Devin, V. Felten, C. Pagnout, S. Pain-Devin et al. 2016. Integrated assessment of ceria nanoparticle impacts on the freshwater bivalve *Dreissena polymorpha*. Nanotoxicology 10:935–944. doi:10.3109/17435390.2016.1146363

Glatzel, P., L. Jacquamet, U. Bergmann, F.M.F. de Groot, and S.P. Cramer. 2002. Site-selective EXAFS in mixed-valence compounds using high-resolution fluorescence detection: A study of iron in Prussian Blue. Inorg. Chem. 41:3121–3127. doi:10.1021/ic010709m

Glatzel, P., and A. Juhin. 2013. X-ray absorption and emission spectroscopy. In: D.W. Bruce, D. O'Hare, and R.I. Walton, editors, Local structural characterisation. John Wiley & Sons, Chichester, UK. p. 89–171. doi:10.1002/9781118681909.ch2

Gorczyca, A., V. Moizan, C. Chizallet, O. Proux, W. Delnet, E. Lahera et al. 2014. Monitoring morphology and hydrogen coverage of subnanometric Pt/γ-Al_2O_3 particles by in situ HERFD-XANES and quantum simulations. Angew. Chem. Int. Ed. 53:12426–12429.

Gräfe, M., E. Donner, R.N. Collins, and E. Lombi. 2014. Speciation of metal(loid)s in environmental samples by X-ray absorption spectroscopy: A critical review. Anal. Chim. Acta 822:1–22. doi:10.1016/j.aca.2014.02.044

Grush, M.M., G. Christou, K. Hamalainen, and S.P. Cramer. 1995. Site-selective XANES and EXAFS: A demonstration with manganese mixtures and mixed-valence complexes. J. Am. Chem. Soc. 117:5895–5896. doi:10.1021/ja00126a047

Hall, E.R., C.J. Pollock, J. Bendix, T.J. Collins, P. Glatzel, and S. Debeer. 2014. Valence-to-core-detected X-ray absorption spectroscopy: Targeting ligand selectivity. J. Am. Chem. Soc. 136:10076–10084. doi:10.1021/ja504206y

Hämäläinen, K., D.P. Siddons, J.B. Hastings, and L.E. Berman. 1991. Elimination of the inner-shell lifetime broadening in X-ray absorption spectroscopy. Phys. Rev. Lett. 67:2850–2853. doi:10.1103/PhysRevLett.67.2850

Hazemann, J.-L., O. Proux, V. Nassif, H. Palancher, E. Lahera, C. Da Silva et al. 2009. High resolution spectroscopy on an X-ray absorption beamline. J. Synchrotron Radiat. 16:283–292. doi:10.1107/S0909049508043768

Heald, S.P. 2015. Strategies and limitations for fluorescence detection of XAFS at high flux beamlines. J. Synchrotron Radiat. 22:436–445. doi:10.1107/S1600577515001320

Henderson, G.S., F.M.F. de Groot, and B.J.A. Moulton. 2014. X-ray absorption near-edge structure (XANES) spectroscopy. Rev. Mineral. Geochem. 78:75–138. doi:10.2138/rmg.2014.78.3

Hong, J., J.R. Peralta-Videa, C. Rico, S. Sahi, M.N. Viveros, J. Bartonjo et al. 2014. Evidence of translocation and physiological impacts of foliar applied CeO_2 nanoparticles on cucumber (*Cucumis sativus*) plants. Environ. Sci. Technol. 48:4376–4385. doi:10.1021/es404931g

Izumi, Y., F. Kiyotaki, T. Minato, and Y. Seida. 2002. X-ray absorption fine structure combined with fluorescence spectrometry for monitoring trace amounts of lead adsorption in the environmental conditions. Anal. Chem. 74:3819–3823. doi:10.1021/ac025550p

Jaklevic, J., J.A. Kirby, M.P. Klein, A.S. Robertson, G.S. Brown, and P. Eisenberger. 1977. Fluorescence detection of exafs: Sensitivity enhancement for dilute species and thin films. Solid State Commun. 23:679–682. doi:10.1016/0038-1098(77)90548-8

Johann, H.H. 1931. Die erzeugung lichtstarker röntgenspektren mit hilfe von konkavkristallen. Z. Phys. 69:185–206. doi:10.1007/BF01798121

Johansson, T. 1933. Über ein neuartiges, genau fokussierendes röntgenspektrometer. Z. Phys. 82:507–528. doi:10.1007/BF01342254

Joly, Y., and S. Grenier. 2016. Theory of X-ray absorption near edge structure. In: J.A. Van Bokhoven and C. Lamberti, editors, X-ray absorption and X-ray emission spectroscopy: Theory and applications. Wiley & Sons, Hoboken, NJ. p. 73–97. doi:10.1002/9781118844243.ch4

Kelly, S.D., S.R. Bare, N. Greenlay, G. Azevedo, M. Balasubramanian, D. Barton et al. 2009. Comparison of EXAFS foil spectra from around the world. J. Phys. Conf. Ser. 190:012032. doi:10.1088/1742-6596/190/1/012032

Kopittke, P.M., P. Wang, E. Lombi, and E. Donner. 2017. Synchrotron-based X-ray approaches for examining toxic trace metal(loid)s in soil–plant systems. J. Environ. Qual. doi:10.2134/jeq2016.09.0361

Kowalska, J.K., F.A. Lima, C.J. Pollock, J.A. Rees, and S. DeBeer. 2016. A practical guide to high-resolution X-ray spectroscopic measurements and their applications in bioinorganic chemistry. Isr. J. Chem. 56:803–815. doi:10.1002/ijch.201600037

Kühn, T.-J., J. Hormes, N. Matoussevitch, H. Bönnemann, and P. Glatzel. 2014. Site-selective high-resolution X-ray absorption spectroscopy and high-resolution X-ray emission spectroscopy of cobalt nanoparticles. Inorg. Chem. 53:8367–8375. doi:10.1021/ic5000183

Lambertz, C., P. Chernev, K. Klingan, N. Leidel, K.G.V. Sigfridsson, T. Happe, and M. Haumann. 2014. Electronic and molecular structures of the active-site H-cluster in [FeFe]-hydrogenase determined by site-selective X-ray spectroscopy and quantum chemical calculations. Chem. Sci. (Camb.) 5:1187–1203. doi:10.1039/c3sc52703d

Llorens, I., E. Lahera, W. Delnet, O. Proux, A. Braillard, J.-L. Hazemann et al. 2012. High energy resolution five-crystal spectrometer for high quality fluorescence and absorption measurements on an X-ray absorption spectroscopy beamline. Rev. Sci. Instrum. 83:063104. doi:10.1063/1.4728414

Lohße, A., S. Borg, O. Raschdorf, I. Kolinko, E. Tompa, M. Pósfai et al. 2014. Genetic dissection of the *mamAB* and *mms6* operons reveals a gene set essential for magnetosome biogenesis in *magnetospirillum gryphiswaldense*. J. Bacteriol. 196:2658–2669. doi:10.1128/JB.01716-14

Lombi, E., G.M. Hettiarachchi, and K.G. Scheckel. 2011. Advanced in situ spectroscopic techniques and their applications in environmental biogeochemistry: Introduction to the special section. J. Environ. Qual. 40:659–666. doi:10.2134/jeq2010.0542

López-Moreno, M.L., G. de la Rosa, J.A. Hernández-Viezcas, J.R. Peralta-Videa, and J.L. Gardea-Torresdey. 2010. XAS corroboration of the uptake and storage of CeO_2 nanoparticles and assessment of their differential toxicity in four edible plant species. J. Agric. Food Chem. 58:3689–3693. doi:10.1021/jf904472e

Luster, J., and R. Finlay. 2006. Handbook of methods used in rhizosphere research. Swiss Federal Research Institute WSL, Birmensdorf, Switzerland.

Ma, C., S. Chhikara, B. Xing, C. Musante, J.C. White, and O. Parkash Dhankher. 2013. Physiological and molecular response of *Arabidopsis thaliana* (L.) to nanoparticle cerium and indium oxide exposure. ACS Sustain. Chem.& Eng. 1:768–778. doi:10.1021/sc400098h

Manceau, A., M. Enescu, A. Simionovici, M. Lanson, M. Gonzalez-Rey, M. Rovezzi et al. 2016. Chemical forms of mercury in human hair reveal sources of exposure. Environ. Sci. Technol. 50:10721–10729. doi:10.1021/acs.est.6b03468

Manceau, A., C. Lemouchi, M. Enescu, A.-M. Gaillot, M. Lanson, V. Magnin et al. 2015. Formation of mercury sulfide from Hg(II)□thiolate complexes in natural organic matter. Environ. Sci. Technol. 49:9787–9796. doi:10.1021/acs.est.5b02522

Manceau, A., M. Marcus, and T. Lenoir. 2014. Estimating the number of pure chemical components in a mixture by X-ray absorption spectroscopy. J. Synchrotron Radiat. 21:1140–1147. doi:10.1107/S1600577514013526

Masih, D., Y. Izumi, K. Aika, and Y. Seida. 2007. Optimization of an iron intercalated montmorillonite preparation for the removal of arsenic at low concentrations. Eng. Life Sci. 7:52–60. doi:10.1002/elsc.200620171

Mijovilovich, A., Hayashi, H., Kawamura, N., Osawa, H., Bruijnincx, P. C. A., Klein Gebbink et al. 2012. K_β detected high-resolution XANES of Fe^{II} and Fe^{III} models of the 2-His-1-carboxylate motif: Analysis of the carboxylate binding mode. Eur. J. Inorg. Chem. 10:1589–1597. doi:10.1002/ejic.201101075

Milne, C.J., T.J. Penfold, and M. Chergui. 2014. Recent experimental and theoretical developments in time-resolved X-ray spectroscopies. Coord. Chem. Rev. 277–278:44–68. doi:10.1016/j.ccr.2014.02.013

Nagy, K.L., A. Manceau, J.D. Gasper, J.N. Ryan, and G.R. Aiken. 2011. Metallothionein-like multinuclear clusters of mercury(II) and sulfur in peat. Environ. Sci. Technol. 45:7298–7306. doi:10.1021/es201025v

Newville, M. 2014. Fundamentals of XAFS. Rev. Mineral. Geochem. 78:33–74. doi:10.2138/rmg.2014.78.2

Ortega, R., A. Carmona, I. Szlachetko, and P.L. Solari. 2012. X-ray absorption spectroscopy of biological samples: A tutorial. J. Anal. At. Spectrom. 27:2054–2065. doi:10.1039/c2ja30224a

Parks, J.M., A. Johs, M. Podar, R. Bridou, R.A. Hurt, S.D. Smith et al. 2013. The genetic basis for bacterial mercury methylation. Science 339:1332–1335. doi:10.1126/science.1230667

Poulin, B.A., G.R. Aiken, K.L. Nagy, A. Manceau, D.P. Krabbenhoft, and J.N. Ryan. 2016. Mercury transformation and release differs with depth and time in a contaminated riparian soil during simulated flooding. Geochim. Cosmochim. Acta 176:118–138. doi:10.1016/j.gca.2015.12.024

Rehr, J.J., and R.C. Albers. 2000. Theoretical approaches to X-ray absorption fine structure. Rev. Mod. Phys. 72:621–654. doi:10.1103/RevModPhys.72.621

Rollin-Genetet, F., C. Seidel, E. Artells, M. Auffan, A. Thieìry, and C. Vidaud. 2015. Redox reactivity of cerium oxide nanoparticles induces the formation of disulfide bridges in thiol-containing biomolecules. Chem. Res. Toxicol. 28:2304–2312. doi:10.1021/acs.chemrestox.5b00319

Rovezzi, M., and P. Glatzel. 2014. Hard X-ray emission spectroscopy: A powerful tool for the characterization of magnetic semiconductors. Semicond. Sci. Technol. 29:023002. doi:10.1088/0268-1242/29/2/023002

Rovezzi, M., Lapras, C., Manceau, A., Glatzel, P., and R. Verbeni. 2017. High energy-resolution x-ray spectroscopy at ultra-high dilution with spherically bent crystal analyzers of 0.5 m radius. Rev. Sci. Instrum. 88:013108. doi:10.1063/1.4974100

Sá, J., J. Czapla-Masztafiak, E. Lipiec, Y. Kayser, D.L.A. Fernandes, J. Szlachetko et al. 2016. Resonant X-ray emission spectroscopy of platinum(II) anticancer complexes. Analyst 141:1226–1232. doi:10.1039/C5AN02490K

Safonov, V.A., L.N. Vykhodtseva, Y.M. Polukarov, O.V. Safonova, G. Smolentsev, M. Sikora et al. 2006. Valence-to-core X-ray emission spectroscopy identification of carbide compounds in nanocrystalline Cr coatings deposited from Cr(III) electrolytes containing organic substances. J. Phys. Chem. B 110:23192–23196. doi:10.1021/jp064569j

Sarret, G., E. Pilon Smits, H. Castillo-Michel, M.P. Isaure, F.J. Zhao, and R. Tappero. 2013. Use of synchrotron-based techniques to elucidate metal uptake and metabolism in plants. Adv. Agron. 119:1–82. doi:10.1016/B978-0-12-407247-3.00001-9

Sheng, G., Q. Yang, F. Peng, H. Li, X. Gao, and Y. Huang. 2014. Determination of colloidal pyrolusite, Eu(III) and humic substance interaction: A combined batch and EXAFS approach. Chem. Eng. J. 245:10–16. doi:10.1016/j.cej.2014.02.021

Skyllberg, U., P.R. Bloom, J. Qian, C.M. Lin, and W.F. Bleam. 2006. Complexation of mercury(II) in soil organic matter: EXAFS evidence for linear two-coordination with reduced sulfur groups. Environ. Sci. Technol. 40:4174–4180. doi:10.1021/es0600577

Soldati, A.L., D.E. Jacob, P. Glatzel, J.C. Swarbrick, and J. Geck. 2016. Element substitution by living organisms: The case of manganese in mollusc shell aragonite. Sci. Rep. 6:22514. doi:10.1038/srep22514

Stojanoff, V., K. Hämäläinen, D.P. Siddons, J.B. Hastings, L.E. Berman, S. Cramer, and G. Smith. 1992. A high-resolution X-ray fluorescence spectrometer for near-edge absorption studies. Rev. Sci. Instrum. 63:1125–1127. doi:10.1063/1.1143112

Swarbrick, J.C., U. Skyllberg, T. Karlsson, and P. Glatzel. 2009. High energy resolution X-ray absorption spectroscopy of environmentally relevant lead(II) compounds. Inorg. Chem. 48:10748–10756. doi:10.1021/ic9015299

Szlachetko, M., M. Berset, J.-C. Dousse, J. Hoszowska, and J. Szlachetko. 2013. High-resolution Laue-type DuMond curved crystal spectrometer. Rev. Sci. Instrum. 84:093104. doi:10.1063/1.4821621

Takahashi, Y., T. Uruga, H. Tanida, Y. Terada, S. Nakai, and H. Shimizu. 2006. Application of X-ray absorption near-edge structure (XANES) using bent crystal analyzer to speciation of trace Os in iron meteorites. Anal. Chim. Acta 558:332–336. doi:10.1016/j.aca.2005.11.043

Tella, M., M. Auffan, L. Brousset, J. Issartel, I. Kieffer, C. Pailles et al. 2014. Transfer, transformation, and impacts of ceria nanomaterials in aquatic mesocosms simulating a pond ecosystem. Environ. Sci. Technol. 48:9004–9013. doi:10.1021/es501641b

Tella, M., M. Auffan, L. Brousset, E. Morel, O. Proux, C. Chanéac et al. 2015. Chronic dosing of a simulated pond ecosystem in indoor aquatic mesocosms: Fate and Transport of CeO_2 nanoparticles. Environ. Sci. Nano 2:653–663. doi:10.1039/C5EN00092K

Thomas, S.A., and J.F. Gaillard. 2017. Exogenous cysteine promotes sulfide production and four-fold Hg(II)-S coordination in actively metabolizing *Escherichia coli*. Environ. Sci. Technol. doi:10.1021/acs.est.6b06400

Thomas, S.A., T.Z. Tong, and J.F. Gaillard. 2014. Hg(II) bacterial biouptake: The role of anthropogenic and biogenic ligands present in solution and spectroscopic evidence of

ligand exchange reactions at the cell surface. Metallomics 6:2213–2222. doi:10.1039/C4MT00172A

Vogel, C., O. Krüger, H. Herzel, L. Amidani, and C. Adam. 2016. Chemical state of mercury and selenium in sewage sludge ash based P-fertilizers. J. Hazard. Mater. 313:179–184. doi:10.1016/j.jhazmat.2016.03.079

von Hámos, L. 1932. Röntgenspektroskopie und Abbildung mittels gekrümmter Kristallreflektoren. Naturwissenschaften 20:705–706. doi:10.1007/BF01494468

Westre, T.E., P. Kennepohl, J.G. DeWitt, B. Hedman, K.O. Hodgson, and E.I. Solomon. 1997. A multiplet analysis of Fe K-edge 1s → 3d pre-edge features of iron complexes. J. Am. Chem. Soc. 119:6297–6314. doi:10.1021/ja964352a

Yamamoto, T. 2008. Assignment of pre-edge peaks in K-edge X-ray absorption spectra of 3d transition metal compounds: Electric dipole or quadrupole? XRay Spectrom. 37:572–584. doi:10.1002/xrs.1103

Zeyons, O., A. Thill, F. Chauvat, N. Menguy, C. Cassier-Chauvat, C. Oréar et al. 2009. Direct and indirect CeO_2 nanoparticles toxicity for *Escherichia coli* and *Synechocystis*. Nanotoxicology 3:284–295. doi:10.3109/17435390903305260

Zhang, P., Y. Ma, Z. Zhang, X. He, J. Zhang, Z. Guo et al. 2012. Biotransformation of ceria nanoparticles in cucumber plants. ACS Nano 6:9943–9950. doi:10.1021/nn303543n

2.1.3.3 Supplementary information

Olivier Proux[1], Eric Lahera[1], William Del Net[1], Isabelle Kieffer[1], Mauro Rovezzi[1], Denis Testemale[2], Mohammed Irar,[2] Sara Thomas,[2,3,4] Antonio Aguilar-Tapia[2], Elena F. Bazarkina[2,5], Alain Prat[2], Marie Tella[6], Mélanie Auffan[7], Jérôme Rose[7], Jean-Louis Hazemann[2*]

[1] *Observatoire des Sciences de l'Univers de Grenoble (OSUG), UMS 832 CNRS - Univ. Grenoble Alpes, F-38041 Grenoble, France*

[2] *Inst. Néel, UPR 2940 CNRS - Univ. Grenoble Alpes, F-38000 Grenoble, France*

[3] *Department of Civil and Environmental Engineering, Northwestern University, Evanston, Illinois 60208, United States*

[4] *Laboratoire de Chimie et Biologie des Métaux (LCBM) UMR 5249 CNRS - CEA- Univ. Grenoble Alpes, F-38054 Grenoble, France*

[5] *Institute of Geology of Ore Deposits, Mineralogy, Petrography and Geochemistry, Russian Academy of Sciences, IGEM RAS, 119017 Moscow, Russia*

[6] *Centre de coopération Internationale en Recherche Agronomique pour le Développement (CIRAD), US 49 Analyse, TA B-49/01, F-34398 Montpellier Cedex 5, France*

[7] *Centre de Recherche et d'Enseignement de Géosciences de l'Environnement (CEREGE) UM34, UMR 7330, CNRS - Aix-Marseille Université, IRD, Collège de France F-13545 Aix en Provence, France*

* Corresponding authors (jean-louis.hazemann@neel.cnrs.fr)

Figure List

Table List

1. XAS measurement detection limit using solid state detector

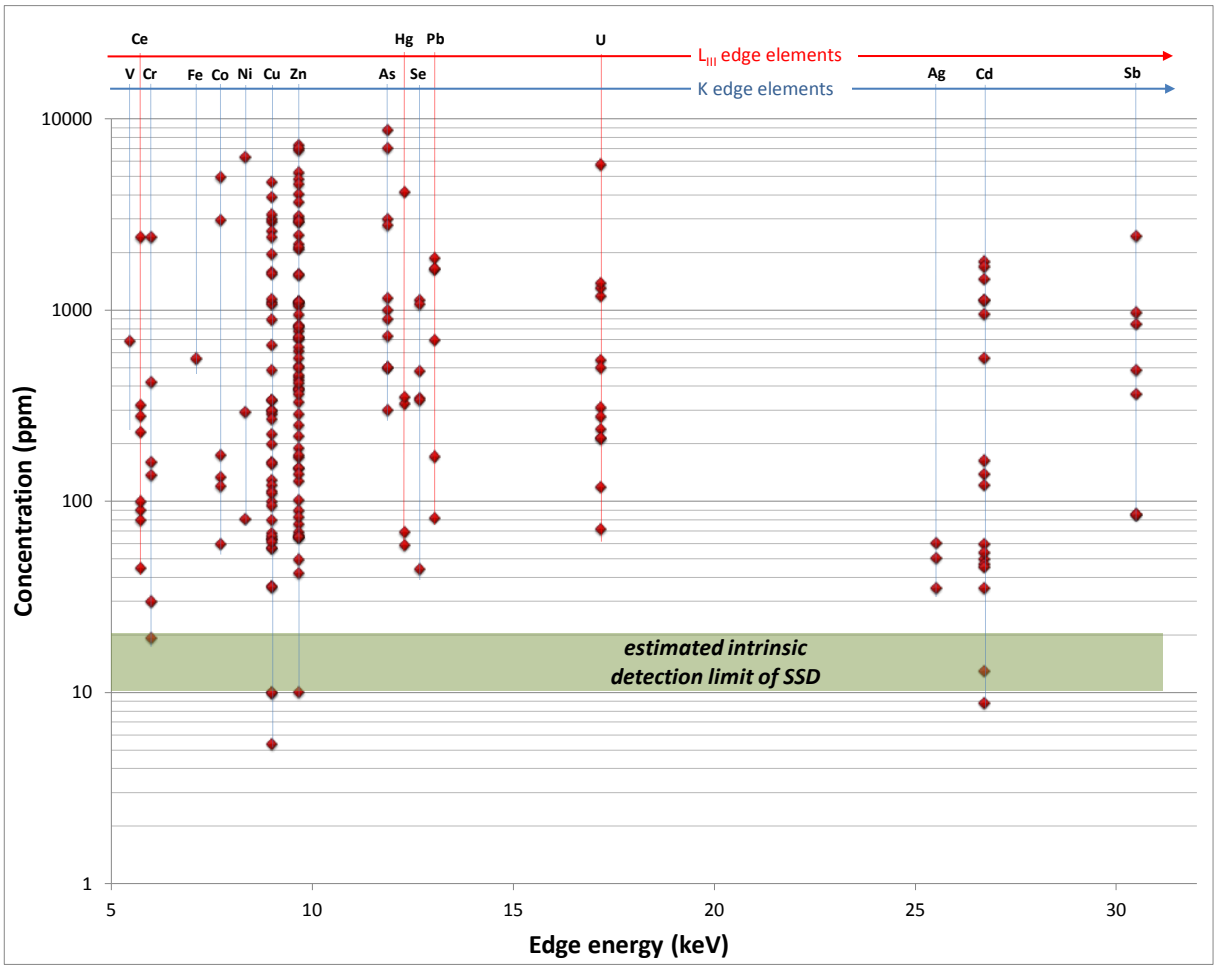

Fig. S1. Concentration for XAS experiments performed on CRG-FAME beamline at ESRF (red diamond) in the environmental and biogeochemistry science fields (53 publications from 2002 to 2016) using a solid state detector. Green area: estimated intrinsic detection limit using solid state detector (from Hazemann et al., 2009). Concentration are expressed in ppm (parts-per-million) mass fraction.

2. Crystal analyzer spectrometer characteristics and spectroscopic data

Crystal Analyzer Spectrometer on CRG-FAME and CRG-FAME/UHD at ESRF

On the CRG-FAME beamline (BM30b, ESRF, Grenoble, France), we developed a CAS in the Johann geometry (Hazemann et al., 2009; Llorens et al., 2012). The spectrometer is equipped with 5 spherically bent crystals in a Rowland geometry (Fig. S2). A helium bag (not shown on Fig. S2) is used to limit the absorption of the fluorescence signal on the x-ray path from the sample to the crystals –and to the detector. Photons diffracted by the crystals can be focused on a SDD with a 50 mm^2 active area. The narrow energy bandwidth of the CAS allows unwanted X-ray events (mainly scattering processes) to be excluded from the selected fluorescence signal diffracted by the crystals and thus to improve the signal-to-background ratio. Another possibility is to use a 2D hybrid photon counting pixel detector (in our case an XPAD-S70) with a 75x15 mm^2 active area and a 130x130 μm^2 pixel size. This kind of detector produces a high quality signal as the electronic noise can be avoided by adjusting the detection threshold above the noise individually for each pixel. The large detection area enables the measurement of the diffracted photons as the focus point can be quite large when Bragg angle becomes smaller than 90°.

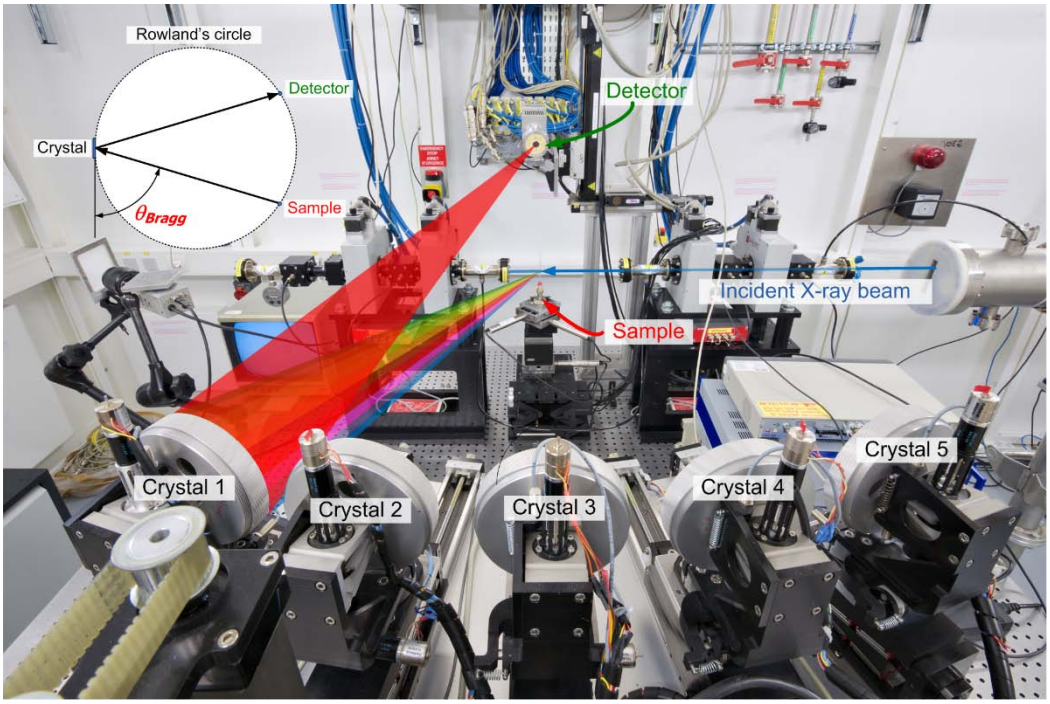

Fig. S2. View of the Crystal Analyzer Spectrometer on the FAME-UHD beamline. The sample, crystal & detector are located on the Rowland's circle. Due to the vertical geometry of the crystals all the Rowland's circles corresponding to each crystal are crossing on the same point on the detector. In operation a helium bag limits the air absorption on the sample-crystal-detector path (not present on the picture).

The spectrometer was initially designed with a 0.5 m radius of curvature for the bent crystals. This short radius increases the solid angle of the detection and it is very well adapted for diluted systems (Hazemann et al., 2009; Rovezzi et al., 2017). However, manufacturing this kind of crystals is very delicate inducing a perfectible crystal quality (technological

difficulties in their elaboration process and a decrease of the energy resolution induced by microstrains inside the Si wafer) and the geometrical error in the Johann configuration seriously limits the practical range of their use (see below). Thus, we adapted the initial spectrometer (Llorens et al., 2012) to accept crystals with a 1 m radius of curvature decreasing simultaneously both restrictions. This 5-crystal spectrometer is now installed on the FAME/UHD (BM16) beamline at the ESRF.

Crystal analyzer characteristics

In order to limit the geometric aberrations of Johann's geometry, the crystal needs to be chosen to have a Bragg angle as close as possible to 90°. We calculate the Bragg angle on each point of the crystal by considering (Fig. S3.a) :

The sample on $S\left(R.\cos^2\theta,\ 0,\ -R.\sin\theta.\cos\theta\right)$ (1)

A point M on the surface crystal $M\left(X,\ Y,\ Z\right)$ (2)

The unitary orientation vector on the surface crystal

$$\vec{v}\left(-X/R,\ -Y/R,\ -Z/R\right) \quad (3)$$

The crystal surface is on a circle centred on O and radius *R* so $X^2+Y^2+Z^2=R^2$ (4)

$$\overrightarrow{MS}.\vec{v}=\left|\overrightarrow{MS}\right|.\sin[\theta(X,Y,Z)] \quad (5)$$

(1) to (5) gives

$$\sin[\theta(X,Y,Z)]=\frac{-\cos\theta\ (\cos\theta\ X-\sin\theta\ Z)+R}{\sqrt{R^2.\cos^2\theta\ -2R\cos\theta(\cos\theta\ X-\sin\theta\ Z)+R^2}}$$

$$E\ (keV)=\frac{12.3984}{2\times d_{crystal}(\text{Å})\times\sin[\theta(X,Y,Z)]}$$

Energy calculation due to the Johann's error has been performed on each point of the crystal for one kind of crystal, (Si555), two emission lines corresponding to two different Bragg angles, and two radii of curvature (Fig. S3.b to e). This calculation is based only on geometrical consideration and doesn't take into account the local strain of the crystal on each point (Rovezzi et al., 2017). The main result is that only the horizontal central part of the crystal allows to select the appropriate energy of photons, especially *i)* when the Bragg angle is far from 90° and *ii)* when the radius of curvature is small. We propose on Table S2 (K-edge) and Table S3 (L_{III}-edge) optimized reflection for different fluorescence lines energy which satisfy this angular conditions, *i.e.* having the Bragg angle as close as possible to 90°.

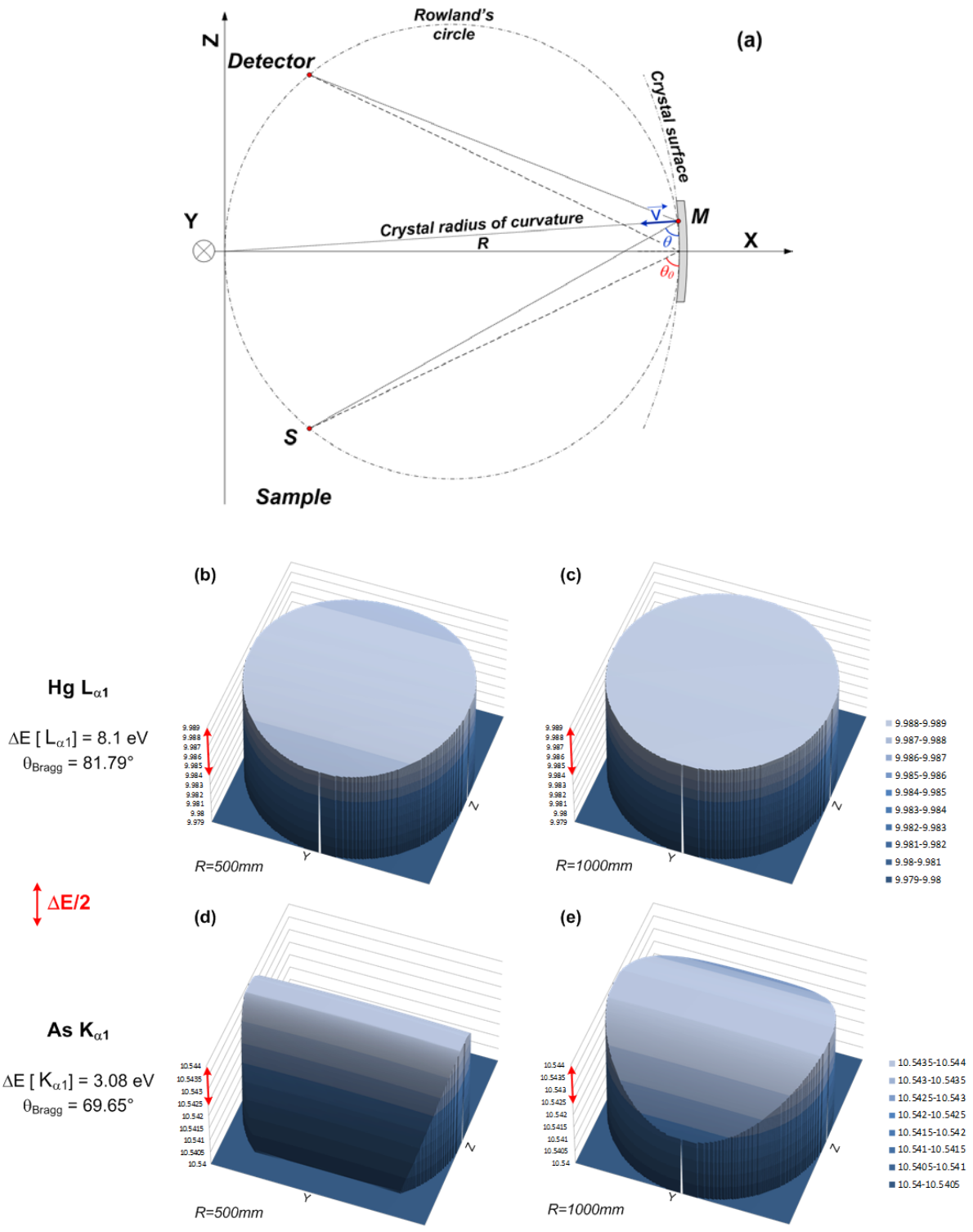

Fig. S3. Calculation of the spatial distribution of the energy diffracted by a Si(555) crystal analyzer due to the Johann's error (diameter : 100 mm). Z-axis : diffracted energy (keV). (a) Schematic view of the crystal in the Johann's geometry, with the remarkable geometric points used for the calculation. (b-e) 3D views of the energy diffracted on each point of the crystal surface optimised for Hg $L_{\alpha1}$ (b-c) and As $K_{\alpha1}$ (d-e) lines. The red double arrow represent half of X-ray line widths, ΔE. X-ray line widths values were taken from Salem and Lee (1976) for Hg $L_{\alpha1}$, from Krause and Oliver (1976) for As $K_{\alpha1}$.

Crystal Analyzer Spectrometer on XAS beamlines worldwide

Table S1 gathered examples of beamlines equipped with CAS dedicated to HERFD-XAS measurements.

Table S1. Examples of XAS beamlines equipped with a CAS

Facility	Beamline	Energy range	Spectrometer	Reference
Alba, Barcelona, Spain	CLÆSS	6.4 - 12.5 keV	Johannson	Simonelli et al. (2016)
APS, Argonne, USA	7ID-D	6 - 24 keV	Johann	March et al. (2011)
ESRF, Grenoble, France	BM20	3.5–25 keV	Johann	Kvashnina et al. (2016)
ESRF, Grenoble, France	ID26	2.4 - 27 keV	Johann	Glatzel et al., (2009, 2013)
ESRF, Grenoble, France	BM30b / BM16	4.8 - 22 keV	Johann	Hazemann et al. (2009) Llorens et al. (2012)
NSLS II, Brookhaven, USA	8-ID		Johann	
SLS, Villingen, Switzerland	SuperXAS	5 - 15 keV	Von Hamos	Szlachetko et al. (2012)
SLS, Villingen, Switzerland	SuperXAS	4.5 - 35 keV	Johann	Kleymenov et al. (2011)
SSRF, Shanghai, China	BL14W1	4 - 50 keV	Johann	Gao et al. (2013)
SSRL, Stanford, USA	BL 6.2	4 - 18 keV	Johann	Sokaras et al. (2013)
SOLEIL, Saint-Aubin, France	MARS	3.5 - 36 keV	Johann	Llorens et al. (2014)
SOLEIL, Saint-Aubin, France	GALAXIE	2.3 - 12	Johann	Céolin et al. (2013)
SPring-8, Sayo, Japan	BL11XU	4.8 - 12	Johann	Ishii et al. (2013)

High Energy Resolution Fluorescence Detected XANES

The sharpening effect of the XANES spectra measured with an energy resolution around the core hole has been demonstrated by de Groot et al. (de Groot et al., 2002). Let us considered a resonant inelastic x-ray scattering (RIXS), *i.e.* the acquisition of the emission intensity in a bi-dimensional energy space, where the X-axis is the energy of the excitation photons (the incident photon selected by the monochromator) and the Y-axis the energy of the emitted photons (detected by CAS). A schematic RIXS contour plot is shown on Fig. S4, RXES characteristic of a well-defined electronic transition (a pre-edge for example). The HERFD-XANES measurement is the integration, at a constant emission energy *vs.* the excitation energy, of this plot. If the energy resolution of the CAS is around (or smaller than) the energy bandwidth of the final state, the intensity increase due to the transition will occur on a reduce energy range, $\Gamma_{app.}$, the apparent energy bandwidth of the probed transition. $\Gamma_{app.}$, is given by

$$\Gamma_{app.} = 1 \Big/ \sqrt{\frac{1}{\Gamma_{int.}^2} + \frac{1}{\Gamma_{fin.}^2}}$$

where $\Gamma_{int.}$ and $\Gamma_{fin.}$ are the intermediate and final state core hole lifetime broadening.

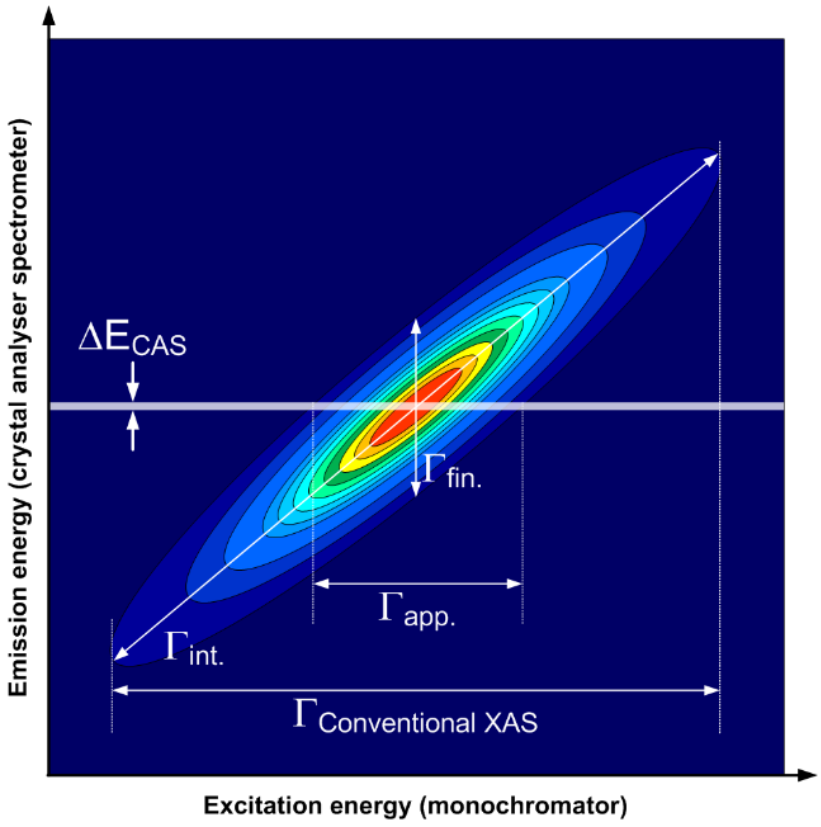

Fig. S4. Schematic RIXS contour plot close to an absorption edge, characteristic of a resonance like a pre-edge feature for a 3d transition metal

Table S2. Emission lines energy, crystal analyzer characteristics, monochromator bandwidth, natural widths of atomic levels involved in the K-edge absorption and emission processes, and apparent core hole lifetime bandwidth. The monochromator bandwidth is calculated considering Si220 crystals, with a $\Delta E/E=5.6x10^{-5}$. §: X-ray Data Booklet, 2009. ‡ : Campbell and Papp, 2001.

Element		Spectrometer		Monochromator	Core hole lifetime broadening (eV)				
Name	Emission line (E, eV)§	Crystal analyzer	θ_{Bragg} (°)	ΔE_{mono} (eV)	Γ_{1s} (eV) ‡	$\Gamma_{2p3/2}$ (eV) ‡	$\Gamma_{3p3/2}$ (eV) ‡	$\Gamma_{app.}$ $K_{\alpha 1}$	$\Gamma_{app.}$ $K_{\beta 1,3}$
Ti	$K_{\alpha 1}$ (4510.84)	Ge400	76.33	0.28	0.89	0.25	1.2	0.24	0.71
	$K_{\beta 1,3}$ (4931.81)	Ge331	75.58						
V	$K_{\alpha 1}$ (4952.20)	Ge331	74.69	0.31	0.96	0.28	1.2	0.27	0.75
	$K_{\beta 1,3}$ (5427.29)	Ge422	81.54						
Cr	$K_{\alpha 1}$ (5414.72)	Ge422	82.48	0.34	1.02	0.32	1.2	0.31	0.78
	$K_{\beta 1,3}$ (5946.71)	Si333	85.87						
Mn	$K_{\alpha 1}$ (5898.75)	Ge333	74.85	0.37	1.11	0.36	1.2	0.34	0.81
	$K_{\beta 1,3}$ (6490.45)	Si440	84.20						
Fe	$K_{\alpha 1}$ (6403.84)	Ge440	75.46	0.40	1.19	0.41	1.23	0.39	0.86
	$K_{\beta 1,3}$ (7057.98)	Ge620	79.09						
Co	$K_{\alpha 1}$ (6930.32)	Si620	74.88	0.43	1.28	0.47	1.27	0.44	0.90
	$K_{\beta 1,3}$ (7649.43)	Ge444	82.96						
Ni	$K_{\alpha 1}$ (7478.15)	Si620	74.88	0.47	1.39	0.53	1.3	0.50	0.95
	$K_{\beta 1,3}$ (8264.66)	Ge642	82.83						
Cu	$K_{\alpha 1}$ (8047.78)	Si444	79.32	0.50	1.49	0.61	1.8	0.56	1.15
	$K_{\beta 1,3}$ (8905.29)	Ge800	79.86						
Zn	$K_{\alpha 1}$ (8638.86)	Si642	81.42	0.54	1.62	0.68	2.15	0.63	1.29
	$K_{\beta 1,3}$ (9572.0)	Ge555	82.48						
Ga	$K_{\alpha 1}$ (9251.74)	Si800	80.77	0.58	1.76	0.77	2.3	0.71	1.40
	$K_{\beta 1,3}$ (10264.2)	Si555	74.39						
Ge	$K_{\alpha 1}$ (9886.42)	Si660	78.44	0.62	1.92	0.86	2.3	0.78	1.47
	$K_{\beta 1,3}$ (10982.1)	Ge844	77.87						
As	$K_{\alpha 1}$ (10543.72)	Si555	69.65	0.66	2.09	0.94	2.25	0.86	1.53
	$K_{\beta 1,3}$ (11726.2)	Ge844	66.30						
Se	$K_{\alpha 1}$ (11222.4)	Ge844	73.09	0.71	2.28	1.02	2.2	0.93	1.58
	$K_{\beta 1,3}$ (12495.9)	Ge880	82.822						
Br	$K_{\alpha 1}$ (11924.2)	Ge844	64.21	0.75	2.49	1.11	2.15	1.01	1.63
	$K_{\beta 1,3}$ (13291.4)	Si880	76.32						
		Ge777	88.43						

Kr	$K_{\alpha 1}$ (12649)	Ge880	78.57	0.80	2.71	1.19	1.1	1.09	1.02
	$K_{\beta 1,3}$ (14112)	Si777	78.73						

Table S3. Emission lines energy, crystal analyzer characteristics, monochromator bandwidth, natural widths of atomic levels involved in the L_{III}-edge absorption and emission processes, and apparent core hole lifetime bandwidth. The monochromator bandwidth is calculated considering Si220 crystals, with a $\Delta E/E=5.6x10^{-5}$. [§]: X-ray Data Booklet, 2009. [‡] : Campbell and Papp, 2001.

Element		**Spectrometer**		**Monochromator**	**Core hole lifetime broadening (eV)**		
Name	Emission line (E, eV)[§]	Crystal analyzer	θ_{Bragg} (°)	ΔE_{mono} (eV)	$\Gamma_{2p3/2}$ (eV) [‡]	Γ_{3d} (eV) [‡]	$\Gamma_{app.}$ $L_{\alpha 1}$
Ba	$L_{\alpha 1}$ (4466.26)	Ge400	78.96	0.29	3.02	0.67	0.65
La	$L_{\alpha 1}$ (4650.97)	Si400	79.03	0.31	3.12	0.7	0.68
Ce	$L_{\alpha 1}$ (4840.2)	Ge331	80.71	0.32	3.19	0.72	0.70
Eu	$L_{\alpha 1}$ (5845.7)	Ge333	76.95	0.39	3.62	0.9	0.87
Ir	$L_{\alpha 1}$ (9175.0)	Si800	84.46	0.63	5.24	1.99	1.86
Pt	$L_{\alpha 1}$ (9442.3)	Ge660	79.99	0.65	5.39	2.08	1.94
Au	$L_{\alpha 1}$ (9713.3)	Si660	85.71	0.67	5.54	2.18	2.03
Hg	$L_{\alpha 1}$ (9988.8)	Si555	81.79	0.69	5.71	2.28	2.12
Pb	$L_{\alpha 1}$ (10551.5)	Si555	69.54	0.73	6.07	2.48	2.30
U	$L_{\alpha 1}$ (13614.7)	Ge777	77.40	0.96	8.2	3.5	3.22

3. Radiation damages

Effect of radiations damages was estimated on a Pt catalyst. The conventional and HERFD XANES spectra (Fig. S5) were recorded simultaneously on the CRG-FAME beamline at the ESRF (Proux et al., 2005). A two-crystal Si(220) monochromator is located between two Rh-coated mirrors. The beam size on the sample was around 300 x 200 µm² (H x V, FWHM) thanks to the sagittal focus by the 2nd crystal of the monochromator and the vertical one by the 2nd mirror. The 1st crystal of the monochromator is liquid nitrogen cooled in order to limit the thermal bump and so to increase the energy resolution, close to the intrinsic resolution or the Si crystals (Proux et al., 2006). The flux on the sample was around $5x10^{11}$ photons/s. One spherically bent Ge (660) crystal (R=1000mm, from XRS Tech LLC., New Jersey, USA) was tuned to the $L\alpha_1$ fluorescence line. The total energy resolution of the

CAS was measured at 1.3 eV from the measurement of the elastic scattering signal. Conventional measurement was performed in the transmission mode.

The sample was a Pt/γ-Al_2O_3 powder with a 0.3%wt Pt loading. The powder was kept under inert atmosphere on a quartz capillary. The beam was kept at the same position for the 4 spectra in order to estimate the radiation damages before the *operando* experiment. More details can be found in Gorczyca et al. (2014).

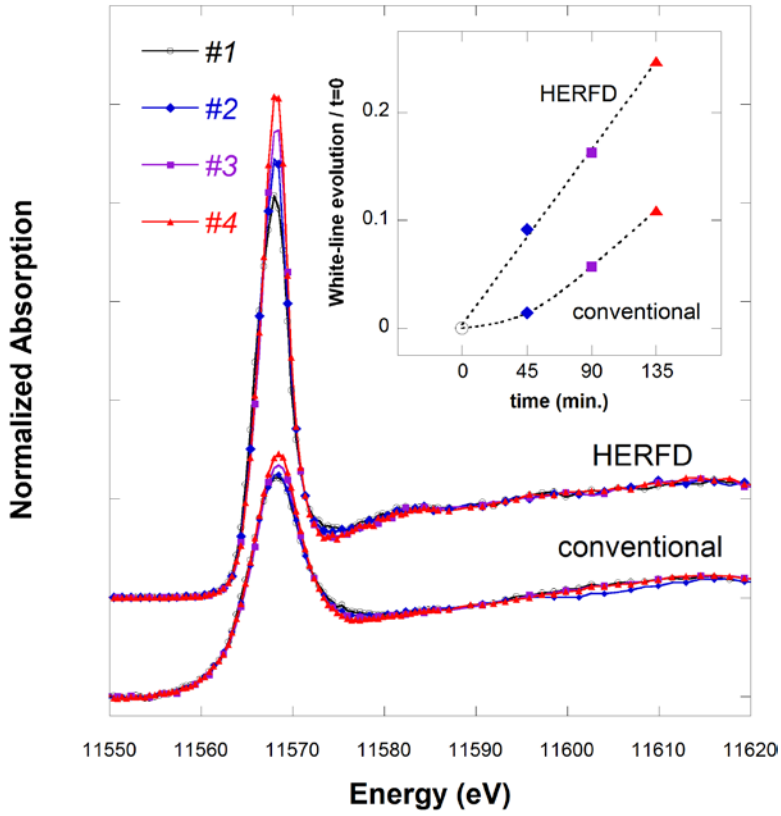

Fig. S5. Conventional and HERFD XANES measurements at the Pt L_{III}-edge or a Pt/γ-Al_2O_3 powder. Insert : relative evolution of the white-line height with respect to the first scan (t=0)

4. Preparation and XAS measurement of the Hg standards

α-HgS: Cinnabar was purchased from Sigma-Aldrich (CAS Number: 1344-48-5). Both the HR- and conventional XANES were measured at room temperature.

β-HgS: Metacinnabar was synthesized in the laboratory using two 500 mL gas washing bottles equipped with coarse fritted glass tips connected in series and placed on magnetic stirrers. The first flask contained a solution of HCl, ~ 3M, and the second flask a solution of 200 mL of ~ 0.1 M mercury(II) perchlorate hydrate – $Hg(ClO_4)_2$ (Sigma-Aldrich CAS Number: 304656-34-6**)**. Stirring bars were placed in each bottle and a low flow of pure N_2 gas was used to degas both flasks to remove all dissolved oxygen. After about 30 minutes of flushing, a large flake of sodium hydrosulfide hydrate (Sigma-Aldrich CAS Number 207683-19-0**)** was added to the bottle containing the acid to evolve a stream of H_2S/N_2 gas in the second flask. The flow of gases was maintained for about 1 hour while a black precipitate formed in the second flask. The precipitate was then collected after transferring the suspension to another flask to perform successive washing/settlings steps to remove remaining salt using deionized water. The wet powder was dried overnight at 60 ^oC and characterized by XRD to confirm the creation of pure metacinnabar. Both HR and conventional XANES measured at room temperature.

$Hg(SR)_2$: $Hg(Cysteine)_2$ standards representing $Hg(SR)_2$, where Hg is linearly coordinated to 2 sulfur atoms, were prepared according to the methods in Jalilehvand et al. (2006) and Manceau et al. (2016), for the conventional and HR-XANES, respectively. For the conventional XANES sample, a 1.1 M H_2Cysteine solution was prepared in boiled Milli-Q water purged with N_2 gas for ~1 hour. Under N_2 atmosphere in a reaction vessel, 1.713 g of $Hg(NO_3)_2 \bullet H_2O$ was added to 50 mL of cysteine stock solution. Upon the addition of Hg^{II} to cysteine, a white precipitate of $Hg_2H_2(Cysteine)_2$ formed. The precipitate was collected and used as the $Hg(Cysteine)_2$ standard (scanned at RT). For the HR-XANES sample, H_2Cysteine and $Hg(ClO_4)_2$ were mixed in 10 mL oxygen-free Milli-Q water to achieve 0.5 mM total Hg, 1 mM total cysteine, and a pH of 3. The aqueous $Hg(Cysteine)_2$ was scanned as a reference at ~10 K.

$Hg(SR)_4$: The $Hg(Cysteine)_{4(aq)}$ standard representing $Hg(SR)_4$, where Hg is tetrahedrally coordinated to 4 sulfur atoms, was prepared according to the methods in Jalilehvand et al. (2006). Using oxygen-free Milli-Q, $Hg(NO_3)_2 \bullet H_2O$ or $Hg(ClO_4)_2$ was added to a cysteine solution to achieve a total Hg concentration of 50 – 70 mM and a cysteine:Hg ratio of 10:1. The pH was adjusted to ~11 dropwise with 1 M NaOH. The conventional XANES were scanned at RT, while the HR-XANES were scanned at ~10 K.

5. Principal Component Analysis and Least-Square Fitting XANES studies

All this analysis was performed using the Demeter program (Ravel and Newville, 2005), version 0.9.24.

Artificial multicomponent spectra were calculated from two sets of pure Hg component spectra obtained in conventional and HERFD mode. The ratio between each reference spectra were randomly obtained and the two sets of 50 multicomponent spectra were calculated using the same set of ratios. After combination, a noise was added to each spectrum, noise corresponding to 0.0025 of the edge step. The different steps of analysis are summarized on Fig. S6, from the this spectrum calculation to the scree plot. The results of the ratio adjustment are shown on Fig. S7. for the β-HgS, $Hg(Cys)_2$ and $Hg(Cys)_4$ sets of spectra (conventional and HERFD).

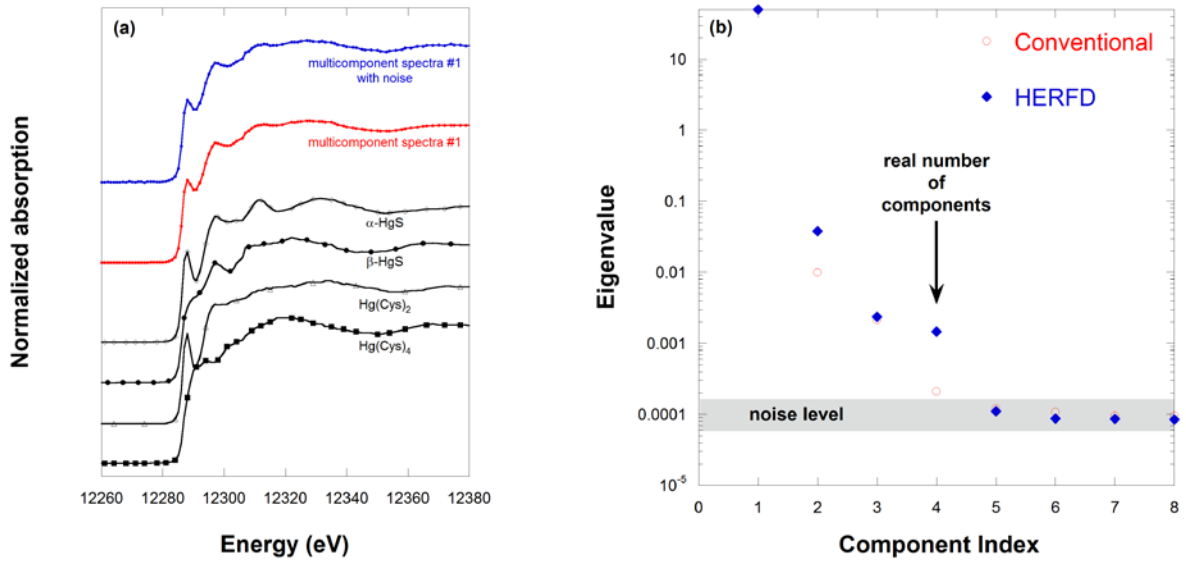

Fig. S6. Example of multicomponent spectrum calculation (a, sample #1 calculated from HERFD reference spectra). Scree plot of the PCA analysis (b).

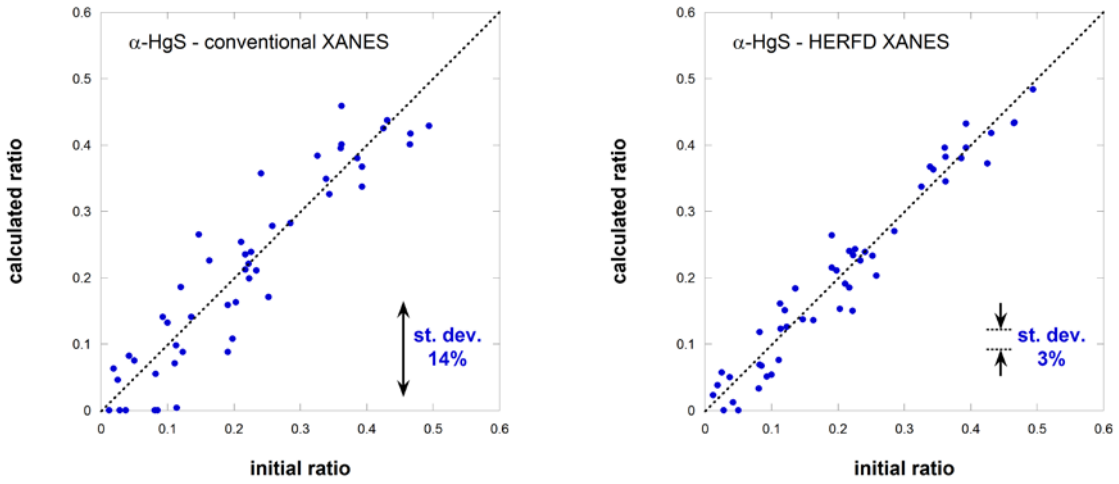

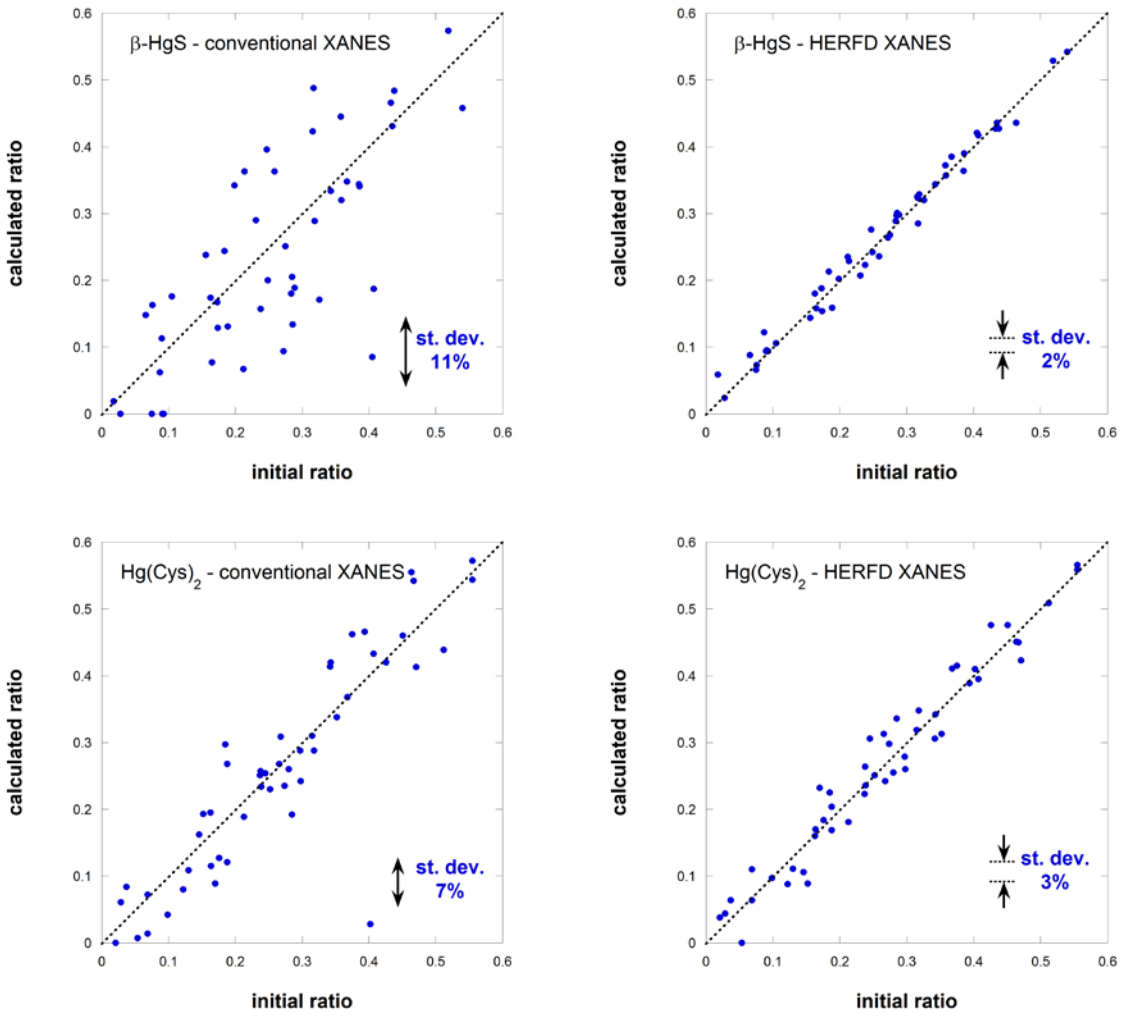

Fig. S7. Results of the Least Square Fitting analysis of the α-HgS, β-HgS, and $Hg(Cys)_2$ ratio in the random synthetic multicomponent set of XANES, obtained in conventional (left) and HERFD (right) mode. Comparison between the ratio obtained from the adjustment and from the spectrum calculation.

6. References

Atrian Blasco, E. L., Cerrada, E., Conte-Daban, A., Testemale, D., Faller, P., Laguna, M., and C. Hureau. 2015. Copper(I) targeting in the Alzheimer's disease context: a first example using the biocompatible PTA ligand. Metallomics 7:1229-1232. doi:10.1039/C5MT00077G

Aucour, A.-M., Bedell, J.-P., Queyron, M., Magnin, V., Testemale, D., and G. Sarret. 2015. Dynamics of Zn in an urban wetland soil-plant system: Coupling isotopic and EXAFS approaches. Geochim. Cosmochim. Acta 160:55-69. doi:10.1016/j.gca.2015.03.040

Aurelio, G., Fernandez-Martinez, A., Cuello, G.J., Roman-Ross, G., Alliot, I., and L. Charlet. 2010. Structural study of selenium(IV) substitutions in calcite. Chem. Geol. 270:249-256. doi:10.1016/j.chemgeo.2009.12.004

Bazarkina, E. F., Pokrovski, G. S., Zotov, A. V., and J.-L. Hazemann. 2010. Structure and stability of cadmium chloride complexes in hydrothermal fluids. Chem. Geol. 276:1-17. doi:10.1016/j.chemgeo.2010.03.006

Bodeï, S., Manceau, A., Geoffroy, N., Baronnet, A., and M. Buatier M. 2007. Formation of todorokite from vernadite in Ni-rich hemipelagic sediments. Geochim. Cosmochim. Acta 71:5698-5716. doi:10.1016/j.gca.2007.07.020

Cancès, B., Juillot, F., Morin, G., Laperche, V., Alvarez, L., Proux, O., Hazemann, J-L., Brown Jr., G. E., and G. Calas. 2005. XAS evidence of As(V) association with iron oxyhydroxides in a contaminated soil at a former arsenical insecticide processing plant. Environ. Sci. Technol. 39:9398-9405. doi:10.1021/es050920n

Cancès, B., Juillot, F., Morin, G., Laperche, V., Polya, D., Vaughan, D.J., Hazemann, J.-L., Proux, O., Brown Jr., G. E., and G. Calas. 2008. Changes in arsenic speciation through a contaminated soil profile: a XAS based study. Sci. Total Environ. 397:178-189. doi:10.1016/j.scitotenv.2008.02.023

Campbell, J. L., and T. Papp. 2001. Widths of the atomic K-N7 levels. At. Data Nucl. Data Tables 77:1–56. doi: 10.1006/adnd.2000.0848

Carrière, M., Thiebault, C., Milgram, S., Proux, O., and B. Gouget. 2006. Citrate does not change Uranium chemical speciation in cell culture medium but increases its toxicity and accumulation in NRK-52E cells. Chem. Res. Toxicol. 19:1637-1642. doi:10.1021/tx060206z

Céolin, D., Ablett, J. M., Prieur, D., Moreno, T., Rueff, J. P., Marchenko, T., Journel, L., Guillemin, R., Pilette, B., Marin, T., and M. Simon. 2013. Hard X-ray Photoelectron Spectroscopy on the GALAXIES beamline at the SOLEIL synchrotron. J. Electron Spectrosc. 190:188–192. doi:10.1016/j.elspec.2013.01.006

Chaurand, P., Rose, J., Briois, V., Olivi, L., Hazemann, J.-L., Proux, O., Domas, J., and J.-Y. Bottero. 2007. Environmental impacts of steel slag reused in road construction: a

crystallographic and molecular (XANES) approach. J. Hazard. Mat. 139:537–542. doi:10.1016/j.jhazmat.2006.02.060

Cheignon, C., Faller, P., Testemale, D., Hureau, C., and F. Collin. 2016. Metal-catalyzed oxidation of Aβ and the resulting reorganization of the Cu binding sites promote ROS production. Metallomics 8:1081-1089. doi:10.1039/C6MT00150E

Chevreux S., Llorens I., Solari P. L., Roudeau S., Devès G., Carmona A., Testemale D., Hazemann J.-L., Ortega R., "Coupling of native IEF and Extended X-ray Absorption Fine Structure to characterize zinc binding sites from p*I* isoforms of SOD1 and A4V pathogenic mutant. Electrophoresis 33 (2012) 1276–1281. doi:10.1002/elps.201100596

Collin, B., Doelsch, E., Keller, C., Cazevieille, P., Tella, M., Chaurand, P., Panfili, F., Hazemann, J-L., and J. D. Meunier. 2014. Copper distribution and speciation in bamboo exposed to a high Cu concentration and Si supplementation. First evidence on the presence of reduced copper bound to sulfur compounds in Poaceae. Environ. Pollut. 187:22-30. doi:10.1016/j.envpol.2013.12.024

Collins, R. N., Tran, N. D., Bakkaus, E., Avoscan, L., and B. Gouget. 2006. Assessment of isotope exchange methodology to determine the sorption coefficient and isotopically exchangeable concentration of selenium in soils and sediments. Environ. Sci. Technol. 40:7778-7783. doi:10.1021/es061528s

Collins, R. N., Bakkaus, E., Carrière, M., Khodja, H., Proux, O., Morel, J.-L., and B. Gouget. 2010. Uptake, localization and speciation of cobalt in *Triticum aestivum L.* (wheat) and *Lycopersicon esculentum M.* (tomato). Environ. Sci. Technol. 44:2904–2910. doi:10.1021/es903485h

Conte-Daban, A., Day, A., Faller, P., and C. Hureau. 2016. How Zn can impede Cu detoxification by chelating agents in Alzheimer's disease: a proof-of-concept study. Dalton Trans. 45:15671-15678. doi:2010.1039/C6DT02308H

Doelsch, E., Basile-Doelsch I., Rose J., Masion A., Borschneck, D., Hazemann, J.-L., Saint Macary, H., and J. Y. Bottero. 2006. New combination of EXAFS spectroscopy and density fractionation for the speciation of chromium within an andosol. Environ. Sci. Technol. 40:7602-7608. doi:10.1021/es060906q

Froideval, A., Del Nero, M., Gaillard, C., Barillon, R., Rossini, I., and J.-L. Hazemann. 2006. Uranyl sorption species at low coverage on Al-hydroxide: TRLFS and XAFS studies. Geochim. Cosmochim. Acta 70:5270-5284. doi:10.1016/j.gca.2006.08.027

Gao, X., Gu, S., Gao, Zou, Y., Jiang, Z., Zhang, S., Wei, X., Yu, H., Sheng, G., Duan, P., and Y. Huang. 2013. A high-resolution X-ray fluorescence spectrometer and its application at SSRF. X-Ray Spectrom. 42:502–507. doi:10.1002/xrs.2511

Glatzel, P., Sikora, M., Smolentsev, G., and M. Fernández-García. 2009. Hard X-ray photon-in photon-out spectroscopy. Catal. Today 145:294–299. doi:10.1016/j.cattod.2008.10.049

Glatzel, P., Weng, T.-C., Kvashnina, K., Swarbrick, J., Sikora, M., Gallo, E., Smolentsev, N., and R.A. Mori. 2013. Reflections on hard X-ray photon-in/photon-out spectroscopy for electronic structure studies. J. Electron Spectros. Relat. Phenomena 188:17–25. doi:10.1016/j.elspec.2012.09.004

Gorczyca, A., Moizan, V., Chizallet, C., Proux, O., Delnet, W., Lahera, E., Hazemann, J.-L., Raybaud, P., and Y. Joly. 2014. Monitoring morphology and hydrogen coverage of subnanometric Pt/γ-Al_2O_3 particles by in situ HERFD-XANES and quantum simulations. Angew. Chem. Int. Ed. 53:12426-12429. doi:10.1002/anie.201403585

Guiné V., Spadini L., Sarret G., Muris M., Delolme C., Gaudet J.-P., and J. M. F. Martins. Zinc sorption to three gram-negative bacteria: Combined titration, modeling, and EXAFS study. Environ. Sci. Technol. 40 (2006) 1806-1813. doi:10.1021/es050981l

Hazemann, J.-L., Proux, O., Nassif, V., Palancher, H., Lahera, E., Da Silva, C., Braillard, A., Testemale, D., Diot, M.-A., Alliot, I., Delnet, W., Manceau, A., Gélébart, F., Morand, M., Dermigny, Q., and A. Shukla. 2009. High Resolution Spectroscopy on an X-ray Absorption Beamline. J. Synchrotron Radiat. 16:283-292. doi:10.1107/s0909049508043768

Huguet, S., Isaure, M.-P., Bert, V., Laboudigue, A., Proux, O., Flank, A.-M., Vantelon, D., and G. Sarret. 2015. Impact of *Arabidopsis halleri* growth on cadmium localization and speciation in highly contaminated dredged sediment. Sci. Tot. Env. 536:468-480. doi:10.1016/j.scitotenv.2015.07.026

Ishii, K., Jarrige, I., Yoshida, M., Ikeuchi, K., Inami, T., Murakami, Y., and J. Mizuki. 2013. Instrumental upgrades of the RIXS spectrometer at BL11XU at SPring-8. J. Electron Spectrosc. 188:127–132. doi:10.1016/j.elspec.2012.12.003

Isaure, M.P., Manceau, A., Geoffroy, N., Laboudigue, A., Tamura, N., and M.A. Marcus. 2005. Zinc mobility and speciation in soil covered by contaminated dredged sediment using micrometer-scale and bulk-averaging X-ray fluorescence, absorption and diffraction techniques. Geochim. Cosmochim. Acta 69:1173-1198. doi:10.1016/j.gca.2004.08.024

Isaure, M.P., Huguet, S., Meyer, C.L., Castillo-Michel, H., Testemale, D., Vantelon, D., Saumitou Laprade, P., and N. Verbruggen. 2015. Evidence of various mechanisms of Cd sequestration in the hyperaccumulator *Arabidopsis halleri*, the non accumulator *Arabidopsis lyrata* and their progenies by combined synchrotron-based techniques. J. Exp. Bot. 66:3201-3214. doi:10.1093/jxb/erv131

Jalilehvand, F., Leung, B. O., Izadifard, M., and E. Damian. 2006. Mercury(II) cysteine complexes in alkaline aqueous solution. Inorg. Chem. 45:66-73. doi:10.1021/ic0508932

Kirpichtchikova, T., Manceau, A., Spadini, L., Panfili, F., Marcus, M., and T. Jacquet. 2006. Speciation and solubility of heavy metals in contaminated soil using X-ray microfluorescence, EXAFS spectroscopy, chemical extraction, and thermodynamic modelling. Geochim. Cosmochim. Acta 70:2163-2190. doi:10.1016/j.gca.2006.02.006

Kleymenov, E., van Bokhoven, J. A., David, C., Glatzel, P., Janousch, M., Alonso-Mori, R., Studer, M., Markus Willimann, M., Bergamaschi, A., Henrich, B. and M. Nachtegaal. 2011. Five-element Johann_type x-ray emission spectrometer with a single-photon-counting pixel detector. Rev. Sci. Instrum. 82:065107. doi:10.1063/1.3600452

Krause, M. O., and J. H. Oliver. 1979. Natural widths of atomic K and L levels, Kα X-Ray lines and several KLL Auger lines. J. Phys. Chem. Ref. Data 8:329-338. doi:10.1063/1.555595

Kvashnina, K. O., and A. C. Scheinost. 2016. A Johann_type X-ray emission spectrometer at the Rossendorf beamline. J. Synchrotron Rad. 23:836–841. doi:10.1107/S1600577516004483

Laurette, J., Larue, C., Llorens, I., Jaillard, D., Jouneau, P.-H., Bourguignon, J., and M. Carrière. 2012. Speciation of uranium in plants upon root accumulation and root-to-shoot translocation: a XAS and TEM study. Environ. Exp. Bot. 77:87-95. doi:10.1016/j.envexpbot.2011.11.005

Le Pape, P., Quantin, C., Morin, G., Jouvin, D., Kieffer, I., Proux, O., Ganbaja, J., and S. Ayrault. 2014. Zinc speciation in the suspended particulate matter of an urban river (Orge, France): influence of seasonality and urbanization gradient. Environ. Sci. Technol. 48:11901-11909. doi:10.1021/es500680x

Levard, C., Doelsch, E., Rose, J., Masion, A., Basile-Doelsch, I., Proux, O., Hazemann, J.-L., Borschneck, D., and J.-Y. Bottero. 2009. Ni speciation within an andosol: an original laboratory approach. Geochim. Cosmochim. Acta 73:4750-4760. doi:10.1016/j.gca.2009.05.053

Llorens, I., Lahera, E., Delnet, W., Proux, O., Braillard, A., Hazemann, J.-L., Prat, A., Testemale, D., Dermigny, Q., Gelebart, F., Morand, M., Shukla, A., Bardou, N., Ulrich, O., Arnaud, S., Berar, J.-F., Boudet, N., Caillot, B., Chaurand, P., Rose, J., Doelsch, E., Martin, P., and P. L. Solari. 2012. High energy resolution five-crystal spectrometer for high quality fluorescence and absorption measurements on an X-ray Absorption Spectroscopy beamline. Rev. Sci. Instrum. 83:063104. doi:10.1063/1.4728414

Llorens, I., Solari, P.L., Sitaud, B., Bès, R., Cammelli, S., Hermange, H., Othmane, G., Safi, S., Moisy, P., Wahu, S., Bresson, C., Schlegel, M.L., Menut, D., Béchade, J.-L., Martin, P., Hazemann, J.-L., Proux, O., and C. Den Auwer. 2014. X-ray Absorption Spectroscopy investigations on radioactive matter using MARS beamline at SOLEIL synchrotron. Radiochim. Acta 102:957-972. doi:10.1515/ract-2013-2241

Manceau, A., Tommaseo, C., Rihs, S., Geoffroy, N., Chateigner, D., Schlegel, M., Tisserand, D., Marcus, M.A., Tamura, N., and Z. S. Chen. 2005. Natural speciation of Mn, Ni and Zn at the micrometer scale in a clayey paddy soil using X-ray fluorescence, absorption, and diffraction. Geochim. Cosmochim. Acta 69:4007-4034. doi:10.1016/j.gca.2005.03.018

Manceau, A., Tamura, N., Celestre, R.S., MacDowell, A.A., Geoffroy, N., Sposito, G., and H.A. Padmore. 2003. Molecular-scale speciation of Zn and Ni in soil ferromanganese

nodules from Loess soils of the Mississippi basin. Environ. Sci. Technol. 37:75-80. doi:10.1021/es025748r

Manceau, A., Marcus, M. A., Tamura, N., Proux, O., Geoffroy, N. and B. Lanson. 2004. Natural speciation of Zn at the micrometer scale in a clayey soil using X-ray fluorescence, absorption, and diffraction. Geochim. Cosmochim. Acta 68:2467-2483. doi:10.1016/j.gca.2003.11.021

Manceau, A., and A. Matynia. 2010. The Nature of Cu bonding to natural organic matter. Geochim. Cosmochim. Acta 74:2556–2580. doi:10.1016/j.gca.2010.01.027

Manceau, A., Simionovici, A., Lanson, M., Perrin, J., Tucoulou, R., Bohic, S., Fakra, S. C., Marcus, M., Bedell, J.P., and K. Nagy. 2013. *Thlaspi arvense* binds Cu(II) as a bis-(L-histidinato) complex on root cell walls in an urban ecosystem. Metallomics 5:1674-1684. doi:10.1039/c3mt00215b

Manceau, A., Enescu, M., Simionovici, A., Lanson, M., Gonzalez-Rey, M., Rovezzi, M., Tucoulou, R., Glatzel, P., Nagy, K. L., and J.-P. Bourdineaud. 2016. Chemical forms of mercury in human hair reveal sources of exposure. Environ. Sci. Technol. 50:10721–10729. doi:10.1021/acs.est.6b03468

March, A.M., Stickrath, A., Doumy, G., Kanter, E.P., Kraessig, B., Southworth, S.H., Attenkofer, K., Kurtz, C.A., Chen, L. X., and L. Young. 2011. Development of high-repetition-rate laser pump/x-ray probe methodologies for synchrotron facilities. Rev. Sci. Instrum. 82:073110. doi:10.1063/1.3615245

Marcus, M. A., Manceau, A., and M. Kersten. 2004. Mn, Fe, Zn and As speciation in a fast-growing ferromanganese marine nodule. Geochim. Cosmochim. Acta 68:3125-3136. doi:10.1016/j.gca.2004.01.015

Nagy, K. L., Manceau, A., Gasper, J. D., Ryan, J. N., and G. R. Aiken. 2011. Metallothionein-like multinuclear clusters of mercury(II) and sulfur in peat. Environ. Sci. Technol. 45:7298–7306. doi:10.1021/es201025v

Panfili, F., Manceau, A., Sarret, G., Spadini, L., Kirpichtchikova, T., Bert, V., Laboudigue, A., Marcus, M.A., Ahamdach, N., and M.F. Libert. 2005. The effect of phytostabilization on Zn speciation in a dredged contaminated sediment using scanning electron

microscopy, X-ray fluorescence, EXAFS spectroscopy and principal components analysis. Geochim. Cosmochim. Acta 69:2265-2284. doi:10.1016/j.gca.2004.10.017

Pokrovski, G., Schott, J., Farges, F. and J.-L. Hazemann. 2003. Iron (III)-silica interactions in aqueous solution : Insights from X-ray absorption fine Structure. Geochim. Cosmochim. Acta 67:3559-3573. doi:10.1016/S0016-7037(03)00160-1

Pokrovsky, O.S., Pokrovski, G.S., Schott, J., and A. Galy. 2006. Experimental study of germanium adsorption on goethite and germanium coprecipitation with iron hydroxide: X-ray absorption fine structure and macroscopic characterization. Geochim. Cosmochim. Acta 70:3325-3341. doi:10.1016/j.gca.2006.04.012

Pokrovsky, O.S., Pokrovski, G.S., Shirokova, L.S., Gonzalez, A.G., Emnova, E.E., and A. Feurtet-Mazel. 2012. Chemical and structural status of copper associated with oxygenic and anoxygenic phototrophs and heterotrophs: possible evolutionary consequences. Geobiology 10:130-149. doi:10.1111/j.1472-4669.2011.00303.x

Pradas del Real, A. E., Castillo-Michel, H. A., Kaegi, R., Sinnet, B., Magnin, V., Findling, N., Villanova, J., Carrière, M., Santaella, C., Fernandez-Martinez, A., Levard, C., and G. Sarret. 2016. Fate of Ag-NPs in sewage sludge after application on agricultural soils. Environ. Sci. Technol. 50:1759-1768. doi:10.1021/acs.est.5b04550

Priadi, C., Morin, G., Ayrault, S., Maillot, F., Juillot, F., Llorens, I., Testemale, D., Proux, O., and G. E. Brown Jr. 2012. X-ray Absorption Fine Structure evidence for amorphous zinc sulfide as a major zinc species in suspended matter from the Seine river downstream of Paris, Ile-de-France, France. Environ. Sci. Technol. 46:3712–3720. doi:10.1021/es2041652

Proux, O., Biquard, X., Lahera, E., Menthonnex, J.-J., Prat, A., Ulrich, O., Soldo, Y., Trévisson, P., Kapoujvan, G., Perroux, G., Taunier, P., Grand, D., Jeantet, P., Deleglise, M., Roux, J.-P., and J.-L. Hazemann. 2005. FAME: a new beamline for X-ray absorption investigations of very-diluted systems of environmental, material and biological interests. Phys. Scripta 115:970-973. doi:10.1238/Physica.Topical.115a00970

Proux, O., Nassif, V., Prat, A., Ulrich, O., Lahera, E., Biquard, X., Menthonnex, J.-J., and J.-L. Hazemann. 2006. Feedback system of a liquid nitrogen cooled double-crystal monochromator: design and performances. J. Synchrotron Radiat. 13:59-68. doi:10.1107/S0909049505037441

Ravel, B., and M. Newville. 2005. ATHENA, ARTEMIS, HEPHAESTUS: data analysis for X-ray absorption spectroscopy using IFEFFIT. J. Synchrotron Radiat. 12:537–541. doi:10.1107/S0909049505012719

Renard, F., Putnis, C.V., Montes-Hernandez, G., Ruiz-Agudo, E., Hovelmann, J., and G. Sarret. 2015. Interactions of arsenic with calcite surfaces revealed by in-situ nanoscale imaging. Geochim. Cosmochim. Acta 159:61-79. doi:10.1016/j.gca.2015.03.025

Rovezzi, M., Lapras, C., Manceau, A., Glatzel, P., and R. Verbeni. 2017. High energy-resolution x-ray spectroscopy at ultra-high dilution with spherically bent crystal analyzers of 0.5 m radius. Rev. Sci. Instrum. 88:013108. doi:10.1063/1.4974100

Salem, S. I., and P. L. Lee. 1976. Experimental widths of K and L X-ray lines. At. Data Nucl. Data Tables 18:233–244. doi:10.1016/0092-640X(76)90026-7

Sammut, M.L., Rose, J., Fiani, E., Depoux, M., Ziebel, A., Hazemann, J.-L, Proux, O., and Y. Noack. 2008. Determination of zinc speciation in steel plant flying dust. Chemosphere 70:1945–1951. doi:10.1016/j.chemosphere.2007.09.063

Sammut, M.L., Noack, Y., Rose, J., Hazemann, J.-L., Proux, O., Depoux, M., Ziebel, A., and E. Fiani. 2010. Speciation of Cd and Pb in dust emitted from sinter plant. Chemosphere 78:445-450. doi:10.1016/j.chemosphere.2009.10.039

Sarret, G., Saumitou-Laprade, P., Bert, V., Proux, O., Hazemann, J.-L., Traverse, A., Marcus, M., and A. Manceau. 2002. Forms of zinc accumulated in hyperaccumulator *Arabidopsis halleri*. Plant Physiol. 130:1815-1826. doi:10.1104/pp.007799

Sarret, G., Balesdent, J., Bouziri, L., Garnier, J.M., Marcus, M.A., Geoffroy, N., Panfili, F., and A. Manceau. 2004. Zn speciation in the organic horizon of a contaminated soil by micro X-ray fluorescence, micro and powder EXAFS spectroscopy and isotopic dilution. Environ. Sci. Technol. 38:2792-2801. doi:10.1021/es035171t

Schlegel, M.L., and A. Manceau. 2013. Binding mechanism of Cu(II) at the clay-water interface by powder and polarized EXAFS spectroscopy. Geochim. Cosmochim. Acta 113:113-124. doi:10.1016/j.gca.2013.03.019

Schreck, E., Dappe, V., Sarret, G., Sobanska, S., Nowak, D., Nowak, J., Stefaniak, E. A., Magnin, V., Ranieri, V., and C. Dumat. 2014. Foliar or root exposures to smelter

particles: Consequences for lead compartmentalization and speciation in plant leaves. Sci. Tot. Env. 476-477:67-676. doi:10.1016/j.scitotenv.2013.12.089

Simonelli, L., Marini, C., Olszewski, W., Avila Perez, M., Ramanan, N., Guilera, G., Cuartero, V. and K. Klementiev. 2016. CLÆSS: the hard x-ray absorption beamline of the ALBA CELLS synchrotron. Cogent Physics. 3:1231987. doi:10.1080/23311940.2016.1231987

Sokaras, D., Weng, T.-C., Nordlund, D., Alonso-Mori, R., Velikov, P., Wenger, D., Garachtchenko, A., George, M., Borzenets, V., Johnson, B., Rabedeau, T., and U. Bergmann. 2013. A seven-crystal Johann_type hard x-ray spectrometer at the Stanford Synchrotron Radiation Lightsource. Rev. Sci. Instrum. 84:053102. doi:10.1063/1.4803669

Straczek, A., Sarret, G., Manceau, A., Hinsinger, P., and B. Jaillard. 2008. Zinc distribution and speciation in roots of various genotypes of tobacco exposed to Zn. Environ. Exp. Bot. 63:80-90. doi:10.1016/j.envexpbot.2007.10.034

Szlachetko, J., M. Nachtegaal, E. de Boni, M. Willimann, O. Safonova, J. Sa et al. 2012. A von Hámos X-ray spectrometer based on a segmented-type diffraction crystal for single-shot X-ray emission spectroscopy and time-resolved resonant inelastic X-ray scattering studies. Rev. Sci. Instrum. 83:103105. doi:10.1063/1.4756691

Takahashi, Y., Manceau, A., Geoffroy, N., Marcus, M.A., and A. Usui. 2007. Chemical and structural control of the partitioning of Co, Ce, and Pb in marine ferromanganese oxides. Geochim. Cosmochim. Acta 71:984–1008. doi:10.1016/j.gca.2006.11.016

Tella, M., and G.S. Pokrovski. 2009. Antimony(III) complexing with O-bearing organic ligands in aqueous solution: An X-ray absorption fine structure spectroscopy and solubility study. Geochim. Cosmochim. Acta 73:268-290. doi:10.1016/j.gca.2008.10.014

Tella, M., and G.S. Pokrovski. 2012. Structure and stability of pentavalent antimony complexes with aqueous organic ligands. Chem. Geol. 292-293:57-68. doi:10.1016/j.chemgeo.2011.11.004

Tella, M., Auffan, M., Brousset, L., Issartel, J., Kieffer, I., Pailles, C., Morel, E., Santaella, C., Artells E., Rose J., Thiéry, A., and J.-Y. Bottero. 2014. Transfer, transformation and

impacts of ceria nanomaterials in aquatic mesocosms simulating a pond ecosystem. Environ. Sci. Technol. 48:9004–9013. doi:10.1021/es501641b

Trepreau, J., Grosse, C., Mouesca, J.-M., Sarret, G., Girard, E., Petit-Haertlein, I., Kuennemann, S., Desbourdes, C., de Rosny, E., Maillard, A. P., Nies, D. H., and J. Covès. 2014. Metal sensing and signal transduction by CnrX from Cupriavidus metallidurans CH34: role of the only methionine assessed by a functional, spectroscopic, and theoretical study. Metallomics 6:263-273. doi:10.1039/C3MT00248A

Vespa, M., Lanson, M., and A. Manceau. 2010. Natural attenuation of zinc pollution in smelter-affected soil. Environ. Sci. Technol. 44:7814–7820. doi:10.1021/es101567u

X-ray Data Booklet. 2009. Center for X-ray Optics and Advanced Light Source, Lawrence Berkeley National Laboratory (http://xdb.lbl.gov/)

2.2 In situ HP-HT set-up

2.2.1 Autoclave and cell

A high pressure/high temperature cell dedicated to X-ray absorption spectroscopy, small angle X-ray scattering, and inelastic X-ray scattering techniques is presented. The P and T parameters are controlled independently and their range allow the study of aqueous solutions (T≤ 500 °C and P≤ 2000 bar) and liquid metals and glasses (T≤ 1700 °C and P≤ 2000 bar). The autoclave technology is inspired from previous high pressure/high temperature equipments but great improvements are achieved. Original high pressure windows have been developed to ensure both pressure resistance and low absorbance combined with large angular aperture. Different configurations are available for the internal cell that contains the sample whether it is aqueous or not. A picture and a first general diagram can be found in FIG. 2.5 and FIG 2.6.

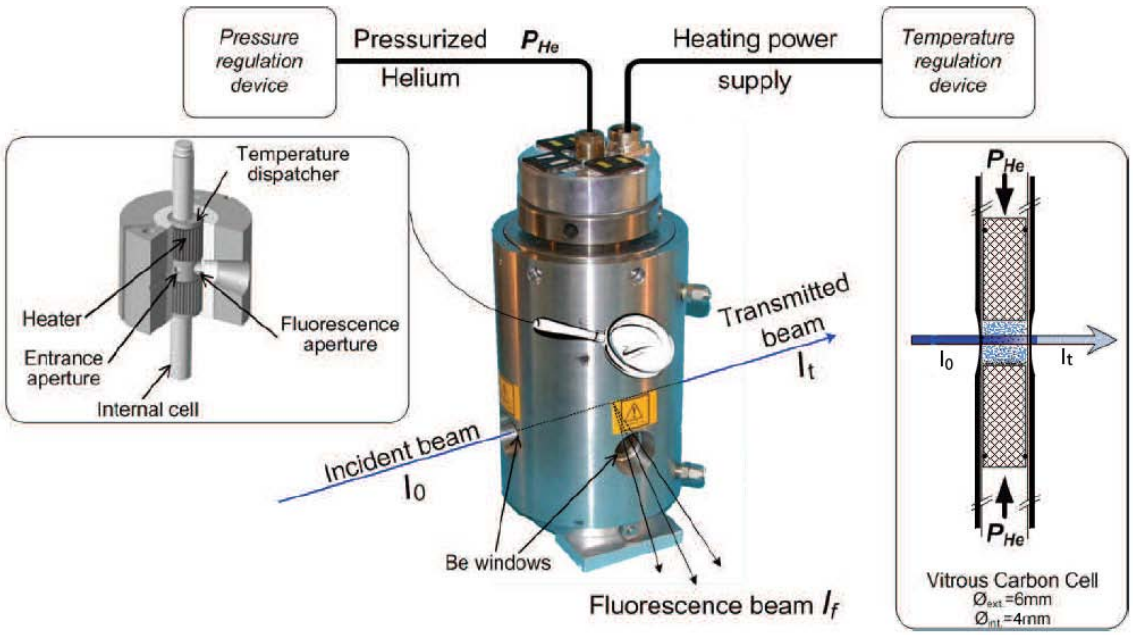

FIG. 2.5 - Schematic view of the high pressure/high temperature vessel used for XAS measurements.[2] The gas pressure inside the vessel is stabilized with a special pressure regulation device.[123]

2.2.2 The pressure regulation

This autoclave consists of an internal part, containing the heating elements as well as the sample holder, surrounded by helium under pressure in a double-walled cylinder head. The double wall system allows the circulation of chilled water. The circulation makes it possible to evacuate the heat produced by the furnace while maintaining the body of the autoclave and the windows at low temperature. Hence, the body of the autoclave and the windows are be preserved from thermal shocks or changes in the physical properties of the materials used. For example, the resistance properties of materials to pressure will change if they are subjected to an elevated temperature: the thermal expansion of the different

components of the autoclave would be different in particular for the windows and the steel of the body of the autoclave, which can cause the joints to exit their throat. The water circulation also helps to lower the temperature during the cooling down of the samples, saving time during the experiments.

The helium pressure is supplied by an electric compressor (more particularly a membrane compressor from Nova Swiss, able to work up to 3000 bar). At the outlet of the compressor, the regulation of the pressure of helium applied in the autoclave is ensured by a system developed in our institute "Néel Institiute" by R. Bruyère *et al.*[123] as part of the CNRS High Pressure Technology Network.

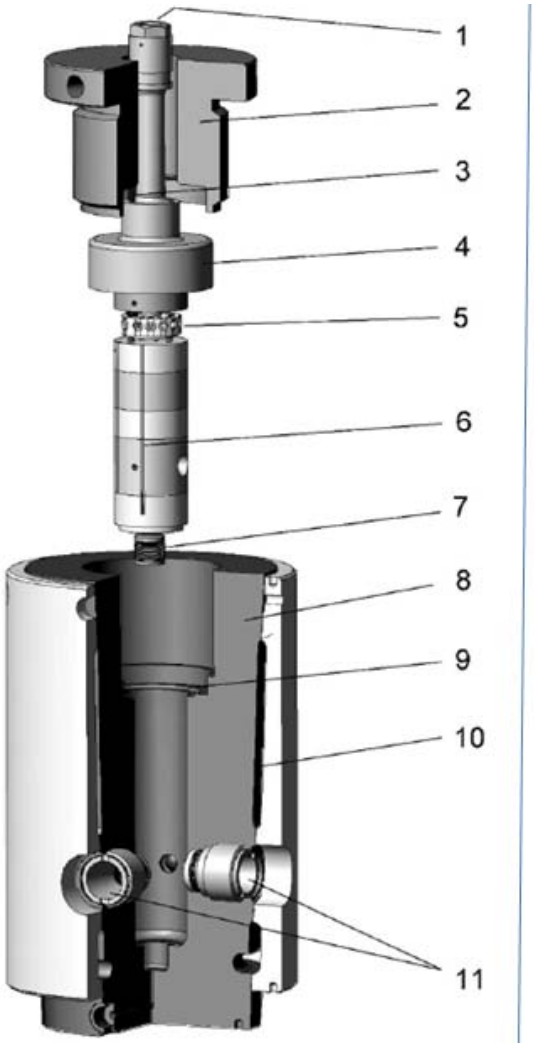

1. He inlet through the HP vessel plug.
2. HP vessel nut to hold tight the vessel plug.
3. Pyrophyllite leadthroughs.
4. HP vessel plug.
5. Thermocouples and electrical leads connections to the internal part.
6. Thermocouple (one visible out of two).
7. Bellows of the internal cell.
8. HP vessel.
9. Vitton seal.
10. Water cooling circulation.
11. Windows (two out of three): the visible parts are the locknuts. The size of the HP vessel s8d is 242 mm3150 mm.

FIG. 2.6 - Schematic showing the constituent elements of the autoclave (HP/HT) set-up.

Pressure control ensures a constant pressure in our autoclave with a relative accuracy of ± 0.2 bar. The advantage of this system is that it is possible to compensate fluctuations of

pressure, in particular at increasing the temperature (which tends to increase the applied pressure), or caused by leakage. These can be present either in the autoclave, If deposits are present on the surface of the seal (item (9) in FIG. 2.6) or in the high-pressure fittings.

The body of the cell is made from X13 stainless steel, which does not oxidize and present interesting mechanical properties. The HP seal between the vessel and the plug is achieved with a vitton seal and an antiextrusion brass Δ-ring located in the area 9 in FIG. 2.6. The role of the plug is to introduce the He inlet, the thermocouples and electrical wires into the internal part. The technological solution chosen is conical pyrophyllite leadthroughs.

2.2.3 The Temperature regulation

The heating system consists of a resistive furnace ((4) in FIG. 2.7), composed for a molybdenum wire of 0.4 mm in diameter, with a high electrical current circulating, Wrapped around the sample area. The wire is slid into tubes of alumina in a "flûte de pan" type arrangement to isolate the mollybdene wire. The oven is wrapped around a cylindrical copper tube (3) which contains the internal cell (9) for better homogenization of the temperature. An insulating block made of boron nitride makes easier to assemble by constraining the final shape of the furnace. A thermally insulating ceramic made of alumina (7) surrounds the whole. The control of the temperature is made using an Eurotherm and a DC power supply from Midec (power supply type SK 60-30) by operating in voltage limitation. For our samples, the order of magnitude of the power dissipated by the furnace corresponds to an external supply of (12 A x 10 V), for a temperature of 200 °C.

A K-type thermocouples are housed in holes drilled in the tube in order to measure the temperature as close to the sample as possible. The resulting temperature gradient between the thermocouples holes and the inner part of the internal cell has been determined precisely. As it is visible in FIG. 2.7, all these elements are confined in insulating ceramic elements both to avoid heat outflow and for highpressure safety reasons. Since the sample region probed by the photons beam is at the center of the heating zone, all the heating elements have three apertures corresponding to the three windows of the HP vessel.

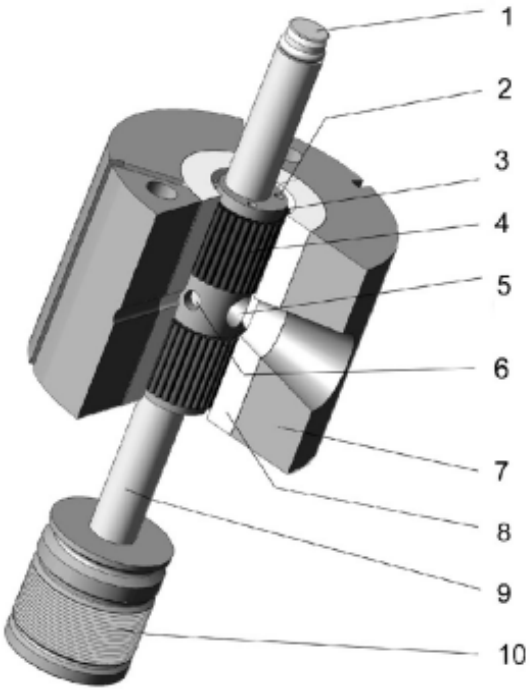

1. Internal cell cap.

2. Thermocouple housing in the copper tube.

3. Copper tube.

4. Resistive furnace.

5+6. Beam windows in the copper tube.

7+8. insulating ceramic elements.

9. Alumina internal cell.

10. Bellows for aqueous samples.

FIG. 2.7 - 3D drawing of the internal part in the configuration for aqueous samples (Heating and sample). Note that the heating principle is identical in the case of nonaqueous samples.

2.2.4 The windows of the Autoclave

The window of autoclave play an important role to resist the pressure of helium inside the cell. Different types of windows ensure the passage of the beam. They must all satisfy two types of criteria, while adapting to the chosen experiment: firstly, they must resist the pressure of helium inside the autoclave, which will result in different geometric criteria depending on the material used. The beryllium windows used for the X-ray absorption measurements which have a dome shape allows good resistance to pressure for a relatively small thickness.

Secondly, they must not alter the beam path through them: the use low absorption coefficients materials must be selected. (Thus, the low density and the small atomic number of the beryllium used in X ray absorption allows it to absorb as little as possible of the beam), moreover, the geometry of the windows do not have to alter the focus of the beam. In our case, I had used three Be windows (2 with the direction of the beam, and the other one at 90° for fluorescence measurements) with a thickness 0.8 mm, and density 1.85 g/cm^3. The most polyvalent windows, for XAS and IXS techniques, are made in Be. Extruded Be SR200 is chosen for its compromise between good mechanical and low absorption properties[2].

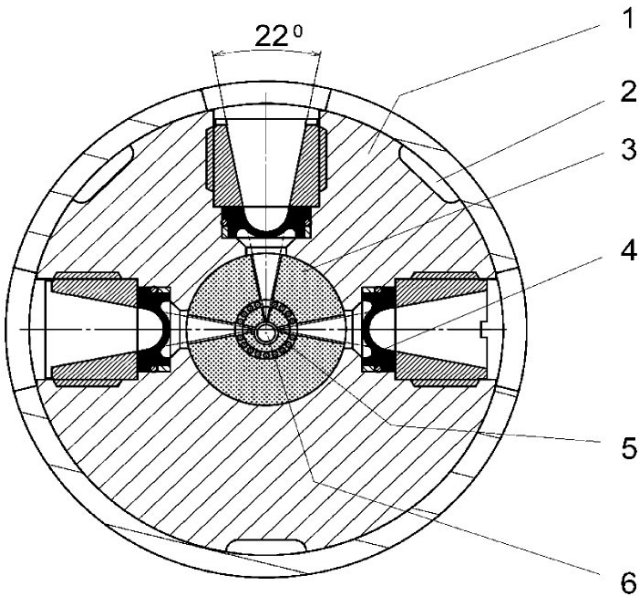

1. HP vessel main part (spiece 8 in Fig. 2.6).

2. Water cooling circulation (spiece 10 in Fig. 2.6).

3. Alumina insulating pieces.

4. Beryllium window.

5+6. Furnace and internal cell.

FIG. 2.8 - Drawing of the general windows geometry (two on the beam axis, and one at 90°). The setup is drawn with Be windows (0.8 mm Be window in our case).

In order to minimize the elastic scattering radiation, we choose to place the fluorescence window at 90 ° of the incident beam, as shown in the sectional drawing 2.8. There is no elastic scattering parallel to the polarization of the beam but (on the CRG-FAME-BM30B at the ESRF) is perpendicular to the axis of the incident beam because the polarization at the exit of the electron storage ring is perpendicular to the tangent of the ring. By positioning at 90°, we thus suppress the elastic diffusion. FIG. 2.9 shows a Be window used in my experiments.

FIG. 2.9 - Picture showing the 0.8 mm Be window, Which install 3 of them in the area 4 in FIG. 2.8

2.2.5 The thermocouples

We manufacture K-type thermocouples using two wires (FIG. 2.10), one in chromel (alloy of nickel and chromium), and the other one in alumel (alloy of nickel, 5% aluminum and silicon). The principle of measuring thermocouples is based on the Seebeck effect. In theory, two different metals are connected by two welds at different temperatures, which generates a potential difference depending on the temperature difference between the two welds. In our case, a single weld between the alumel and the chromel is placed where the measurement of the temperature is required, and the electronics of the eurotherm plays the role of compensation of the "cold" weld. K-type thermocouples allow measurement over a wide temperature range (-270 ° C to 1372 ° C); the accuracy obtained with this system is 0.1% in absolute value.

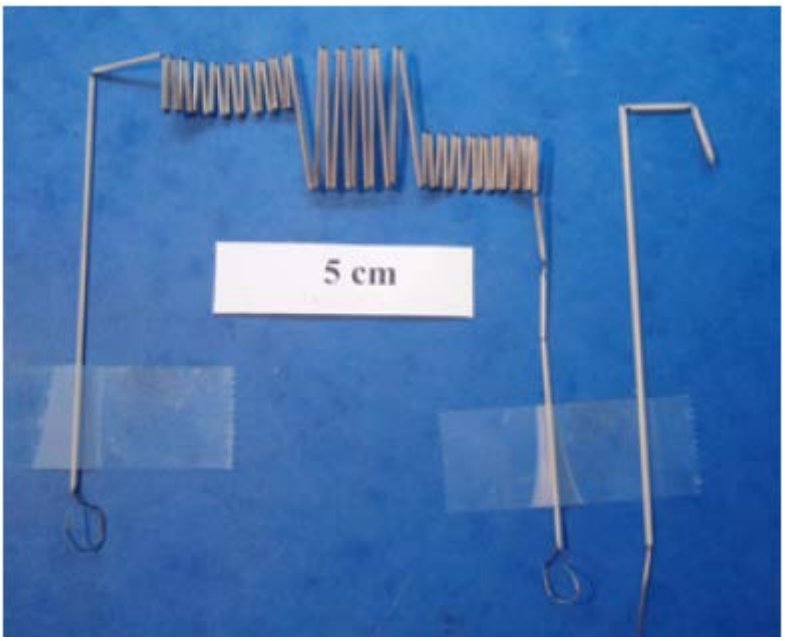

FIG. 2.10 - Photograph of an oven (left) and a thermocouple (right) used in our experiments.

To isolate the two wires of the thermocouple, the weld of which is placed near the sample zone, the latter are slid into alumina rods (FIG. 2.10). The two thermocouples as well as the heating system are placed as close as possible to the sample space, in order to have a reading and a control as accurate as possible of the temperature. The order of magnitude of the distance is in both cases of 5 mm. Despite these precautions, there is a temperature gradient between the one measured by the thermocouples and that actually applied to the sample. This gradient depends on the geometry of the autoclave used, in particular the windows, constitute a cold zone. Thermal exchanges are also favored by the applied helium pressure. It is possible to measure this gradient for each autoclave by indirect measurements of temperature, in particular measurements of the density of pure water, by its absorption of X-ray beam. In the next chapters, it will explained how this gradient probem for water and other fluids in the next chapters. Finally, since the thermocouples and oven used in our

experiments have a limited life time (between 3 and 10 weeks of experiments), it is particularly interesting to make them by myself.

2.2.6 The inner carbon cell

The internal cell is a tube with two pistons located on both sides (FIG. 2.11). The choice of the material for these elements will be discussed in section 2.3.6, Indeed, as for windows, the internal cell used for each type of experiment must modify as little as possible the beams which pass through it. For example, the minimum absorption will correspond to a minimum wall thickness, and a polished surface will allow the passage of a visible beam. It is also important to ensure that the internal cell is chemically inert (no interaction with the beam) during temperature and pressure experiments.

O-rings (viton or silicone according to experience) can be inserted into grooves in the outer part of the pistons. O-ring insure that no leaks of the medium get out from the cell when it's under the pressure. It can also be obtained by small differences in diameter between the piston and the cell (of the order of 5 μm). The pistons allow the transfer of pressure between the sample space and the environment gas (during compression and heating of the sample, as well as when cooling down).

FIG. 2.11 - Photograph of a vitreous carbon cell used for absorption measurements X (absorption and fluorescence). The pistons are shown with length 38 mm and 28 mm.

There are two main experimental configurations of the internal setup, corresponding to two types of samples: either liquid metals or aqueous samples (FIG. 2.11). In the former case, the melting liquid expands upwards in the cell in an expansion canal, however remaining in the heated volume to avoid any partial solidification of the sample. The same canal is also used to trap the escaping metallic vapor that could otherwise deposit elsewhere in the vessel, on the beam pathway (HP windows, heater, etc)[2]. Such experimental configuration is used, for example, for EXAFS investigations of liquid metal.

For the aqueous samples, the main cylindrical sapphire tube is the same, but a pair of bellows are placed at the bottom that transfer pressure to the sample. This element enables to isolate the aqueous sample from the He atmosphere. Furthermore, it acts as a reservoir, since its contact with the water cooled HP vessel cools it down and allows the liquid inside to remain at the ambient density. With such a set-up, pressure and temperature prospection of the phase diagram with strong variations of the sample density can be achieved in the (30 - 600 °C) and (1 - 2000 bar) ranges[2].

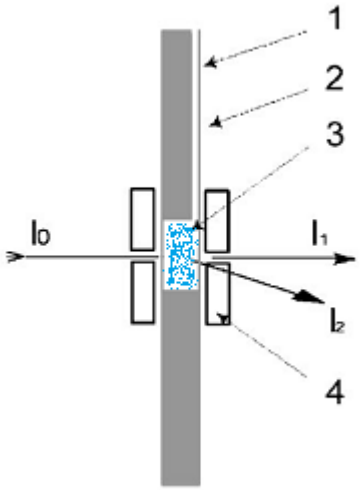

FIG. 2.12 - Sketch of the two internal set-up. I_0, I_1, and I_2 correspond to the incident, transmitted, and fluorescence (or scattered) beams for aqueous samples. (1) Cylindrical internal cell with two inner tubes (in gray) above and below the sample. (2) Canal for the expanding sample. (3) Liquid metal sample. (4) Furnace.

2.3 Experimental set-up adaptation

Different parameters determine the choice of material, whether for windows or internal cells: The lowest possible signal disturbance, maximum transmission of the beam (because, a low fluorescence in number of photons is measured in absorption X). In the case of the internal cells a minimal reactivity between the sample and its container, in particular at high

temperature. In this section, I make the general remarks concerning the choice of materials, and I briefly summarize these elements in each section adapted to the techniques used.

Crystallinity of materials It is important to describe the materials used in the case of X-ray absorption, It is essential to avoid the monocrystalline materials which produce Bragg diffraction peaks which are a function of the energy of the incident beam and which will particularly interferes with the measured signal. Measurements only require materials that are transparent to visible radiation.

Beam transmission The transmission of the beams naturally depends on the material traversed, but also on the incident energy. The materials conventionally used in the study of high temperature and high pressure fluids are diamond, quartz, or silica. Beryllium is more rarely used because of its machining difficulties. These materials satisfy the criteria mentioned above, mainly the absorption of the beam and the strength considering the pressure, I chose to represent the variation of the transmission of the beam as a function of the incident energy a beryllium and carbon. Thus, I will list the mass attenuation coefficient for carbon, beryllium, and other materials used in XAS measurements in chapter 3.

Throughout the range of energy represented (including XAS measurements with incident energies up to 15.4 KeV), The material having the best transmitted fraction is beryllium. Monocrystalline beryllium is expensive, this material can be used in the case where a polycrystalline material is required, in the case of XAS. Beryllium ca not be used for internal cells, we have chosen to use beryllium for windows, and more precisely, polycrystalline beryllium manufactured by Brush Wellman by hot pressing.

The second material with a low absorption in our case is the carbon, It is therefore interesting in our study can be used. For the amorphous materialsto study by XAS, vitreous carbon internal cells are adapted to the required conditions. Indeed, experimental tests have shown that the vitreous carbon is inert, in particular respect to phenomena of precipitation, dissolution, etc. In summary, the materials used in the case of X-ray absorption spectroscopy are therefore beryllium and vitreous carbon.

X-Ray Absorption Spectroscopy. X-ray absorption measurements require the passage of an incident beam transmitted with characteristic dimensions of (200 μm X 300 μm) on the CRG-FAME Beamline-BM30B at the ESRF. In the case of transmission measurements, the window size can be small. However, for fluorescence measurements, a compromise between a large collecting angle (to improve signal quality) and an angular opening allowing the system to resist the applied pressure must be considered. This led us to choose an aperture angle of 22 ° for fluorescence window. For the tranmission windows, we have chosen identical windows for experimental flexibility, In particular, have only one type of window to be manufactured, and be able to exchange them if necessary. Same Be windows have been used for Conventional XAS and also FDMNES-XAS measurements.

Choice of windows The material with minimal absorption of the X-ray in the energy range of synchrotron radiation is beryllium, which also has good mechanical properties. More precisely, extruded beryllium of the PF60 type is used in our case. A dome shape is used such configuration has a high resistance of pressure. The thickness is almost the same (2.5 to 0.8 mm depending on the applied pressure) for the entire angular opening, and the solid angle of detection is 22°.

Choice of the internal cell In my case of measurement, we use a vitreous carbon cell (FIG. 2.11). On my study tests were carried out using carbon cells. In contrast to previous tests on alumina Al_2O_3, showed that alumina absorbed much more radiation.[31] In this case, it had a tendency to be porous, and to let helium pass into the solution. Whereas, the vitreous carbon and the pistons are also porous, but in a smaller proportion. The inside diameter of the cell is 4 mm, and the outside diameter 6 mm. The cell length is 100 mm, the wall thickness is 0.5 mm, but around 0.3 mm with the beam path (along beam axis).

Finally, In this chapter, I focused on the concepts of XAFS and XAS methods on both techniques, Absorption and fluorescence. I described the autoclave we used in all our experiments. It was designed for XAS measurements and for other types of experiments *i.e.* X-ray diffraction, Raman scattering, SAXS, etc. Temperature and pressure regulation vary independently making possible to reach a high temperature and pression precision . Crystal analyzer spectrometers (CAS) based on a Johann-type geometry have been developed for multi purposes, the most important is to get more accurate data than in conventional fluorescence detectors. Moreover, technical details around materials (types, shapes, functions, etc.) used during the experiments.

2.4 Summary (English)

In this chapter, I have illustrated the X-ray Absorption Spectroscopy (XAS) theoretically and the application in the field of my study with two main parts of XAS spectra which are XANES and EXAFS. HERFD-XAS coupled with Crystal Analyzer Spectrometer (CAS) based on a Johann_type geometry used in this work is presented. I described the autoclave we used in all our experiments. This autoclave, originally designed for absorption measurements X, has been adapted over time and for other types of techniques, namely X-ray diffraction at small and large angles, optical Raman, etc. High precision in temperature and pressure regulation is possible by separating the heating and pressurizing system, which can thus vary independently. High precision in temperature and pressure regulation is possible by separating the heating and pressurizing system, these two parameters thus being able to vary independently.

2.5 Summary (French)

Dans ce chapitre, Je présente la spectroscopie d'absorption des rayons X (XAS) d'un point de vue théorique ainsi que son application dans le domaine de l'étude sur les fluides supercritiques avec les deux parties principales des spectres XAS c'est à dire le XANES et l'EXAFS. Une attention particulière est donnée à la spectroscopie haute résolution HERFD-XAS et au développement du Spectromètre associé utilisant la géométrie de type Johann. Je décris également l'autoclave que nous avons utilisé dans toutes nos expériences. Cet autoclave, conçu à l'origine pour des mesures d'absorption X, a été adapté au cours du temps pour d'autres types de techniques, à savoir la diffusion X aux petits et grands angles, le Raman optique, ... etc. Une grande précision dans la régulation en température et en pression est possible grâce au découplage du système de chauffage et de mise sous pression. Ces deux paramètres pouvent ainsi varier de manière indépendante.

Chapter 3: *Results*

3. Results

3.1 Density measurements

3.1.1 Mass attenuation coefficient calculations (μ/ρ)

The sample density can be estimated using transmission measurements. The sample absorbance A is calculated as the logarithm of the ratio between the incident and the transmitted intensity $I_t/I_0 = \exp[- (\mu/\rho) x]$. The Beer-Lambert law (or Beer's law) is the linear relationship between absorbance and concentration of absorbing species and it is usually written as:

$$Absorption = \frac{\mu}{\rho_E} \rho_{material}.X + A \tag{16}$$

μ/ρ is the mass attenuation coefficient at a given energy (cm^2/g), $\rho_{material}$ is the density of the solution (g/cm^3), X is the sample thickness (cm), and A is the baseline of experiment set-up. Transmission experiments can be achieved by placing two detectors (usually ionization chambers) in the beam path; one before (I_0) and one after the sample (I_t). The attenuation of the X-ray beam in the transmission mode is related to the sample thickness X, and the intensity of the incident beam, and (I_0). The baseline (A) of the experiments depend on the type of material on te beam bath and incident energy.

The absorption is a function of the density *i.e.* ∫ abs. = f(ρ). A part of beam is absorbed by materials on the beam bath *i.e.* Be windows, air, etc, it depends of the thicknesses of these materials which in turn implies plays the role of the flux (number of photon). The mass attenuation coefficient, μ/ρ, and the mass energy-absorption coefficient, μ_{en}/ρ, are basic quantities used in calculations of the penetration and the energy deposition by photons (x-ray, γ-ray) in biological, shielding and other materials.

The μ/ρ values are taken from the current photon interaction database at the National Institute of Standards and Technology, Table 2 shows the values of μ/ρ theoretically used at certain energies. I obtained two values using two method of calculations (Hephaestus and Illinois institute of technology). At increasing the energy, the μ/ρ decrease because the intensity. Table 2 shows the μ/ρ values used in the experiments at different energies.

Table 2: X-Ray Mass Attenuation Coefficients (μ/ρ) for the elements have used in the experiments at different energies given in two databases (Hephaestus and Illinois).[8,9]

	15.044 KeV			15.0 KeV			13.7 KeV			13.5 KeV			15.4 KeV	
Elements	**Hef.**	**ILL.**		**Hef.**	**ILL.**		**Hef.**	**ILL.**		**Hef.**	**ILL.**		**Hef.**	**ILL.**
C	0.1139	0.1052		0.1147	0.106		0.1433	0.132		0.1486	0.137		0.1077	0.0997
Be	0.0956	0.0884		0.096	0.0887		0.1097	0.1006		0.1123	0.1029		0.0926	0.0858
H	0.3760	0.398		0.376	0.3979		23.197	0.397		0.379	0.3968		0.376	0.398
O	1.8210	1.7211		1.836	1.7351		2.369	2.2394		2.470	2.3357		1.707	1.6137
He	0.2090	0.2165		0.209	0.2166		0.215	0.2198		0.216	0.2204		0.208	0.2158
Na	4.654	4.5624		4.694	4.6024		6.126	6.0377		6.397	6.3108		4.347	4.2556
Cl	17.692	18.008		17.843	18.163		23.197	23.688		24.204	24.728		16.532	16.81
Br	111.012	108.68		111.85	109.46		140.96	136.48		146.34	141.39		104.53	102.59
Cs	60.580	60.353		61.06	60.833		77.617	77.729		80.70	80.879		56.880	56.652

The calculations of μ/ρ which is depends on both an incident energy (ev) and on the density of material (g/cm^3), have been carried out by two methods in a unit cm^2/g. The first one was performed using Hephaestus software Ifeffit set-up, we calculate an absorption coefficient μ (cm^{-1}), then divide it by the density of material at ambient condition which have collected by O. Sohnel and P. Novotny[124] and by Ivan D. Zaytsev and Georgiy G. Aseyev[125]. The second one was performed calculating μ/ρ of the elements at given energy by Illinois institute of technology[9], number of sample moles, and atomic mass (amu) which has been performed by using equation (17):

$$\frac{\mu}{\rho}(A,B,...) = \frac{\sum \frac{\mu}{\rho}(X_i) \times M_i}{\sum M_i \times X_i} \qquad (17)$$

Whereas, Mi is the molar mass (g/mol), X_i is the number of moles, A, B, ..., are solution components.

3.1.2 Absorption measurements by classical XAS

X-ray absorption spectroscopy (XAS) were often used in the literature to study supercritical fluids, such as supercritical water and "aqueous solutions". supercritical water (Pc = 220.6 bar, Tc = 273.95 °C, and critical density ρc = 0.322 g/ml) and aqueous solutions studied by XAS. The measurements of density is a good study molecular dynamics in hydrogen bonded liquids such as water, because the water behavior is changing with high pressure and high temperature when exposed to an x-ray coming from the synchrotron with an energy.[80,126]

The HP/HT cell used for these experiments has been described in details by Testemale *et al*.[2] A schematic view of the set-up is shown in FIG. 1. The general principle consists of a helium pressurized autoclave, and an internal sample container embedded in the heater. The main feature of the cell is then that the temperature and the pressure can be adjusted independently and are both stabilized by two independent pressure and temperature regulation devices.[123] For this particular study, the internal cell was in glassy carbon with a wall thickness machined down to 100 μm at the X-ray beam position, in order to limit the absorbance of the set-up as much as possible. The cell consists of an external water-cooled high-pressure vessel equipped with three 0.8 mm thick beryllium windows enabling collection of fluorescence and transmission signals at a maximum pressure of ~600 bar. The sample was contained inside a glassy carbon (1.42 g/cm^3) tube with an internal diameter of 4 mm. The pressure is applied to the sample by two glassy carbon pistons, using helium as a pressure medium. The glassy carbon tube is placed inside a small cylindrical resistive heater; the heater and tube are then installed inside the high-pressure vessel.

All eperiments have been performed at European Synchrotron Radiation Facility (ESRF) storage ring in Grenoble is a 6.03 GeV ring and was operated in 7/8 multi-bunch mode with a maximum current of 200 mA. X-ray absorption spectroscopy experiments were performed on the CRG-FAME beamline (BM30B). FAME is a bending magnet beam line with a double crystal Si(220) monochromator, and an energy resolution of 0.46 eV, *i.e.* (ΔE/E) of 0.691 at the Br K-edge. The setup at the FAME beam line has been described by Proux et al.[121,127]. Spectra were recorded in transmission mode (~2 hours/scan data collection time) at different incident energies, using a double-crystal Si(220) monochromator[127]. The size, around 300×200 μm^2 (H×V, full width half maximum values), and the position of the X-ray spot on the sample were kept constant during the data acquisition. The incident and transmitted beam intensities, I_0 and I_1, were measured with Si diodes. The full beam delivered by the bending magnet source was focused in the horizontal plane by the 2nd crystal of the monochromator and by the 2nd Rh-coated mirror in the vertical plane. Finally, a feedback system was used to maximize the output of the two-crystal X-ray monochromator.[121]

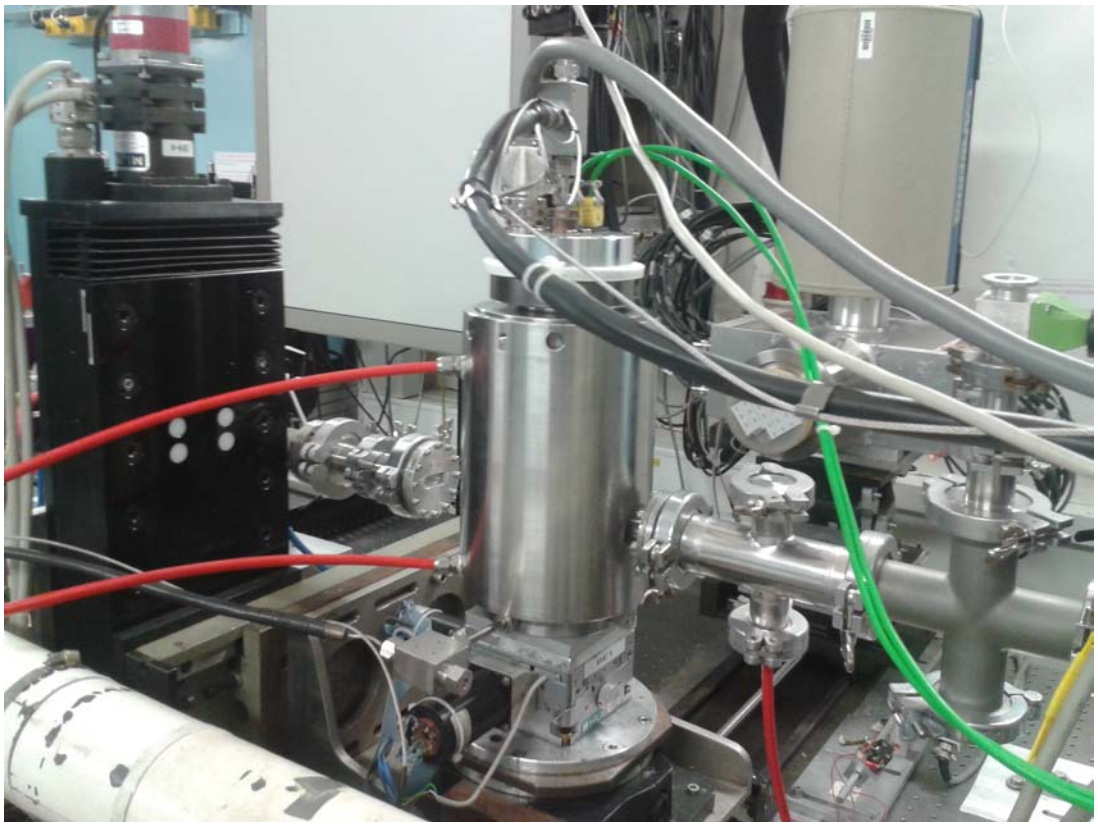

FIG. 3.1 - Setup of classical XAS measurements in the experimental hutch of FAME beamline "BM30b" at ESRF synchrotron.

The following Table (3) illustrates the measured absorption of each material on the beam path of an experimental set-up at given energy. It depends on the response of the two detectors I_0 and I_1. They are arranged as follows: the beamline empty to calculate the absorption of beryllium windows of the beamline between 1_0 and I_1, the HP (0.8 mm) and thermal screens (25 µm) beryllium windows of the autoclave, then we put the glassy carbon cell, and then 300 bar of Helium, after that we put H_2O.

Table 3: Absorption at each points at the setup of the experiment (from incident to transmitted beam) as well as the aqueous solution in autoclave under 1 bar and/or 300 bars pressure at 13.7 KeV.

# of Scan	Abs. @ 13.7 KeV	Be(20µm) (Double)	Air Line	Air Auto	Be(auto.) 0.8 mm (Double)	Be(screen) 25 µm (Double)	He 1b	He 300b	C. Cell (Double)	Sample
1	-1.116	√	√							
2	-0.987	√	√	√	√					
3	-0.975	√	√	√	√	√				
4	-0.986	√	√		√	√	√			
5	-0.943	√	√		√	√		√		
6	-0.939	√	√		√	√	√		√	
7	-0.04	√	√		√	√		√	√	$\sqrt{}_{H2O}$

With an absorption measured values for some materials in the beamline at given energy, the Table 4 illustrates the comparison between the experimental and theoretical calculation for some materials and solutions.

Table 4: The experimental and theoretical absorptions for the materials and solutions at 13.7KeV.

Absorption / **Material**	**Experimentally**	**Theoretically**
4 mm of H_2O	0.8545	0.8583
0.3 mm of Carbon x 2	0.0477	0.043
0.825 mm of Beryllium x 2 } Autoclave 0.3 mm of Carbon x 2 }	0.177	0.185
0.825 mm of Beryllium x 2 of Autoclave	0.141	0.107
Be (screen) 25µm x 2	0.012	0.016

The calculation of densities by classical XAS have been perfored using several methods under isobaric processes at given incident energies. The final method described bellow has been adapted for water and aqueous solutions, the methods were used as shown in bellow:

1) We get the absorption measured values of fluids as a function of temperature, then we normalize the date using equation (18):

$$Normalization = \frac{[abs2(T)_{Liquid}(\exp.\_300b)] - [abs2(emptycell\_300bHe;30°C)]}{[abs2_{Liquid}(\exp.\_300b;30°C)] - [abs2(emptycell\_300bHe;30°C)]} \quad (18)$$

Then, we multiply the normalized data by the density of water at ambient condition. This method have errors at high temperature, the value of densities obtainedis lower than real densities, and it is not possible to apply the same method to other solutions because the density is higher than water at ambient condition.

2) We get the absorption measured values of fluids as a function of temperature, then we apply the measured base line (A) with the sample thickness (X) fixed at 4mm. This method have errors in the value of A, because this value (taken at 25°C and isobar value) and the value of densities at high temperature are lower than real densities, as well as, the pressure regulation has an error at high pressure.

3) We get the absorption measured values of H_2O as a function of temperature, using an equation (16), we calculate X and A with comparison the first ansd an end point of temperature, then, we apply these values on the data measured. This method have errors in the value of A and X, because these values are faraway than measured *i.e*. X = 4.4 mm. The end value of expected density is higher than real temperature, this is not logic.

4) We get the absorption measured values of H_2O as a function of temperature, using the PyMca software. Then we can get the shift of temperature by derivative carve. we have taken this shift and add it to the end point of temperature. Then, we calculate the X and A by an equation (16) between the first and end point of temperature. This method have errors in the value of A and X, because these values are faraway than measured *i.e*. X = 4.4 mm. The end point of expected density is higher than real. As well as, when doing the shift must be subtracted not add, according to the thermocouple in autoclave is far a bit than center of cell.

5) We get the absorption measured values of H_2O as a function of temperature, getting the shift in temperature using PyMca software. Then we subtracted the shift of endpoint measured. Then, we calculate the X and A using en equation (16) between the first point and end of temperature. This method have errors in the value of A and X, because these values are faraway than measured. But this method has less error than those above mentioned.

6) We get the absorption measured values of H_2O as a function of temperature, getting the shift in temperature with the minimum value of the derivative curve calculated by the PyMca software. Then, we subtracted the shift of endpoint measured. Then, we manipulate the values of X and A, we tried to have X value fixed as much as possible and A calculated at

ambient condition by equation (16). In the case of the first and end points, they have not same with theoretical values, we manipulate them to be adjusted. The end point of this method is lower than the measured one as shift value calculated with the logic value of thermocouple. This method has been adopted to apply it for all aqueous solutions in all our experiments.

3.1.3 Results on pure water (H_2O)

X-ray absorption measurements in Milli-Q water were performed as a function of temperature from 30 to 500°C at pressures 28.0, 30.0, 34.5, and 40.0 MPa in order to calibrate the experimental setup. The density of water at this conditions changes from liquid-like to gas-like crossing the critical isochore curve (0.322 g/cm^3) above the critical T-P point as shown in FIG. 3.2. According to the equation (16), at constant energy (13.5, 13.7, 15.0, 15.4 keV), the total absorption measured in transmission mode is a function of the experimental set-up absorption (A= baseline, which takes in account te absorption from beryllium windows, sample container, air and helium beam path), sample thickness and sample density. During heating, only sample density is changing and thus the absorption is appropriate for the measurements of density evolution. The comparison between theoretical and experimental density of pure water was then used for temperature calibration. To recalculate the "real" temperature (T_{real}) at the working part of the cell (*i.e.* at the level of the "cold" optical windows) was recalculated from the experimental pure water density. Temperature gradients correction by linear fit between T_{real} and T_{cell} (*i.e.* the regulation temperature value) measured in our study are close to those observed previously[128] (FIG. 3.3) . However, in this study detailed analysis of these gradients has been performed (FIG. 3.3).

During heating experiment, the absorption was measured by 7 points from 30°C to 350°C (heating step of ~46°C), and by 151 points from 350°C to 500°C (heating step of 1°C). Each absorption measurement was performed after the stabilization of temperature at ±0.04°C and pressure at ± 0.15 bar at least during 10 seconds.

Temperature gradients are illustrated in FIG. 3.3. This gradients can be explained by 1) heat transfer and dissipation by materials used in our experimental set-up (beryllium windows, glassy carbon tube, pressurized helium, ceramics of furnace, etc), 2) the design of the furnace containing three optical non heated windows, 3) water properties. Heat loss from the set-up (1 and 2 listed above) is expected to increase linearly with temperature. Nonlinear dependence of T_{cell} - T_{real} value on density is observed for all pressures. These data reflect thermo physical properties of water. Despite the fact that heat transfer critical enhancement and possible heat transfer deterioration are difficult to be quantified from our measurements, some analogies can be drawn. Thus for example, the T_{cell} -T_{real} minimum roughly overlap with the maximum of specific heat capacity of H_2O (FIG. 3.4) when approaching the pseudocritical isochore (ρ_c = 0.322 g/cm^3) and thus this minimum seems to correlate with critical heat transfer enhancements. These new data allow to validate our experimental setup and to estimate the temperature gradients for other aqueous solutions. For these simple linear approximation was applied (see FIG..3). The maximum temperature errors associated related to nonlinear temperature gradients are estimated to be 10 °C. The linear equation used for

temperature correction and comparison between corrected and real temperatures are given in FIG. 3.3. These equations were applied for temperature correction in other aqueous solutions.

The base line A and internal diameter X of carbon cells are expected for water as a reference by several methods as mentioned in the previous section (section 3.2). One of them has been adopted method to expect the diameter X and base line A. The values must be not faraway than measured and logically must be the last point of T. real less than T. measured. Form equation (16), we calculate an experimental density taking in acoount the A and X expected values. These values of density are compared with same theoretical density values by NIST database[1], then we can estimate the real temperatures.

Three apertures are present in the heater and vessel for the incident, transmitted and fluorescence beams. These apertures induce a small temperature difference between the value given by the thermocouple close to the furnace and the real sample temperature. Although the thermocouple sits near the sample, it is placed outside the glassy carbon tube and not exactly at the beam position. In order to obtain the temperature of the fluid at the beam location, the temperature was calibrated by measuring the density of pure water by its X-ray absorption[129–131], and then retrieving the temperature of the solution at the beam position using the well-known equation of state of pure water (NIST database)[1]. After estimation the real temperature, we get the parameters of a linear equation by the fit of measured and real temperature. The FIG. 3.3 shows the fit curve between measured and real temperature.

The experimental critical points shown in FIG. 3.2 matched the critical isochore curve exactly with the real temperature calculated. We calculated the density of water and expecting for solutions based on the reference (water) at same pressure and energy for same experiment. In FIG. 3.2, for pure water at 280 bar, the point on critical isochore curve at 59.4 bar and 22.05 °C from the theoretical critical point of H_2O, while at 300 bar, the point on critical isochore curve at 79.4 bar and 28.05 °C from the theoretical critical point of H_2O, also at 345 bar, the point on critical isochore curve at 124.4 bar and 44.05 °C from the theoretical critical point of H2O, and at 400 bar, the point on critical isochore curve at 179.4 bar and 64.05 °C from the theoretical critical point of H_2O. From the calibration of water temperature (section 2.1) to get the real temperature, we can estimate for the solutions as well by extract the linear fit parameters between a measured temperature and real. The difference between the measured and real temperatures is showed in FIG. 3.3. It is clear that the temperature difference at first point of T. measured is 0 °C and the last measured is 33 °C.

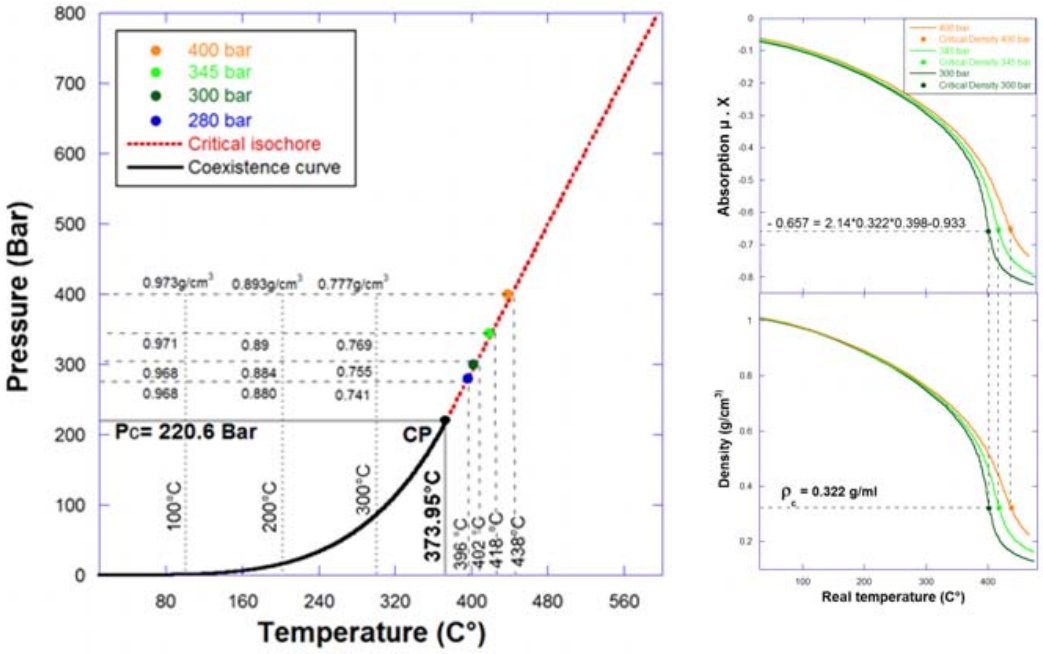

FIG. 3.2 - Liquid gas coexistence curve and critical isochore for pure water, calculated according to Ref.[1] (left). The solid lines mark the boundaries of the supercritical domain, the horizontal dashed lines the experimental isobars and the vertical ones the corresponding values of the temperature. Experimental absorption and density for pure water as a function of temperature " T without gradient temperature for isobaric process (right). Solid colour points are experimental T-P values at ρc extracted from absorption at given energy 13.7 KeV.

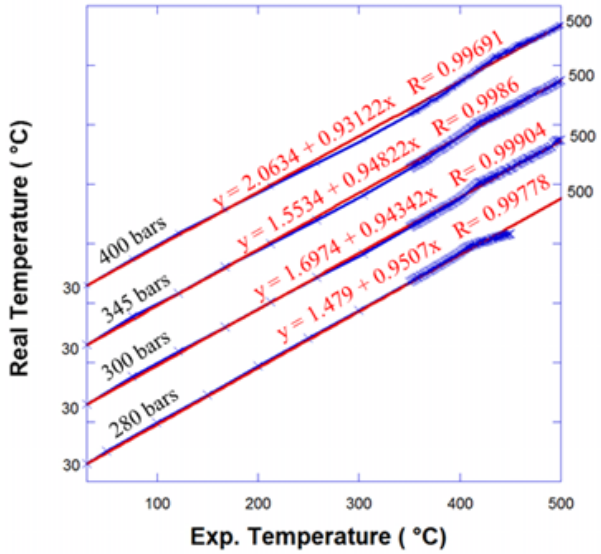

FIG. 3.3 - The fit of real and experimental temperature in pure water at different pressures (280, 300, 345, 400 bars) . Temperature different between cell (T_{cell}) and real (T_{real}) values as a function of experimental density. Measurements are offset for clarity.

The temperature is extracted from the experiment is measured temperature *i.e.* gradient temperature, technically, the foil which is responsible to heat the solutions *i.e.* thermocouples, is surrounding at top and bottom parts of a carbon cell inside the autoclave, so for this reason the temperature at the centre of solution must be less than thermocouples measurements. The temperature different increases up to around 350 °C then decreases up to 403 °C for 300 bars and 345 bars, and decreases up to 414 °C for 400 bars in real temperature values. It should be noted here that the conductivity decreases up to 350 °C then increases up to the critical density for their pressures, then start to decrese as a function of temperature.

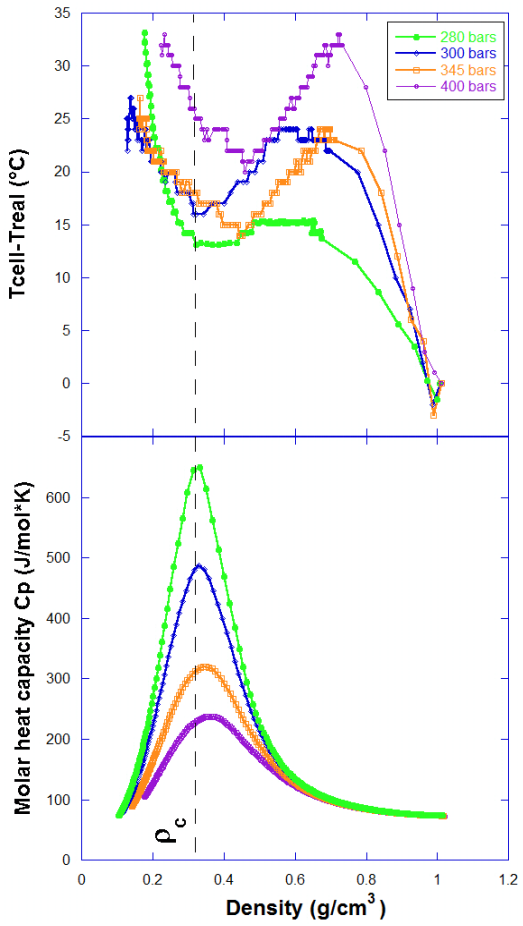

FIG. 3.4 - Temperature difference between T_{cell} and T_{real} values measured in pure water (up) in comparison with it's specific heat capacity (down) in isobaric conditions as a function of density. Straight line corresponds to critical density.

The temperature extracted from the experiment is measured temperature *i.e.* gradient temperature, technically, the foil is responsible to heat the solutions *i.e.* thermocouples, is surrounding at top and bottom parts of a carbon cell inside the autoclave, so for this reason the temperature at the centre of solution must be less than thermocouples measurements. The temperature increases value around 350 °C then decreases up to 403 °C for 300 bars and 345 bars, and decreases up to 414 °C for 400 bars in real temperature values. It should be noted

here that the conductivity decreases up to around value 350°C then increases up to the critical density for their pressures, then start to decrese as a function of temperature.

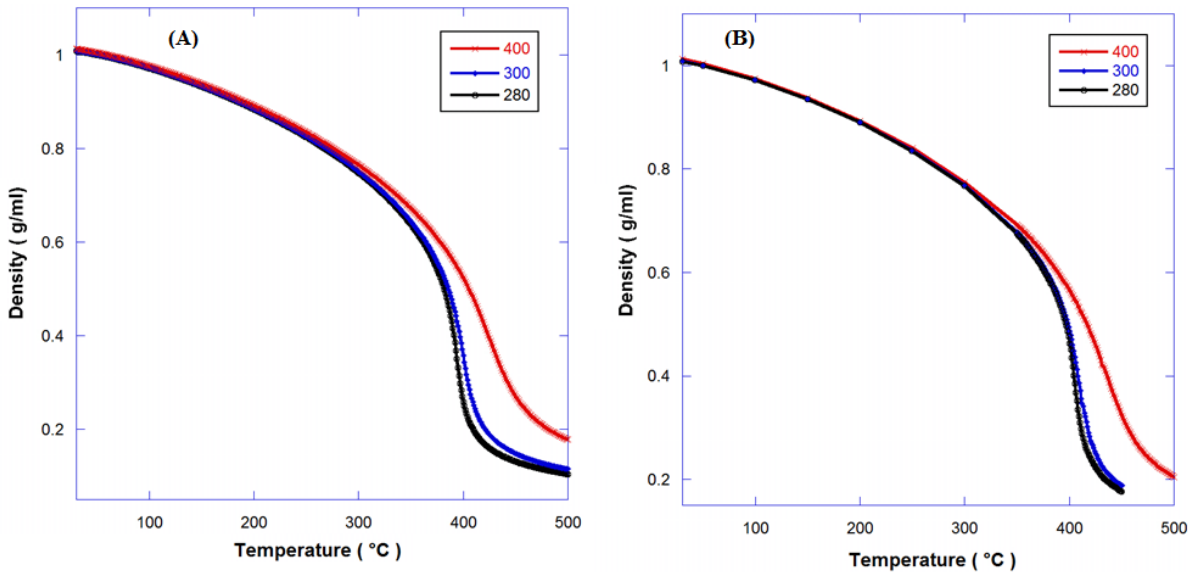

FIG. 3.5 - A) Theoretical density has taken from NIST[1] and B) Calculated density of pure water as a function of temperature extracted from X-ray absorption experiments at (280, 300 and 400 bar) done at 15 KeV.

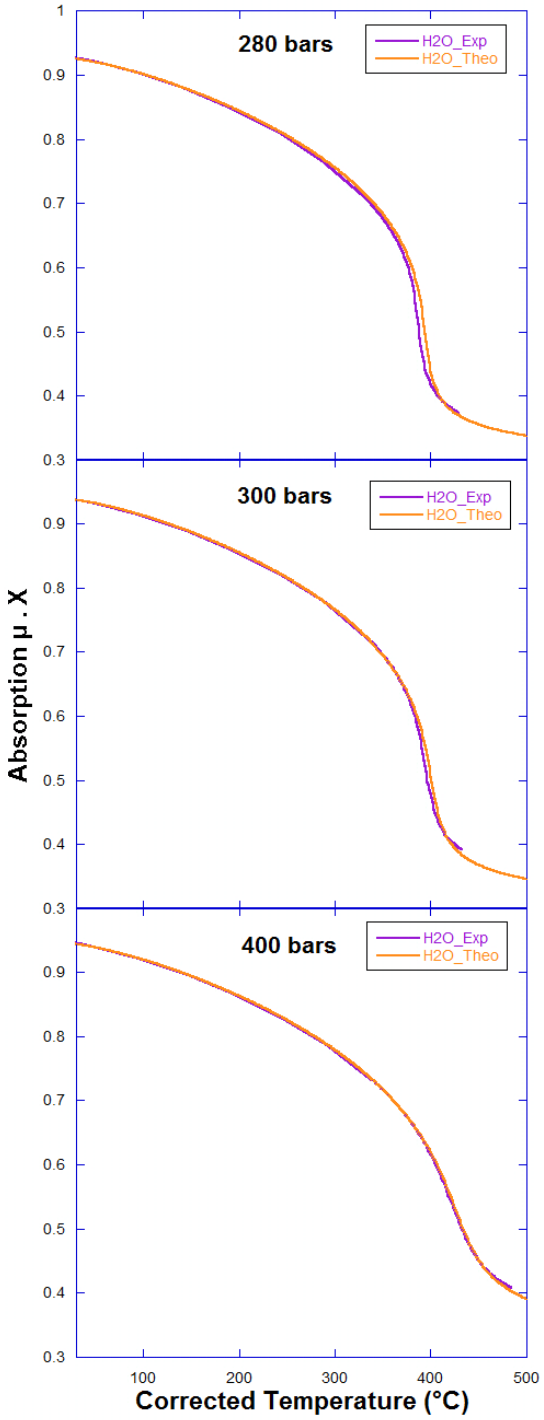

FIG. 3.6 - Experimental and theoretical fit comparison X-ray absorption of water at 280 bras, 300 bars and 400 bars at 15 KeV. The best base line (A) expected is 0.2563 of 280 bars, 0.2666 of 300 bars, and 0.27127 of 400 bars. The best sample thickness is 0.398 mm for all pressures used. (Theoretical extracted values from NIST database [1]).

A reference mili-Q water have been performed at several pressures as shown in FIG. 3.6, on isochore curve, the critical points are fixed at same value of critical density of water 0.322 g/cm^3. The points measured have been done with 7 points from 30°C to 350°C, and 150

points from 350°C to 500°C. The theoretical critical density value of water at 280 bars is 0.322 g/cm^3 which has been recorded at temperature 395 °C, the experimental density value has been observed at temperature 406 °C, ΔT = - 11 °C; Likewise at 300 bars, the theoretical critical density value of water bars is 0.322 g/cm^3 at temperature 402 °C, the experimental density value has been observed at temperature 411 °C, whereas ΔT = - 9 °C; as well as, at 400 bars, the theoretical critical density value of water bars is 0.322 g/ cm^3 at temperature 438 °C, the experimental density value has been observed at temperature 446 °C, whereas ΔT = - 8 °C.

Table 4: Measured and expected values of X and A at certain energies and pressures for XAS experiments - the expected values from H_2O measured.

Experiment	Energy (KeV)	Press. bar	A Measured	A Expected	X (cm) Expected	Comments
Feb. 2016	15.044	300	1.547	1.5108	0.398	Measured at 300 bar and 30°C; Δ abs. He (between 1b and 300b) = 0.042
June 2016	15	280	0.304	0.2563	0.398	Measured at 300 bar and 30°C; Δ abs. He (between 1b and 300b) = 0.029
		300		0.2666	0.398	
		400		0.27127	0.398	
Sep. 2016	13.7	300	- 0.8935	- 0.93334	0.398	Measured at 300 bar and 30°C; Δ abs. He (between 1b and 300b) = bar
		345		- 0.9301	0.398	
		400		- 0.92626	0.398	
Dec. 2016	13.5	300	1.2877	1.2853	0.395	Measured at 300 bar and 30°C; Δ abs. He (between 1b and 300b) = 0.0378 bar
	15.4	300		1.3648	0.393	

FIG. 3.7 shows the temperature as a unction of density of water for theoritical and experimental values, we observed that there is a fit in both values after corected the tempereture values. In the liquid phase the density decreases rapidly with the temperature at any given pressure as shown in FIG. 3.7.

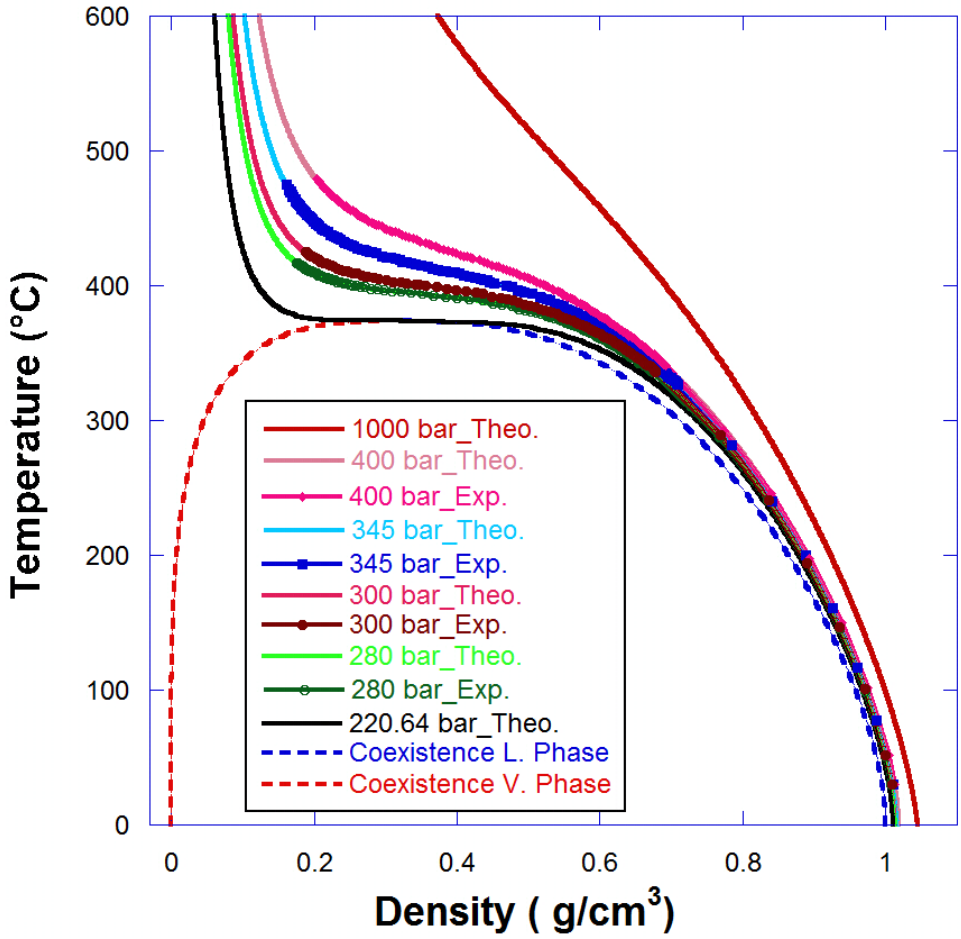

FIG. 3.7 - T–ρ diagram for H_2O. The solid curves represent an experimental and theoretical p–ρ isotherms at selected temperatures. The dashed curve represents the coexistence curve bounding the region of vapor–liquid equilibrium. The critical point is located at the top of the coexistence curve.

3.1.4 Results on NaCl electrolytes

NaCl is the principle solute in the water at the hydrosphere, and the PVTx properties of the binary system NaCl-H_2O are use to modeling and understanding of the majority of these waters. The properties of the two-phase surface of this important system are of particular importance to the understanding of hydrothermal processes associated with magmatic activity, because they represent the extreme boundaries of P and T for which hydrothermal circulation can occur. Density controls buoyancy and relative vertical stability of fluid masses. This study presents an explanation of ion-pairing at supercritical conditions and a compilation of the density coexisting liquids and vapors on the two phases surface of the systemNaCl-H_2O for the temperature range 30 °C to 500 °C under isobaric process 280, 300, 345 and 400 bar. The present work uses an conventional XAS with temperature from ambient to supercritical conditions at different concentrations. This study will give me a strong feedback of NaCl behavior at supercritical condition because there are several studies published such as (James

L. BISCHOFF and Kenneth S. PITZER). Properties of the system NaCl-H_2O system over the range of interest also have general implications for theoretical studies of ionic salts. Over the P-T range of interest the two phases surface of NaCl-H_2O undergoes a rather complex geometric change from below the critical point of pure water to above it's critical point. Accurate theoretical modeling of this system is a particular challenge[73,74,86,96,132].

In this study, we have calculated the real temperature by the pure water with the best estimation of the base line (A) and sample thickness (X) (section 3.2) and we calculated the experimental density. Then, we compared the measured temperature to abtain parameters of linear equation to apply them on a solution measured temperature to calculate the corrected temperature, then we used the same equation on the solutions at same experiment and pressure. In the case of NaCl-H_2O we use equation, theory model of densities have been obtained from of Driesner database[3,4], then using an equation (16) to calculate the absorption for a comparison with an experimental.

The experiments were performed using XAS measurements on NaCl aqueous solution at different concentrations (0.3, 0.5, and 1.0 mol/kg) using an incident energy of 13.7 KeV under isobaric conditions (300 and 400 bar) as a function of temperature. The samples were stored in a desiccator under nitrogen at 0.1 bar. Then the samples were put in to an oven to kick out humidity. Absorption increases with pressure and deceases with temperature. The experimental curves compared with theoretical curves have been obtained from Driesner software - 0.2 version after expected the best value of thickness of sample "X" and base line "A" to estimate the real temperature. In order to compere the results obtained for mili-Q water reference, theoretical curve was obtained from NIST database[1].

FIG.3.8 shows XAS measurements as a function of temperature for NaCl aqueous solutions, we observe that the NaCl-1.0M has more absorption than others, whereas the absorption at ambient conditions are in order 0.0467, 0.06, 0.133 and 0.31 for ($0.3M_{300bar}$, $0.3M_{400bar}$, 0.5M and 1.0M respectively). For NaCl-0.3M300bar, the absorption start go down from 30 °C to 363 °C progressively, then, increase to 367 °C significantly, thereafter, slip down drastically; Δ abs. = 0.3672 (30 °C to 363 °C) and 0.4 (367 °C to 411 °C) with a decrease to water at 420°C. The peak appears at 367 °C with peak size is 0.012 (4%). The phase separation accurs theroretically at 408°C.

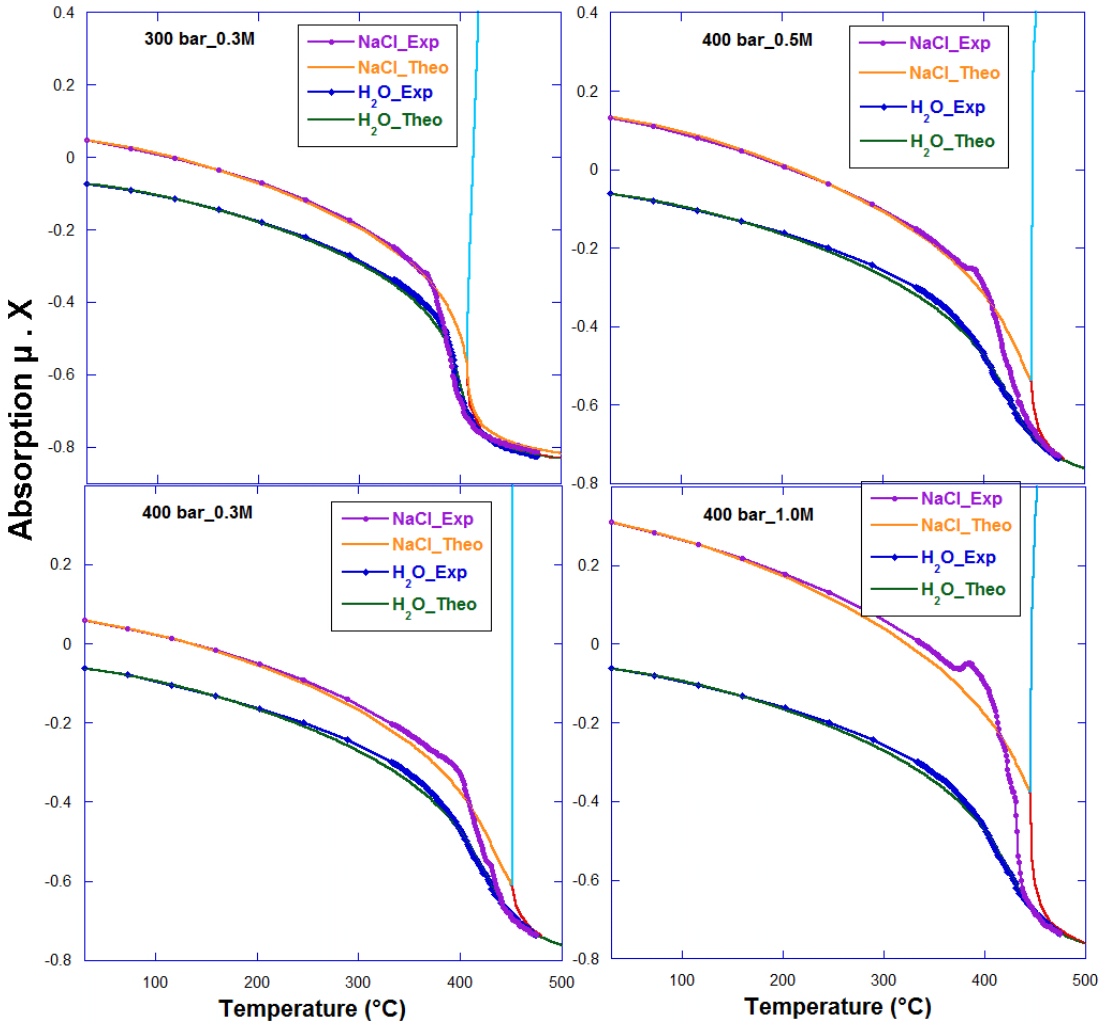

FIG. 3.8 - Experimental X-ray absorption measurements in transmission mode for NaCl aqueous solutions at 13.7KeV as a function of temperature in comparison with pure water and theoretical prediction. The expected base line is - 0.9262 and sample thickness 0.398 cm, theoretical fit values of NaCl have been obtained from Thomas Driesner software "sawatflinc_ptx, version 0.2".[3,4]

For NaCl-0.3M400bar, the absorption starts to decrease from 30 °C to 375 °C progressively. Then, absorption increases at 395 °C significantly, after this point it decreases drastically, Δ abs. = 0.334 (30 °C to 375 °C) and 0.4 (375 °C to 450 °C) with decrease to water at 440°C. The peak appears at 395 °C with a peak size of 0.02 (6%). The phase separation accurs theroretically at 452°C.

For NaCl-0.5M, the absorption starts to decrease from 30 °C to 382 °C progressively, then, it increase at 391 °C significantly. Thereafter, absorption decreases drastically. Δabs. = 0.383 (30 °C to 382 °C) and 0.45 (391 °C to 460 °C) with a decrease to water at 452°C. In this case, The peak appears at 391 °C with a peak size of 0.025 (9%). The phase separation accurs theroretically at 448°C.

For NaCl-1.0M, the absorption starts to decrease from 30 °C to 370 °C progressively, then, it increases at 385 °C significantly. Thereafter, it decreases drastically. Δabs. = 0.37 (30 °C to 370 °C) and 0.602 (385 °C to 440 °C) with a decrease to water at 438°C. In this case, The peak appears at 385 °C with a peak size of 0.052 (51%). The phase separation accurs theroretically at 452°C.

When we increase the ions in NaCl aqueous solution, we observe that after the peaks, the curve takes away than theoretical curve (ΔT increase), due to the phase separation at that region of temperature occurs before than les concentration of same solution.

When doing experiments of NaCl-H_2O under isobaric process, we observe the two-phase region start from certain temperature *i.e.* 444 °C of 1.0 mol/kg at 400bar. An accurate portrayal of the pressure-temperature-composition (P-T-x) relations of the two-phase surface. The two-phase region of NaCl-H_2O undergoes a rather complex geometric change from below the critical point of pure water to above, and the properties of the system change dramatically. The critical pints in the FIG. 5 have been performed by the Driesner program under isobaric process at several concentrations and pressures. we can estimate the vapor-liquid isotherms by knowing the compositions (x: mol of fraction) of certain temperature, then the weight percent of NaCl-H_2O.

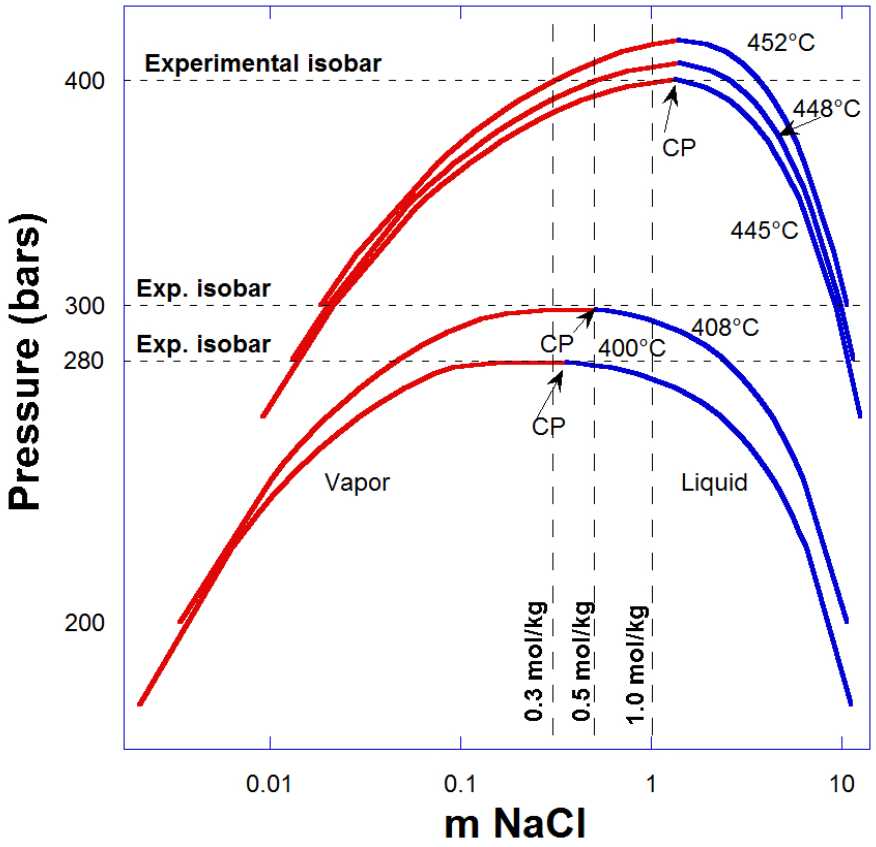

FIG. 3.9 - Compilation of theoretical data for vapor-liquid isotherms of NaCl-H_2O from 399°C to 451°C have been extracted from Thomas Driesner program "sawatflinc_ptx, version 0.2"[3,4].

The shift of the critical point and isochore with the addition of ions causes a change of the phase separation at a given T and P. starting from isobar value, increasing the temperature step by step by measuring an absorption, starting decrease the absorption with temperature up to certain value, then increase to few steps of temperature, and then observing he gas phase starting to separate of liquid phase with increase the separation with temperature. The addition of ions shifts the critical point to higher T and P; but in the case of isobaric process, the critical point shifts at low temperature when add ions.

Based on a comparison of the NaCl solutions, the phase separation observes with the addition of the ions can be compared with the increases from a shift of the critical point. But it is worth questioning whether this shift of the critical point is sufficient to explain the ion-pairing whereas the measuring was in macroscopic scale. The distance to the critical point at the crossing of the critical isochore can be evaluated from the experimental results as follows:

- For pure water at 280 bar, the isochore is crossed at 59.4 bar and 21.55 °C from the Pc and Tc, while at 300 bar it is crossed at 79.4 bar and 28.55 °C from the critical point. The difference in T at the crossing of the isochore is 7 °C for a difference of P of 20 bar.

- For NaCl aqueous solution (0.3 mol/kg), the isochore is crossed at about 48.63 bar and 21.69 °C from the Pc and Tc of water. For NaCl aqueous solution (0.5 mol/kg), the isochore is crossed at about 75.48 bar and 32.36 °C from the Pc and Tc of water. For NaCl aqueous solution (1.0 mol/kg), the isochore is crossed at about 136.52 bar and 54.86 °C from the critical point of water.

- All critical points of NaCl solutions are crossed the isochore curve with shift in temperature of 0.3 mol/kg is 3.33 °C, and of 0.5 mol/kg is 3.56 °C and of 1.0 mol/kg is 2.45 °C.

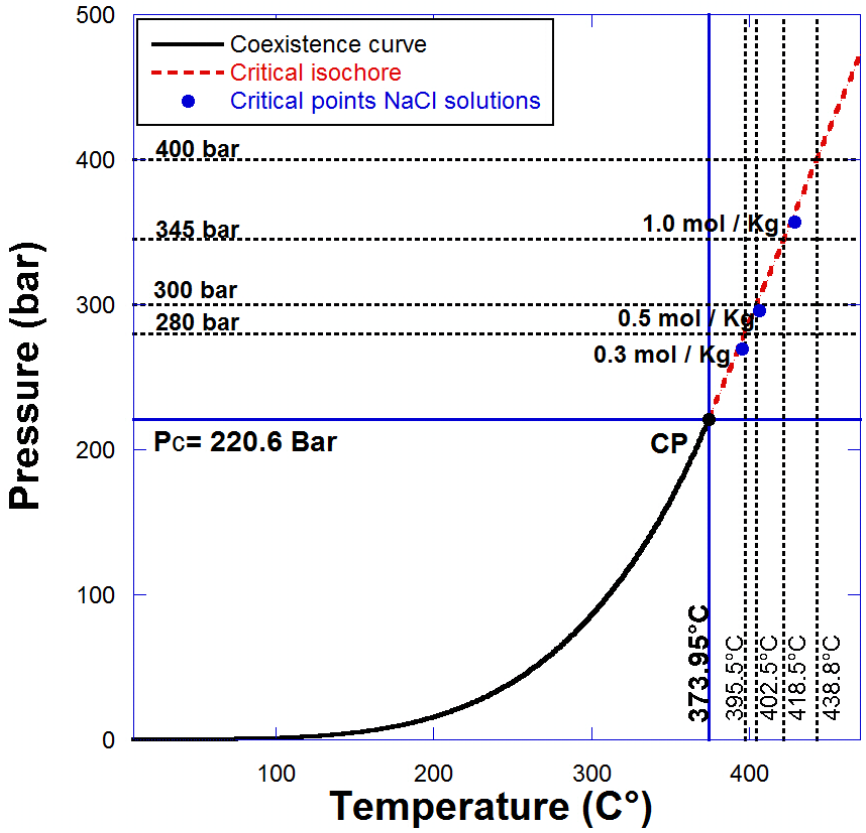

FIG. 3.10 - Liquid gas coexistence curve and critical isochore for pure water, calculated according to Ref.[1], and critical points of NaCl aqueous solutions (0.3 mol/kg, 0.5 mol/kg and 1.0 mol/kg). The solid lines mark the boundaries of the supercritical domain, the horizontal dashed lines the experimental isobars and the vertical ones the corresponding values of the temperature.

X-Ray Mass Attenuation Coefficients (μ/ρ) for the solutions measured by the number of moles for each elements of a solution using the equation (19) at a certain energy, μ/ρ was obtained from Illinois database.[9] The weight percent was calculated using equation (19):

$$Wt\% = \left(\frac{M_{salt} \cdot \ C_{salt}}{\left(M_{salt} \cdot \ C_{salt} \right) + \left(N_{H2O} - C_{salt} \right) * M_{H2O}} \right) * 100\% \qquad (19)$$

Where, M is the molar weight (g/mol), C is the concentration (mol/L) and N is the number of moles of H_2O per liter.

Table 5: The physical quantities of aqueous solutions at various concentrations with an absorption coefficient at 15KeV.

Phys. quantity / Sample	Salt Weight (gm)	Molar Mass (amu)	μ/ρ (cm^2/gm)	Weight percent
H_2O	25	18.015	1.585	100%
NaCl_1.0M	1.465	58.439	2.207	5.61%
NaCl_0.5M	0.737	58.439	1.907	2.86%
NaCl_0.3M	0.441	58.439	1.78	1.73%
LiCl_1.0M	1.062	42.39	2.14	4.13%
LiCl_0.5M	0.534	42.39	1.87	2.1%
LiCl_0.3M	0.322	42.39	1.758	1.26%

It is interesting to study the influence of varying the NaCl concentration on the critical point under isobaric onditions as a function of the temperature. FIG. 3.10 shows the evolution of the density difference between experimental and theoretical. A small density difference is observed the beginning then it increases at approaching the critical poin region at supercritical region and specially when increase the ions. FIG 3.9 shows that of these critical points are crossed the critical isochore. These critical points represent the phase separation of NaCl-H_2O with the compilation of the density coexisting liquids and vapors on the two phases. The values of the phase separation were obtained from Driesner database pogram.

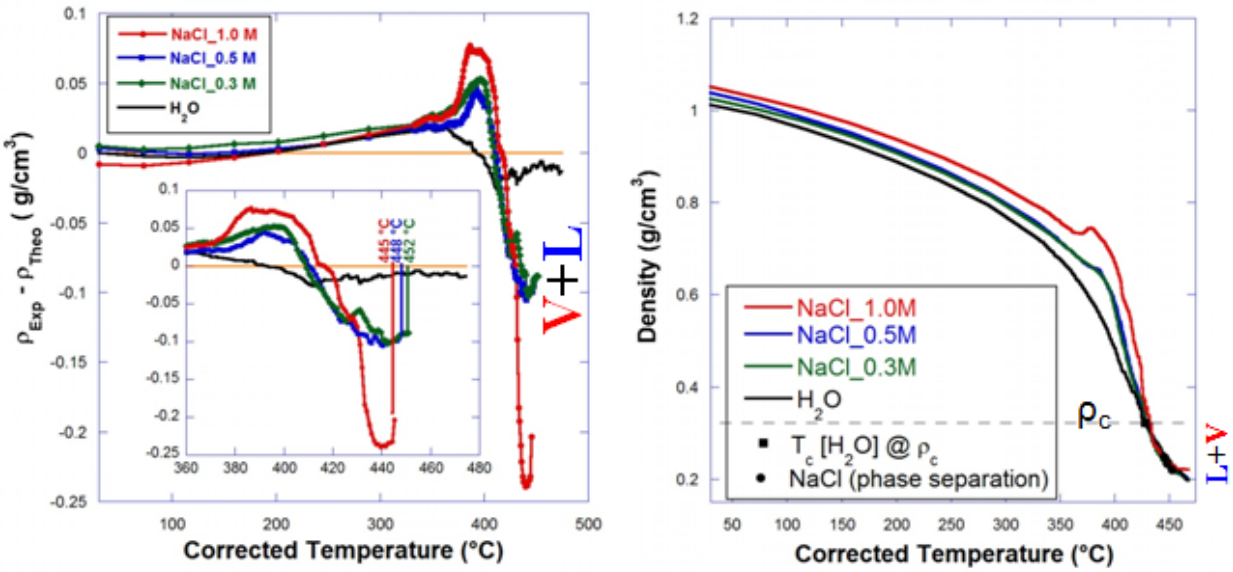

FIG. 3.11 - Different density of experimental and theoretical absorption in transmission mode measured in NaCl aqueous solutions at 13.7KeV as a function of temperature in comparison with pure water and theoretical prediction at 400 bars (left). Experimental X-ray absorption in transmission mode measured in NaCl aqueous solutions at 13.7KeV as a function of temperature in comparison with pure water and theoretical prediction at 400 bars (right). The expected base line is - 0.9301 and sample thickness 0.398 cm, theoretical fit values of NaCl were obtained from Thomas Driesner software "sawatflinc_ptx, version 0.2".[3,4]

The different behavior due to the concentration of the ions can result from the proximity of these ions in the high density areas: at low concentrations, only the interactions between the water molecules control the density fluctuation, whereas for high concentrations the properties of the fluid depend on the interaction between the ions and the network of the water molecules and the interaction between the ions themself. To observe the phase separation in sodium chloride aqoueos solutions were measured at different concentrations and isobaric values conditions. To perform this experiments we fixed the upper piston 64 mm, and a piston 15 moved 2 mm from the sample.

Table 6: Phase separation temperature for NaCl at 300 bar, 13 KeV, and different concentrations with upper piston 64 mm fixed.

Samples	Temperature (°C)	Notes
NaCl_0.3M	420	The abs. decrease with temperature; starting from 470 °C at gas phase, the abs. increase then decrease.
NaCl_1.0M	395	The abs. decrease with temperature, at 380°C increases then decrease at 395 °C.
NaCl_2.0M	365	The abs. decrease with temperature; to observe starting increase before phase separation must be before 355 °C.

Povodyrev et al.[5] they presented a critical locus of sodium chloride aqueous solutions, their data indicate a strong dependence of the critical temperature of NaCl aqueous solutions on salt concentration, especially in the limit of pure water as shown in FIG. 3.12. Critical pressures and densities also showed strong dependence on salt concentration. They proposed a new set of equations for the critical locus and compare the results with evaluations reported previously by a number of investigators. The equations do not have a singular behavior at infinite dilution and yield a consistent description of the existing experimental data. The equation for the critical temperature incorporates a crossover function to account for an apparent dip in the critical line observed experimentally in the range of 0.003 to 0.005 mass fraction of NaCl.

Critical point properties of pure water		Tc H_2O	647.096	K	
		Pc H_2O	22.064	Mpa	
		ro_c H_2O	322	kg.m^-3	
Parameters in Eqs. (1)-(3) for the Critical Locus of NaCl-H2O Solutions up to 30 Per Cent of NaCl by Mass	Critical temperature Tc	T1	38.688		
		T2	-53.982		
		T3	651.093		
		T4	10.9		
		T5	-0.39821		
		T6	0.01688		
		w1	17.034		
		w2	0.37587		
	Critical pressure pc	p1	0.20176		
		p2	1.14E-03		
		p3	-5.60E-06		
		p4	8.05E-09		
	Critical density ρc	r1	66.868		
		r2	1.37E+01		
		r3	-6.31E-04		
w: per cent of sodium chloride by mass		w	1.73	%	
w_mol: mol of sodium chloride by liter	0.3	f1	552.308695		
w_mass: per cent of sodium chloride by mass	1.73%	f2	668.855706		
molar weight NaCl	58.443	Tc NaCl	668.86	K	395.705706
molar weight H2O	18.0148	pc NaCl	26.94	Mpa	269.378298
		ρc NaCl	402.98	kg.m^-3	0.40297566

FIG. 3.12 - Vapor-liquid critical locus of sodium chloride aqueous solution. given at certain concentration showing the parameters used in the equations.[5]

The values of the critical pressure, critical temperature, and critical density of sodium chloride aqueous solution are mentioned in Table 7 have shown in the FIG. 3.13.

Table 7: The physical characteristics of water and aqueous solution of sodium chloride at various concentrations as well the weight of salts[10].

Materials / Characteristics	H_2O Mili-Q	NaCl_0.3M	NaCl_0.5M	NaCl_1.0M
Critical pressure (bar)	220.640	269.4	296	359.2
Critical Temperature (°C)	373.946	395.71	406.27	429.57
Critical Density (g/ml)	0.322	0.40298	0.43730	0.49696
Weight percent% of NaCl	0	1.73	2.86	5.61

We have carried out other isobar XAS measurement on NaCl 1.0 mol/kg at 345 bars and 13.7 KeVusing two piston configurations. Upper Fixed at 64 mm with the beam path near to the upper part of the sample, and Lower Fixed 34 mm with a beam path near to the lower part of the sample. corresponding to two different pistons configurations to observe the phase separation shift in supercritical conditions and the size of peak. The sample height is 2 mm. The pressure usedis bellow the critical pressure for NaCl 1.0 mol/kg (Table 7), in order to observe the aqueous solution behavior below a critical pressure.

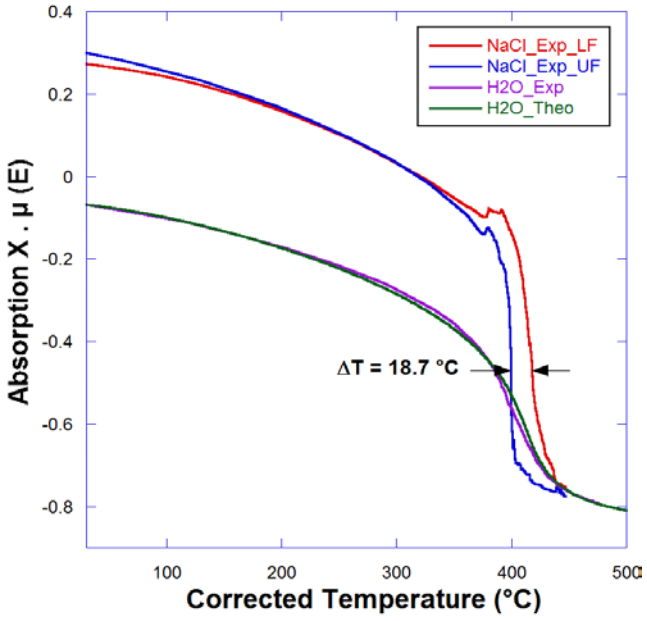

FIG. 3.13 - Experimental X-ray absorption measured in transmission mode of NaCl aqueous solutions 1.0 mol/kg at 13.7 KeV as a function of temperature under isobaric conditions at 345 bars in comparison with pure water and the theoretical prediction. The expected base line is - 0.9301 and sample thickness 0.398 cm. LF: Lower Fixed and UF: Upper Fixed.

FIG. 3.13 shows XAS measurements as a function of temperature for NaCl aqueous solutions, both absorption at 30°C must be the same, but the pressure regulation was not same for both, ΔP = +/- 0.5 bar. For NaCl-1.0M_{UF}, the absorption starts to decrease from 30 °C to 375 °C progressively, then, increase at 380 °C significantly, thereafter, it decreases drastically; Δ abs. = 0.44 (30 °C to 375 °C) and 0.644 (380 °C to 438 °C) with a decrease to water at 438°C. The peak appears at 380 °C with a peak size of 0.03 (20%).

For NaCl-1.0M_{LF}, the absorption starts decrease from 30 °C to 375 °C progressively, then, it increases at 380 °C significantly, thereafter, it decrease drastically. Δabs. = 0.37 (30 °C to 375 °C) and 0.658 (380 °C to 438 °C) with a decrease to water at 438°C. The peak appears at 380 °C with a peak size of 0.032 (29%).

The peak area of NaCl-1.0M_{LF} is higher than NaCl-1.0M_{UF} with a temperature, the shift in temperature between them is ΔT = 18.7 °C. At 399.5 °C, NaCl-1.0M_{UF} has intersected the curve of water in anomalous behavior then precipitate with water in due the temperature, because in upper fixed method and beam path in the upper part of a sample, the pressure bellow of the critical point. The absorption go down drastically from -0.2 to -0.7 in ΔT = 6.5 °C with transforming to a gas phase (in upper part of sample) in a quick process than water and in small ΔT. Whereas, the absorption go down drastically of NaCl-1.0M_{LF} from -0.2 to -0.7 in ΔT = 27 °C. In the other hands, NaCl-1.0M_{LF} has a normal behavior but with an extension with a temperature because in the case of lower fixed takes a time to arrive two phases than other method, whereas, the phase separation start observed from upper to lower part of a sample. Therefore, the phase separation observed for NaCl-1.0M_{UF} before NaCl-1.0M_{LF}.

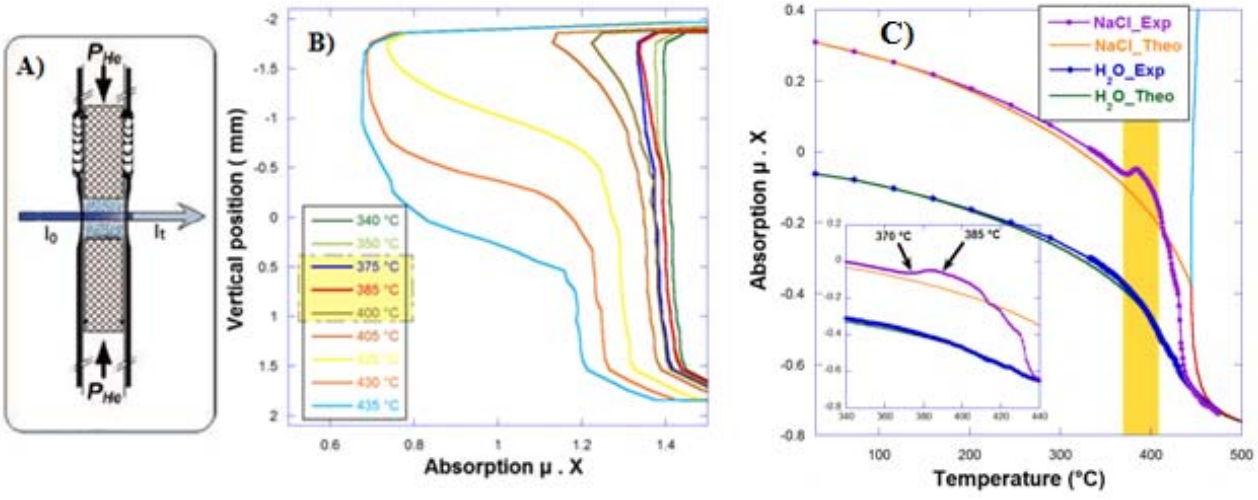

FIG. 3.14 - Experimental X-ray absorption in transmission mode measured in NaCl_1.0M aqueous solutions at 13.7KeV as a function of temperature in comparison with pure water and theoretical prediction at 400 bar. A) A carbon cell adapting for HPHT, B) scan of the carbon cell in vertical axis, C) classical XAS measurement. The expected base line is - 0.9301 and sample thickness 0.398 cm, theoretical fit values of NaCl have been extracted by Thomas Driesner program "sawatflinc_ptx, version 0.2"[3,4]. The beam path at the center of cell.

The comparison of NaCl 1 mol/kg aqueous solution at 400 bars, the peak in the FIG. 3.14-C illustrates that start at 370 °C up to the maximum at 385 °C. We observe this peak by doing scan of the vertical position of a carbon cell (FIG. 3.14 A and B) then, start the phase separation. The liquid-gas phases as shown in the FIG. 3.19 B begins from upper part to lower during of temperature, this is due for two reasons, the first is that a thermocouple is near an upper part of the cell, and the second, is physical thermal properties of gas exist at upper part of cell. By calculate the ration of phase separation appearance theoretically by Driesner database program, it was 26% at 444 °C. The compare of this ration to an experimental result of same solution, it has a fit at 415 °C as expected temperature but the real temperature must be higher because the thermocouple does not exist at center of solution. XAS measurements have been confirmed observing the ion pairing and the phase separation with liquid-gas phases.

Table 8: The vertical position of both regions gas and liquid which correlate to real temperatures of NaCl at 1.0 mol/kg and 400 bars using upper fixed piston method.

Cell T (°C)	**Corr. T (°C)**	**Vertical Pos.(mm)**	**Exp. Absorption**	**Density (g/cm^3)**	**Real Temp. (°C)**
355	340	- 1.65	1.394	0.8272409	293
		1. 15	1.424	0.85445277	273
390	375	- 1.65	1.3319	0.77091232	332
		1. 15	1.388	0.82179852	298
400	385	- 1.65	1.338	0.7764454	329
		1. 15	1.41	0.8417539	283
415	400	- 1.65	1.222	0.670113343	382
		1. 15	1.38	0.813191598	304
420	405	- 1.65	1.1333	0.589790298	412
		1. 15	1.35	0.786024841	322
435	420	- 1.65	0.7377	0.231551327	468
		1. 15	1.29	0.731691326	353

3.1.5 Other electrolytes (Cl, Br, NO_3, and SO_4)

We present XAS measurements using a several group of solutions with different ions (XCl, XBr, XNO3 and XSO4) at different concentrations and isobaric conditions and different incident energies, X represent the alkaline group (cation). Moreoveras, XAS measurements were performed using different solutions to compare the groups each other with changing the cation like $ZnSO_4$, $ZnBr_2$ and $ZnCl_2$, to observe the evolutions of these groups at supercritical region, evolution of ion-pairing and phase separation.

Water is a primary fluid studied. The solvent power of a given fluid depends on its density. The density has a great influence on the solute–solvent interactions and can be adjusted controlling pressure and/or temperature. Increasing the pressure leads to liquid-like density of the supercritical fluid, thus increasing the probability of interactions between the solute and the solvent, including dispersion, polar, and hydrogen-bonding[18,35,39,93,108,133]. Consequently, the solubility increases with pressure. Increasing temperature leads to a density reduction (and, therefore, to a decrease in both solvent power and solute solubility), which are more pronounced at pressure levels close to the critical point. However, the temperature not only affects the density of the solvent, but it also leads to an increase in the vapor pressure of the solute with increasing temperature. We chose sulfate and nitrate solutions to see the evolution of ions with alkaline group and zinc charges at supercritical fluids through isobaric processes.

In this study, we calculated the real temperature for pure water with the best estimation of the base line (A) and sample thickness (X) (section 3.2), then we calculate the experimental density. For pure water, we compare the temperature measured and real to obtain the parameters of linear equation to apply it on a solution measured temperature to calculate the corrected temperature, where we can benefit to use same equation applying on the solutions at same experiment and pressure. In the case of (Cl^-, Br^-, NO_3^-, and SO_4^-), we use same an equation of 16, we multiplied the density of water[1] with the ratio of mass to transform them become per Kg of solution, *i.e*. if the mass of H_2O is 25g, we multiply by 40 to become 1000 g, and in the case of solutions, we add the mass of salt to mass of H_2O and multiply by 40. Then using an equation (16) to calculate the absorption for a comparison with an experimental.

XAS measurements were performed on LiCl solutions at different concentrations (0.3 mol/kg, 0.5 mol/kg, and 1.0 mol/kg) using X-ray incident energy of 15 KeV at isobar conditions (300 and 400 bar) as a function of the temperature. The samples were stored in a glassy box (dessicator) under nitrogen 0.1 bar. Then samples was located into an oven to dry it. The experimental curves compared with theoretical curves have been calculated with a new method " transform the total of mass to Kg of solution " after expected the best value of thickness of sample "X" and base line "A" to estimate the real temperature. Comparison with the reference mili-Q water, the theoretical curve compared is extracted from NIST database[1].

The experimental results are presented in the FIG. 3.15 of density measurements according to an equation (16), regarding to the concentrations in mol/kg, a tendency in solubility can be determined ($LiCl_{0.3M} > LiCl_{0.5M} > LiCl_{1.0M}$)[134], all LiCl experimental data can be described with a good agreement with the approach mentioned above.

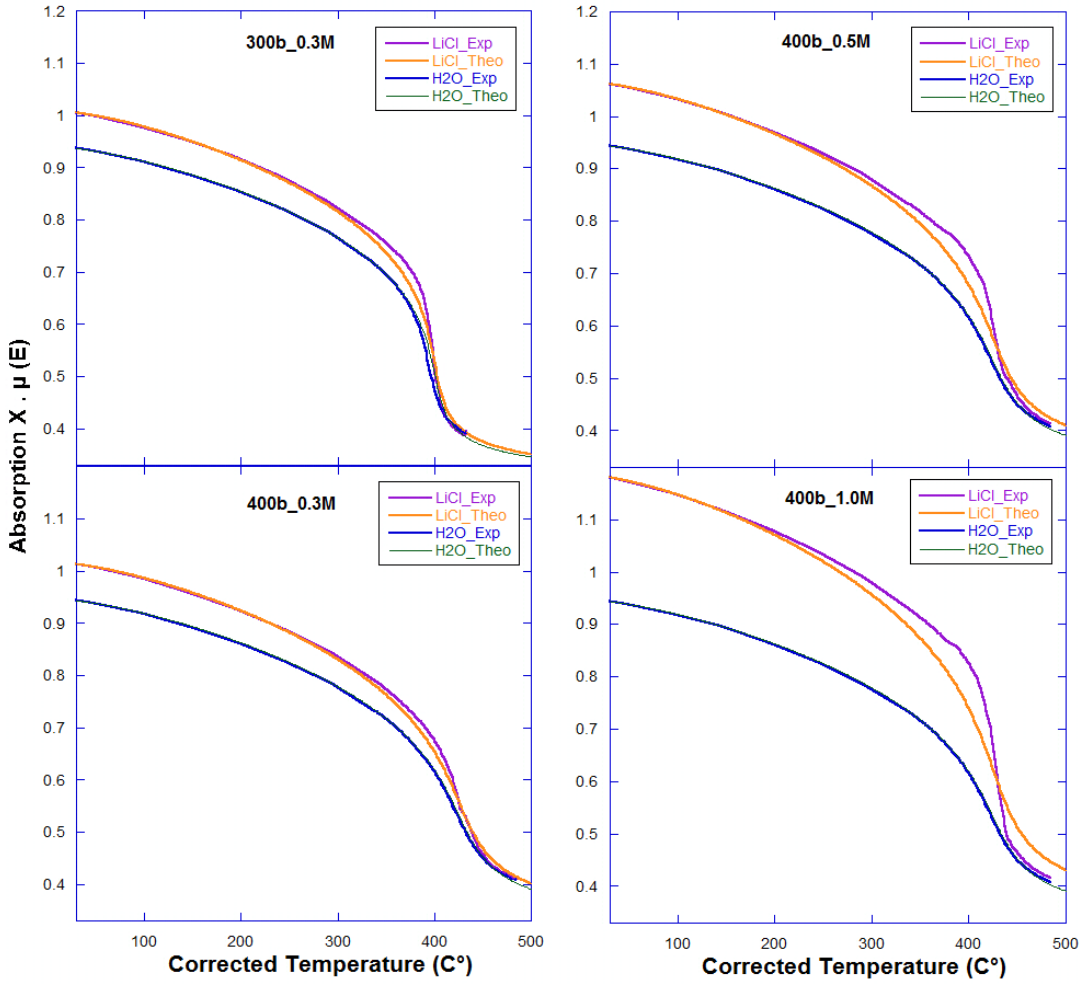

FIG. 3.15 - Experimental X-ray absorption in transmission mode measured in LiCl aqueous solutions at 15 KeV as a function of temperature in comparison with pure water and theoretical prediction. The expected base line is 0.27127 and sample thickness 0.398 cm.

FIG. 3.15 shows XAS measurements as a function of temperature for LiCl aqueous solutions. It can be observed that the LiCl-1.0M has a higher absorption than others. The absorption at ambient conditions are 1.0059, 1.01, 1.06 and 1.018 for ($0.3M_{300bar}$, $0.3M_{400bar}$, 0.5M and 1.0M respectively). The weight of salt increases 1.26%, 2.09% and 4.135% (LiCl_0.3M, LiCl_0.5M and LiCl_1.0M respectively). For LiCl-$0.3M_{300bar}$, the absorption starts decreasing from 30 °C to 370 °C progressively, and then, it decrease drastically. Δabs. = 0.27 (30 °C to 370 °C) and 0.347 (370 °C to 450 °C) with a decrease to water at 407°C. There is no observing a peak at supercritical region in this case.

For LiCl-$0.3M_{400bar}$, the absorption start desreasing from 30 °C to 370 °C progressively, then, it decreases drastically; Δ abs. = 0.271 (30 °C to 370 °C) and 0.31 (370 °C to 450 °C) with a decrease to water at 455°C. There is no observing a peak at supercritical region in this case.

For LiCl-0.5M, the absorption start decreasing from 30 °C to 376 °C progressively, then, increase to 385 °C in a peak slightly, thereafter, it decreases drastically; Δ abs. = 0.279 (

30 °C to 374 °C) and 0.328 (385 °C to 460 °C) without appear a decrease to water. In this case, a peak appears at 385 °C with a peak size of 0.009 (0.9%).

For LiCl-1.0M, the absorption start decsreasing from 30 °C to 370 °C progressively, then, increase to 385 °C significantly, thereafter, it decreases drastically; Δ abs. = 0.31 (30 °C to 374 °C) and 0.42 (385 °C to 460 °C) without appear a decrease to water. In this case, a peak appears at 385 °C with a peak size of 0.011 (1.6%).

When we increase the ions in LiCl aqueous solution, we observed that after the peaks, the curve takes away than theoretical curve ΔT increase, when the concentration of the solution increase.

Bromide, Chloride, Sulfate, and Nitrate aqueous solutions:

XAS measurements for (bromide, bhloride, sulfate, and nitrate) aqueous solutions 0.3 mol/kg were performed with incident energy 15 KeV at isobar condition 300 bar as a function of temperature. The experimental curves compared with the reference mili-Q water, the theoretical curve compared is extracted from NIST database[1] after expected the best value of thickness of sample "X" and base line "A" to estimate the real temperature. The expected base line is removed in this case to be able compare samples with each others, according their values are not same (Table 4).

The aqueous solutions in FIG. 3.14 are interesting to study the phase separation phenomena, with expecting for exist ion-pairing correlations. bromide aqueous solutions are good candidate to study the influence of cations distribution, however, the cation charges are different and may affect the density fluctuation. By estimation of the number of ions in the density fluctuation. For a concentration of 0.3 mol/kg, there is 1 mole of XBr for on average 185 moles of water (*i.e.* 93 per cation). The spatial distribution of ions was homogeneous up to supercritical domain, their addition would change the density contrast. However, we observed that the change of the absorption is proportional to the density contrast, this shows that the ions are distributed inhomogeneously. In other words, the distribution of ions is different in the low density areas and in the high-density areas.

FIG.3.16 shows the XAS measurements as a function of temperature of 0.3 mol/kg aqueous solutions at incident energy 15KeV, in case of Bromide aqueous solutions, we observe that the ZnBr2 has more absorption than others, whereas the absorption at ambient conditions are in order 1.557, 1.895, 2.475 and 3.5 for (LiBr, KBr, CsBr and $ZnBr_2$ respectively). For LiBr, the absorption start go down from 30 °C to 360 °C progressively, then, increase to 369 °C significantly, thereafter, slip down drastically; Δ abs. = 0.557 (30 °C to 360 °C) and 0.854 (369 °C to 405 °C) with a decrease to water at 420°C. The peak appears at 369 °C with peak size is 0.067 (6.9%).

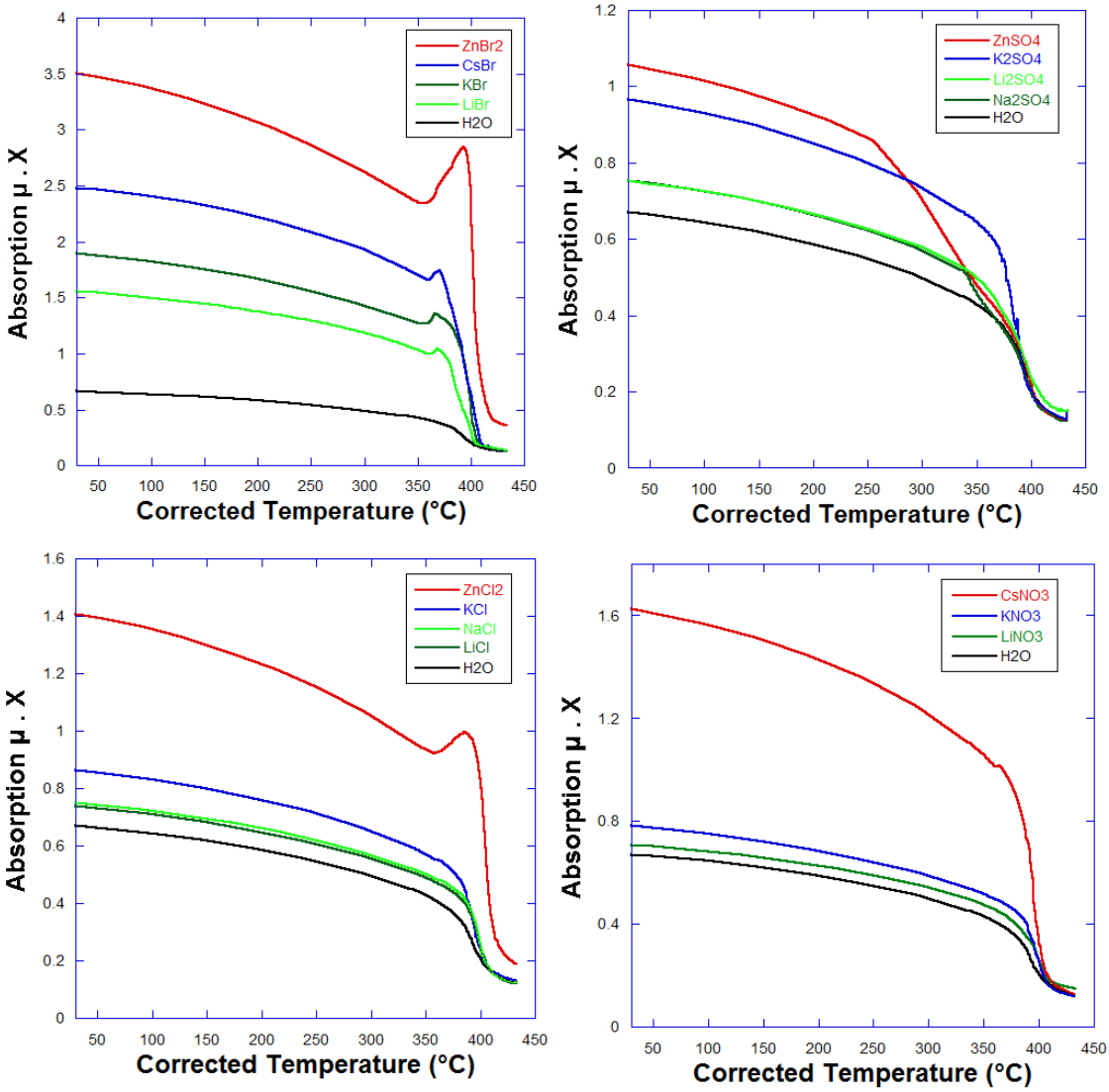

FIG. 3.16 - Experimental X-ray absorption measured in transmission mode for bromide, chloride, sulfate, and nitrate aqueous solutions (0.3 mol/kg) at 15KeV as a function of temperature in comparison with pure water at 300 bar. Sample thickness is 0.398 cm, without base line.

For KBr, the absorption start decreasing from 30 °C to 355 °C progressively. Then, increase to 369 °C significantly, thereafter, it decreases drastically. Δabs. = 0.625 (30 °C to 355 °C) and 1.178 (369 °C to 410 °C) with a decrease to water at 420°C. The peak appears at 369 °C with a peak size of 0.116 (9.5%).

For CsBr, the absorption start decreasing from 30 °C to 360 °C progressively. Then, increase to 369 °C significantly, thereafter, it decreases drastically. Δabs. = 0.815 (30 °C to 360 °C) and 1.563 (369 °C to 410 °C) with a decrease to water at 420°C. In this case, the peak appears at 369 °C with a peak size of 0.16 (10.5%).

For $ZnBr_2$, the absorption start decreasing from 30 °C to 355 °C progressively. Then, increase to 393 °C significantly, thereafter, it decreases drastically. Δabs. = 1.154 (30 °C to

355 °C) and 2.46 (393 °C to 425 °C) without a decrease to water at any given temperature. In this case, the peak appears at 393 °C with a peak size of 0.728 (34%).

In the case of chloride aqueous solutions, we observed that $ZnCl_2$ exhibits a significant anomalous density while KCl has a small effect in supercritical region. The other solutions do not exhibit anomalous changes in density with a decrease to water at 408 °C. The absorption increased significantly at 387°C for $ZnCl_2$ with a peak size of 0.14 (16.3%) without a decrease to water. The absorption increase as well with weak effect at 361°C for KCl with a peak size of 0.01 (1.8%).

In the case of sulfate aqueous solutions, we have observed that some of sulfates have homogeneous behavior up to specific temperature, the drop down suddenly being to precipitation value. $ZnSO_4$ drop down at 254°C with a decrease to water at 404°C. Na_2SO_4 drop down at 337°C with a decrease to water at 404°C. Li_2SO_4 drop down at 357°C without a decrease to water. K_2SO_4 has no anomalous behavior, but there is unstable pressure in the mean value in the region after critical point. The reason for some sulfates have dropped down suddenly is due to the bonds between the molecules are beak down with temperature depending of atomic mass of cations and the concentration of these solutions.

In the case of nitrate aqueous solutions, we have observed that $CsNO_3$ has a bit effect anomalous density. The other solutions have no anomalous changes in density. The absorption increase in weak effect at 365°C for $CsNO_3$ with peak size is 0.015 (6.5%) with a decrease to water at 430°C. The decrease to water for KNO_3 at 407°C with a bit slip down below of gaze phase of H_2O, while as LiNO3 has no decrease to water at concentration 0.3mol/kg.

Sulfates and Nitrates aqueous solutions with a concentration 1.0M at 400 bars, incident energy is 12.5 KeV as a function of temperature. The experimental curves compared with the reference mili-Q water at given pressure, after expected the best value of thickness of sample "X" which was 0.398 mm, and base line "A" which was 0.482 to estimate the real temperature. we used the temperature from 30°C to 350°C with 15 points and from 350°C to 500°C with 50 points; the pressures are 300 bars, and 400 bars with stability +/- 0.3 bar and +/- 0.08 °C. The experimental derivative shift value is 1 °C of a theoretical critical density of water, in other words, the value of thermocouple was accurate and near than a theoretical critical density.

The FIG. 3.17 shows the XAS measurements as a function of temperature for sulfate aqueous solutions, we observe that the Na_2SO_4 has more absorption than Li_2SO_4, whereas the absorption at ambient conditions are in order 2.11, and 1.86 for (Na_2SO_4, and Li_2SO_4 respectively). For Na_2SO_4, the absorption start decreasing from 30 °C to 345 °C progressively, then, it decreases drastically; Δ abs. = 0.47 (30 °C to 345 °C) and 0.89 (345 °C to 455 °C) with a decrease to water of 475°C.

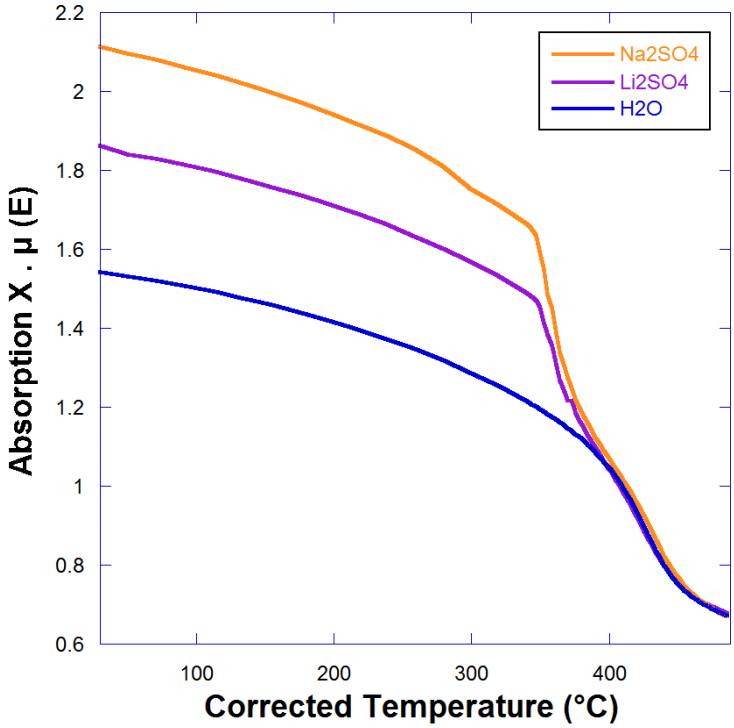

FIG. 3.17 - Experimental X-ray absorption measured in transmission mode for sulfate aqueous solutions 1.0 mol/kg at 12.5 KeV as a function of temperature in comparison with pure water at 400 bar. Sample thickness is 0.398 cm, and base line is 0.482.

For Li_2SO_4, the absorption start go down from 30 °C to 350 °C progressively, then, slip down drastically; Δ abs. = 0.4 (30 °C to 350 °C) and 0.736 (350 °C to 460 °C) with a decrease to water at 475°C.

In the cases of sulfate, we observe that the density (absorption) decrease progressively then, slip down drastically in anomalous behavior at 445 °C for Na_2SO_4, and 450 for Li_2SO_4. In these cases, the reason goes back to the bonds between the sulfate and atoms is break up to certain value of a temperature, the bonds net are collapse whereas, the atoms precipitate at the bottom of sample holder.

FIG. 3.18 shows the XAS measurements as a function of temperature for Nitrate aqueous solutions, we observe that the $CsNO_3$ has more absorption than others, whereas the absorption at ambient conditions are in order 6.793, 2.63 and 1.61 for ($CsNO_3$, $RbNO_3$ and $LiNO_3$ respectively). For $CsNO_3$, the absorption start go down from 30 °C to 387 °C progressively with a little phase, then, increase to 399 °C significantly, thereafter, slip down drastically; Δ abs. = 2.468 (30 °C to 387 °C) and 3.86 (399 °C to 445 °C) with a decrease to water at 480°C. The peak appears at 399 °C with peak size is 0.639 g/ml (15.4%).

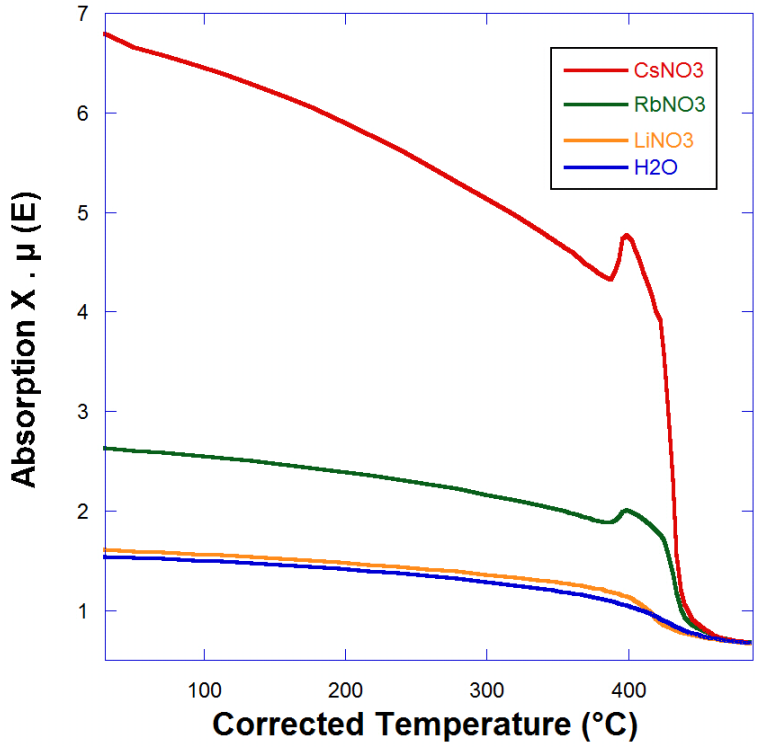

FIG. 3.18 - Experimental X-ray absorption measured in transmission mode nitrate aqueous solutions at 12.5 KeV for 1.0 mol/kg as a function of temperature in comparison with pure water at 400 bar. Sample thickness is 0.398 cm, and base line is 0.482.

For $RbNO_3$, the absorption start decreasing from 30 °C to 387 °C progressively, then, increase to 399 °C significantly, thereafter, it decreases drastically; Δ abs. = 0.742 (30 °C to 387 °C) and 1.18 (399 °C to 445 °C) with a decrease to water at 480°C. The peak appears at 399 °C with a peak size of 0.16 g/ml (8.7%) .

For $LiNO_3$, the absorption decreasing down from 30 °C to 387 °C progressively, then, it decreases drastically; Δ abs. = 0.487 (30 °C to 400 °C) and 0.26 (400 °C to 423 °C) with a decrease to water at 460°C. In this case, there is no increase in the absorption, the curve has a normal behavior without anomalous a peak.

The liquid-gas phase separation was observed of supercritical aqueous solutions by XAS measurements as a function of temperature. Isobaric conditions (300 and 400 bar) ware used at different incident X-ray energies 12.5, 13 and 13.5 KeV as shown in the Tables 8, 9, and 10 . To observe the phase separation, two pistons configuration were used. The first one consists in locate the lower piston at 34mm and the upper piston at 38mm, with space capacity 2mm. For this configurations the lower piston was fixed. For the second configuration the lower piston was located at 15mm and the upper piston at 64mm allowing a space capacity 2mm. For this configuration the upper piston was fixed.

Table 9: The temperature at which it appears the phase separation for solutions at 400 bar, 12.5 KeV, and at concentration 1.0M with upper piston 64 mm is fixed.

Samples	Temperature (°C)	Notes
$CsNO_3$_1.0M	410	The abs. decrease with temperature, at 395°C increases then decrease at 405 °C.
$LiNO_3$_1.0M	405	The abs. decrease with temperature, without observe increasing for the abs.
Na_2SO_4_1.0M	365	The abs. decrease with temperature, at 375 °C and 410 °C in gas phase, the abs. increase then decrease.
Li_2SO_4_1.0M	410	The abs. decrease with temperature; at 365 °C to 400 °C in gas phase, the abs. increase then decrease (Peak).

XAS measurements at 300 bars and lower piston fixed, the energies used as illustrated in the Table 10, but for NaBr, we used an energy before and after Br-edge, the beam path was in the center of sample. The phase separation appears for NaCl_5.0M$_{UF}$ before NaCl_5.0M$_{LF}$.

Table 10: The temperature at which it appears the phase separation for solutions at 300 bar, and at different concentrations and energies with down piston 34 mm is fixed.

Samples	Energy (KeV)	Temperature (°C)	Notes
NaCl_5.0M	12.5	435	The abs. decrease with temperature, at 395°C increases then decrease at 425 °C.
NaBr_1.0M	13.0	410	No observe increasing for the abs. before phase separation
NaBr_1.0M	13.5	400	The abs. decrease with temperature, to observe starting increase before phase separation must be before 400 °C.

XAS measurements at 300 bars and the upper piston fixed, the energies used as illustrated in the Table 11. For NaBr and HBr, an energy before and after Br-edge was used, the beam path was in the center of sample. There is not a decrease to water of HCl and HBr because the origin of these samples are aqueous solutions, and we mixed them with salts to observe the shift of a phase separation. There is a shift when HBr and HCl are used, even at diluted HBr and NaBr solution (0.5M). The solutions containing (NaBr and HBr) were diluted to 0.5M to avoid complete absorption of the beam from the solution.

Table 11: The temperature at which it appears the phase separation for aqueous solutions at 300 bar, and at different concentrations and energies with upper piston 64 mm is fixed.

Samples	Energy (KeV)	Temperature (°C)	Notes
NaCl_1.0M HCl_1.0M	12.5	370	The abs. decrease with temperature, to observe starting increase before phase separation must be before 350 °C.
NaBr_0.5M HBr_0.5M	13.0	405	The abs. decrease with temperature, at 380°C increases then decrease at 395 °C.
NaBr_0.5M HBr_0.5M	13.5	350	The abs. decrease with temperature, to observe starting increase before phase separation must be before 350 °C.

In this aqueous solutions, isobar XAS measurements were performed for LiBr 1.0 mol/kg at 345 bars and an incident X-ray energy of 13.7 KeV, using both piston configurations. This pressure is bellow the critical pressure of LiBr 1.0 mol/kg (FIG. 3.19) to observe the aqueous solution behavior below a critical pressure LiBr has a higher molar mass than NaCl.

FIG. 3.19 shows XAS measurements as a function of temperature for LiBr aqueous solutions, the pressure regulation was not same exactly for both at30 °C, where ΔP = +/- 0.5 bar. For LiBr-1.0M_{UF}, the absorption start decreasing from 30 °C to 376 °C progressively, then, increase to 381 °C significantly, thereafter, it decreases drastically; Δ abs. = 1.518 (30 °C to 376 °C) and 3.0 (381 °C to 406 °C) with decrease to water at 406°C. The peak appears at 381 °C with a peak size of 0.328 (16%).

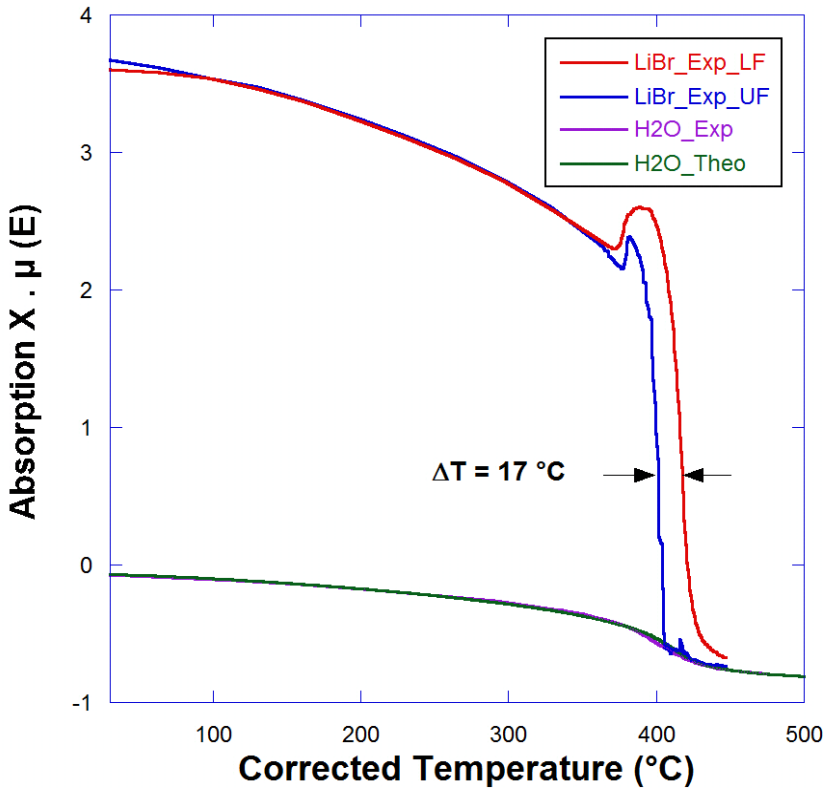

FIG. 3.19 - Experimental X-ray absorption measured in transmission mode for LiBr aqueous solutions (1.0 mol/kg) at 13.7KeV as a function of temperature under isobaric conditions of 345 bars in comparison with pure water and theoretical prediction. The expected base line is -0.9301 and sample thickness 0.398 cm. LF: Lower Fixed and UF: Upper Fixed.

For LiBr -1.0M_{LF}, the absorption start decreasing from 30 °C to 372 °C progressively. Then, increase to 389 °C significantly, thereafter, it decreases drastically. Δabs. = 1.3 (30 °C to 372 °C) and 3.24 (389 °C to 440 °C) without a decrease to water was observed in this case, if we take a long temperature rage, it will happens. The peak appears at 389 °C with a peak size of 0.407 (18.5%).

The peak area of LiBr-1.0M_{LF} has more extension with a temperature than NaCl-1.0M_{UF}, the difference in temperature between them is ΔT = 17 °C. At 415 °C, LiBr-1.0M_{UF} has a non regulation pressure. In this case, absorption did not intersect with water curve because LiBr has higher molar mass than NaCl. The absorption of NaCl-1.0M_{UF} decrease drastically from 1.7 to 0.0 in ΔT = 7 °C changing in a gas phase (in upper part of sample) in a quick process. Whereas, the absorption decrease drastically of LiBr-1.0M_{LF} from 1.7 to 0.0 in ΔT = 11 °C. In the other hands, the phase separation observed for LiBr-1.0M_{UF} before LiBr-1.0M_{LF}.

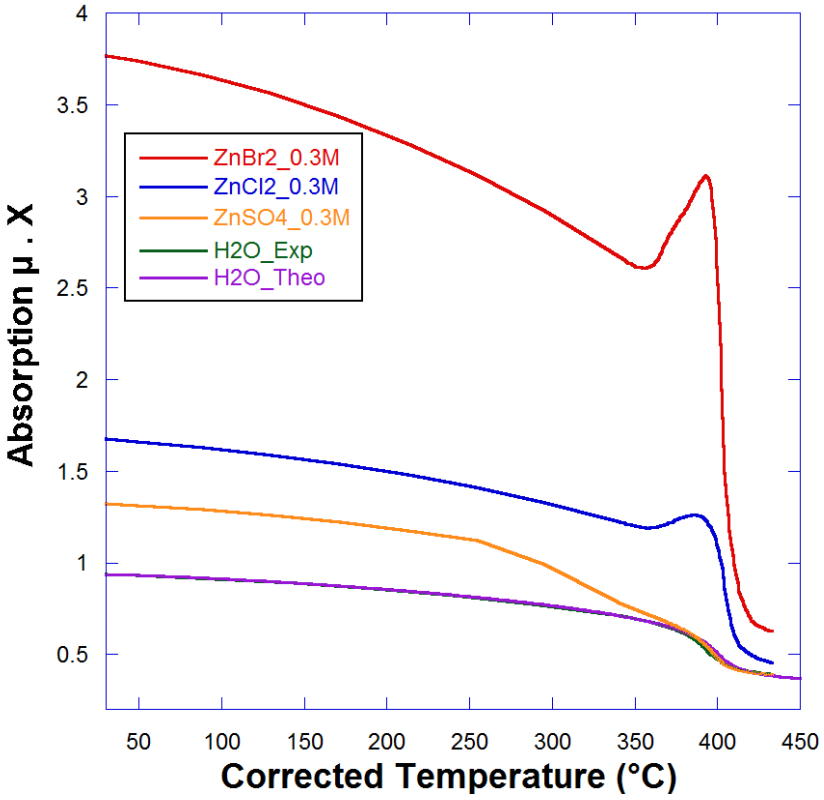

FIG. 3.20 - Experimental X-ray absorption measured in transmission mode of zinc aqueous solutions (0.3 mol/kg) at 15 KeV as a function of temperature under isobaric process of 300 bars in comparison with pure water and theoretical prediction. The expected base line is 0.2666 and sample thickness 0.398 cm.

XAS measurement were performed on different of zinc solutionsat 300 bar and a concentration of 0.3 mol/kg. All details have been found in FIG. 3.16 . Different zinc solutions with different anions is observedn. The absorption depending of the mass attenuation coefficient (μ/ρ), where, μ/ρ is 3.29 cm^2/g, 4.49 cm^2/g, and 8.06 cm^2/g for ($ZnSO_4$, $ZnCl_2$ and $ZnBr_2$ respectively), as well as, it depends on the incident energy which have been carried out on 15 KeV.

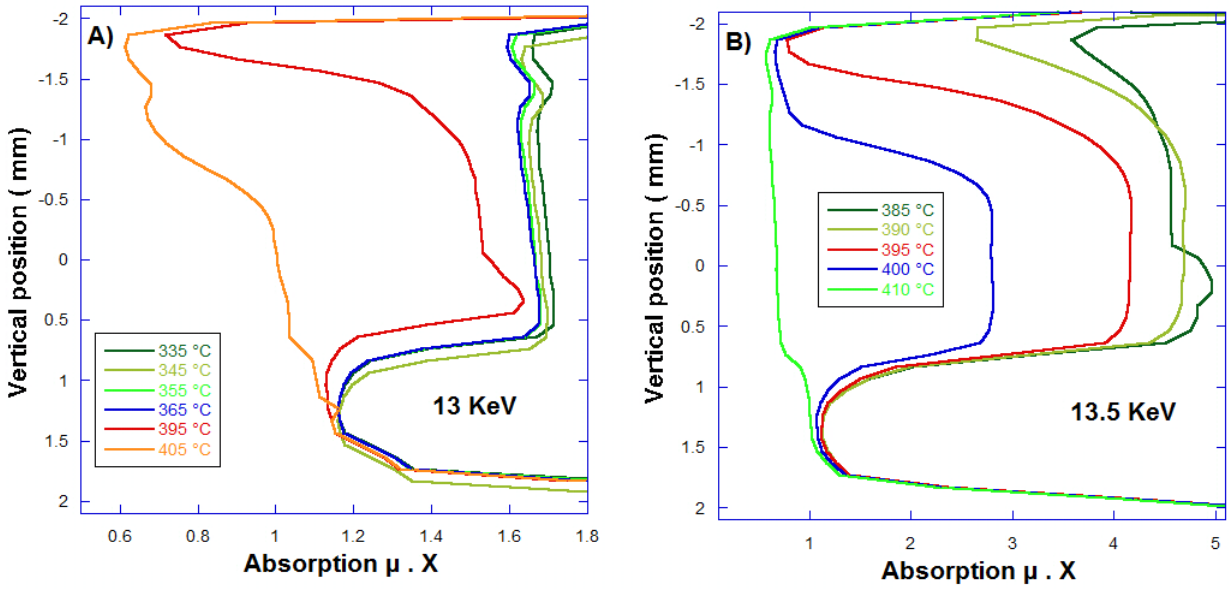

FIG. 3.21 - Scan of the carbon cell in vertical position of an experimental X-ray absorption in transmission mode measured in NaBr_1.0M aqueous solutions at 13 KeV (A) and 13.5 KeV (B) as a function of temperature at 400 bars. The expected base line is 0.482 and sample thickness 0.398 cm, The beam path fixed at lower part of cell.

3.2 HERFD-XAS measurements for Br and Rb

X-ray absorption spectroscopy (XAS) has made major contributions on geophysical research. XAS) is the measurement of transitions from core electronic states of the metal to the excited electronic states and the continuum; the former is known as X-ray absorption near-edge structure (XANES), and the latter as extended X-ray absorption fine structure (EXAFS). These two methods give complementary structural information, the XANES spectra reporting electronic structure and symmetry of the metal site, and the EXAFS reporting numbers, types, and distances to ligands and neighboring atoms from the absorbing element.

XAS allows us to study the local structure of the element of interest without interference from absorption by the water or air. X-ray spectroscopy of bromide aqueous solutions have been a challenge due to the low relative concentration of the element of interest in the sample . We have performed XANES and XAFS measurements on FAME beamline at ESRF for aqueous solutions from ambient to supercritical region. We have been propped Br K 1s threshold (13.474 KeV) and Rb K 1s threshold (15.2 KeV) measurements with a transmission and HERFD-XAS.

X-ray absorption spectroscopy experiments were performed on the CRG-FAME beamline (BM30B), located at the European Synchrotron Radiation Facility storage ring in Grenoble, operating in filling mode at 6 GeV. The experimental details and the set-up were

discussed in section 3.2. We used the autoclave with a crystal analyzer set-up of Si (880) and an angle α 13.673° (FIG. 3.22 and FIG. 3.24). Alkaline bromide aqueous solutions were prepared by dissolving weighted amounts of salts (XBr, 99.999%, Sigma-Aldrich) where, X is Li, Na, K, Rb, and Cs with concentrations 0.3 and 1.0 mol/kg. Spectra were recorded both in fluorescence and transmission modes (~40 min/scan data collection time), at the Br K-edges, using a double-crystal Si(220) monochromator[129]. The size, 300×200 μm^2 (H×V, full width half maximum values), and the position of the X-ray spot on the sample were kept constant during the data acquisition. The full beam delivered by the bending magnet source was focused in the horizontal plane by the 2nd crystal of the monochromator and by the 2nd Rh-coated mirror in the vertical plane. Finally, a feedback system was used to maximize the output of the two-crystal X-ray monochromator[121]. Acquisitions of the XAS spectra μ(E) were recorded simultaneously in the transmission ($\mu_t(E).d = \ln(I_0/I_t)$ and in the fluorescence mode (μ_f (E) $\propto I_f/I_0$) where d is the thickness of the sample, I_0, I_t, I_f are the intensities of the incident, transmitted and fluorescence beams, respectively (FIG. 2.5). Fluorescence detection was achieved using a vortex SDD fluorescence detector.

Measurements were performed under isobaric conditions, 280, 300 and 600 bars from ambient to supercritical conditions. 3 spectra for each temperature is given before critical temperature of water and 6 spectra after this value of temperature. The ecperimental set-up used was in Rowland circle geometry, the detector is located above the sample, along the z_{det} axis (see FIG. 3.22). The total path length from the sample to the diffracting bent crystal and then to the detector equals 1 m. therefore operation under helium atmosphere is compulsory in order to minimize the absorption, using a helium balloon in the area of Rowland circle between the autoclave, detector and CAS.

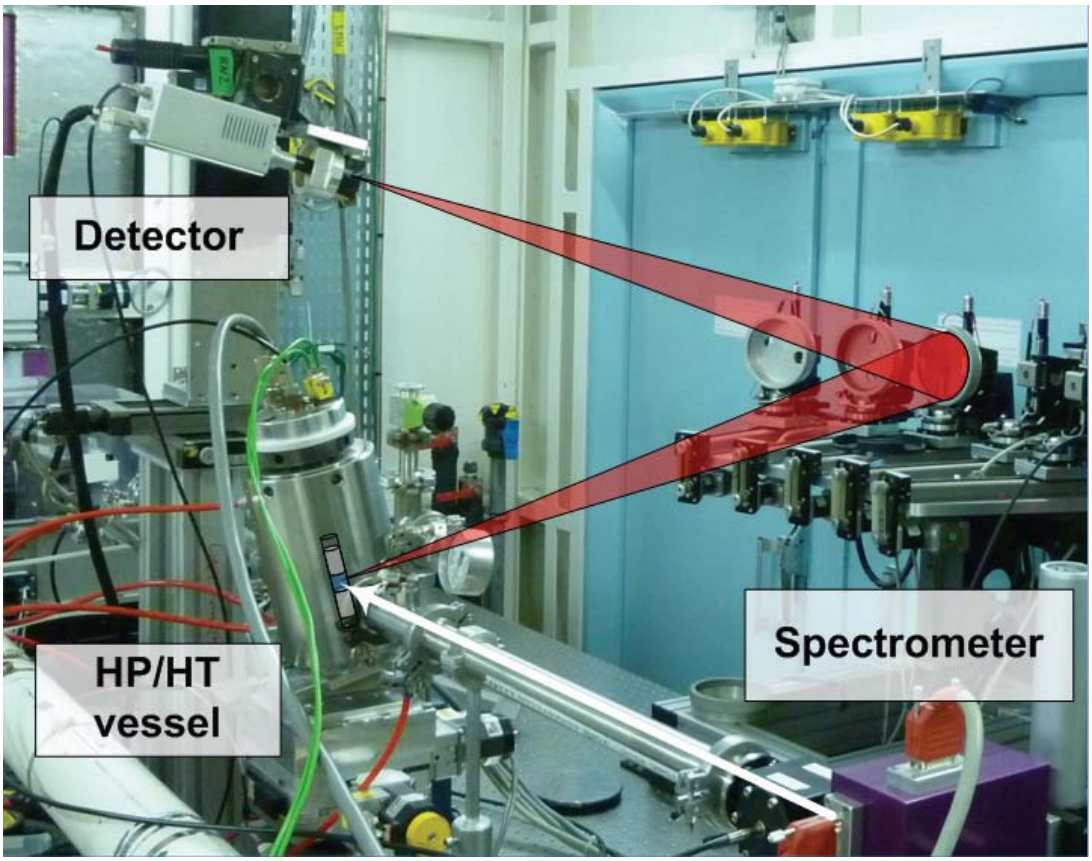

FIG. 3.22 - Set-up in the experimental hutch located in BM30B /CRG FAME beamline at ESRF, Grenoble - France.

The milli-Q water have been tested a carbon cell on XAS measurements in absorption mode, a performance of crystal analyzer spectrometer at Br $K_{\beta 1,3}$ and 280 bars from ambient to supercritical conditions. We have tested the water in the first experiment on FAME beamline to measure the absorption with energy range. As shown in the FIG. 3.23 that the absorption decreases with temperature. The absorption at 400°C is decreasing significantly because we are exceed the critical point. The base line (A) is 0.83 eV and sample thickness (X) is 0.398 cm.

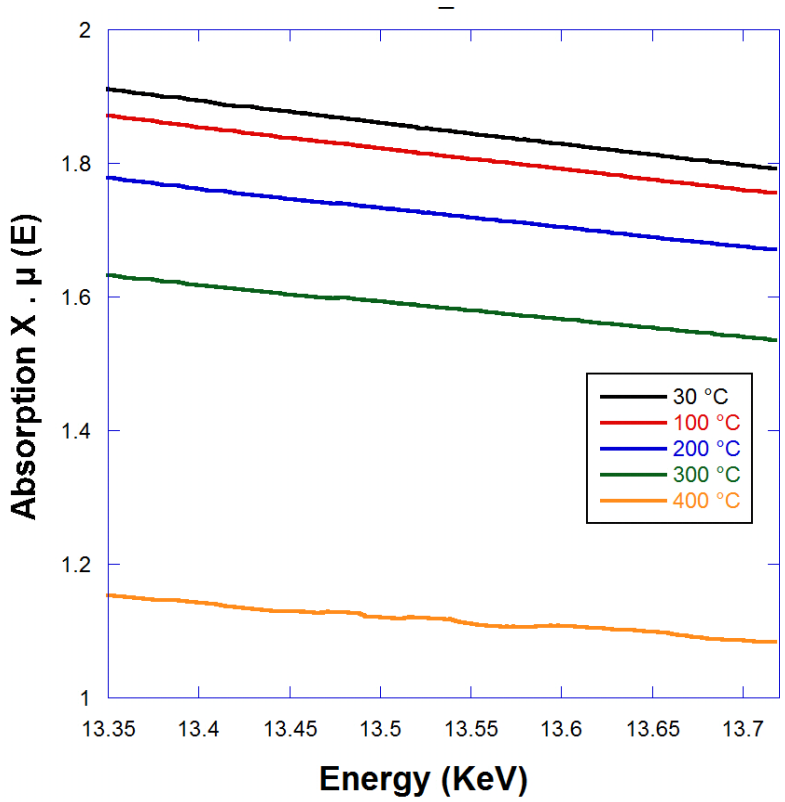

FIG. 3.23 - Experimental X-ray absorption measured in transmission mode for milli-Q water at isobaric condition (280 bars) as a function of temperature.

3.2.1 XANES analysis

XANES spectra recorded on both transmission mode (T-mode) and HERFD-XAS detection for representative compositions at different pressure and temperature conditions are reported in FIG. 3.24. A qualitative description of the XANES data is presented. All spectra display a constant absorption edge at E_0 = 13474 eV with a relativelyintense white line with peak at a constant energy of 13478 eV. The XANES spectrum of the 5 wt% (solid salts) alkaline bromide aqueous solution at room conditions. 95% of Boron nitride of sample mass have been used to insure that there is no interaction with a target sample, because of its characteristics of excellent thermal and chemical stability. The fluorescence spectra at lower molar mass have the same shape with transmission spectra but the difference increases when concntration is higher. This difference is obtained, thanks to the resolution of crystal analyzer spectrometer (CAS). The pre-edge feature in Br K-edge spectra has been attributed to electronic transitions between the 1s core level to an unoccupied p state (BURATTINI et al., 1991).[135] The white lines of RbBr and KBr are different than others which are due to combination of electrons to an unoccupied levels by the multiple scattering of an absorbing atom and neighbors.

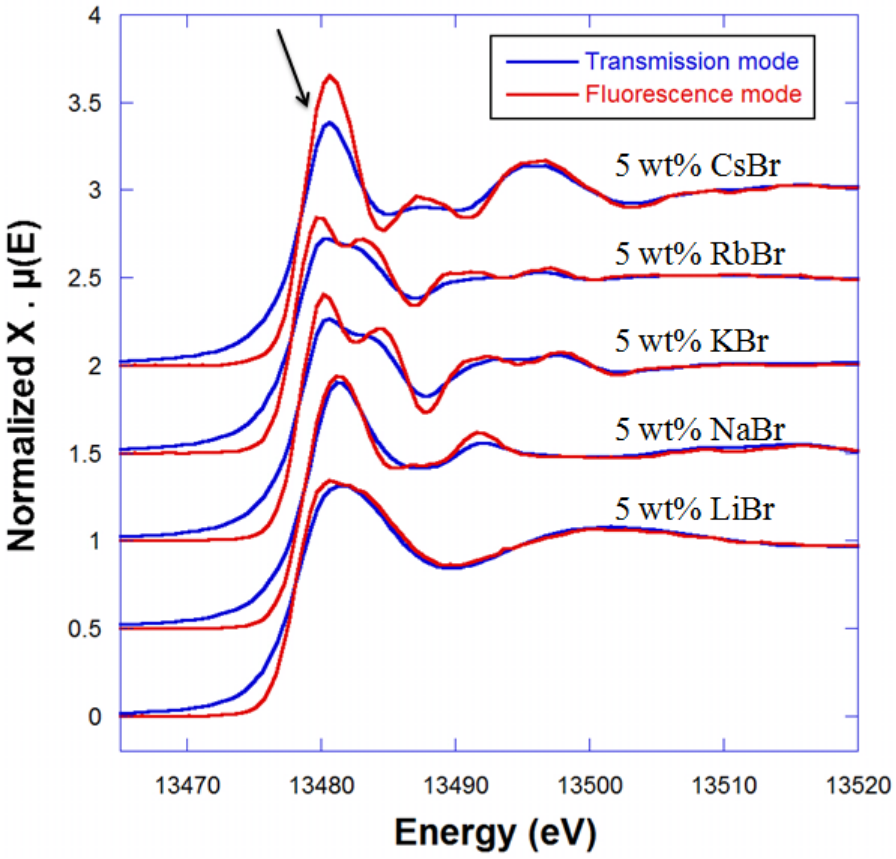

FIG. 3.24 - Normalized XANES spectra at Br-K edge of 5 wt% alkaline Bromide salts at ambient conditions in transmission mode and HERFD-XAS collected from. Spectra are offset for clarity. The black arrow shows the pre-edge and peak features of high resolution of crystal analyzer spectrometer (CAS).

To calibrate the crystal analyzer spectrometer (CAS) and the detector height, as well as the positions of CAS, autoclave, analyzer angle, bragg angle and crystal reflection type, as shown in the FIG. 3.25. The vertical size of the beam is 100μm. All these elements positions have been installed based on Rowland circle with a diameter 1m. The reflection used for the CAS is Si(880) given an angle of 76 °. Woith this setup, the total theoretical energy resolutions *i.e.* Johann geometry, reflection Si(880), Si 220 of monochromator is 0.89 eV while the value experimentally measured is 1.4 eV.

Tests cristaux sur plusieurs rangées

data	rayon de courbure	1000 mm	**cristal**	5.4307 Å	5.4307 Å (Si)
	distance interplanaire	0.480 Å	**indice**	8 (h)	5.657 Å (Ge)
	taille verticale du faisceau	100 µm		8 (k)	
				0 (l)	

énergie			**résolutions théoriques**	**ΔE (eV)**
	énergie de l'analyseur	**13.2914 keV**	due à la réflexion utilisée 2.01E-06	0.03
	angle (α) de l'analyseur	13.673 °	due à l'approximation de Johann	0.33
	angle de Bragg θ=90-α	76.327 °	due à la taille verticale du faisceau	0.32
			total spectromètre	0.46
positions (hauteur du faisceau: 400mm/table)			ligne (Si(220)	0.77
	Xcristal	**944.125 mm**		
cristal central, γ=0°	Zcristal	**629.680 mm**	total ligne + spectromètre	0.89
	Zdétecteur	**859.360 mm**		
	distance cristal - échantillon	**971.661 mm**		

test avec plusieurs rangées		***correction angulaire***	***hauteur du faisceau sur le détecteur***	gamma
2 rangées de cristaux	cristal du haut, γ=4°	**0.069 °**	**861.822 mm**	4
	cristal du haut, γ=-4°	**0.067 °**	**861.660 mm**	-4
3 rangées de cristaux	cristal du haut, γ=8°	**0.279 °**	**869.675 mm**	8
	cristal central	**0.000 °**	**859.360 mm**	0
	cristal du haut, γ=-8°	**0.261 °**	**868.355 mm**	-8

largeur du faisceau	**11.16 mm**
hauteur centrale du faisceau	**mm**

FIG. 3.25 - Crystal tests of different energy ranges with two kind of crystal reflections Si and Ge. Analyzer energy, analyzer angle (α), bragg angle and elements positions are shown. The theoretical resolution (ΔE) of Br $K\beta_{1,3}$ is 0.89 eV whereas, experimentally is 1.4 eV.

Br-K edge XANES spectra in transmission mode and HERFD-XAS have been carried out for alkaline bromide aqueous solutions in energy range of 400 eV at different pressures and concentrations from ambient to supercritical regions. FIG. 3.26 shows T-mode XAS spectra of solutions. The spectra measured are nearly logical, thereby demonstrating the applicability of T-mode XAS, as performed in the present work, as a quantitative technique for Br K-edge XAS in solutions. Further evidence for the reliability of T-mode XAS is presented in FIG. 3.26 at different pressures, which compares the difference spectra for some alkali bromide solutions measured by T-mode XAS as a function of temperature. The concentration is 0.3 mol/kg and 280 bars, increase the temperature means the number of water molecules decrease, so the white line of the spectra must be decrease. We observe by transmission mode that white line of RbBr and LiBr begins increase at 389 °C. All solutions have peaks areas expander than salts (references), and pre-edges shifted to the lower energy when increase the temperature. The crystals RbBr and KBr have two combinations of absorption at white line located at 13480 eV and 13483 eV.

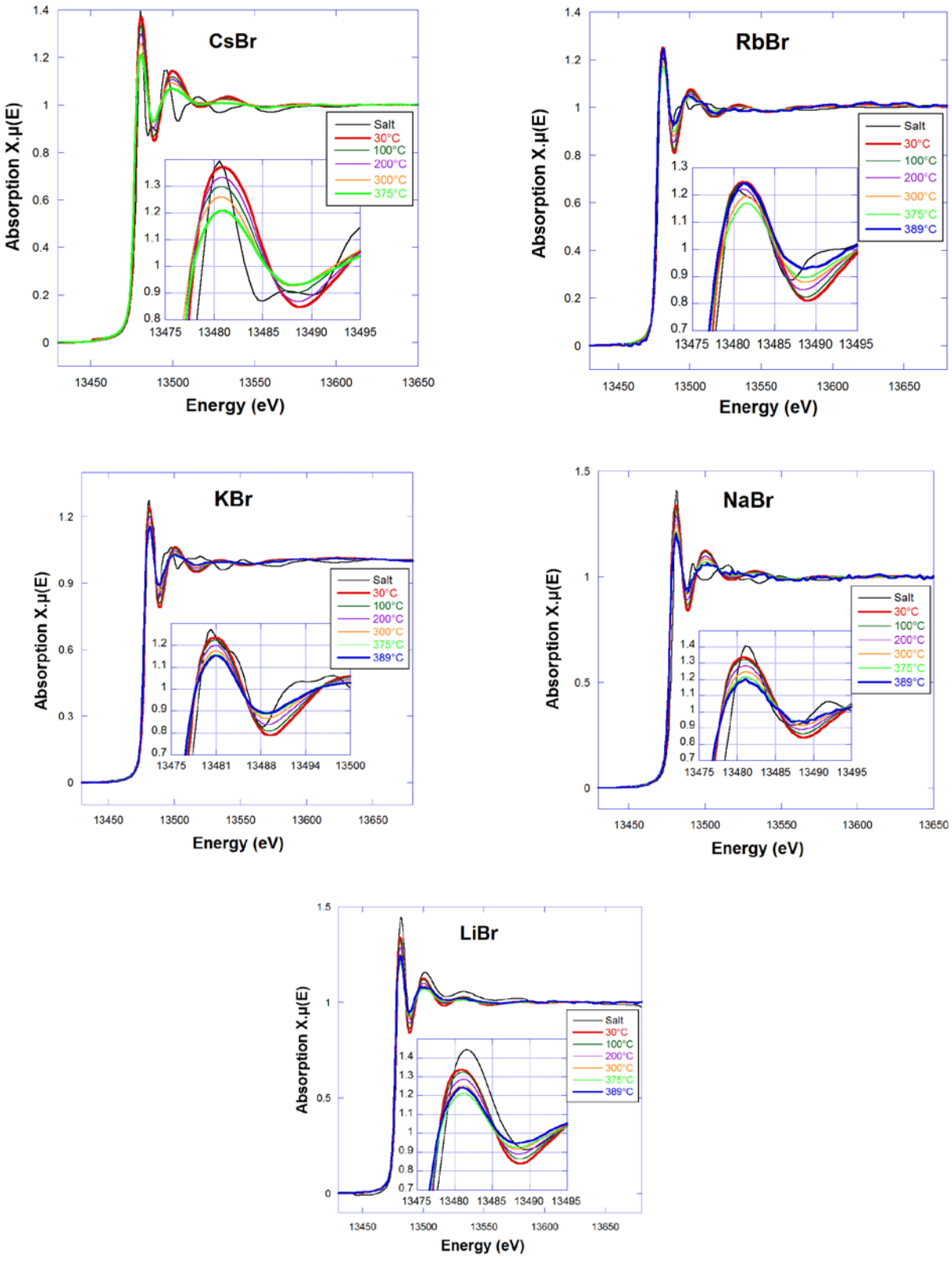

FIG. 3.26 - Normalized Br-K edge XANES spectra collected in transmission mode on alkaline bromide aqueous solutions (0.3 mol/kg) at 280 bars from ambient to supercritical conditions.

FIG. 3.27 shows Br-K edge XANES spectra in fluorescence mode at 0.3 mol.kg and 280 bars for alkaline solutions and corresponding salt reference. Clearly, the spectrum of salts (references) have white lines more structured than aqueous solutions.

We observe that pre-edges of CsBr are shifted towards low energies when temperature increased. The white lines decreased with temperature up to 395 °C, then, at 395 °C increase in anomalous behavior with two combinations of absorption occur clearly, as well as, the peak seems with two combinations at 30°C . For RbBr, pre-edge shifted to lower energy when increase the temperature. All whit lines have two combinations of absorption, the white lines decreases with temperature until 389 °C, then increase in anomalous behavior with two combinations. For KBr, the theoritecal spectrum has shown that there are two combination of absorption, pre-edge shifted to lower energy when the temperature increased. All whit lines have two combinations of absorption, the white lines decreased with temperature up to 389 °C, then increase in anomalous behavior with two combinations. For NaBr, the pre-edge shifted to lower energy when increase the temperature. First two temperate have two combinations of absorption, the white lines decreases with temperature until 389 °C, then increase in anomalous behavior with two combinations too. For LiBr, the pre-edge shifted to lower energy when increase the temperature. All whit lines have two combinations of absorption, the white lines decreases with temperature until 389 °C, then increase in anomalous behavior with two combinations.

From ambient to supercritical region of all alkaline bromide aqueous solutions, it was observed the white lines increase with two combinations of absorption in function of temperature. At ambient temperature, the higher combination located in the left part of the peak, and the other part located in the right, in the contrary, at supercritical region, we observed that the combinations still have two values with shift the higher to the right side and lower to the left. In other words, the higher combination has shifted to a higher energy with a temperature and lower combination has shifted to a lower energy with a temperature. Table 12 shows the white lines of fluorescents spectra of alkaline bromide aqueous solutions at 280 bar.

In other words for all solution, the heigh of the white line (hydration) decreases with the temperature until 375 °C and then increases (Table 12). Clearly there is a structural change above 375 °C.

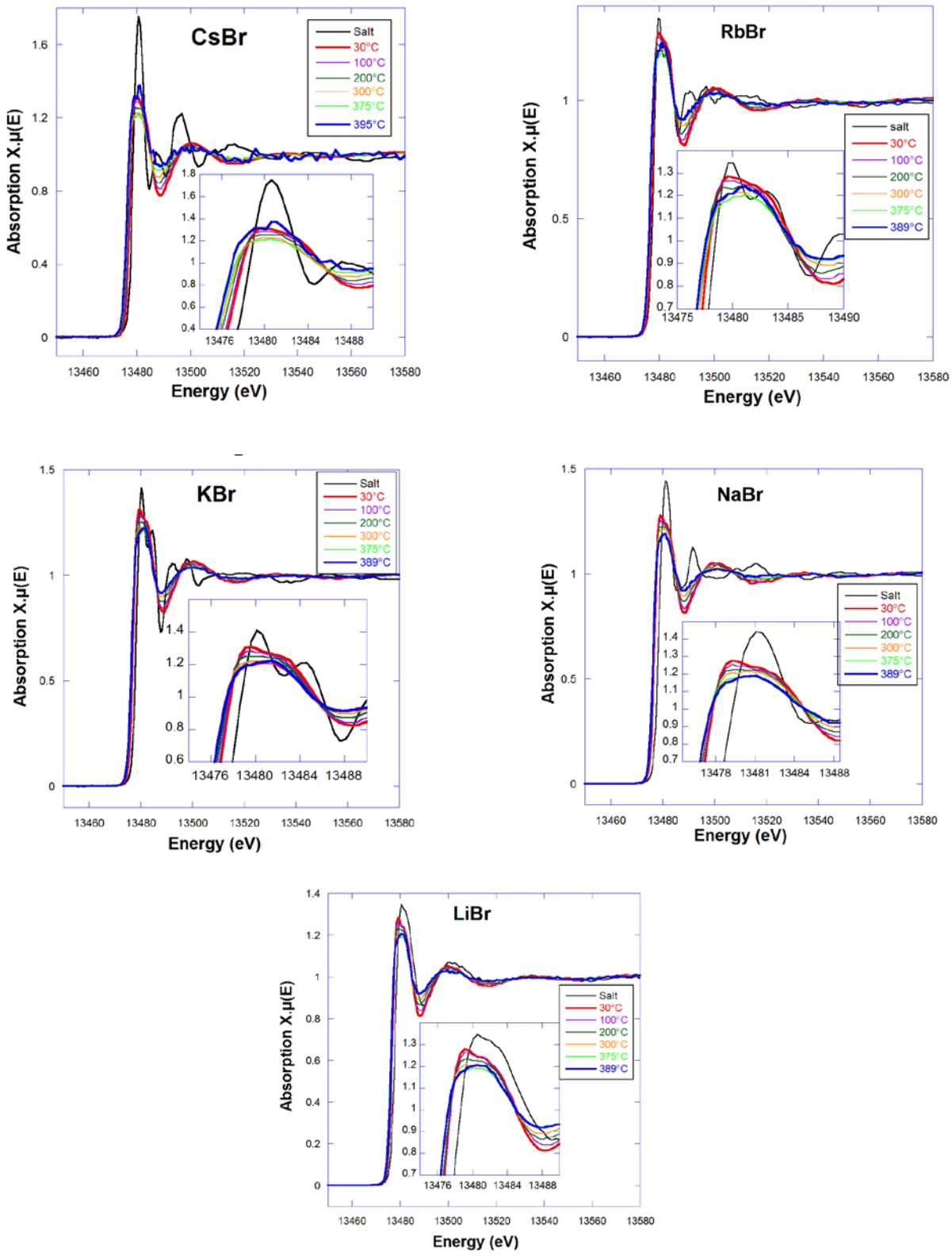

FIG. 3.27 - Normalized Br-K edge XANES spectra collected in HERFD-XAS for alkaline bromide aqueous solutions (0.3 mol/kg) at 280 bar from ambient to supercritical conditions.

Table 12: White line values of alkaline bromide aqueous solutions collected in HERFD-XAS (0.3 mol/kg) at 280 bar as a function of temperature.

Temperature (°C)	CsBr	RbBr	KBr	NaBr	LiBr
30	1.3172	1.2846	1.2855	1.276	1.2792
100	1.2874	1.2677	1.2666	1.253	1.265
200	1.2545	1.2404	1.2363	1.2244	1.2324
300	1.2254	1.216	1.2109	1.214	1.2092
375	1.2178	1.2028	1.1997	1.1849	1.1909
389	-	1.2427	1.2099	1.1929	1.2053
395	1.3774	2.8056	-	-	1.2856

FIG. 3.28 shows spectra recorded in transmission detection mode at two pressures 300 and 600 bar for 0.3 mol/kg CsBr and compared to the salt spectrum. The white lines at 300 bars decrease harmoniously without anomalous behavior. The white lines at 600 bars decrease until 400 °C then increase at 450°C with anomalous behavior at pre-edge. The spectra shifted to the lower energy when increase the temperature at pre-edges.

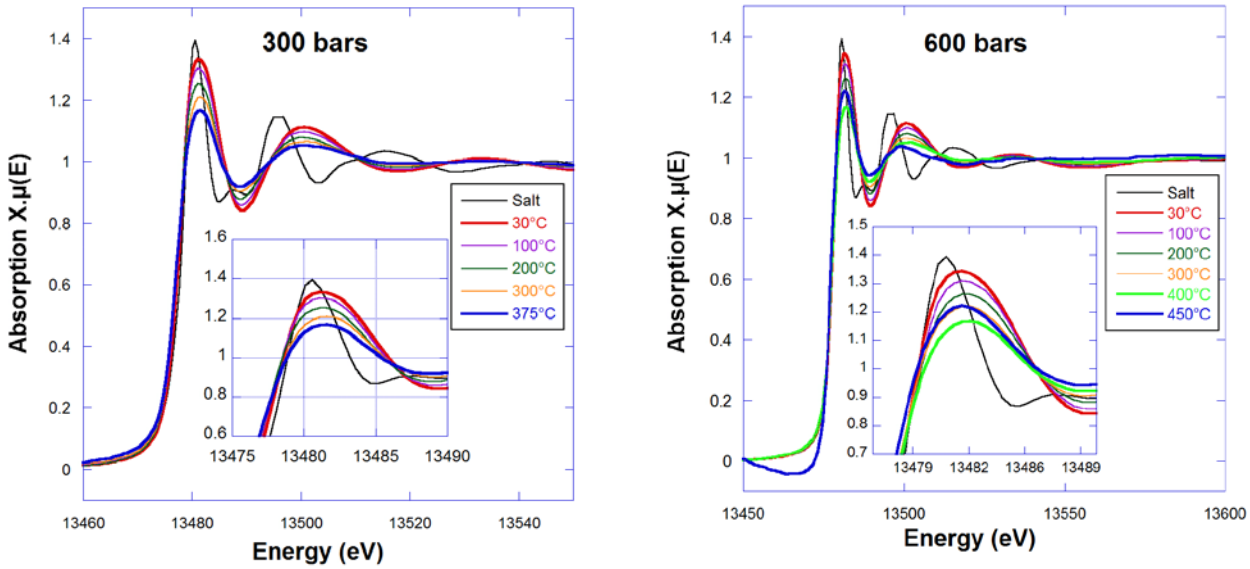

FIG. 3.28 - Normalized Br-K edge XANES spectra collected in transmission detection mode of cesium bromide aqueous solutions (0.3 mol/kg) at 300 and 600 bar from ambient to supercritical conditions.

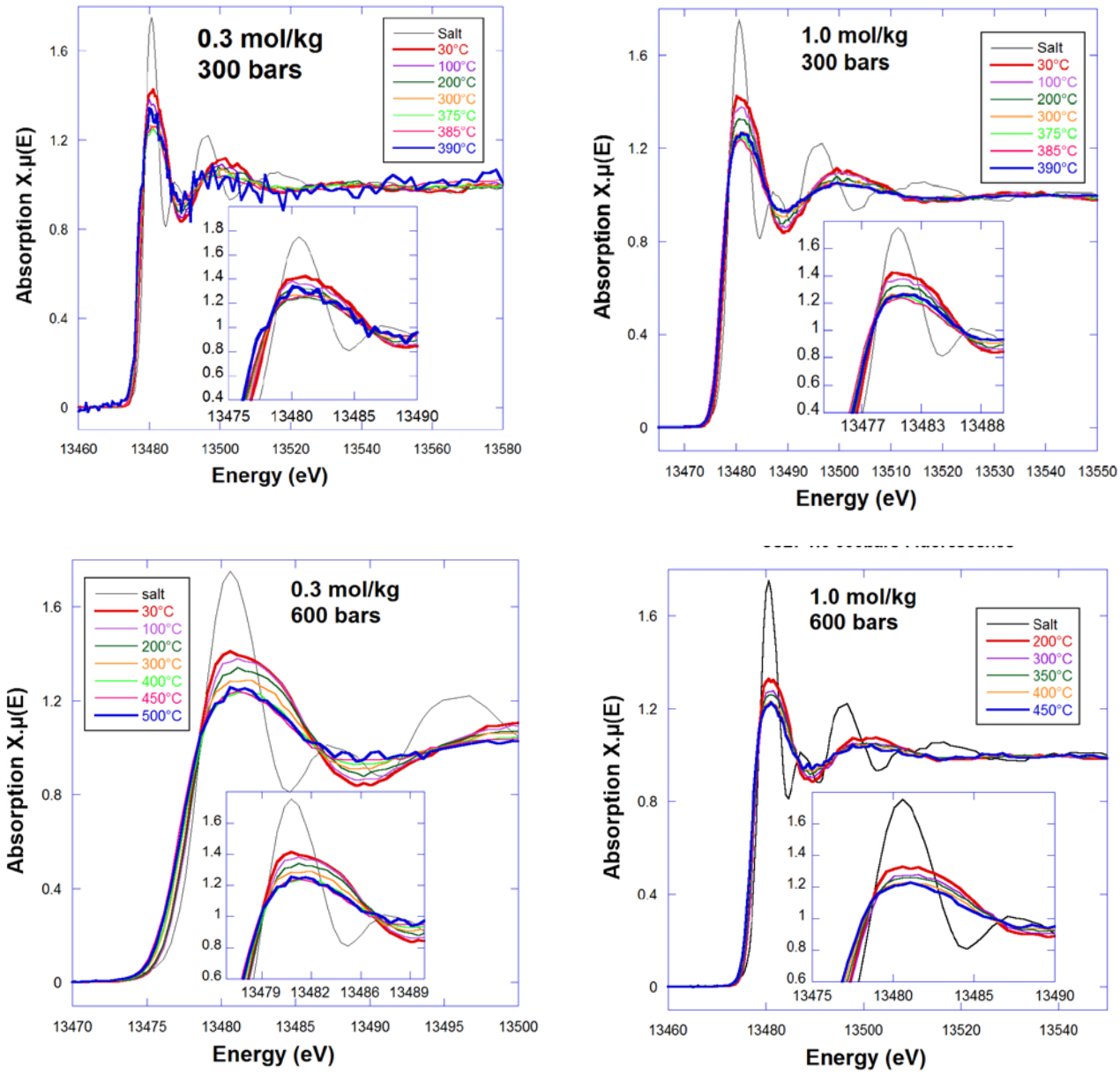

FIG. 3.29 - Normalized Br-K edge XANES spectra collected in HERFD-XAS of cesium bromide aqueous solutions (0.3 mol/kg and 1.0 mol/kg) at 300 and 600 bar from ambient to supercritical conditions.

To see the influence of ions at supercritical region, XAS measurements were performed on cesium bromide aqueous solutions (0.3 mol/kg and 1.0 mol/kg) and under two isobaric conditions at 300 and 600 bar FIG. 3.29.

- For CsBr 0.3 mol/kg at 300 bars, pre-edges shifted to lower energy when increase the temperature. The combinations of absorption are clear at peak of ambient located at left part (lower energy) of the peak but there is a noise at supercritical region, the white lines decreases with temperature until 375 °C, then increase in anomalous behavior with large ratio of noise at 390°C, as well as, we observed around the edge ~

13477 ev of cesium bromide spectrum a feature corresponding to the 1s to 4p transition[135].

- For CsBr 0.3 mol/kg at 600 bars, pre-edges shifted to lower energy when increase the temperature except the spectrum at 390°C shifted to high energy. The combinations of absorption are clear at peak of ambient located at left part (lower energy) of the peak but start shifted to the right of peak (higher energy) with temperature, the white lines decreases with temperature until 385 °C, then increase in anomalous behavior.

- For CsBr 1.0 mol/kg at 300 bars, pre-edges shifted to lower energy when increase the temperature. The combinations of absorption are clear at peak of ambient located at left part (lower energy) of the peak but start shifted to the right of peak (higher energy) with temperature, the white lines decreases with temperature until 400 °C, then increase in anomalous behavior.

- For CsBr 1.0 mol/kg at 600 bars, pre-edges shifted to lower energy when increase the temperature. The combinations of absorption are not clear at peaks but there are an evidence at the peaks which implies most probably of ion-pairs exist. the white lines decreases with temperature without observe an increase of a white line at SC temperature.

The spectra at SC region exhibit noise due to the sensitivity of Br K-edge with HERFD-XAS. The theoretical spectra have been recorded at ambient conditions, the solutions indicate that anions and cations are interconnected by an extended network of hydrogen bonds. Hydrogen-anion contacts dominate the interactions and each bromide ion is in close contact with six hydrogen atoms, with different bonds length.[136]

Table 13: White line values of Cesium bromide aqueous solutions at different concentrations and pressures as a function of temperature.

Temperature (°C)	**CsBr 0.3M 300bars**	**CsBr 1.0M 300bars**	**CsBr 0.3M 600bars**	**CsBr 1.0M 600bars**
30	1.4281	1.4137	1.4217	-
100	1.3832	1.3819	1.3788	-
200	1.3412	1.3418	1.3289	1.3289
300	1.2666	1.288	1.2689	1.2789
375	1.2496	-	1.2451	1.2611
385	1.2616	-	1.2394	-
390	1.3421	-	1.2667	-

400	-	1.2338	-	1.2335
450	-	1.2418	-	1.2277

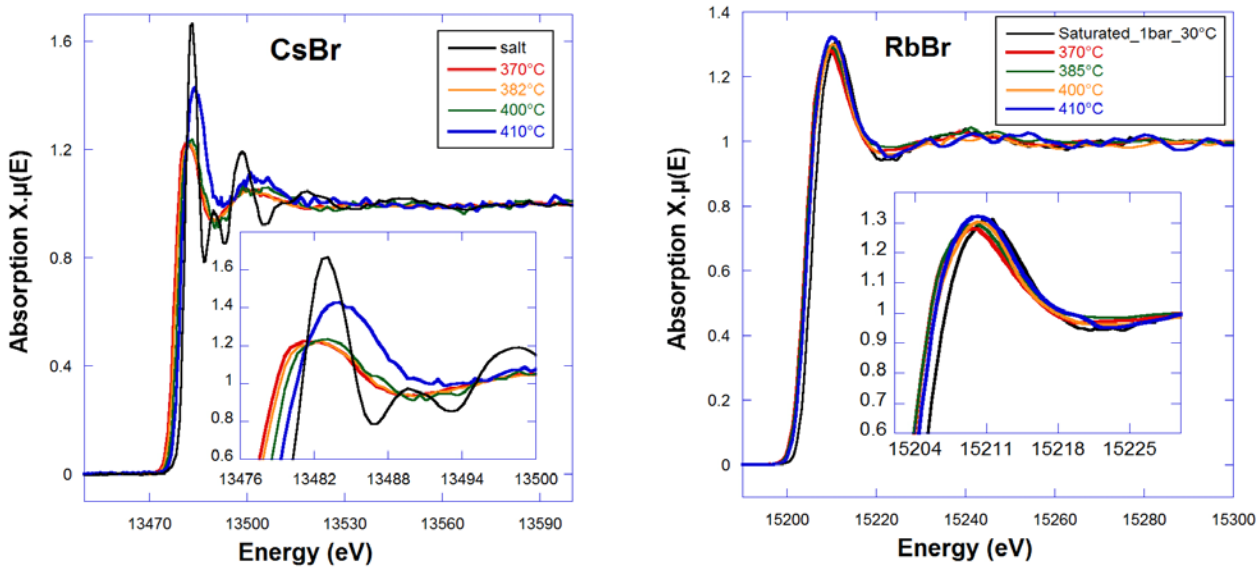

FIG. 3.30 - Normalized Br-K edge and Rb-K edge XANES spectra collected in HERFD-XAS on cesium and rubidium bromide aqueous solutions (0.3 mol/kg) at 300 bar at supercritical region. Black spectrum in left figure is 5 wt% CsBr and black spectrum in right figure is saturated RbBr 6.0 mol/kg.

FIG. 3.30 shows spectra have been carried out of CsBr and RbBr at 0.3 mol/kg and isobaric process of 300 bars at SC region. The analysis of the spectra is illustrated as following:

- For CsBr, we observed that pre-edges shifted to higher energy when increase the temperature of SC spectra started from 382°C. The combinations of absorption are not clear occur but there are an evidence of ion-pairs on peaks of white lines, the white lines increase with temperature from 382 °C to 410°C, the spectrum at 410°C has an anomalous behavior with significant shift of the peak to higher energy which is implies an exist of ion-pairing clearly (Table 13). The theoretical spectrum is anhydrous CsBr 5 wt%.

- For RbBr, we observe that pre-edges shifted to higher energy when increase the temperature of SC spectra started from 385°C. The white lines increase with temperature from 385 °C to 410°C. The reference spectrum is a saturated solution 6.0 mol/kg recorded at ambient conditions.

Table 14: White line values of cesium and rubidium bromide aqueous solutions (0.3 mol/kg) at 300 bar as a function of temperature at supercritical region.

Temperature (°C)	CsBr	RbBr
370°C	1.2232	1.2199
382°C	1.2247	1.1811
400°C	1.2366	1.2389
410°C	1.4308	1.2408

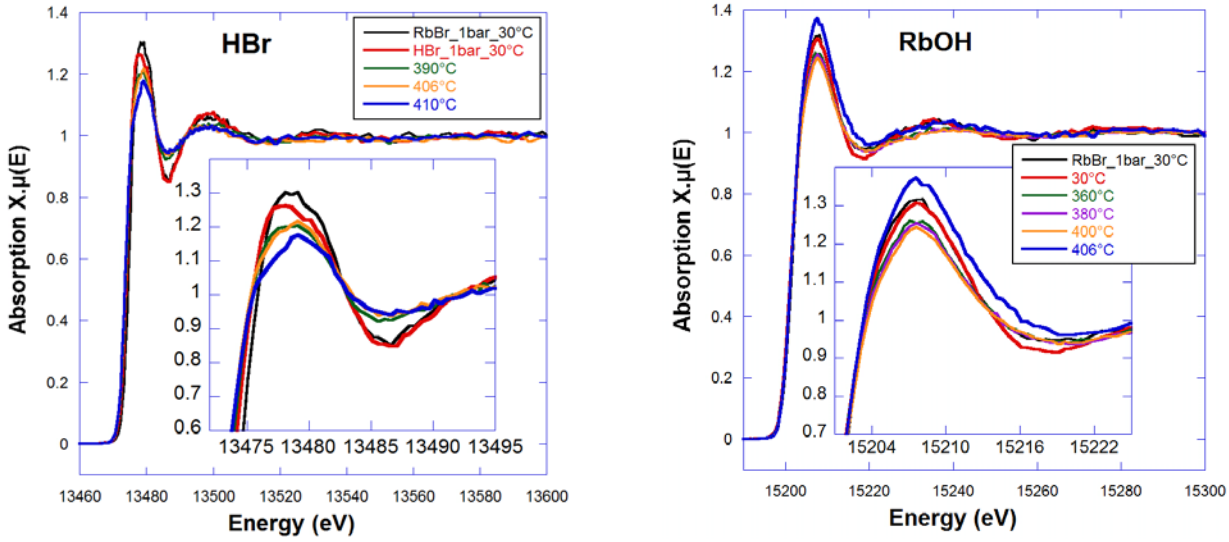

FIG. 3.31 - Normalized Br-K edge and Rb-K edge XANES spectra collected in HERFD-XAS (0.3 mol/kg) at 300 bar and of Hydrogen bromide and Rubidium hydroxide aqueous solutions from ambient to supercritical conditions. Black spectra are saturated RbBr 6.0 mol/kg.

FIG. 3.31 shows spectra have been carried out of CsBr and RbBr at 0.3 mol/kg and isobaric process of 300 bars from ambient to SC region. The analysis of the spectra is illustrated as following:

- For HBr, we observe that pre-edges shifted to lower energy when increase the temperature. The white lines decrease with temperature, the spectrum at 406°C has an anomalous behavior by increase the white line obviously. The reference spectrum corresponds to a saturated solution 6.0 mol/kg at ambient conditions at both Br K-edge and Rb K-edge.

- For RbOH, we observe that pre-edges haven't shifted when increase the temperature. The white lines decrease with temperature, the spectrum at 406°C has an anomalous

behavior by increase the white line obviously. The reference spectrum is corresponds to a saturated solution 6.0 mol/kg has performed at ambient conditions at both Br K-edge and Rb K-edge.

The Br K-edge XANES fluorescence white lines at different Pressures and concentrations of alkaline bromide aqueous solutions as a function of temperature from ambient to supercritical conditions are shown in the FIG. 3.32. From ambient temperature, the white lines decrease by dehydration process up to certain value of temperature, it's shown clearly that at 280 bars, the white line decreases up to 375°C, at 300 bars, the white line decreases up to 390°C, and up to 400°C at 600 bars. Then they start increase in an anomalous behavior. The evidence of anomalous effect is clear at 280 bars and 300 bars with 0.3 mol/kg comparing with others at 600 bars and 0.3 mol/kg. This observation of XANES fluorescence white lines is important which is indicate of a new local structure which can be linked to the formation of ion-pairing.

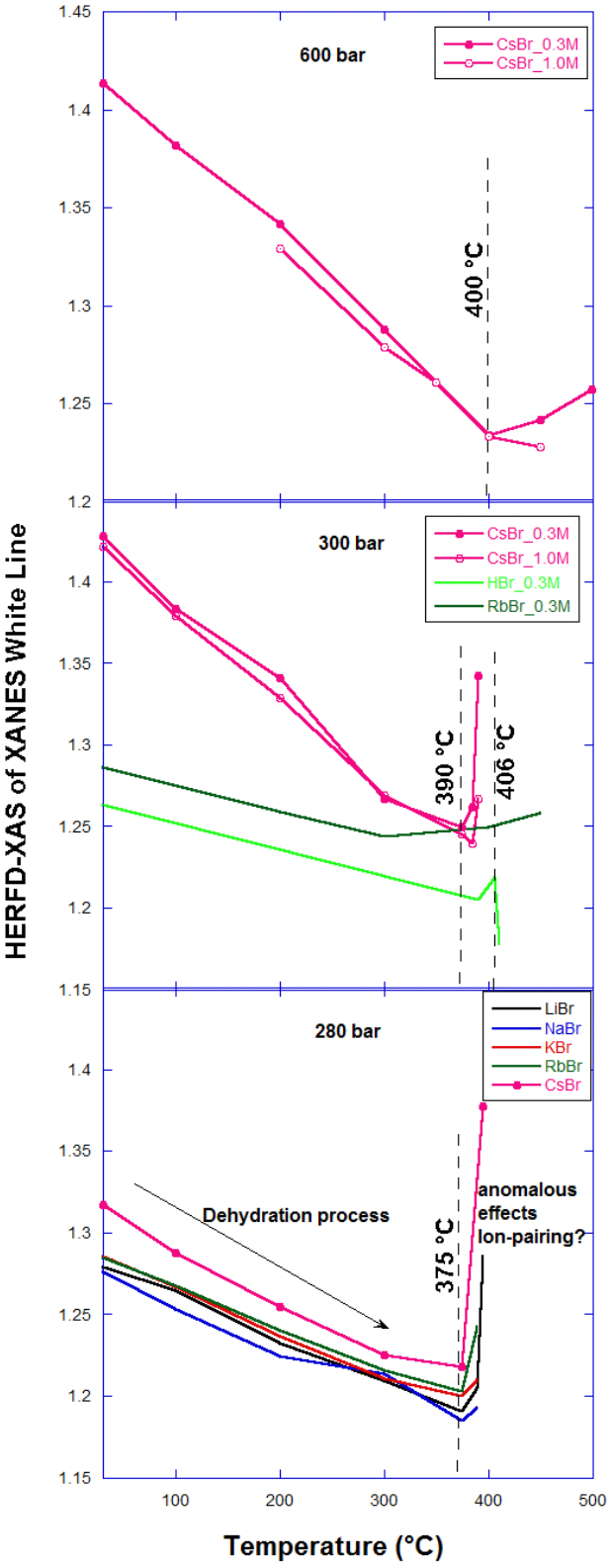

FIG. 3.32 - Br K-edge XANES white lines collected in HERFD-XAS of alkaline bromide aqueous solutions (0.3 mol/k and 1.0 mol/kg) at 280, 300, and 600 bar as a function of temperature. The black arrow shows the dehydration process before increase the white lines. The vertical dashed line is guide the temperature value by increase the white line in anomalous effect.

3.2.2 EXAFS analysis

X-ray Absorption Spectroscopy has been widely used to characterize the speciation of ions in aqueous solutions from ambient to supercritical (or hydrothermal) conditions (for a recent review on the subject see for example Brugger et al.[137]). In this context several extended x-ray absorption fine structure studies concerning Br speciation are noticeable :

- on trivalent salts such as $GaBr_3$[138], YBr_3.[139]
- on divalent salts such as $ZnBr_2$[140,141], $MnBr_2$.[142]
- on monovalent such as RbBr[143], KBr and CsBr.[107]

The number of studies focused on the Br, the anion, is smaller than the number of studies focused on the cations. Two main reasons for this, linked to two difficulties.

One of the difficulty for this kind of studies is intrinsic to the electronic properties of Br : multi-electronic excitation (MEE) occurs, which modified slightly the shape of the X-ray absorption signal after-edge. For Br, two main MEE decay channels have to be considered, corresponding to 1s to 3d and 1s to 3p transitions.[144] Height, position in energy and width of these transitions depend on the considered system (Table 15). This effect, if it is not taken into account, modify the shape of the EXAFS oscillations. EXAFS software can correct easily it, but this is still a correction, with the errors associate with it : which MEE parameters do we have to consider ? Do my corrections induce an artefact of not ?

Table 15 : Br multi-electronic excitation characteristics

Double-excitation		1s → 3d			1s → 3p		
Ref.	Compound	$E_{d-e} - E_s$ (eV)	H	ΔE (eV)	$E_{d-e} - E_s$ (eV)	H	ΔE (eV)
144	HBr	90±5	0.05±0.01	20±10	200±10	0.016±0.004	50±10
	Br_2	105±10	0.4±0.2	60±20	190±10	0.019±0.005	50±10
145	NBr solution	91	0.05		205	0.018	
	$EuBr_3$ eth. sol.	80			203		
146	KBr aq. sol.	77	0.02		203	0.0025	

The other difficulty of EXAFS measurement performed on Br in aqueous solution is that even the structure in ambient conditions is badly known, because there is a large Br-H_2O distribution of distances and coordination numbers (see for example the recent work of Antalek *et al.*)[147]. The initial parameters needed to perform relevant EXAFS simulations are then difficult to define. To determine by EXAFS in our case if there is Br-X (where X is an alkaline element) bound in supercritical conditions among the Br-H_2O bounds (which persists in these conditions)[143], remains then challenging.

XAS measurements were collected at the Br K-edge from ambient to supercritical conditions at 300 bars, on FAME beamline. The HP-HT setup is the one previously described and developed by Testemale et al.[2] Measurements have been done both in fluorescence and transmission modes, using a Ge 30-element solid state detector for the fluorescence detection.

Five Br-alkaline salts were probed in aqueous solutions : LiBr (0.3 mol/l), NaBr (0.3 mol/l), KBr (0.3 mol/l), RbBr (0.05 and 0.3 mol/l) and CsBr (0.3 mol/l).

EXAFS extraction was performed using Athena software. We apply the MEE Br correction parameters given by D'Angelo *et al.* for HBr.[144] We did not perform any simulations, but we calculated the backscattering amplitude functions for each Br-alkaline pair. This calculation was done with Artemis (FEFF6.0).

In order to better show the small differences we expect between the signals, we plot the difference EXAFS spectra, taking as a reference the EXAFS spectrum in ambient conditions of each set of spectra. This technique is named DiffEXAFS and "it may be used to examine any situation where the modulation of a sample property results in some small degree of atomic perturbation on a local scale.[148]

The EXAFS signals derived from the normalized of alkaline bromide aqueous solutions spectra reported in the FIG. 3.33 (k^2-weighted EXAFS spectra) and FIG. 3.34 (difference k^2-weighted EXAFS spectra).

The first observation is that the EXAFS signals are completely dominated by the low k-region signal, characteristic of the Br–O backscattering. By looking at the difference spectra (FIG. 3.34) we can see clearly that the amplitude of oscillations decreased with the temperature :

- progressive dehydration occurs with temperature,
- Br is still bound to water molecules at high temperature, in the SC conditions, as found by Ferlat et al.[107,143]

The second observation is that at high temperature, the difference EXAFS signals seems to increase in the high k-region (arrow on FIG. 3.34). This increase might be due to Br-alkaline ion pairing :

- for LiBr and NaBr no effect is visible, but in these cases the acquisition was performed only up to 350°C (precipitation occurs after). Moreover, if ion-pairing would occur,

the effect will be superimposed to the Br-O signal, backscattering amplitudes being maximum in the same k region.

- for KBr, RbBr and CsBr, this increase occurs at 375°C or 400°C. The increase can be seen as an inversion of the local maxima of the oscillations

Br is hydrated in ambient conditions, and this hydration remains up to the SC conditions. Modifications in the evolution of the EXAFS spectra with temperature seem to indicate that ion-pairing occurs for KBr, RbBR and CsBr in SC conditions.

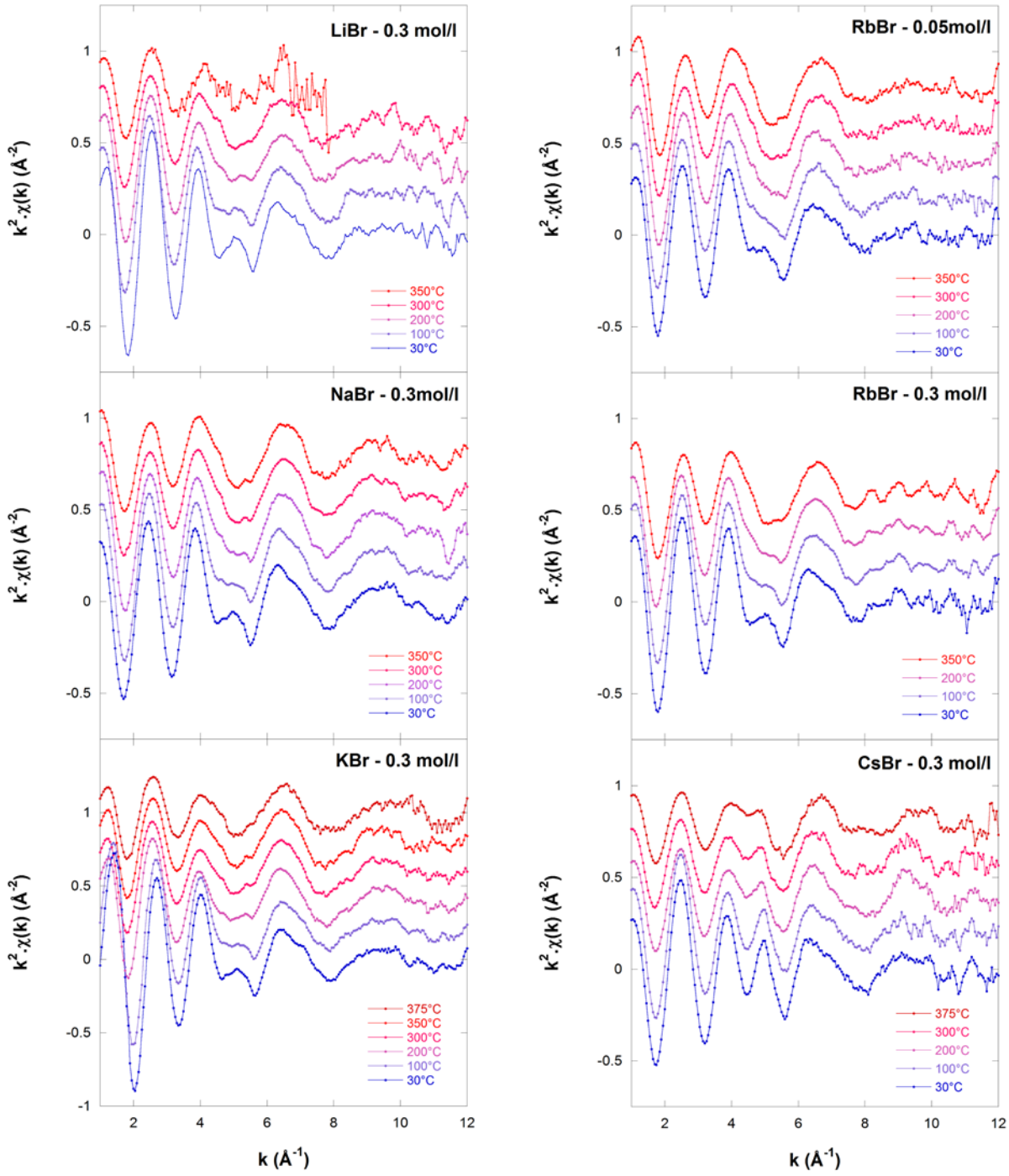

FIG. 3.33 - Br k-edge k^2-weighted EXAFS oscillation of alkaline aqueous solutions at 300 bar as a function of temperature. Spectra are corrected from the MEE effects.

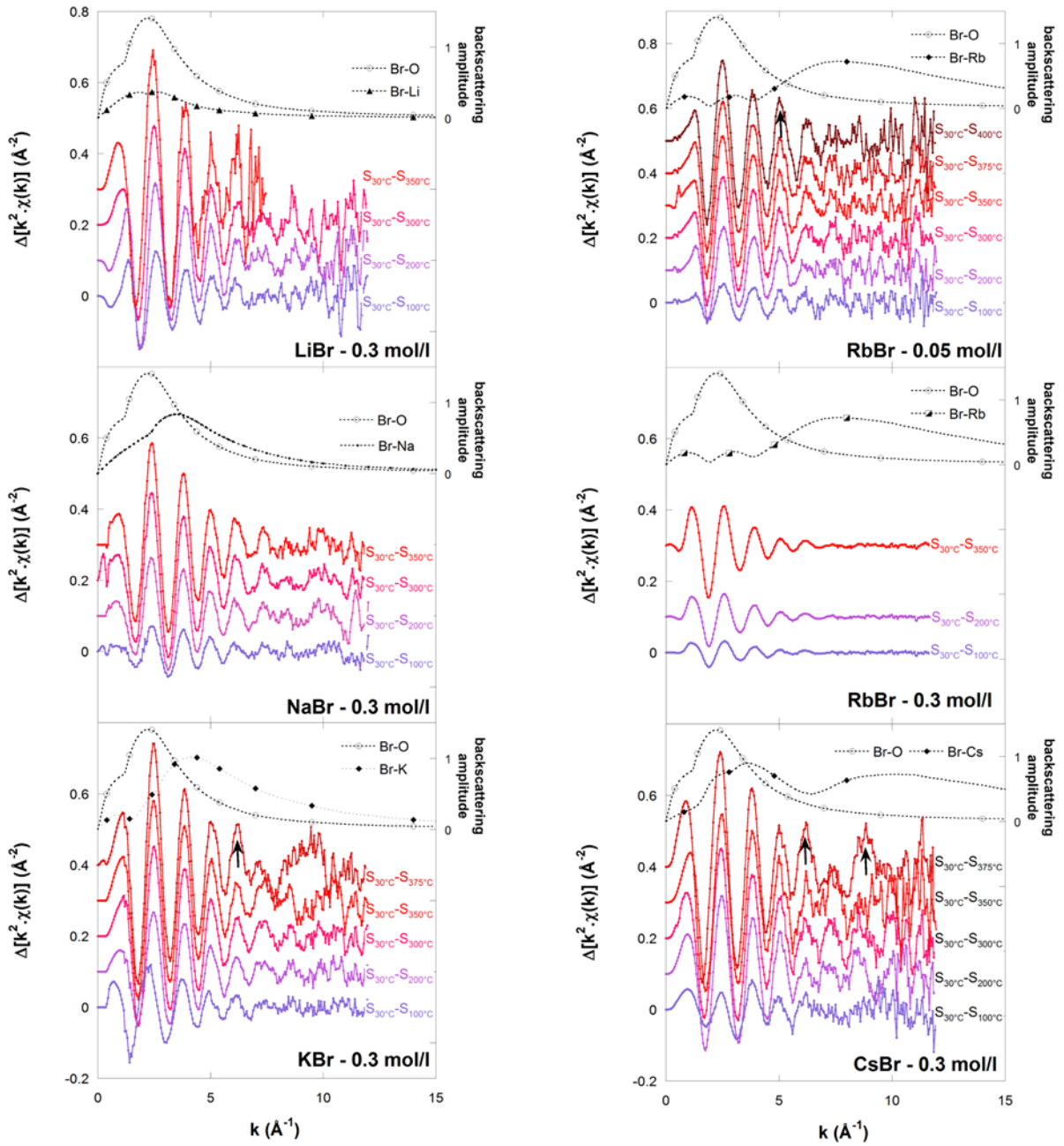

FIG. 3.34 - Br k-edge k^2-weighted DiffEXAFS oscillation of alkaline aqueous solutions at 300 bar as a function of temperature. Spectra are corrected from the MEE effects. Br-O and Br-alkaline backscattering amplitude functions were superimposed to determine visually if ion pairing occurs.

3.3 Summary (English)

In this chapter, I have clarified the phase separation (liquid-gas) and ion-pairing correlation using conventional XAS measurement and Crystal Analyzer Spectrometer (CAS) of aqueous solutions from ambient to supercritical region.

The experimental measurements of water and aqueous solutions (Alkaline bromide, chloride, nitrate, and sulfate) have been performed at different concentrations and pressures as a function of temperature. Phase separations of some solutions have been observed and ion-pairing correlation in SC region. I have performed XANES analysis. The experimental densities have been calculated by several methods. XANES results have proved the effect of ion-pairing in the white lines. EXAFS spectra have proved that there is an ion-pairing in supercritical condition by increase of the signature of cation-anion amplitude with temperature. Crystal analyzer Spectrometer (CAS) has been used at Br K-edge of alkaline group.

The white lines decrease by dehydration process up to certain value of temperature, and then they start increase in an anomalous behavior. The evidence of anomalous effect is clear at 280 bars and 300 bars with 0.3 mol/kg. This observation of XANES fluorescence white lines can be correlated to the existance of ion-pairing.

3.4 Summary (French)

Dans ce chapitre, J'ai mis en évidence la séparation de phases (liquide-gaz) et sa corrélation avec la formation de paires d'ion par des mesures conventionnelles d'absorption XAS et par des mesures haute résolution par cristaux analyseurs sur des solutions aqueuses des conditions ambiantes aux conditions supercritiques.

Les mesures expérimentales sur l'eau et les solutions aqueuses (Bromo alcalin, chlorure, nitrate et sulfate) ont été effectués à différentes concentrations et pressions en fonction de la température. La séparation de phases a été observée pour certaines solutions et celle ci a pu être corrélée à l'appariement d'ions dans la région SC. J'ai effectué des analyses XANES. Les densités expérimentales ont été calculées par plusieurs méthodes. Les résultats XANES ont montré également l'appariement d'ions à partir de l'évolution de la raie blanche. Les spectres EXAFS ont prouvé également l''existance de cet appariement d'ion avec l'augmentation du signal d'amplitude correspondant à la présence de paires d'ion. La haute résolution par l'utilisation d'un spectromètre à cristaux analyseurs (CAS) a été utilisés au seuil du Br pour différents cations.

Les raies blanches diminuent selon le processus de déshydratation jusqu'à une certaine valeur de température, puis elles commencent à augmenter dans un comportement anormal. L'effet anormal est particulièrement claire à 280 bars et 300 bars pour une concentration en sel de 0,3 mole / kg. Cette observation des raies blanches permet également de valider l'apparition de paires d'ion.

Chapter 4: *Discussion and Conclusion*

4. Discussion and conclusion

4.1 History of ion-pairs

Several studies and a lot of experiments measurements have been carried out on phase separation of aqueous solutions and ion-pairing on Br-Kedge from ambient to supercritical conditions at different concentrations.

The Liquid-Vapor relation for the system NaCl-H_2O has been studied by **Bischoff** et al [3,4,108,132]. He has performed an experimental data on the vapor-liquid equilibrium relations were compiled and compared in order to provide an important estimate of the P-T-x surface between 300°C to 500°C. He has been presented the results in theoretical modeling to the understanding of two-phase behavior in saline geothermal systems. Also, he has carried out an experimental data for the densities of liquids and vapors on the two-phase surface of system NaCl at same region of temperature, a range for which the system changes from subcritical behavior. Data for the NaCl critical line and for the three-phase assemblage halite+ liquid + vapor were first evaluated over a much wider T-P range.

Hydration of the bromine ion in a supercritical 1:1 aqueous electrolyte has been carried out by G. Ferlat et al [107,143]. Extended x-ray absorption fine structure (EXAFS) measurements have been carried out on 0.2 molal RbBr aqueous solutions at the Br-K edge from ambient to supercritical (SC) conditions, *i.e.* from density $\rho = 1.02$ to $\rho = 0.42$ g cm^{-3} and temperatures from 35 to 450 °C. The model used leads to an excellent agreement of the EXAFS spectra computed from the generated configurations with the experimental ones. Both show, in particular, a strong persistence of the Br^- ion first shell coordination at supercritical conditions. A strong reduction of the EXAFS amplitude is observed with decreasing value of the sample density. This is in good agreement with previous experiments of Wallen et al[149]. They interpreted this as a reduction of the hydration number of Br^-. In contrast, our simulations show a persistence of a high amount of water molecules around the Br^- ion in the SC state.

XAS measurements have been performed by Cécile da silva et al[108,138]. on both at the Ga and Br K-edges on aqueous $GaBr_3$ solutions. The isobaric experiments have been recorded at 30 MPa from ambient temperature to 670 K for two $GaBr_3$ concentrations (0.017 and 0.17 mol/dm^3). At room temperature, Ga^{3+} and Br^- ions are fully solvated, surrounded by water O atoms at 1.97 Å (Ga–O) and 3.37 Å (Br–O). When the temperature is elevated, Ga^{3+} cations precipitate as gallium oxy-hydroxide colloids while Br^- anions remain solvated. When the temperature increases, Ga^{3+} cations precipitate as $GaO(OH)_{(s)}$ in the temperature range over 370–600 K, while Br^- ions remain completely solvated. For higher temperatures, Ga^{3+} cations are remarkably re-dissolved (25% and 50% for 0.017 and 0.17 mol/dm^3 respectively), ion-pairing occurs and pure or mixture tetrahedral specie complexes are formed ($R_{Ga–Br}$=$R_{Br–Ga}$= ≈2.31 Å).

Table 16: Ion-pairing in aqueous solutions at supercritical conditions, M = mol / l

Ions	**Reference**	**Ion-pairing in supercritical conditions**
Zn^{2+} , Br^{-}	[150,151]	Ion-pairing for $ZnBr_4^{2-}$, $ZnBr_3^{-}$, $ZnBr_2$, and $ZnBr^{+}$ ([1.0M])
Na^{+}, Br^{-}, Cl^{-}, and I^{-}	[152]	Ion-pairing for NaBr, NaCl, and NaI compounds
Rb^{+}, Br^{-}	[149]	RbBr compound ([RbBr = 0.02 to 1.5M]) and [2M]
Ga^{3+}, Br^{-}	[138]	$GaBr_3$ ([0.017 and 0.17 mol/dm^3]).
Cs^{+}, Cl^{-}	[153]	CsCl compound with ([0.30 to 7.15M])
Na^{+}, Cl^{-}	[154], This study	NaCl compound ([0.3 to 1.1 M])
K^{+}, Rb^{+}, Cs^{+}, and Br^{-}	This study	KBr, RbBr and CsBr compounds with ([0.3M])
H^{+}, Br^{-}	This study	HBr compound with ([0.3M])
Rb^{+}, OH^{-}	This study	RbOH compound with ([0.3M])

Compares different systems probed by XAS where monovalent, divalent or trivalent cations are in aqueous solutionwith a halide anion (Br^{-} or Cl^{-}).We limit the comparison to the studies in which the initial concentration of salts in solution is low enough to avoid significant ion-pairing at ambient conditions. Ion-pairing has not been observed for monovalent systems, even if molecular dynamic simulations predict a significant amount of such pairing in supercritical conditions. Ion-pairing occurs for all these divalent or trivalent systems.

4.2 Solvent density measurements

A methodology based on simple X-Ray absorption is proposed to detect and observe the evolution of density of hydrothermal solution from ambiant to supercritical conditions. Phase-separation can also be detected and followed by this method. The water measurements has been carried out and compared with theoretical value. This comparison allows us to demonstrate the existence of a thermal gradient in our experimental setup. This gradients can be explained by 1) heat transfer and dissipation by materials used in our experimental set-up (Beryllium in windows, glassy carbon in sample container, pressurized helium, ceramics of furnace, ...), 2) design of the furnace containing three optical non heated windows, 3) water properties. Heat loss from the set-up is expected to increase linearly with temperature. Nonlinear dependence of T_{cell} - T_{real} value on density is observed for all pressures. These data reflect thermo physical properties of water. Despite the fact that heat transfer critical enhancement and possible heat transfer deterioration are difficult to be quantified from our measurements, some analogies can be drawn. Thus for example, the minimum gradient

roughly overlap with the maximum of specific heat capacity of H_2O when approaching the pseudocritical isochore (ρ_c = 0.322 g/cm^3) and thus this minimum seems to correlate with critical heat transfer enhancements. These new data allow to validate our experimental setup and to estimate the temperature gradients for other aqueous solutions.

4.3 Density anomaly and ion pairing

Conventional X-ray absorption spectroscopy (XAS) measurements on water and supercritical aqueous solutions (aqueous bromide, aqueous chloride, aqueous nitrate and aqueous sulfate) were carried out from ambient to supercritical conditions. The temperature was increased from 30 °C to 500 °C along several isobars between 280 and 400 bars. The incident energies were between 12.5 to 15.4 KeV. We obtained experimental evidence of the shift of the critical point and isochore and their dependence on the ions concentration of NaCl (0.3 mol/kg, 0.5 mol/kg and 1.0 mol/kg). We also observed the anomalous densities in supercritical region (SC) with a phase-separation with a compilation data for vapor-liquid for some aqueous solutions at given energy. The relative density increase in this critical zone is more pronounced in order Li < Na < K < Rb < Cs for both bromides and chlorides. Structural changing in SC region (anomalous density) leads to the existence of Ion-pairing.

The effects of temperature, density, and solution concentration have been explored in detail. The primary factor affecting the decrease in hydration under supercritical conditions is the high temperature of the system. The fluid density and the salt concentration have only a minor effect on the hydration structure. The interpretation of the XANES spectra clearly indicates a drastic change in the local structure of the fluid at the time of the appearance of this anomaly, which can be interpreted by the appearance of ion pairing. These new observations are related to the structural change of the solvent and mainly to the evolution of local structure of the solvent and the local order around ions.

Schematically, when increasing the temperature at a given pressure, a progressive dehydratation of ions is observed. Then correlated with critical heat transfer enhancements of water, we observe the formation of ion pairing leading to an suddenly jump in density. However, a first shell of solvatation is always presents, indicating certainly that we are in presence of outsphere complex. This anomaly is following by a demixion in two phases.

4.4 Perspectives

This work is based only on one method (XAS). Our observations need to be confirmed by complementary studies. It will be important to caracterized the structural change of the solvent by Raman. Indeed, Raman spectroscopy provides spectra of the water molecules vibrations and thus information about their geometrical organisation, related to the number and the arrangement of the hydrogen bonds. In complement, these measurements under supercritical conditions were also completed by “Ab initio” molecular dynamics calculation.

To confirm the density anomaly followed by the phase separation, we propose also to perform similar experiment below the critical point and to reproduce and caracterize the phase separation liquid vapor for pure water and sodium choride solution.

5. Bibliography

1. E. Lemmon, M. McLinden, and D. F. Thermophysical properties of fluid systems, in WebBook de Chimie NIST, Base de Donnees Standard de Reference NIST Numero 69, National Institute of Standards and Technology, edited by P.J. Linstrom and W.G. Mallard. Gaithersburg MD, 20899. (2000). Available at: http://webbook.nist.gov.

2. Testemale, D., Argoud, R., Geaymond, O. & Hazemann, J. L. High pressure/high temperature cell for x-ray absorption and scattering techniques. *Rev. Sci. Instrum.* **76,** 1–5 (2005).

3. Driesner, T. The system H2O-NaCl. Part II: Correlations for molar volume, enthalpy, and isobaric heat capacity from 0 to 1000°C, 1 to 5000 bar, and 0 to 1 XNaCl. *Geochim. Cosmochim. Acta* **71,** 4902–4919 (2007).

4. Driesner, T. & Heinrich, C. A. The system H2O-NaCl. Part I: Correlation formulae for phase relations in temperature-pressure-composition space from 0 to 1000°C, 0 to 5000 bar, and 0 to 1 XNaCl. *Geochim. Cosmochim. Acta* **71,** 4880–4901 (2007).

5. Povodyrev, A. & Anisimov, M. Critical locus of aqueous solutions of sodium chloride. *Int. J.* … **20,** 1529–1545 (1999).

6. Calculation of Density, Enthalpy and Entropy for Supercritical Carbon Dioxide with Examples. Available at: http://www.criticalprocesses.com/ Calculation %25 20 of %25 20 density, %25 20 enthalpy %25 20 and %25 20 entropy %25 20o f %25 20 carbon %25 20dioxide.htm. Retrieved, 12-17 (2007).

7. Sapkale, G. N., Patil, S. M., Surwase, U. S. & Bhatbhage, P. K. Supercritical Fluid Extraction. *Int. J. Chem. Sci* **8,** 729–743 (2010).

8. Model fitting with Ifeffit ‘Athena, Artemis, and Hephaestus, XAS Data Analysis Software’. Available at: http://bruceravel.github.io/demeter/.

9. CSRRI ‘Center for Synchrotron Radiation Research and Instrumentation’. *Illinois institute of technology* Available at: https://web.iit.edu/csrri.

10. A.A. Povodyrev, M.A. Anisimov, J.V. Sengers, W. L. Marshall, and J. M. H. L. S. Critical Locus of Aqueous Solutions of Sodium Chloride. *Int. J. Thermophys* **20,** 1529–1545 (1999).

11. Guissani, Y. & Guillot, B. a Computer Simulation Study of the Liquid-Vapourr Coexistence Curve of Water. *J. Chem. Phys.* **98,** 8221 (1993).

12. D. A. Palmer, R. Fernández - Prini, A. H. H. Aqueous Systems at Elevated Temperatures and Pressures: Physical Chemistry in Water, steam and Hydrothermal Solutions. *Elsevier Ltd* (2004).

13. Yao, Makoto, Y. H. Dielectric Relaxation of supercritical water and methanol. *J. Mol. Liq.* **97,** 207–220 (2002).

14. Arai, A. A., Morita, T. & Nishikawa, K. Analysis to obtain precise density fluctuation of supercritical fluids by small-angle X-ray scattering. *Chem. Phys.* **310,** 123–128 (2005).

15. Mason, P. E. & Brady, J. W. ‘ Tetrahedrality ’ and the Relationship between Collective Structure and Radial Distribution Functions in Liquid Water ‘ Tetrahedrality ’ and the Relationship between Collective Structure and Radial Distribution Functions in Liquid Water. *Society* 5669–5679 (2007). doi:10.1021/jp068581n

16. L. J. Henderson. The Fitness of the Environment, an Inquiry Into the Biological Significance of the Properties of Matter. *Am. Nat.* **Vol. 47,** 105–115 (1913).

17. Yamaguchi, T. *et al.* Collective dynamics of supercritical water. *J. Phys. Chem. Solids* **66,** 2246–2249 (2005).

18. Prendergast, D. & Galli, G. X-ray absorption spectra of water from first principles calculations. *Phys. Rev. Lett.* **96,** 1–4 (2006).

19. Skarmoutsos, I. & Samios, J. Local density inhomogeneities and dynamics in supercritical water: A molecular dynamics simulation approach. *J. Phys. Chem. B* **110,** 21931–21937 (2006).

20. Supercritical Fluid Extraction, Density Considerations. Available at: http://eng.ege.edu.tr/ ~otles/ SupercriticalFluidsScienceAndTechnology/ Wc488d76f2c655.htm. Retrieved 2007-11-20.

21. T.Tassaing, Y.Danten, M. B. Infrared spectroscopic study of hydrogen-bonding in water at high temperature and pessure. *J. Chem. Phys.* **3,** 149–158 (2002).

22. Head-Gordon, T. & Hura, G. Water structure from scattering experiments and simulation. *Chem. Rev.* **102,** 2651–2669 (2002).

23. Beta, I. A., Li, J.-C. & Bellissent-Funel, M.-C. A quasi-elastic neutron scattering study of the dynamics of supercritical water. *Chem. Phys.* **292,** 229–234 (2003).

24. Smith, J. D. *et al.* Probing the Local Structure of Liquid Water by X-ray Absorption Spectroscopy<img src=‘http://pubs.acs.org/images/entities/dagger.gif’ border=‘0’>. *J. Phys. Chem. B* 20038–20045 (2006). doi:10.1021/jp063661c

25. Fukui, H., Huotari, S., Andrault, D. & Kawamoto, T. Oxygen K-edge fine structures of water by x-ray Raman scattering spectroscopy under pressure conditions. *J. Chem. Phys.* **127,** 134502 (2007).

26. Wimby, J. M. & Berntsson, T. S. Viscosity and Density of Aqueous Solutions of LiBr, LiCl,ZnBrz, CaC12, and LiN03, 1, Single Salt Solutions. *J. Chem. Eng. Data* 68–72 (1994). doi:10.1021/je00013a019

27. Pioro, I. & Mokry, S. Thermophysical Properties at Critical and Supercritical Conditions. *Heat Transf. - Theor. Anal. Exp. Investig. Ind. Syst.* 573–592 (2011). doi:10.5772/13790

28. PHYSICS: Boundary between supercritical fluid and gaseous phase. Available at: http://physics.stackexchange.com/questions/75087/boundary-between-supercritical-fluid-and-gaseous-phase.

29. Wagner, W., Saul, A. & Pruss, A. International Equations for the Pressure Along the Melting and Along the Sublimation Curve of Ordinary Water Substance. *J. Phys. Chem. Ref. Data* **23,** 515–527 (1994).

30. Cansell F., M.H. Delville, and P. S. *Fluides Supercritiques et Matériaux. Ed. par l'Institut National Polytechnique de Lorraine*. (Institut National Polytechnique de Lorraine, 1999. École d'été, 1999).

31. Cécile Da Silva. Études Structurales Et Vibrationelles Des Liaisons Hydrogène En Solution Aqueuse Supercritique. (Joseph Fourier University, 2008).

32. Ohtaki, H. Effects of temperature and pressure on hydrogen bonds in water and in formamide. *J. Mol. Liq.* **103–104,** 3–13 (2003).

33. Verma, M. P. Steam tables for pure water as an ActiveX component in Visual Basic 6.0. *Comput. Geosci. AA(Geotermia, Inst. Investig. Electr. Av. Reforma 113, Col. Palmira, Apartado Post. 1-475, Cuernavaca Morelos 62490, Mex.* **29,** 1155–1163 (2003).

34. Monika Fuxreiter, Mihaly Mezei, István Simon, R. O. Interfacial water as a 'hydration fingerprint' in the noncognate complex of BamHI. *Biophys. J.* **89,** 903–911 (2005).

35. Wernet, P. *et al.* Spectroscopic characterization of microscopic hydrogen-bonding disparities in supercritical water. *J. Chem. Phys.* **123,** (2005).

36. M. Bernabei, A. Botti, F. Bruni, M. A. Ricci, and A. K. S. Percolation and three-dimensional structure of supercritical water. *Phys. Rev. E 78, 021505* **78,** (2008).

37. Gerschel, A. *Liaisons intermoléculaires. Les forces en jeu dans la matière condensée*. (1995).

38. J.H. Guo, Y. Luo, A. Augustsson, J.E. Rubensson, C. Såthe, H. Å. & H. Siegbahn, and J. N. X-ray emission spectroscopy of hydrogen bonding and electronic structure of liquid water. *Phys. Rev. Lett.* **89,** 137402 (2002).

39. Sit, P. H. L. *et al.* Hydrogen bonding and coordination in normal and supercritical water from x-ray inelastic scattering. *Phys. Rev. B - Condens. Matter Mater. Phys.* **76,** 1–7 (2007).

40. Kumar, R., Schmidt, J. R. & Skinner, J. L. Hydrogen bonding definitions and dynamics in liquid water. *J. Chem. Phys.* **126,** 1–12 (2007).

41. Jorgensen, W. L., Chandrasekhar, J., Madura, J. D., Impey, R. W. & Klein, M. L. Comparison of simple potential functions for simulating liquid water. *J. Chem. Phys.* **79,** 926 (1983).

42. Guillot, B. A reappraisal of what we have learnt during three decades of computer

simulations on water. *J. Mol. Liq.* **101,** 219–260 (2002).

43. Isaacs, E. D. *et al.* Covalency of the Hydrogen Bond in Ice: A Direct X-Ray Measurement. *Phys. Rev. Lett.* **82,** 600–603 (1999).

44. Ghanty, T. K., Staroverov, V. N., Koren, P. R. & Davidson, E. R. Is the hydrogen bond in water dimer and ice covalent? *J. Am. Chem. Soc.* **122,** 1210–1214 (2000).

45. Romero, A. H., Silvestrelli, P. L. & Parrinello, M. Compton scattering and the character of the hydrogen bond in ice Ih. *J. Chem. Phys.* **115,** 115–123 (2001).

46. Poater, J., Fradera, X., Solà, M., Duran, M. & Simon, S. On the electron-pair nature of the hydrogen bond in the framework of the atoms in molecules theory. *Chem. Phys. Lett.* **369,** 248–255 (2003).

47. Gorbaty, Y. E. & Kalinichev, A. G. Hydrogen Bonding in Supercritical Water. 1. Experimental Results. *J. Phys. Chem.* **99,** 5336–5340 (1995).

48. Mizan, T. I., Savage, P. E. & Ziff, R. M. Temperature dependence of hydrogen bonding in supercritical water. *J. Phys. Chem. A* **100,** 403–408 (1996).

49. Barbiellini, B. & Shukla, A. Ab initio calculations of the hydrogen bond. *Phys. Rev. B* **66,** 235101–4 (2002).

50. Postorino, P., Tromp, R.H., Ricci, M-A., Soper, A.K., Neilson, G. W. The Interatomic Structure of Water at Supercritical Temperatures. *Nature* **363,** 210–211 (1993).

51. Hoffmann, M. M. & Conradi, M. S. Are there hydrogen bonds in supercritical water? *J. Am. Chem. Soc.* **119,** 3811–3817 (1997).

52. A. A. Chialvo, P. T. C. Hydrogen bonding in supercritical water. *J. Chem. Phys.* **101,** 4466–4469 (1994).

53. Yamanaka, K., Yamaguchi, T. & Wakita, H. Structure of water in the liquid and supercritical states by rapid x-ray diffractometry using an imaging plate detector. *J. Chem. Phys.* **101,** 9830–9836 (1994).

54. Narten, A. & Levy, H. Liquid Water: Molecular Correlation Functions from X-Ray Diffraction. *J. Chem. Phys.* **55,** 2263–2269 (1971).

55. Soper, A. K.; Bruni, F.; Ricci, M. A. Bridge over troubled water: the apparent discrepancy between simulated and experimental non-ambient water structure. *J. Phys. Condens. Matter* 9263–9267 (1996).

56. Soper, a K., Bruni, F. & Ricci, M. a. Site–site pair correlation functions of water from 25 to 400° C: Revised analysis of new and old diffraction data. *J. Chem. Phys.* **106,** 247 (1997).

57. Hura, G. *et al.* A high-quality x-ray scattering experiment on liquid water at ambient conditions A high-quality x-ray scattering experiment on liquid water at ambient conditions. **9140,** 3–5 (2013).

58. Postorino, P., Ricci, M. A. & Soper, A. K. Water above its boiling point: Study of the temperature and density dependence of the partial pair correlation functions. I. Neutron diffraction experiment. *J. Chem. Phys.* **101,** 4123 (1994).

59. Roberto J. Fernandez-Prini, Horacio R. Corti, M. L. J. *High-temperature aqueous solutions : thermodynamic properties*. (CRC Press, Boca Raton, 1992).

60. Ikushima, Y., Hatakeda, K., Saito, N. & Arai, M. An in situ Raman spectroscopy study of subcritical and supercritical water: The peculiarity of hydrogen bonding near the critical point. *J. Chem. Phys.* **108,** 5855–5860 (1998).

61. Tassaing, T., Bellissent-Funel, M. C., Guillot, B. & Guissani, Y. The partial pair correlation functions of dense supercritical water. *Eur. Lett.* **42,** 265–270 (1998).

62. Yamaguchi, T. Structure of subcritical and supercritical hydrogen-bonded liquids and solutions. *J. Mol. Liq.* **78,** 43–50 (1998).

63. Harriman, A. & Sauvage, J.-P. A strategy for constructing photosynthetic models: porphyrin-containing modules assembled around transition metals. *Chem. Soc. Rev.* **25,** 41 (1996).

64. Tucker, S. C. Solvent Density Inhomogeneities in Supercritical Fluids. *Chem. Rev.* **99,** 391–418 (1999).

65. Lívia Pártay and Pál Jedlovszky. Line of percolation in supercritical water. *J. Chem. Phys.* **123,** 1–6 (2005).

66. Kalinichev, A. G. & Churakov, S. V. Size and topology of molecular clusters in supercritical water: a molecular dynamics simulation. *Chem. Phys. Lett.* **302,** 411–417 (1999).

67. C.A Eckert, D.H Ziger, K.P. Johnston, T. K. E. The use of partial molal volume data to evaluate equations of state for supercritical fluid mixtures. *Fluid Phase Equilib.* **14,** 167–175 (1983).

68. Stanley, H. E. *Introduction to phase transitions and critical phenomena*. (1971).

69. Tucker, S. C. & Maddox, M. W. The Effect of Solvent Density Inhomogeneities on Solute Dynamics in Supercritical Fluids: A Theorethical Perspective. *J Phys Chem B* **102,** 2437–2453 (1998).

70. Jay-Gerin, J. P. *et al.* Effect of water density on the absorption maximum of hydrated electrons in sub- and supercritical water up to 400 °c. *J. Chem. Phys.* **129,** (2008).

71. Egorov, S. A. Local density augmentation in attractive supercritical solutions. III. How important is the solute-solvent interaction range? *J. Chem. Phys.* **116,** 2004–2010 (2002).

72. Egorov, S. A. Local density augmentation in attractive supercritical solutions. II. Application to electronic line shifts. *J. Chem. Phys.* **113,** 1950–1957 (2000).

73. Chialvo, A. A., Cummings, P. T., Cochran, H. D., Simonson, J. M. & Mesmer, R. E. Na+–Cl− ion pair association in supercritical water. *J. Chem. Phys.* **103,** 9379 (1995).

74. Petsche, I. B. & Debenedetti, P. G. Solute-solvent interactions in infinitely dilute supercritical mixtures: a molecular dynamics investigation. *J. Chem. Phys.1* **91,** 7075–7084 (1989).

75. NISHIKAWA, K. & TANAKA, I. Correlation Lengths and Density-fluctuations In Supercritical States of Carbon-dioxide. *Chem. Phys. Lett.* **244,** 149–152 (1995).

76. Narikiyo, O. Comment on "correlation length and density fluctuations in supercritical states of carbon dioxide. *Chem. Phys. Lett.* **290,** 188 (1997).

77. Narikiyo, O. Comment on "correlation length and density fluctuations in supercritical states of carbon dioxide. *Chem. Phys. Lett.* **290,** 185–187 (1997).

78. Nishikawa, K. & Morita, T. Inhomogeneity of molecular distribution in supercritical fluids. *Chem. Phys. Lett.* **316,** 238–242 (2000).

79. Nishikawa, K., Tanaka, I. & Amemiya, Y. Small-Angle X-ray Scattering Study of Supercritical Carbon Dioxide. *J. Phys. Chem.* **100,** 418–421 (1996).

80. Morita, T., Kusano, K., Ochiai, H., Saitow, K. & Nishikawa, K. Study of inhomogeneity of supercritical water by small-angle x-ray scattering. *J. Chem. Phys.* **112,** 4203–4211 (2000).

81. Sullivan, D. & Neilson, G. Small angle neutron scattering from D2O in the critical region. *J. Phys.* … **3531,** (2000).

82. Bonetti, M., Romet-Lemonne, G., Calmettes, P. & Bellissent-Funel, M. C. Small-angle neutron scattering from heavy water in the vicinity of the critical point. *J. Chem Phys.* **112,** 268–274 (2000).

83. Testemale, D. Structures locales en solution aqueuse supercritique. (Joseph Fourier University, 2003).

84. Driesner, T.; Seward, T. M.; Tironi, I. G. Molecular dynamics simulation study of ionic hydration and ion association in dilute and 1 molal aqueous sodium chloride solutions from ambient to supercritical conditions. *Geochim. Cosmochim. Acta* **62,** 3095–3107 (1998).

85. Egorov, S. ., Yethiraj, a & Skinner, J. . Local density enhancement in dilute supercritical solutions. *Chem. Phys. Lett.* **317,** 558–566 (2000).

86. Gao, J. Simulation of the Na+Cl- Ion Pair in Supercritical Water. *J. Phys. Chem.* **98,** 6049–6053 (1994).

87. Kanakubo, M. *et al.* Studies on solute-solvent interactions in gaseous and supercritical carbon dioxide by high-pressure H-1 NMR spectroscopy. *J. Phys. Chem. B* **104,** 2749–2758 (2000).

88. J.-P. Hansen, I. R. M. *Theory of simple liquids*. (Academic Press, 1976).

89. Robinson, R. A.; Stokes, R. H. *Electrolyte Solutions*. (Butterworth: London, 1965).

90. Harned, H. S.; Owen, B. B. *The Physical Chemistry of Electrolytic Solutions*. (1985).

91. Kajimoto, O. Solvation in supercritical fluids: Its effects on energy transfer and chemical reactions. *Chem. Rev.* **99,** 355–389 (1999).

92. Cacace MG, Landau EM, R. J. The Hofmeister series: salt and solvent effects on interfacial phenomena. *Q Rev Biophys* 30:241–77 (1997).

93. Marcus, Y. ViscosityB-coefficients, structural entropies and heat capacities, and the effects of ions on the structure of water. *J. Solution Chem.* **23,** 831 (1994).

94. Marcus, Y. & Hefter, G. Ion pairing. *Chem. Rev.* **106,** 4585–4621 (2006).

95. Collins, K. D. Charge Density-Dependent Strength. **72,** 65–76 (1997).

96. Scheiman, M. a. & Jarvis, N. L. Surface potentials of aqueous electrolyte solutions. *J. Phys. Chem.* **72,** 74–78 (1968).

97. Leberman, R. & Soper, A. K. Effect of high salt concentrations on water structure. *Nature* **378,** 364–366 (1995).

98. Solutions, A., Conference, G., Physics, C. & Issue, S. Preface. *Chem. Phys.* **258,** 107–108 (2000).

99. Petsche, I. B. & Debenedetti, P. G. Influence of solute-solvent asymmetry upon the behavior of dilute supercritical mixtures. *J. Phys. Chem.* **95,** 386–399 (1991).

100. Debenedetti, P. G. Clustering in dilute, binary supercritical mixtures: A fluctuation analysis. *Chem. Eng. Sci.* **42,** 2203–2212 (1987).

101. Chialvo, A. A., Cummings, P. T., Simonson, J. M. & Mesmer, R. E. Solvation in high-temperature electrolyte solutions. I. Hydration shell behavior from molecular simulation. *J. Chem. Phys.* **110,** 1064–1074 (1999).

102. Pauling, L. *The nature of the chemical bond*. (Cornell University Press, 1948).

103. Monk, C. B. *Electrolytic Dissociation*. (Academic Press: London, 1961).

104. Davies, C. W. *Ion Association*. (Butterworth: London, 1962).

105. Buchner, R., Samani, F., May, P. M., Sturm, P. & Hefter, G. Hydration and ion pairing in aqueous sodium oxalate solutions. *ChemPhysChem* **4,** 373–378 (2003).

106. Pauling, L. *General Chemistry*. (Linus Pauling Institute of Science and Medicine, 1970).

107. Ferlat, G. *et al.* The quest for ion pairing in supercritical aqueous electrolytes. *J. Mol.*

Liq. **101,** 127–136 (2002).

108. Da Silva-Cadoux, C., Hazemann, J. L., Testemale, D., Proux, O. & Rochas, C. Influence of monovalent ions on density fluctuations in hydrothermal aqueous solutions by small angle X-ray scattering. *J. Chem. Phys.* **136,** (2012).

109. Bordwehr, R. S. von. A History of X-ray absorption fine structure. *Ann. Phys. Fr.* **14,** 377–465 (1989).

110. Rehr JJ, A. R. Theoretical approaches to x-ray absorption fine structure. *Rev. Mod. Phys. 73 [3] 621-654* (2000).

111. *X-Ray Absorption: Principles, Applications, Techniques of EXAFS, SEXAFS and XANES*. (1988).

112. D.E. Sayers, E. A. S. and F. W. L. New technique for investigating noncrystalline structures: Fourier analysis of the extended x-ray absorption fine structure. *Phys. Rev. Lett.* **1204,** (1971).

113. Newville, M. *Fundamentals of XAFS*. (Consortium for Advanced Radiation Sources, 2004).

114. Ortega, R., Carmona, A., Llorens, I. & Solari, P. L. X-ray absorption spectroscopy of biological samples. A tutorial. *J. Anal. At. Spectrom.* **27,** 2054–2065 (2012).

115. Y., J. X-ray absorption near edge structure calculations beyond the mufin-tin approximation. *Phys. Rev. B63 125120-1-10* (2001).

116. Llorens, I. *et al.* High energy resolution five-crystal spectrometer for high quality fluorescence and absorption measurements on an x-ray absorption spectroscopy beamline. *Rev. Sci. Instrum.* **83,** (2012).

117. E. Collart, A. Shukla, F. Gélébart, M. Morand, C. Malgrange, N. Bardou, A. Madouri, and J.-L. P. Spherically bent analyzers for resonant inelastic X-ray scattering with intrinsic resolution below 200 meV. *J. Synchrotron Radiat.* **12,** 473–478 (2005).

118. C. Masciovecchio, U. Bergmann, M. Krisch, G. Ruocco, F. Sette, R. V. A perfect crystal X-ray analyser with meV energy resolution. *Nucl. Instruments Methods Phys. Res. Sect. B Beam Interact. with Mater. Atoms* **111,** 181–186 (1996).

119. Rovezzi, M., Lapras, C., Manceau, A., Glatzel, P. & Verbeni, R. High energy-resolution x-ray spectroscopy at ultra-high dilution with spherically bent crystal analyzers of 0.5 m radius. 1–9 (2016). doi:10.1063/1.4974100

120. Hazemann, J. *et al.* High Resolution Spectroscopy on an X-ray Absorption Beamline To cite this version : *J. Synchrotron Radiat.* **16,** 283–292 (2008).

121. Proux, O. *et al.* Feedback system of a liquid nitrogen cooled double-crystal monochromator : design and performances To cite this version : monochromator : design and performances. *J. Synchrotron Radiat.* **13,** 59–68 (2006).

122. Stern, E. a & Heald, S. M. X-ray filter assembly for fluorescence measurements of x-ray absorption fine structure. *Rev. Sci. Instrum.* **50,** 1579 (1979).

123. Bruyère, R., Prat, A., Goujon, C. & Hazemann, J. A new pressure regulation device using high pressure isolation valves. *J. Phys. Conf. Ser.* **121,** 2–5 (2008).

124. O. Sohnel and P. Novotny. *Densities of Aqueous Solutions of Inorganic Substances*. (Physical Sciences Data Series, 1984).

125. Ivan D. Zaytsev and Georgiy G. Aseyev. *Properties of Aqueous Solutions of Electrolytes*.

126. Morita, T., Takahashi, Y., Tanaka, Y., Arai, A. A. & Nishikawa, K. Density dependences of long-range fluctuations and short-range correlation lengths of CHF3 and CH2F2 in supercritical states. *J. Chem. Phys.* **124,** (2006).

127. Proux, O. *et al.* FAME: a new beamline for x-ray absorption investigations of very-diluted systems of environmental, material and biological interests. *Phys. Scr. Phys. Scr.* **115,** 970–973 (2005).

128. Grundler, P. V. *et al.* Speciation of aqueous tellurium(IV) in hydrothermal solutions and vapors, and the role of oxidized tellurium species in Te transport and gold deposition. *Geochim. Cosmochim. Acta* **120,** 298–325 (2013).

129. Liu, W. *et al.* Speciation and thermodynamic properties for cobalt chloride complexes in hydrothermal fluids at 35-440°C and 600bar: An in-situ XAS study. *Geochim. Cosmochim. Acta* **75,** 1227–1248 (2011).

130. Etschmann, B. E. *et al.* An in situ XAS study of copper(I) transport as hydrosulfide complexes in hydrothermal solutions (25-592??C, 180-600bar): Speciation and solubility in vapor and liquid phases. *Geochim. Cosmochim. Acta* **74,** 4723–4739 (2010).

131. Brugger, J. *et al.* An XAS study of the structure and thermodynamics of Cu(I) chloride complexes in brines up to high temperature (400 °C, 600 bar). *Geochim. Cosmochim. Acta* **71,** 4920–4941 (2007).

132. Bischoff, J. and Pitzer, K. Liquid-Vapor relations for the system NaCl-H2O: Summary of the P-T-x surface from 300 °C to 500 °C. *Am. J. Sci.* **289,** 217–248 (1989).

133. Wernet, P. *et al.* Spectroscopic characterization of microscopic hydrogen-bonding disparities in supercritical water. *J. Chem. Phys.* **123,** 1–7 (2005).

134. Voisin, T. *et al.* Solubility of inorganic salts in sub- and supercritical hydrothermal environment: Application to SCWO processes. *J. Supercrit. Fluids* **120,** 18–31 (2017).

135. Burattini, E., Dangelo, P., Giglio, E., and Pavel, N. V. Exafs study of probe molecules in micellar solutions. *J. Phys. Chem.* **95,** 7880–7886 (1991).

136. Sessa, F., D'Angelo, P., Guidoni, L. & Migliorati, V. Hidden Hydration Structure of Halide Ions: An Insight into the Importance of Lone Pairs. *J. Phys. Chem. B* **119,** 15729–15737 (2015).

137. Brugger J., Liu W., Etschmann B., Mei Y., Sherman D. M., T. D. A review of the coordination chemistry of hydrothermal systems, or do coordination changes make ore deposits? *Chem. Geol.* **447,** 219–253 (2016).

138. Da Silva, C. *et al.* X-ray absorption spectroscopy study of solvation and ion-pairing in aqueous gallium bromide solutions at supercritical conditions. *J. Mol. Liq.* **147,** 83–95 (2009).

139. Merkling P. J., Ayala R., Martínez J. M., Pappalardo R. R., S. M. E. Interplay of computer simulations and x-ray absorption spectra in the study of the bromide hydration structure. *J. Chem. Phys.* **119,** 6647–6654 (2003).

140. Simonet, V. X-ray absorption spectroscopy studies of ionic association in aqueous solutions of zinc bromide from normal to critical conditions. **117,** 7–15 (2002).

141. Simonet, V. *et al.* Structure of aqueous ZnBr 2 solution probed by x-ray absorption spectroscopy in normal and hydrothermal conditions. **116,** 2997–3006 (2002).

142. Chen, Y., Fulton, J. L. & Partenheimer, W. The Structure of the Homogeneous Oxidation Catalyst , Mn (II)(Br - 1) x , in Supercritical Water : An X-ray Absorption Fine-Structure Study. *J. Am. Chem. Soc. 127* 14085–14093 (2005).

143. Ferlat, G. *et al.* Hydration of the bromine ion in a supercritical 1:1 aqueous electrolyte. *Phys. Rev. B* **63,** 134202 (2001).

144. D'Angelo P., Di Cicco A., Filipponi A., P. N. V. Double-electron excitation channels at the Br K edge of HBr and Br2. *Phys. Rev. A 47* 2055–2063 (1993).

145. Y. Ito, T. Mukoyama, S. Emura, M. Takahashi, S. Yoshikado, and K. O. X-ray absorption structures of multielectron excitation in Br. *Phys. Rev. A 51* **51,** 303–308 (1995).

146. J. Padežňik Gomilšek, A. Kodre, I. Arčon, A. M. L.-L. and S. B. Multielectron photoexcitations in x-ray-absorption spectra of 4p elements. *Phys. Rev. A 59* 3078–3081 (1999).

147. Antalek, M. *et al.* Solvation structure of the halides from x-ray absorption spectroscopy. *J. Chem Phys.* 44318 (2016). doi:10.1063/1.4959589

148. Ruffoni M. P., Pettifer R. F., Pascarelli S., Trapananti A., M. O. An introduction to differential EXAFS. *AIP Conf. Proc.* **882,** 838–840 (2007).

149. Wallen, S. L. *et al.* Hydration of Bromide Ion in Supercritical Water: An X-ray Absorption Fine Structure and Molecular Dynamics Study. *J.Phys.Chem.A* **101,** 9632–9640 (1997).

150. Mibe, K., Chou, I.-M., Anderson, A. J., Mayanovic, R. A. & Bassett, W. A. The speciation of aqueous zinc(II) bromide solutions to 500 °C and 900 MPa determined using Raman spectroscopy. *Chem. Geol.* **259,** 48–53 (2009).

151. Testemale, D. *et al.* Small angle x-ray scattering of a supercritical electrolyte solution:

The effect of density fluctuations on the hydration of ions. *J. Chem. Phys.* **122,** 194505 (2005).

152. Rogers, D. M. & Beck, T. L. Quasichemical and structural analysis of polarizable anion hydration. *J. Chem. Phys.* **132,** 1–12 (2010).

153. Max, J.-J. & Chapados, C. Infrared spectra of cesium chloride aqueous solutions. *J. Chem. Phys.* **113,** 6803–6814 (2000).

154. Bondarenko, G. V., Gorbaty, Y. E., Okhulkov, A. V. & Kalinichev, A. G. Structure and hydrogen bonding in liquid and supercritical aqueous NaCl solutions at a pressure of 1000 bar and temperatures up to 500 ??C: A comprehensive experimental and computational study. *J. Phys. Chem. A* **110,** 4042–4052 (2006).